SHOALING INTERNAL SOLITARY WAVES

MARINA BLOKHINA


CENTRE FOR NFLD. STUDIES
MEMORIAL UNIVERSITY
OF NEWFOUNDLAND

SHOALING INTERNAL SOLITARY WAVES

by

Marina Blokhina

A thesis submitted to the
School of Graduate Studies
in partial fulfilment of the
requirements for the degree of
Doctor of Philosophy

Department of Physics and Physical Oceanography
Memorial University of Newfoundland

May 2009

St. John's Newfoundland

Abstract

Internal solitary waves are encountered throughout the ocean and are a key part of coastal water dynamics. With the theoretical basis developed for infinitesimally small weakly-nonlinear waves several decades ago and a fully nonlinear theory still under development, internal waves remain on the front edge of ocean science.

In the present study, properties of high-frequency internal solitary waves propagating in a shallow water environment are studied using both field observations and numerical simulations. An array of bottom moorings and shipboard instruments are used to track internal wave packets propagating towards the flank of the Ile-aux-Lièvres Island (St. Lawrence Estuary). The transformation leading to dissipation of a wave of depression into a number of waves of elevation is documented. The observed spatio-temporal wave characteristics are compared to the first-order Korteveg-de Vries theory and a fully nonlinear two-layer theory.

High resolution two-dimensional nonhydrostatic numerical simulations are performed to supplement the field observations. The focus is on the properties of internal waves of elevation (often referred to as boluses) resulting from the shoaling of the wave of depression onto a linear slope. A hypothesis that boluses play a significant role in mass transport is tested.

This work contributes to better understanding of the mechanisms of internal wave shoaling over linear slopes. The formation of the trapped cores inside waves of elevation is demonstrated using nonhydrostatic numerical simulations. To our knowledge this is a novel result which helps to explain field and laboratory observations of trapped cores. The detailed study of the transport properties of waves of elevation is also done. A simple parametrization of the mass transport caused by waves of elevation is proposed.

Acknowledgements

Writing Acknowledgement section is the last but the most pleasant moment before submitting the finished work. So much time, paper and ink was spent but so many wonderful people were met and so many interesting things happened. I would love to thank all people who were nearby all these years and who help me in many different ways: those who taught the ABC of Oceanography or gave a hand to tackle Matlab problems, those who assisted with scientific issues and those who just gave a smile and a word of support during occasional meetings in the MUN corridors or on the street.

Some of particular people and things who deserve my special gratitude include:

- My supervisor Daniel Bourgault for giving me a chance to work together, for teaching and guidance, for his contagious perpetual energy, for the ability and desire to explain things clearly and simply... I am also grateful to him for developing and sharing a numerical model which became a foundation and a starting point of this study, and for teaching how to use it. I wish to express my special thanks to Daniel for not being bored (or at least not showing that) of reading many written iterations which eventually transformed into this thesis.

- Advising committee - Yakov Afanasyev and Brad deYoung - for valuable ideas which helped to improve the thesis

- The department of Physics and Physical Oceanography for assisting me in all possible issues, for always friendly atmosphere, and for not being just a bureaucratic machine

- My family who is thousands miles away but is always close spiritually for constant care and support throughout my life and these years in particular.

- My little Taras who taught me to value every spare minute, not to sleep at nights and thus to have the most productive time for work.
- Vasily for not letting me give up, for sharing sleepless nights near the computer, for unconditional love and support.
- Everyone who was involved in planning, preparation and carrying on a field work which probably was the most exiting time during my study: again Daniel, Peter Galbraith, Dan Kelley, Jack Foley, Ramzi Mirshak, people who found and returned lost thermistor chain with collected data and all others who was a part of the SLEIWEX project.
- Ivan for helping with corrections and English grammar.
- My dear friends just for being friends.
- Newfoundland weather for not being too good but rather harsh rainy/snowy, windy, foggy etc., which kept me at the office desk.
- NSERC for giving a generous financial support

Sorry to those whom I unintentionally forgot to include I thank you all.

Table of Contents

List of Symbols

List of Figures

List of Tables

Chapter 1

Introduction

1.1 Background and motivation of the study

Wind-driven surface gravity waves are easily observed on the surface of the ocean. Internal waves (IWs), as it is clear from their name, travel in the ocean interior. However, they can also be observed on the ocean surface. With remote sensing techniques, IWs are detected as a series of divergence and convergence slicks with variable sea-surface roughness. Observational results suggest that surface manifestations of internal waves most often arise in places with a rough topography, in the vicinity of banks or islands, on the shelf boundary, in straits, in regions with shear instabilities caused by strong currents, or when the sharp sloping pycnocline is situated close to the surface [*Fedorov and Ginzburg*, 1992]. Historical mention of surface manifestations of oceanic IWs date back to medieval times [*Cartwright*, 1999]. It is now clear that IWs are widespread in the ocean [*Apel*, 2002; *Helfrich and Melville*, 2006; *Staquet*, 2004], lakes [*Boegman et al.*, 2005; *Hutter et al.*, 1998], fjords [*Farmer and Armi*, 1999; *Farmer and Smith*, 1977] and estuaries [*Bourgault and Kelley*, 2003; *Bourgault et al.*, 2005] and play an important role in their dynamics. At the present time, sea-surface signatures of internal waves are routinely detected using optical and radar satellite images [*Apel*, 2002].

IWs owe their existence to the stratified nature of the fluid. A parcel of water within a fluid with a stable stratification will return to its equilibrium position if it has been displaced

from it. The motion of perturbed fluid parcels sets up an oscillation that forms an internal wave with frequency ω. The buoyancy restoring forces acting on a fluid parcel displaced from its equilibrium state depend on the local density difference, which can be characterized by the Brunt-Väisälä (or buoyancy) frequency N defined as

$$[N(z)]^2 = -\frac{g}{\rho_0}\frac{\partial \rho}{\partial z}, \tag{1.1}$$

where g denotes the acceleration of gravity, z is the vertical (upward) coordinate, ρ is the local fluid density and ρ_0 is the reference density. The buoyancy frequency is the maximum allowed frequency with which a wave can propagate. Only internal waves with frequencies $\omega \leq N$ can propagate freely. The lower limit of internal wave frequencies is the Coriolis frequency, f, defined as $f = 2\Omega \sin \varphi$, where Ω is the angular velocity of the earth's rotation and φ is the latitude. On the basis of extensive field studies, *Garrett and Munk* [1979] confirmed that frequencies of most internal waves fall into the range

$$f \leq \omega \leq N. \tag{1.2}$$

The wave frequencies and associated energies form a continuous spectrum (often called the Garret-Munk spectrum, *Garrett and Munk* [1979]), where waves of low frequency have more energy, while those of high frequency have less energy (Figure 1.1).

When an internal wave of frequency ω propagates in a continuously stratified fluid, it is free to move in any direction. The angle of propagation with respect to the vertical, θ, (or the group velocity vector direction) depends on the buoyancy and Coriolis frequencies through the dispersion relation [*LeBlond and Mysak*, 1978]:

$$\omega^2 = N^2 \cos^2 \theta + f^2 \sin^2 \theta. \tag{1.3}$$

If the frequency of the internal wave is close to f, the fluid particle motion is almost horizontal and circular [*Garrett and Munk*, 1979]. However, if the frequency ω approaches N, fluid particle motion inside the wave follows an ellipse inclined to the horizontal and tending to an up-and-down motion at $\omega = N$. At this limit the motion of particles is purely vertical and the wave energy propagates in a purely horizontal direction.

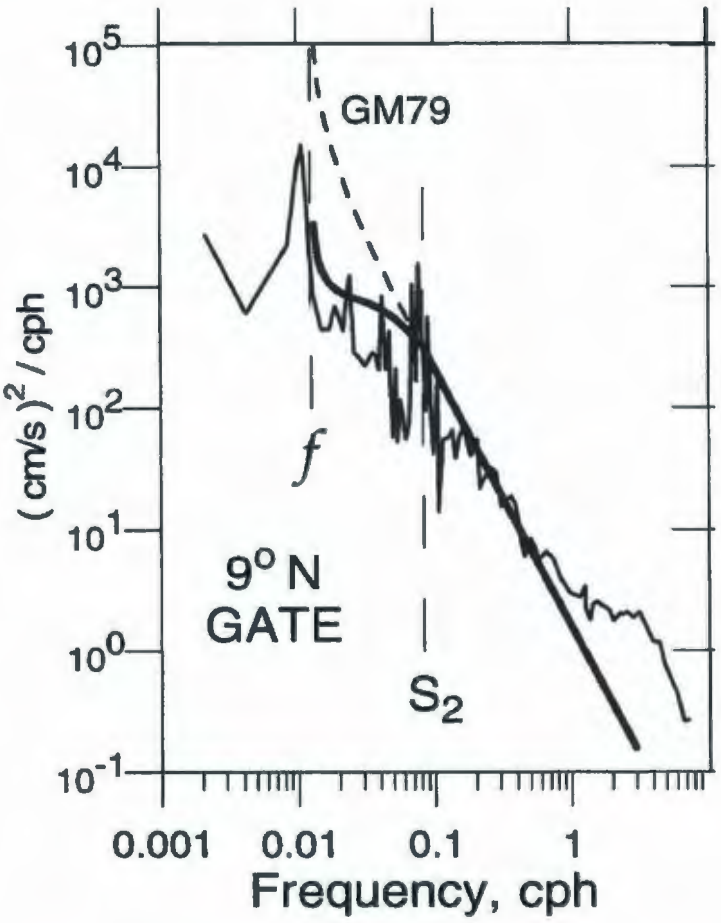

Figure 1.1. Spectrum of internal waves derived from ocean observations, taken from *Garrett and Munk* [1979].

Internal waves span a wide range of spatial and temporal scales. The importance of rotation on the fluid motion is characterized by the ratio of the net acceleration in a fluid to the Coriolis accelerations arising from planetary rotation. This nondimensional ratio is called the Rossby number:

$$Ro = \frac{U}{f L}, \tag{1.4}$$

where U and L are typical velocity and length scales of the fluid motion. When the Rossby number is small, $Ro << 1$, internal waves are subject to both gravity and Coriolis forces. These internal waves are often referred to as inertia-gravity internal waves. Inertia-gravity waves have low frequencies and large wavelengths.

Internal waves at tidal frequency are often called internal tides. They are often generated by the interaction of barotropic tidal currents with steep topographies (whose amplitudes are of the same order of magnitude as the total fluid depth [*Gerkema*, 1996]), such as a sill, seamount or continental shelf break [*Baines*, 1973; *Holloway and Merrifield*, 1999]. Their wavelength is typically a few tens of kilometers and amplitude can reach several tens of meters.

High frequency internal gravity waves often arise as nonlinear steepening of the internal tide [*Holloway et al.*, 1999]. *Gerkema and Zimmerman* [1995] describe this process as an adjustment of the internal tide. They showed that an internal tide changes its form from sinusoidal to cnoidal up to the moment when the nonlinearity would balance nonhydrostatic dispersion. Schematically, the link between tides and solitary waves is as follows:

$$\text{tide} \rightarrow \text{topography interaction} \rightarrow \text{internal tides} \rightarrow \text{internal solitary waves.}$$

Length scales of high frequency internal waves ranging from several hundreds of meters to just a few tens of meters are much shorter than those of inertia-gravity waves and internal tides. The Rossby number in this case is larger than unity and high frequency internal waves are not strongly affected by the Earth's rotation.

The action of the wind and surface waves creates a mixed layer with a sharp pycnocline separating this mixed layer from a second layer of more or less homogeneous denser fluid. Such stratification can often be treated as a two-layer fluid idealization usually employed in the theoretical analysis. In this case internal waves propagate along the interface separating two layers and are often detected as the depression of the pycnocline. In a two-layer system, internal waves can develop a non-linear character. The balance between dispersion and weak non-linearity allows internal waves to retain their shape and to propagate over large distances before they dissipate. Due to this property, IWs are often termed as internal solitons [*Osborne and Burch*, 1980; *Ostrovsky and Stepanyants*, 1989]. Internal solitons often propagate as groups or packets. The number of waves in a packet varies from a few to a few dozens, depending on the generation mechanism and the distance from the generation point.

For the broad range of phenomena termed as internal waves, some clarification in the

terminology is necessary. This present study focuses on one particular type of IWs, namely high-frequency large amplitude non-linear internal solitary waves (ISWs) propagating in two-layer fluid.

Internal waves are important for many reasons. From an engineering point of view, an early motivation for studying them was the unexpectedly large stresses they imposed on offshore oil-drilling rigs. *Cai et al.* [2006] estimated that an internal soliton with an induced current of 2.1 m/s can exert a maximum force equal to one exerted by a surface wave with a wavelength of 300 m and a wave height of 18 m. Therefore such internal waves have to be taken into account for the operation of marine oil platforms and other facilities.

For biologists, internal waves are important because they can carry nutrients from the bottom layer into the upper layer of the ocean. *Armstrong and LaFond* [1966] were among the first to connect high frequency internal waves with a period of around 10 min and amplitude of up to 5 m with differences in silicate and nitrate concentrations recorded simultaneously at several vertical positions off Mission Beach, California. *Haury et al.* [1979] studied the distribution of plankton in the Massachusetts Bay in the region where IWs shoaled and presumably broke. *Leichter et al.* [1998] performed measurements of the concentration of calanoid copepods, crab zoea, and fish larvae on the slope of Conch Reef, Florida Keys (USA). They showed that arrivals of the cold chlorophyll-rich bottom water associated with onshore propagating internal waves are strongly coherent with increased concentrations of zooplankton. This process leads to enhanced biological productivity in the region [*Denman and Gargett*, 1995; *MacIntyre et al.*, 1999].

Geophysicists and environmentalists are interested in the effect of internal waves on the transport of sediments and pollutants. *Cacchione and Drake* [1986] presented laboratory experiments which indicated that elevated velocities (and bottom stresses) caused by shoaling and, possibly, breaking IWs might explain the generation and maintenance of near-bottom nepheloid zones and attached turbid plumes that have been observed over certain continental shelves and slopes. Investigating internal solitary wave packets propagating along a strongly stratified bottom layer on the California shelf, *Bogucki et al.* [1997, 2005] provided observational evidence of the correlation between IWs and benthic particle concentrations. They observed a strong increase in suspended particulate matter in the water column during the passage of an IW packet.

From the physical point of view, as stated by *Garrett and Munk* [1975]: *"Quantifying the transfer of mass and momentum by internal waves, and their role in mixing processes in the ocean, is one of the central tasks of physical oceanography."*

The understanding of the relative importance of different physical mechanisms in the transfer of mass is still far from being complete. For example, in the oceanic surface boundary layer convective motions coexist with and are often dominated by turbulence driven by wind stress acting on the ocean surface [*Garrett*, 1984]. Citing a review paper of *Gargett and Holloway* [1984]: *"... it seems reasonable that a mechanism like convection, which by its nature has vertical velocities much larger than horizontal velocities, will be more effective at mass transport (the buoyancy flux $J_b = -g\rho_0^{-1}\overline{\rho' w'}$ involving the correlation of turbulent vertical velocity w' and density anomaly $\rho' = \rho - \rho_0$) than mechanisms in which vertical velocities are at most no larger than horizontal velocities. Resolving such questions will require observations of the large scales of the turbulent velocity field in the presence of surface-wave velocities that may be much larger–no easy task."*

At the same time, turbulent mixing at the oceanic boundaries also plays an important part in controlling the distribution of heat, salt, and nutrients in the ocean. If the vertical distribution of properties in the water column was controlled by molecular diffusivity (about 10^{-7} m^2 s^{-1} for heat, 10^{-9} m^2 s^{-1} for salt), the whole ocean would consist of a very thin surface layer influenced by the atmosphere on the top of a deep salty and cold homogeneous pool. The continuous stratification we observe everywhere in the ocean suggests a much stronger value of diffusion across lines of constant density, which is usually called diapycnal diffusivity. From knowledge of the overturning circulation, *Munk* [1966] deduced a global value of 10^{-4} m^2 s^{-1} for the diapycnal diffusivity. Similar values were also inferred from semi-enclosed basin budgets [*Hogg et al.*, 1982]. Observations of *Kunze et al.* [1990], *Toole et al.* [1994] and *Caldwell and Moum* [1995] also give evidence that the mixing occurring in the interior of the ocean is too weak to explain the observed distributions of heat and salt. However, values measured in the open ocean by direct tracer experiments [*Ledwell et al.*, 1993] and inferred from microstructure measurements [*Gregg*, 1989] are at least one order of magnitude smaller (0.1×10^{-4} m^2 s m^{-1}) than suggested by *Munk* [1966]. It was hypothesized that one of the possible explanations of the discrepancy is effect of internal waves. This hypothesis has earned more and more support, as observations

of turbulence caused by breaking internal waves near the coast are giving values for the diapycnal diffusivity larger up to several orders of magnitude compared to the deep ocean values [*Carter et al.*, 2005].

Quantifying the process of mixing caused by internal waves is a central task of future development of large-scale numerical models used in physical oceanography [*Wunsch and Ferrari*, 2004]. Existing large scale ocean models cannot account for the turbulence generated by IWs (with length scales ranging from 1 mm to 10 m) because of resolution limitations. The effect of small-scale turbulence must thus be parameterized in terms of large-scale average transport. Several schemes were proposed by *Smagorinsky* [1963], *Mellor and Yamada* [1974], *Scotti and Meneveau* [1993]. However, most traditional turbulence closure models ignore internal waves. Predictions of energy contributed by IWs to turbulence and then dissipated by mixing was suggested by *Henyey et al.* [1986] and refined by *Gregg* [1989]. Although these parameterization schemes work well for some regions [*Gregg*, 1991; *Wesson and Gregg*, 1994], they fail in other locations [*Gargett*, 1999].

Recently, *Kunze et al.* [2006] discussed the latest achievements in the construction of the parameterization for the turbulent dissipation rate ε and eddy diffusivity K, which would take into account internal waves. They noted that two versions of parameterization based on internal wave shear and strain variances predict that eddy diffusivity is a function of both latitude and depth. The turbulence from internal wave field is highly heterogeneous. The average values for K, however, are close to one predicted by *Munk* [1966]. Noting that the elevated values of the eddy diffusivity are indeed observed near steep topography, *Kunze et al.* [2006] suggest that this mixing is extremely localized and it is unclear if breaking internal waves can influence the global values of the diffusivity. Both parameterizations, however, still do not account for mixing from sources other than linear internal waves with a broad bandwidth spectrum. Therefore further investigation of internal waves is needed to establish such parametrization scheme.

1.2 Research Objectives

This dissertation focuses on the interaction of high frequency internal solitary waves with sloping bottoms. By using field observations of shoaling IW packets, transformation of

internal waves of depression into waves of elevation is studied. Numerical simulations are carried out to study the fate of internal waves of elevation. Particular attention is paid to the transport properties of internal waves. The aim of this thesis is to study the propagation and dissipation of high frequency large amplitude internal waves over shoaling topography in an estuarine environment. The main objectives are:

1. To measure in the field the characteristics of shoaling nonlinear internal solitary waves such as amplitude, wavelength, phase speed, energy and their dependence on local environmental parameters, e.g. slope angle, stratification, tidal currents. To construct a climatology, i.e. number of IW occurrences per hour of a tidal period and their energetics, at a site in the St. Lawrence estuary.

2. To study numerically the dependence of ISW characteristics on parameters which can not be modified in field studies, e.g. slope angle.

3. To test Korteveg-de Vries (KdV) and extended Korteveg-de Vries (eKdV) theories against the field observations.

4. To explore the transport properties of internal waves of elevation (often called boluses) caused by the shoaling events.

5. To investigate the properties of boluses formed from the collision of a single wave as compared to the collision of a wave packet consisting of more than one IW.

1.3 Thesis Outline

The dissertation is organized as follows.

Chapter 2 gives a detailed review of relevant literature with emphasis on nonlinear internal solitary waves. According to the dominant physical mechanisms involved, the life history of an IW can be divided into three stages: generation, propagation and decay. In the literature review I will adhere to this subdivision. I will look into the main physical mechanisms involved in the shoaling and breaking processes. One of the most important and least understood aspects of ISWs, mass transport, will be also discussed.

Chapter 3 is focused on methods used in the present study. First, the methodology of field observations, the mooring locations and instrumentation are described. The second part sets up numerical simulations, describes the numerical model used, initial conditions and basic measurement techniques.

Chapter 4 presents the details of field observations. First, single event of a wave transition via shoaling is described. Quantitative results are obtained by measuring the decay of wave amplitude, wavelength, phase speed and energy. Comparison is made with both weakly nonlinear KdV and fully nonlinear two-layer theories. Chapter 4 also deals with climatology of internal waves observed near Ile-aux-Lièvres Island, focusing in particular on how the frequency of IW occurrence and IW energy depend on tidal phase.

Numerical simulations are described in Chapter 5. First, a shoaling of a single internal solitary wave on a slope is studied with several free parameters, such as the amplitude of the wave, slope angle, and stratification. Generation of waves of elevation and their properties are described. Mass transport of the water originating from below the pycnocline, and transport dependence on the amplitude of the incident ISW and the bottom slope is investigated using a passive tracer. Difference in the mass transport caused by a single ISW and an idealized wave train of two ISWs is discussed. A summary and discussion as well as possible future directions follow in Chapter 6.

Chapter 2

Literature review

2.1 Generation of internal solitary waves

Several physical phenomena can generate high frequency internal solitary waves. Moving atmospheric pressure fields and variable wind stress can transfer their energy into the interior of the ocean [*Thorpe*, 1975]. Nonlinear interactions of two surface gravity waves with nearly the same amplitudes and frequencies ω_1 and ω_2 can result in the formation of waves with frequencies $\omega_1 - \omega_2$ and $\omega_1 + \omega_2$, which can satisfy the dispersion relation for the internal waves [*Watson et al.*, 1976]. These mechanisms, however, are relevant to the generation of long internal waves and to the IWs generated in continuous stratification.

A long history of observations has resulted in the understanding that the main mechanism of the generation of high frequency large amplitude IWs is the interaction of strong tidal currents with irregular topography near the continental shelf [*Brandt et al.*, 1996; *Lacombe and Richez*, 1989; *Lee and Beardsley*, 1974]. The observations made by *Apel et al.* [1985] reveal the typical picture of IW generation by an internal tide. The initial disturbance of the pycnocline generated by the tide becomes gradually steeper while approaching the shore. A moving sharp depression of the pycnocline, which is often called an undular bore is formed. The disintegration of the undular bore results in the formation of the packet of ISWs [*Gerkema and Zimmerman*, 1995; *Holloway and Merrifield*, 1999]. Remote sensing by *Zhao et al.* [2004] provides evidence for the baroclinic tide origin of ISWs in the northeastern South China Sea. CTD profiling performed by *Jones and Padman* [1983] during

year-long observations at one location shows a good correlation between the appearance of energetic oscillations of the pycnocline with M2 tide. Numerical simulations of *Lamb* [1994] and *Vlasenko et al.* [1997] provide additional evidence for this mechanism of internal solitary wave packet generation (Figure 2.1).

A packet of internal waves can be also generated by a strong tidal flow moving over the sill [*Cummins et al.*, 2003; *Farmer and Armi*, 1999; *Maxworthy*, 1979]. The lee wave generation mechanism may be described as the generation of an internal lee wave formed by the main pycnocline during the ebb tide. The lee wave is then released when the tide changes from ebb tide to flood tide, and evolves into a rank-ordered ISW packet [*Zhao and Alford*, 2006]. As was observed by *Farmer and Armi* [1999] the shear-flow instability inside the lee wave is sometimes great enough to directly produce ISWs just up-current of the sill. Figure 2.2 illustrates the packet of IWs generated by this mechanism via depression of biological scattering layers sampled with high-frequency echosounders in the Knight Inlet of western Canada [*Farmer and Armi*, 1999; *Farmer and Smith*, 1980]. In this case packets of ISWs can propagate offshore into the deep water or can be trapped in the region just downstream from the sill.

ISWs with amplitudes from 50 to 100 m and wavelengths from 2 to 4 km generated by this mechanism were detected near the restrictions in the Strait of Gibraltar [*Armi and Farmer*, 1988; *Farmer and Armi*, 1988], in the Sulu Sea between the Philippines and Malaysia [*Apel et al.*, 1985; *Liu et al.*, 1985], in the Luzon strait near Taiwan [*Hsu and Liu*, 2000; *Hsu et al.*, 2000; *Lien et al.*, 2005], and the arches of the Andaman and Nicobar Islands in the eastern Indian Ocean [*Alpers et al.*, 1997; *Apel*, 1979; *Osborne and Burch*, 1980].

Nash and Moum [2005] presented evidence of another mechanism of generation of large amplitude internal solitary waves which allowed explanation of observations of ISW packets in the absence of tidal topographic interaction. Their measurements of velocity, density and acoustic backscatter across the Columbia River plume front showed how internal waves can be generated from a river plume that flows as a gravity current into the coastal ocean. This mechanism was formerly known to work in the atmosphere [*Christie et al.*, 1981; *Smith et al.*, 1982], but was found to work equally well in the ocean (see Figure 2.3). When the river plume moves, it grows in size because of the convergence of horizontal velocities at the plume's front. An ISW can be released and propagate freely from the

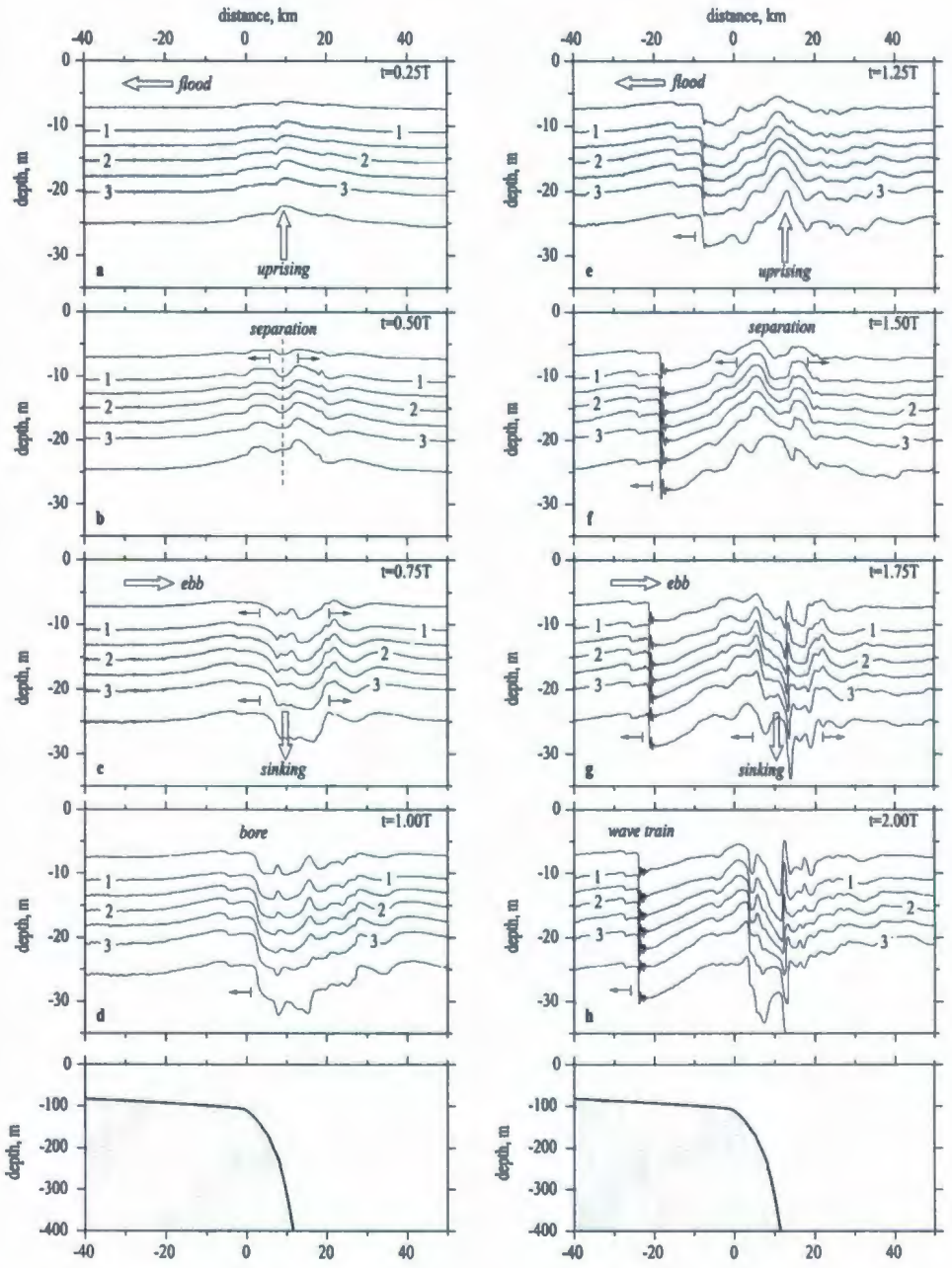

Figure 2.1. Results of numerical simulations showing the generation of internal solitary wave trains by tidal flow. Taken from *Vlasenko et al.* [1997].

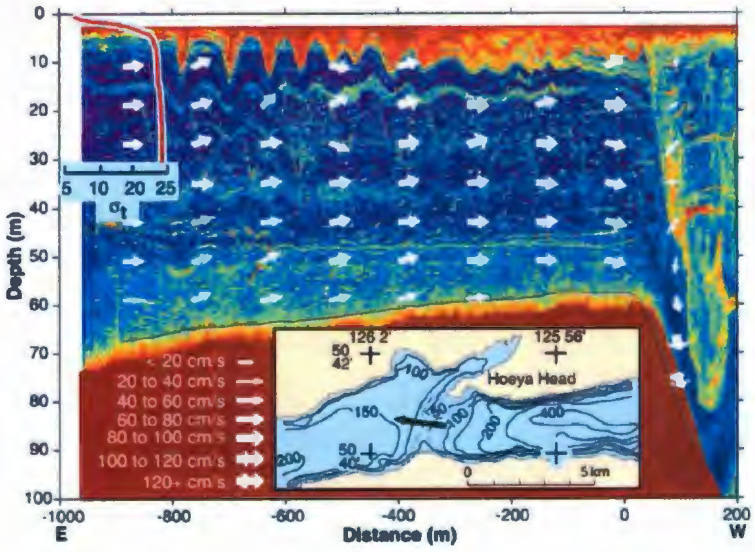

Figure 2.2. Current vectors and acoustic profile showing generation of an internal wave packet during the passage of tidal flow over the sill. Taken from *Farmer and Armi* [1999].

river plume front when the front's propagation speed decreases below the wave speed in the water ahead of it. This mechanism generates rank ordered packets of ISWs with the amplitudes comparable to ones generated by the internal tide.

Although the process of internal wave generation strongly depends on the particular geography of the area, the estimates of *Sandstrom and Elliott* [1984] for the Atlantic coast of Nova Scotia and *Farmer and Freeland* [1983] for the Knight Inlet, British Columbia, show that a large part of the energy (up to 95%) may be transferred from the barotropic tide to the intense high frequency IWs.

2.2 General properties of internal solitary waves

2.2.1 Weakly nonlinear Korteveg-de Vries theory

During early investigations by *Benjamin* [1966], *Benney* [1966], *Keulegan* [1953], and *Long* [1956] and a mathematical theory was developed that has now become standard in studies of ISWs propagation. The derivation starts with 2D governing equations for incompressible,

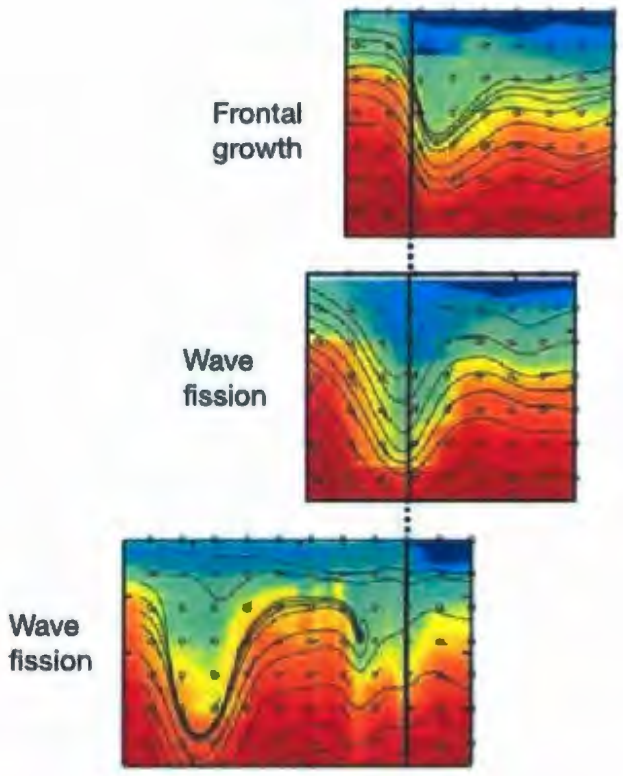

Figure 2.3. Generation of an ISW by the buoyant river flow discharge. The growth of the initial wave (top), fission of the wave (middle) and the free propagation of the ISW is shown. Taken from *Nash and Moum* [2005].

inviscid fluid:

$$\rho\,(u_t + u u_x + w u_z) + p_x = 0, \tag{2.1}$$

$$\rho\,(w_t + u w_x + w w_z) + p_z + g\,\rho = 0, \tag{2.2}$$

$$\rho_t + u\,\rho_x + w\,\rho_z = 0, \tag{2.3}$$

$$u_x + w_z = 0, \tag{2.4}$$

where u and w are horizontal and vertical components of the fluid velocity, p is pressure and ρ is density. Subscripts stand for partial derivatives.

Next, we pick a basic steady state of the fluid described by density $\rho_0(z)$, horizontal velocity u_0 and corresponding hydrostatic pressure $p_0(z)$ such that $(p_0)_z = g\,\rho_0$. Governing

equations can be written relative to the base state as

$$\rho_0 \left(u_t + u_0 u_x + w u_{0z}\right) + p_x = -(\rho + \rho_0) \left(u u_x + w u_z\right) - \rho \left(u_t + u_0 u_x + w u_{0z}\right), \quad (2.5)$$

$$p_z + g\rho = -(\rho + \rho_0) \left(w_t + u_0 w_x + u w_x + w w_z\right), \quad (2.6)$$

$$g \left(\rho_t + u_0 \rho_x\right) - \rho_0 N^2 w = -g \left(u \rho_x + w \rho_z\right), \quad (2.7)$$

$$u_x + w_z = 0, \quad (2.8)$$

where $N(z)$ is the buoyancy frequency as defined in Equation 1.1.

Linear long wave theory is now obtained by linearizing equations 2.5-2.8 around the base state. A solution is sought in the form

$$\eta(x, z, t) = \eta(x - c_0 t)\varphi(z), \quad (2.9)$$

where c_0 is the linear long wave speed, t is time, and $\varphi(z)$ is a vertical mode structure function found as the solution of the boundary value problem:

$$\varphi'' + \frac{N^2(z)}{c^2}\varphi = 0 \quad (2.10)$$

with boundary conditions

$$\varphi(z = 0) = 0 \text{ and } \varphi(z = H) = 0, \quad (2.11)$$

where H is a total depth of water.

This boundary value problem must be solved numerically for general stratifications. The shape of the structure function is illustrated in Figure 2.4. As pointed out by *Vlasenko et al.* [2000] the maximum of the vertical structure function coincides with the maximum of buoyancy frequency only for small amplitude weakly nonlinear internal waves. For ISWs of large amplitude the location of $\varphi(z)$ maximum is shifted and the value of the shift depends on the amplitude of the wave.

Let us now consider the fluid having a two-layer stratification with depths of the upper and lower layers h_1 and h_2. The thin pycnocline is then replaced by an interface sepa-

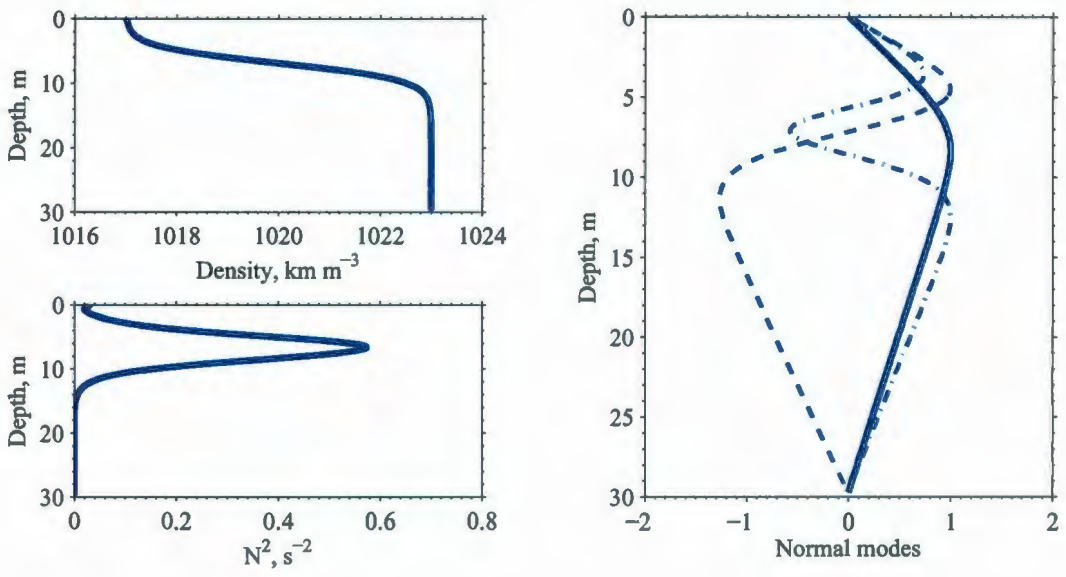

Figure 2.4. The vertical structure function of the first three normal modes given by Equation 2.10 (right panel) for a given density stratification (top left panel) and buoyancy frequency (left bottom panel).

rating the upper and lower fluid. The flow in both layers is assumed irrotational, except at the interface between layers. The displacement of the interface between layers from its equilibrium position is denoted as $\eta(x,t)$.

The next step is to introduce a small parameter in the problem. An appropriate small parameter can be the ratio of the wave amplitude to the depth of the fluid: $\epsilon = a/H$. Expanding variables in Equations 2.5 - 2.8 into series using parameter ϵ and retaining only the leading order terms results in reduction of the governing equations to a single equation for η. This equation is similar in form to the KdV equation derived for surface solitary waves. In the dimensional form with retained quadratic nonlinear terms it reads:

$$\frac{\partial \eta}{\partial t} + (c_0 + \alpha\eta)\frac{\partial \eta}{\partial x} + \beta\frac{\partial^3 \eta}{\partial x^3} = 0, \tag{2.12}$$

where α is a parameter of nonlinearity and β is a dispersion parameter.

This equation describes an internal solitary wave propagating in the positive x-direction with a phase speed c (unidirectional equation). The permanent form of the wave is ensured by the balance between nonlinear and dispersive effects, described by parameters α and β

respectively. Both these parameters are assumed to be small, but comparable to each other:

$$O(\alpha) \sim O(\beta) \ll 1. \tag{2.13}$$

The analytical solution of the KdV equation for a single soliton pulse is

$$\eta(x,z,t) = 2\,\eta_0 \varphi(z) \mathrm{sech}^2\left(\frac{x-ct}{2\,L_w}\right), \tag{2.14}$$

where η_0 is the maximum excursion of the interface, or the wave amplitude and L_w is a measure of the width of the squared hyperbolic secant pulse or ISW wavelength. While the amplitude of the soliton can be considered as a free parameter (one parameter solution), L_w is a function of the ISW amplitude and environmental coefficients. For the case of two-layer stratification, the coefficients α and β are connected to the depth, h, and density, ρ, of the upper layer (subscript 1) and the lower layer (subscript 2) of the fluid as follows:

$$\alpha = \frac{3c}{2h_1h_2}\frac{\rho_2h_1^2 - \rho_1h_2^2}{\rho_2h_1 + \rho_1h_2}, \tag{2.15}$$

$$\beta = \frac{c\,h_1h_2}{6}\frac{\rho_1h_1 + \rho_2h_2}{\rho_2h_1 + \rho_1h_2}, \tag{2.16}$$

where ρ_1 is density of the upper layer and ρ_2 is density of lower layer.

The nonlinear phase speed, c, can be estimated from the relation [see for example *Grue et al.*, 1999]:

$$\frac{c}{c_0} - 1 = \frac{\eta_0(\rho_2h_1^2 - \rho_1h_1^2)}{2h_1h_2(\rho_2h_1 + \rho_1h_2)}, \tag{2.17}$$

where c_0 is the linear speed of gravity waves:

$$c_0^2 = \frac{gh_1h_2(\rho_2 - \rho_1)}{\rho_2h_1 + \rho_1h_2}. \tag{2.18}$$

The wavelength can be found from:

$$\frac{1}{L_w} = \frac{3\eta_0(1 - \rho_1h_2^2/(\rho_2h_1^2))}{4h_2^2h_1(\rho_1/\rho_2 + h_2/h_1)}. \tag{2.19}$$

Figure 2.5 shows the general shape of the interface depression described by Equation

2.14 as well as dependencies of the KdV soliton's nonlinear phase speed and wavelength on the amplitude of the soliton. The invariant shape of the KdV solution and its dependencies on the amplitude and the environmental parameters have been well verified both in the ocean [*Apel et al.*, 1985; *Liu et al.*, 1985; *Ostrovsky and Stepanyants*, 1989], and in laboratory tanks [*Grue et al.*, 1999; *Koop and Butler*, 1981].

A large number of observations have been aimed specifically to test the applicability of Equation 2.12 for the description of high frequency ISWs. Studies of *Lamb* [1998] showed that although oceanic ISWs are capable of retaining their shape for substantial time, strictly speaking ISWs can not be considered as solitons. Results of fully nonlinear numerical simulations showed that two ISWs of different amplitudes propagating in the same direction interact with each other in a manner that is different from the one following from the KdV theory. The KdV equation predicts that solitons after interaction will retain their properties. However, *Lamb* [1998] found that after interacting, the larger of two ISWs grew by 0.23 %, while the smaller ISW was reduced by 0.16 %. Some small amplitude trailing waves are also generated during interaction.

Despite this, numerous observations and laboratory studies (see for the review *Camassa et al.* [2006], *Ostrovsky and Stepanyants* [2005], *Helfrich and Melville* [2006]) showed that small-to-moderate amplitude (with respect, for example, to the depth of a thinner layer) ISWs are in good agreement with weakly nonlinear KdV theory. Laboratory experiments of *Grue et al.* [1999] showed that for the agreement to hold, the ratio of the wave amplitude to the depth of the thinner layer should not exceed 0.4.

Numerous observations [see *Pinkel*, 2000], including satellite remote sensing [*Apel*, 1979, 2002], revealed that despite certain three dimensional effects ISW fronts possess a two dimensional structure. This makes it possible to investigate many aspects of ISWs by treating them in two dimensions, at least during the propagation stage.

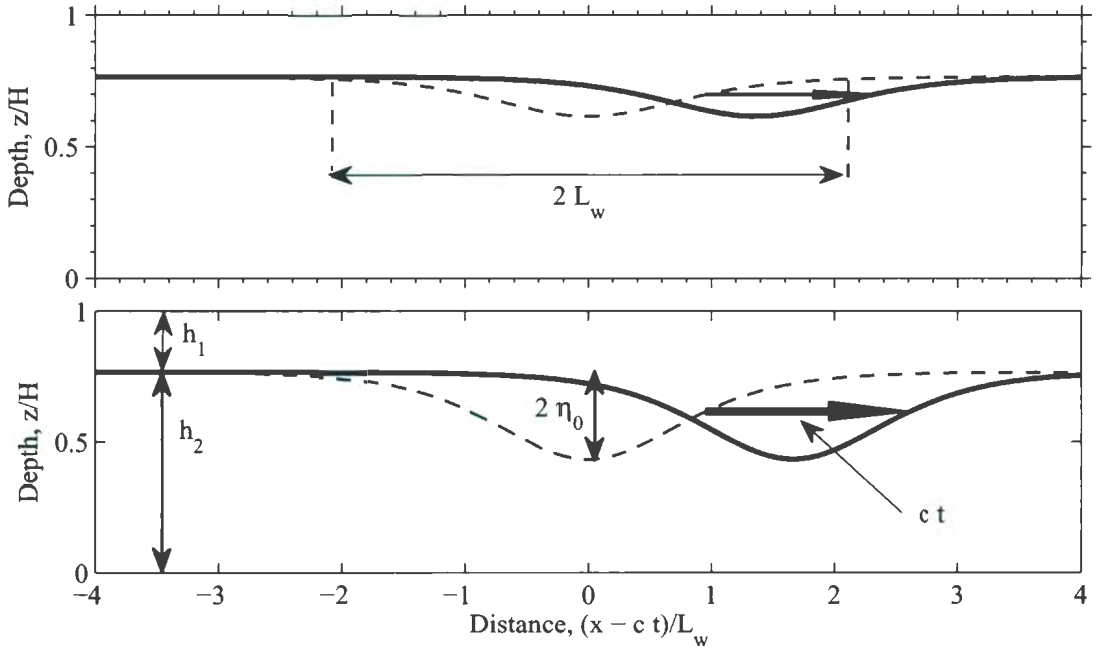

Figure 2.5. Depression of the interface described by the solution of the KdV equation (Equation 2.14) for fluid with a two-layer stratification.

2.2.2 Extended KdV theory

The shallow water formulation of the KdV equation, Equation 2.14, was derived under assumptions that the internal waves are long compared to the total depth of the fluid and that the nonlinearity coefficient is small, $\alpha << 1$. It is expected to work well for waves with small amplitudes compared to the depths of the lower or upper layers. The results of the KdV theory are indeed in good agreement with both field observations of IWs propagation [*Osborne and Burch*, 1980; *Sandstrom and Elliott*, 1984] and laboratory experiments [*Helfrich and Melville*, 1986; *Segur and Hammack*, 1982]. *Koop and Butler* [1981], *Kao et al.* [1985], *Grue et al.* [1997], *Michallet and Barthelemy* [1998] studied ISWs in a system of two immiscible fluids with large density difference and in a continuously stratified fluid. They examined generation and propagation of internal solitons in the laboratory and found that a fully developed soliton satisfies the KdV theory. However, there are certain limitations of the KdV theory. First of all, the agreement becomes poor as the amplitude of the ISWs increases. Secondly, the KdV theory is not capable of describing the passage of ISWs past the turning point, where the coefficient of nonlinearity is vanishing. The turning point for the two-layer fluid is found when $h_1/h_2 = (\rho_1/\rho_2)^{1/2}$ (see Equation 2.15). Thirdly, the one-parameter solution of the KdV theory describes an ISW which, in principle, can have arbitrarily large amplitude. The analogy with surface solitary waves and several studies of ISWs, such as *Amick and Turner* [1986]; *Miles* [1981], suggest that the amplitude of ISWs has a certain maximum for given conditions.

To remedy these problems, several corrections to the KdV equation were proposed based on the accounting of higher-order nonlinearity terms. Retaining both quadratic and cubic nonlinear terms leads to the extended Korteweg - de Vries (eKdV) equation:

$$\frac{\partial \eta}{\partial t} + (c + \alpha\eta + \alpha_1\eta^2)\frac{\partial \eta}{\partial x} + \beta\frac{\partial^3 \eta}{\partial x^3} = 0, \tag{2.20}$$

where the coefficient of cubic nonlinearity is

$$\alpha_1 = \frac{3c}{h_1^2 h_2^2}\left[\frac{7}{8}\left(\frac{\rho_2 h_1^2 - \rho_1 h_2^2}{\rho_2 h_1 + \rho_1 h_2}\right)^2 - \frac{\rho_2 h_1^3 + \rho_1 h_2^3}{\rho_2 h_1 + \rho_1 h_2}\right]. \tag{2.21}$$

The solution of this equation can be expressed as a two-parameter family

$$\eta(x,t) = \eta_0 \left[1 - \frac{4-\kappa}{1 + [2(2-\kappa)\kappa/2]\cosh^2[(x-Vt)/\Delta]} \right], \tag{2.22}$$

where

$$V = c + \frac{\alpha_1 \eta_0^2}{6}(6 - 4\kappa + \kappa^2) \tag{2.23}$$

and

$$\Delta^2 = -24\frac{\beta}{\alpha_1}\eta_0^2(4\kappa - \kappa^2) \tag{2.24}$$

Two parameters describing the eKdV solution are the amplitude of the soliton, η_0, and the dimensionless parameter κ that varies within the limit $0 < \kappa < 2$. This parameter can serve as a measure of nonlinearity of the eKdV soliton. Figure 2.6 shows the shape of the eKdV solution for different values of parameter κ. When $\kappa = 0$, Equation 2.22 reduces to the KdV solution described by Equation 2.14. For increasing values of the parameter κ, the eKdV soliton widens and becomes flat-crested with κ close to 2. When $\kappa = 2$ the soliton becomes infinitely wide and turns into a pair of coupled internal bores, often called a kink-antikink pair [*Ostrovsky and Stepanyants*, 1989] or conjugate flow [*Benjamin*, 1966; *Lamb*, 2000].

Another extension of the KdV equation attempts to account for slow variations of the topography

$$\frac{L_w}{L_H} = O(\beta), \tag{2.25}$$

where L_w is the characteristic length of the wave, L_H is a characteristic length of the depth variation and the parameter β measuring dispersion is defined in Equation 2.16. The equation often called variable coefficient KdV (vKdV) equation can be written as as

$$\frac{\partial \eta}{\partial x} + \left(\frac{\alpha Q}{c^2}\eta + \frac{\alpha_1 Q^2}{c^2}\eta^2 \right) \frac{\partial \eta}{\partial s} + \frac{\beta}{c^4}\frac{\partial^3 \eta}{\partial \tau^3} = 0, \tag{2.26}$$

where a new variable τ, the "running time" is introduced as

$$\tau = \int_0^x \frac{dx}{c} - t. \tag{2.27}$$

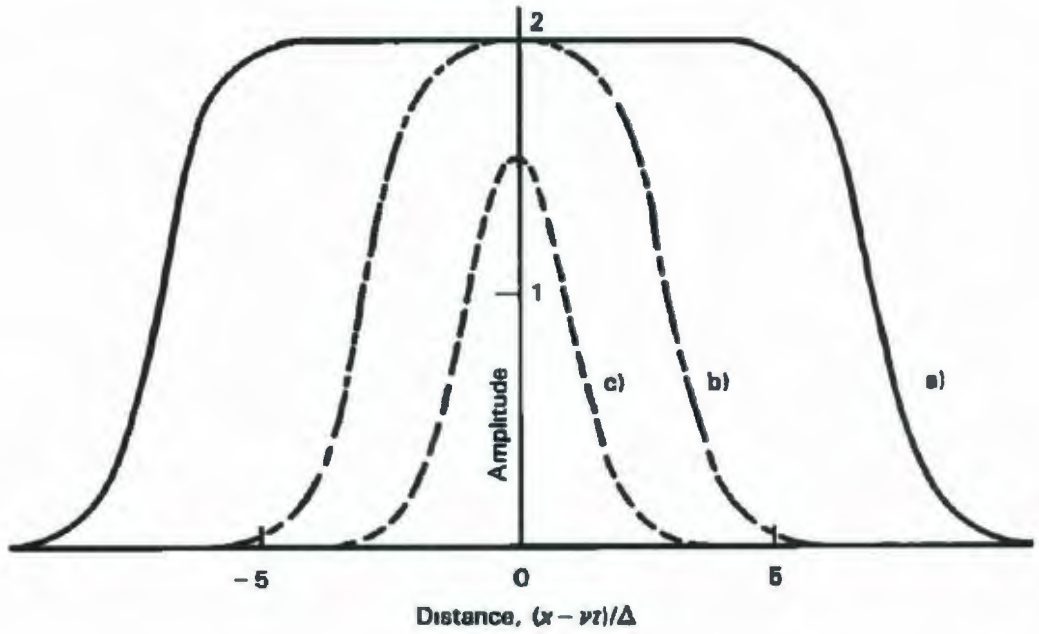

Figure 2.6. Shape of an eKdV soliton (Equation 2.22) plotted for three values of parameter κ: (a) κ=10^{-7}; (b) κ=10^{-4}; (c) κ=10^{-1} (close to the KdV case). Taken from *Ostrovsky and Stepanyants* [1989].

Coefficient Q(x), which accounts for changes in topography is calculated through the relationship

$$Q(x) = \sqrt{\frac{(M\,c^3)_0}{M\,c^3}}, \quad M(x) = \int_{-H}^{0} \frac{\partial \varphi}{\partial z} dz, \tag{2.28}$$

where the subscript '0' indicates the value calculated at some reference point (x_0) in the far field. The vertical structure function $\varphi(x, z)$ is now found from the boundary value problem, analogous to Equation 2.10 with buoyancy frequency N now depending on the horizontal coordinate:

$$\frac{\partial^2 \varphi}{\partial z^2} + \frac{N^2(x,z)}{(c(x))^2}\varphi = 0. \tag{2.29}$$

The solution of this boundary value problem also determines the dependence of the phase speed of the long linear internal waves with horizontal coordinate $c(x)$. The full solution of

Equation 2.26 can be presented in the form:

$$\eta(x,z,t) = \varphi(x,z)\,Q(x)\,\eta(x,t). \tag{2.30}$$

It is clear that the coefficient $Q(x)$ serves as an amplification factor.

Equation 2.26 is not integrable and needs to be solved numerically. Theoretical aspects and applications of the several extensions to the Korteveg-de Vries equation including third order nonlinear term, variable topography, Earth rotation and boundary layer dissipation may be found in *Benney* [1966], *Lee and Beardsley* [1974], *Helfrich and Melville* [1986], *Pelinovsky et al.* [1995], *Holloway et al.* [1999], *Grimshaw* [2001], and *Grimshaw et al.* [2002].

2.2.3 Packets of internal solitary waves

While an isolated internal wave is well described by the single-pulse KdV soliton (Equation 2.14), in the ocean IWs are almost always observed as packets consisting of several oscillations of a quasi-periodic nature. Usually, amplitudes of ISWs are decreasing from the front to the rear of the wave group. In this case it is said that ISWs are rank ordered. However, there are observations showing that the ordering of ISWs can be altered. One possible explanation is that this ISW group was observed close to its generation point where high-mode interactions occur between waves.

Korteweg and de Vries also found a nonlinear periodic solution to their equation, the so called cnoidal wave involving the Jacobian elliptic function, $cn_s(x)$, see for example *Grimshaw* [2001]. This function has a free parameter, ς, that establishes the degree of nonlinearity: $0 < \varsigma^2 < 1$. The KdV cnoidal solution is given by

$$\eta(x,t) = \eta_m + 2\eta_0 cn_s^2[\frac{1}{2}k_0(x-ct)], \tag{2.31}$$

where η_m and η_0 are amplitude factors and k_0 is a wave number. Figure 2.7 shows the cnoidal solution defined on several wavelengths.

There are numerous papers comparing observations of ISWs with different solutions of several versions of the KdV equation: two-layer, extended KdV, rotationally and/or friction-

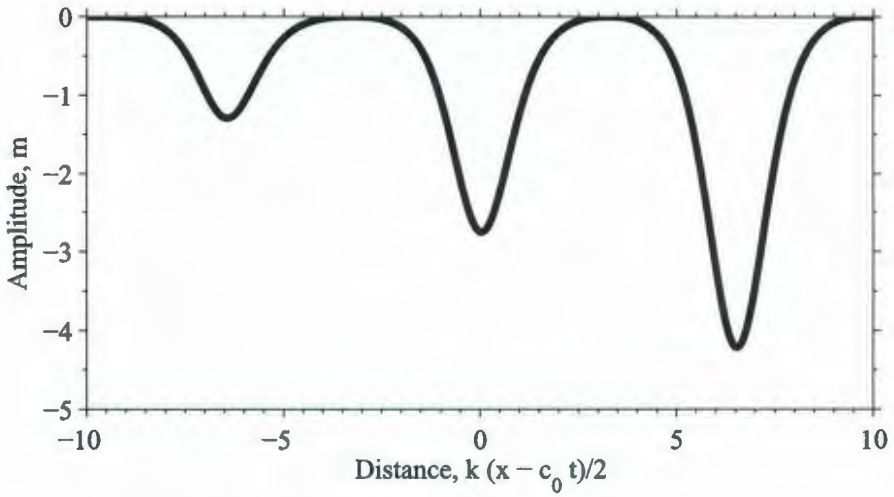

Figure 2.7. Periodic KDV cnoidal wave solution described by Equation 2.31 with parameter $\varsigma = 0.98$.

ally modified KdV. On the other hand, attempts at using the cnoidal solution for comparison with field observation are probably far from being realistic due to unclear mechanisms leading to variability in the number of waves and distances between ISWs comprising the packet. To apply Equation 2.31 to field observations in a consistent way, parameter of nonlinearity ς has to be linked to environmental parameters, such as stratification, distance from the generation point, or tidal phase. This, however, is not a trivial task and no solution exists at the moment.

2.2.4 Fully nonlinear two-layer model

The structure and properties of large amplitude IWs were studied numerically using models with higher-order nonlinearities by *Djordjevic and Redekopp* [1978], *Miles* [1979, 1981], *Koop and Butler* [1981] and *Funakoshi and Oikawa* [1986]. The fully nonlinear model which imposed no limitations on the amplitude of internal wave was developed by *Miyata* [1988], *Grue et al.* [1997], and *Choi and Camassa* [1999], see *Ostrovsky and Grue* [2003] for the review. It was successfully used to explain the results of laboratory observations of

large amplitude IWs [*Michallet and Barthelemy*, 1998] and gave a good comparison with *in situ* measurements in the Celtic Sea [*Ostrovsky and Grue*, 2003].

A fully nonlinear model for internal solitary waves propagating in a two layer fluid was developed by *Grue et al.* [1999]. It is based on the assumption that fluids both in the upper and lower layer are homogeneous and incompressible and that the motion in each of the layers is irrotational such that the velocities may be obtained from potential theory:

$$\vec{v_j} = u_j\,\hat{i} + v_j\,\hat{j} = \nabla\,\varphi_j \tag{2.32}$$

where $j = 1,\ 2$ subscripts for the upper and lower layers, $\hat{i}$ and $\hat{j}$ are unit vectors in horizontal and vertical directions, and φ satisfies the Laplace equation. Introducing the complex variable

$$z = x + i\,y, \tag{2.33}$$

and complex velocities

$$q_j(z) = u_j(x,y)\ -\ c\ -\ i\,v_j(x,y), \tag{2.34}$$

Cauchy's integral theorem is applied to $q_1 + c$ and $q_2 + c$. As a result a set of non-singular Fredholm type integral equations of the second kind is derived:

$$\pi(\gamma_1' + c\,x_\zeta') = \mathrm{PV}\int_I \mathrm{Re}\left(\frac{z_\zeta'}{z'-z}\,c\,y\,d\zeta\right) - \int_I \mathrm{Re}\left(\frac{z_\zeta'}{z^*\ -2ih_1\ -z'}\right) c\,y_\zeta\,d\zeta$$

$$+\int_I \mathrm{Im}\left(\frac{z_\zeta'}{z'\ -\ z} + \frac{z_\zeta'}{z^*\ -2ih_1\ -z'}\right)(\gamma_1 + c\,x_\zeta)d\zeta,\ \ z' \in I, \tag{2.35}$$

$$-\pi(\gamma_2' + c\,x_\zeta') = \mathrm{PV}\int_I \mathrm{Re}\left(\frac{z_\zeta'}{z'-z}\,c\,y\,d\zeta\right) - \int_I \mathrm{Re}\left(\frac{z_\zeta'}{z^*\ +2ih_2\ -z'}\right) c\,y_\zeta\,d\zeta$$

$$+\int_I \mathrm{Im}\left(\frac{z_\zeta'}{z'\ -\ z} + \frac{z_\zeta'}{z^*\ +2ih_2\ -z'}\right)(\gamma_2 + c\,x_\zeta)d\zeta,\ \ z' \in I, \tag{2.36}$$

Here I is the interface between layers parameterized by $z(\zeta)$ and $z_\zeta = dz/\zeta$. PV refers to the principal value of the integral, Re and Im indicate the real and imaginary parts and the star indicates complex conjugate values. This set of equations is then solved numerically by an iterative method. Figure 2.8 shows the solution of the fully nonlinear model for $h_1 = 7$ m

and $h_2 = 23$ m and wave amplitudes of $a = 0.5, 1, 2, 3, 4, 5, 5.5, 6.0$ and 6.5 m.

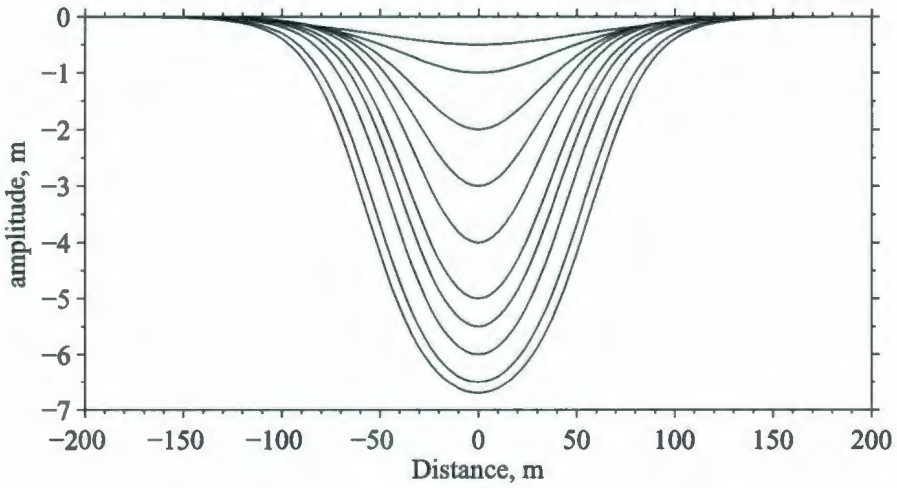

Figure 2.8. Solution of the fully nonlinear model given by Equations 2.35 and 2.36 for $h_1 = 7$ m and $h_2 = 23$ m and wave amplitudes of $a = 0.5$, 1.0, 2.0, 3.0, 4.0, 5.0, 5.5, 6.0 and 6.5 m.

To verify the theoretical results, a set of laboratory experiments were carried out [*Grue et al.*, 1999]. The properties of large amplitude ISWs were studied in a two-layer fluid by application of particle image velocimetry (PIV). *Grue et al.* [1999] compared laboratory-measured velocity profiles, phase speed, amplitude and wavelength with weakly nonlinear KdV and fully nonlinear model. Results agreed well with the traditional KdV equation only for an amplitude of the wave not larger than half of the depth of the deeper layer. The fully nonlinear interfacial model given by Equations 2.35 - 2.36 showed excellent agreement with laboratory experiments for all ISW amplitudes.

The fully nonlinear model of *Grue et al.* [1999] has significantly improved the description of steady ISWs. However the steady-state model has a shortcoming of not being able to model the transient development of ISWs. Another fully nonlinear interfacial model was developed by *Choi and Camassa* [1999]. Starting with the inviscid Euler equations they derived a set of depth-averaged ordinary differential equations for the interface displacement between layers. The only assumption used for the derivation is that the waves are long

compared to the undisturbed thickness of one of the fluid layers. No smallness assumption is made for wave's amplitude.

2.2.5 Numerical simulations of ISWs with nonlinear nonhydrostatic models

Fully nonlinear two-layer models derived by *Grue et al.* [1997] and *Choi and Camassa* [1999] provide a useful tool for the investigation of properties of large amplitude ISWs. Their numerical solutions can be computed readily and inexpensively. These models, however, are also limited to the case when the wave is in steady state. If one is interested in the interaction of ISWs with a sloping bottom or with another ISW, an unsteady numerical model is needed.

The incompressible Euler equations under the Boussinesq approximation were solved by *Lamb* [2002, 2003] to study various aspects of ISW properties and shoaling over a finite width shallow water region. The rigid lid approximation is made which prescribes the surface elevation to be zero at all times and thus removes surface waves from the problem. Equations are discretized using the terrain-following (sigma) coordinate system with constant horizontal spacing and solved using a second-order projection method. Limiting forms of internal waves in an exponential stratification were studied as well as formation of closed streamlines inside waves of depression, [*Lamb*, 2002].

Ocean-scale numerical models usually employ a hydrostatic approximation which results in significant simplifications in calculation of the flow. It is valid when vertical accelerations are small compared to the gravitational acceleration or equivalently $\mathcal{O}(H/L) << 1$, where H and L are characteristic horizontal and vertical length scales of the flow. With increased horizontal resolution, this assumption becomes invalid. Thus, it is necessary to consider non-hydrostatic effects in flow description.

Fringer and Street [1999] developed a large-eddy two-dimensional model which solves Navier-Stokes and scalar transport equations using Boussinesq and rigid lid approximations. This code uses a finite volume formulation on a generalized curvilinear coordinate nonstaggered grid. *Venayagamoorthy and Fringer* [2006] applied this model to the numerical simulations of the interaction of internal waves with a shelf break in a continuous

stratification. Boluses formed via shoaling and breaking of large amplitude IWs have similarities, such as closed recirculation cores, with boluses formed by internal solitary waves.

Vlasenko et al. [2000] presented a numerical model based on the incompressible two-dimensional Euler equations with the Boussinesq approximation. Governing equations in terms of vorticity and two-dimensional stream function are discretized using a finite difference scheme. The structure of large-amplitude ISWs was investigated and compared to weakly nonlinear KdV theory.

Bourgault and Kelley [2004] developed a laterally-averaged two dimensional nonhydrostatic model. A finite-difference scheme is used to discretize governing equations on a variable-mesh z-coordinate C grid. These equations employ the Boussinesq approximation and a free surface. The model was applied to the investigation of ISWs colliding with linear slopes in an idealized laboratory setup (*Bourgault et al.* [2005]) and with quasi-linear slopes in the framework of full-scale oceanic simulations (*Bourgault and Kelley* [2007]).

Large-scale ocean models have been traditionally made hydrostatic which neglects nonhydrostatic pressure and subsequently vertical momentum (e.g. POM [*Blumberg and Mellor*, 1987]; EFDC *Hamrick* [1992]; ROMS: [*Ezer et al.*, 2002; *Haidvogel et al.*, 2000]). With an increase in available computing power, a number of nonhydrostatic ocean models became available. Recently, *Vlasenko and Stashchuk* [2007] applied a three-dimensional nonhydrostatic model developed by the Massachusetts Institute of Technology (MITgcm) for studying the propagation of ISW packets in the Andaman Sea. They showed using numerical simulations that although the propagation of ISWs in deep water can be considered as a two-dimensional process, interaction of ISWs with sloping boundaries, on the other hand, is essentially three-dimensional owing to such effects as wave refraction and energy redistribution.

Use of two nonhydrostatic large-scale models was assessed for the simulation of ISW shoaling over a liner slope by *Berntsen et al.* [2006]. The general circulation z-coordinate MITgcm model [*Marshall et al.*, 1997] and non-hydrostatic version of the Bergen Ocean Model (BOM) σ-coordinate model [*Berntsen*, 2000] were compared for the problem of ISWs breaking on a linear slope. Both models showed similar results and front speeds and wave speeds were in good agreement with laboratory experiments.

2.2.6 Shear instability and the ISW-induced Richardson number

An important nondimensional number associated with ISWs is the ratio of the stabilizing effect of buoyancy to the destabilizing effect of the velocity shear generated by the passing ISW. The Richardson number can be defined as:

$$Ri(x,\, z,\, t) = \begin{cases} \frac{N^2}{S^2}, & \text{if } N^2 \geq 0\,, \\ 0 & \text{if } N^2 < 0\,. \end{cases} \tag{2.37}$$

where

$$S^2 = \left(\frac{\partial u}{\partial z}\right)^2 \tag{2.38}$$

is the square of the vertical shear. *Miles* [1961] gave the proof to the theorem (now known by his name) which establishes a sufficient condition for infinitesimal stability in a parallel, stratified, inviscid flow is that the local Richardson number should everywhere exceed 1/4.

Following *Bogucki and Garrett* [1993] the horizontal velocity induced by an ISW in the coordinate system moving along with the wave is given by

$$u(X, z) = -\frac{c + U(z)}{1 + \eta_0 \varphi'(z) f(X)}, \tag{2.39}$$

where $U(z)$ is a mean background current and $f(X) = \mathrm{sech}^2(x - c\,t)$.

The Richardson number at the ISW wave crest is given by

$$Ri(z) = \frac{N_0^2(z)(1-\eta')^5}{((U(z)+c)\eta'' - U'(z)(1-\eta'))^2}, \tag{2.40}$$

where $N_0^2(z)$ is the undisturbed Brunt-Väisälä frequency and prime denotes the differentiation with respect to z. For the case of two-layer stratification and zero background current this equation can be simplified to

$$Ri(z) = \frac{g'h}{(\Delta u)^2} = \frac{g'\, h(h_1 + \eta_0)(h_2 - \eta_0)}{\eta_0^2 H^2 c^2}, \tag{2.41}$$

where $g' = g(\rho_2 - \rho_1)/\rho$ is the reduced gravity and $\Delta u = u_1 - (-u_2)$ is the difference of velocities in the upper and lower layers. Calculations of *Bogucki et al.* [1997] show

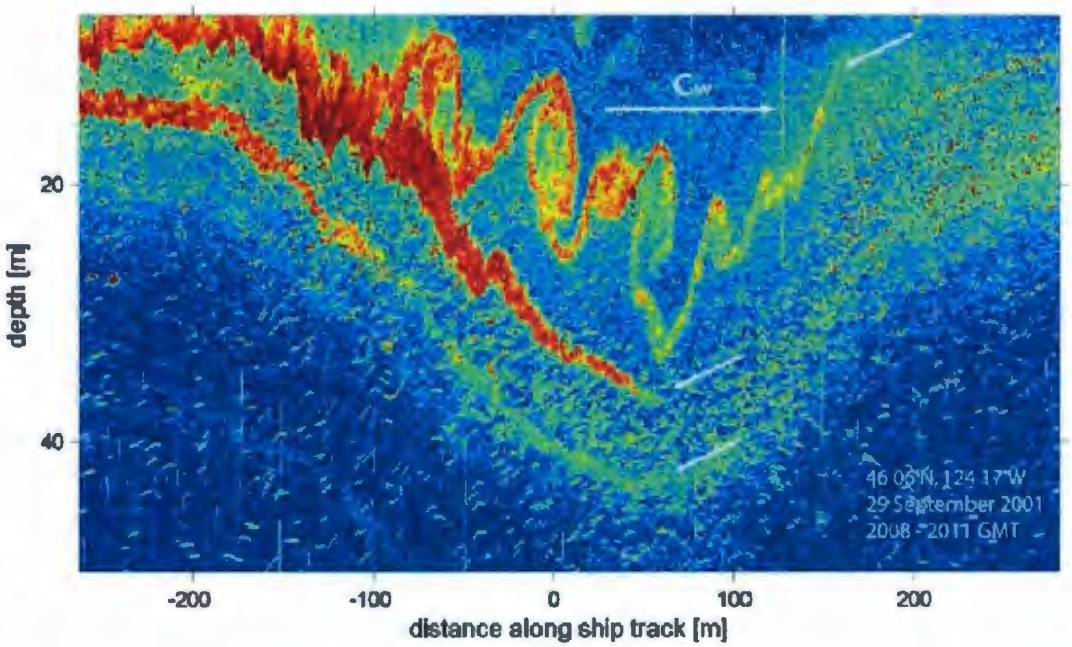

Figure 2.9. Observation of shear instability and growth of the Kelvin-Helmholtz billows. The wave is propagating from left to right. Taken from *Moum et al.* [2003].

that shear associated with the passage of an ISW can be sufficient to result in induced Richardson number of approximately $1/4$. They also indicate the important role of the background current, noting that a relatively small ISW with an amplitude to total depth ratio $\eta_0/H = 0.2$ propagating in the sheared environment ($U_{max}(z) = 10$ cm/s) is able to lower the Richardson number to near the critical value. For comparison, the ISW propagating without the presence of background shear must have $\eta_0/H = 0.75$ to attain the same effect. *Bogucki et al.* [1997] also showed that weakly nonlinear KdV theory can be used as a tool to study ISWs in the regimes when shear instabilities and mixing are possible.

Bogucki and Garrett [1993] proposed a simple model for the shear-induced decay of an internal solitary wave propagating along a finite thickness pycnocline. Simple arguments based on a two-layer KdV formulation show that the wave-induced Richardson number reaches its minimum value on the interface between two layers. During wave propagation, the Richardson number somewhere inside the pycnocline may fall below the critical value

of $1/4$ when the amplitude of the wave exceeds $a_c = 2\,(\Delta h\, h_1)^{1/2}$, where Δh is the width of the pycnocline and h_1 is the depth of the upper layer. In this case, the growth of a shear instability and associated mixing will extract energy from the internal wave. This energy is assumed to go into mixing inside the pycnocline, resulting in the increase of the width of the interface. The internal wave will decrease in amplitude and the local Richardson number will rise above the critical value. This theory gave fairly good agreement with laboratory experiments of *Kao et al.* [1985].

Pinkel [2000] discussed dissipative losses to shear instability of ISWs observed in the Warm Pool of the Western Equatorial Pacific. Although the observed inverse Richardson number was not dramatically affected by a soliton passage, *Pinkel* [2000] noted that local instabilities must be triggered, as they were evidenced from the increases in acoustic scattering strength on the echosounder picture.

Later, *Moum et al.* [2003] presented observations of shear instability induced by a 40 m internal wave moving along the interface accompanied with the groth of Kelvin-Helmholtz billows (Figure 2.9). Their measurements of velocity and density at the interface gave a Richardson number above the critical value, $Ri > 1$. This means that the flow is dynamically stable and no density overturns and instabilities should exist. That contradicts the clearly observed turbulence developing in a manner consistent with shear instability. *Moum et al.* [2003] hypothesized that the drop of the Richardson number could be triggered by currents on scales that are not resolved by their measurement instruments (less than a few meters). Currents that generate a localized shear come from the small-scale strain acting simultaneously on isopycnals and streamlines. The wave strain parameter is defined as

$$\gamma = \frac{\partial\rho/\partial z}{\partial\rho_0/\partial z}, \tag{2.42}$$

where ρ_0 is the undisturbed density profile at any upstream location, (*Moum et al.* [2003]). Calculated strain rate indicates that isopycnals are being spread in the upper and lower layers of the water column, $\gamma < 1$, but at the same time they appear to be compressed by nearly a factor of two ($\gamma \sim 2$) in the vicinity of the pycnocline.

Moum et al. [2003] showed that when inferred from density observations, the velocity profile contained a small-scale spike - the result of the small-scale straining effect of the

wave that could not be detected by velocity measurements. The spike in the velocity field suggests the existence of a thin layer where the local Richardson is below $1/4$, corresponding to the turbulence visible in the echosounder images.

2.3 Propagation of internal solitary waves

IWs can be visually identified as regions of roughness of the ocean surface that are produced by associated surface currents generated by internal waves. Sequences of ocean surface photographs taken from the top of a cliff during several hours or days was first used by *Ewing* [1950] to correlate the areas of variable surface roughness with IW propagation. Time lapse photography is now a simple and convenient way to document the motion of internal waves using their associated "footprints" in coastal waters [*Bourgault and Kelley*, 2003; *Pawlowicz*, 2003]. More advanced techniques of remote observation of IWs include the use of Synthetic Aperture Radar (SAR), sensitive to the roughness of the sea surface. It has been used for the purpose of visual detection of IWs from aircraft [e.g. *Apel*, 2002; *Brandt et al.*, 1996] and space [*Ostrovsky and Stepanyants*, 1989].

Various techniques were developed for the *in situ* observations of IWs. Instruments lowered from a vessel, or dropped freely, are the traditional way to measure the vertical structure of the oceans. The CTD (conductivity, temperature, depth) instrument records electrical conductivity and temperature (and hence salinity and density) as functions of depth as it is lowered from a stationary ship. The recorded time series are then analyzed and particular internal wave events are identified. The equivalent of an array measurement is to use two or more profiles separated horizontally [*Stegen et al.*, 1975] or in time [*Hayes*, 1975].

Recently, *Moum et al.* [2007] presented observations of the propagation of an ISW having traveled more than 100 wavelengths across the Oregon continental shelf. They noticed that during this time the wave traveled with nearly constant speed and an amplitude of about 15 m, but the wavelength gradually decreased from 220 m at the initial stage of propagation to 60 m at the final stage. This was attributed to the significant changes in density stratification along the path of ISW propagation. The shape of the ISW was in general consistent with the KdV solution but at the initial stage of propagation *Moum et al.*

[2007] noted the asymmetric density structure in the ISW profile. They suggested that at early stages the ISW was transforming from the solibore, and so was close to its generation point. With time, the ISW evolved into symmetrical density profile consistent with KdV theory. Indirect estimates of wave kinetic and available potential energies showed that the total energy of the wave decreased from 1.1 to 0.5 MJ m^{-1}. The rate at which wave energy was lost, $dE/dt = 14$ W m^{-1}, was approximately equal to the energy lost to turbulence dissipation inferred from turbulence measurements in the wave cores plus estimates in the wave-induced bottom boundary layer.

Numerical simulations of *Vlasenko et al.* [2005] also show that internal solitary wave propagating over the flat bottom topography evolve in a self-preserving adiabatic manner. This means that an ISW adjusts itself to small variations of the density stratification in such a way that the total energy of the wave remains constant.

2.4 Interaction of internal solitary waves with a sloping bottom

2.4.1 Shoaling effects and breaking

Numerous observations of internal waves in different parts of the world were aimed to investigate the behaviour and properties of IWs on continental shelves [*Apel et al.*, 1985; *Cummins et al.*, 2003; *Filonov and Trasvina*, 2000; *Holloway et al.*, 1999]. These studies reveal the complex picture of interaction of IWs with a sloping bottom. It was shown by *Grimshaw et al.* [1999] using variable coefficient KdV equation and later by *Vlasenko et al.* [2005] using fully nonlinear nonhydrostatic numerical simulations that for a slow variation of the topography, strongly nonlinear IWs are evolving in an adiabatic manner in the course of their propagation, i.e. adjusting the wavelength and amplitude such that the energy of the soliton remains constant.

The adiabatic development of the soliton is terminated when its amplitude becomes comparable with the depth of the layer. The termination process is described as breaking of the ISW which leads to the generation of turbulence and mixing. *Helfrich and Melville* [1986] performed a set of laboratory experiments using a two-layer fluid. ISWs shoaled and

occasionally broke over the linear slope ending with a shelf of a finite depth. Performing routing measurements of the location of the wave breaking, *Helfrich and Melville* [1986] proposed an approximate condition for breaking as the relationship between the depth of the lower layer on the shelf d_S and the amplitude of the incident wave a_0:

$$\frac{-a_0}{d_S} \geq 0.4. \tag{2.43}$$

Several years later *Helfrich* [1992] performed a similar set of laboratory experiments with a slightly different geometry where the depth of the shelf was set to zero. In this case the depth of the lower layer on the shelf d_S is replaced by the depth of the lower layer at the breaking point. However, the breaking condition has remained the same. Both laboratory studies did not find any dependency of the breaking condition (Equation 2.43) on the angle of the slope.

The breaking criterion was extended by *Vlasenko and Hutter* [2002a] based on numerical simulations. The location of wave breaking was defined as the position where the orbital velocities begin to surpass the wave's phase speed for the first time. The criterion proposed by *Vlasenko and Hutter* [2002a] relates the depth of fluid at the location of breaking with the amplitude of the internal wave:

$$\bar{a} = \frac{a_m}{H_b - H_m} = \frac{0.8^o}{\theta} + 0.4, \tag{2.44}$$

where a_m is the depth of the undisturbed pycnocline with maximum depression, and θ is the bottom slope in degrees.

Figure 2.10 shows the curve described by Equation 2.44, which divides the parameter space $\bar{a}$, γ into two halves. If the point is located above the curve, the wave breaks, otherwise, if the point is located below the curve the wave experiences a smooth transition into a packet of waves of elevation. The difficulty associated with the application of criterion 2.44 is that it is not possible to give the answer *a priori* if a given wave is going to break or not. To be able to place a point on this graph, the depth of fluid at the breaking point H_b is necessary. It, however, can only be measured after the breaking event takes place. *Vlasenko and Hutter* [2002b] also noted that criterion 2.44 works poorly for waves with

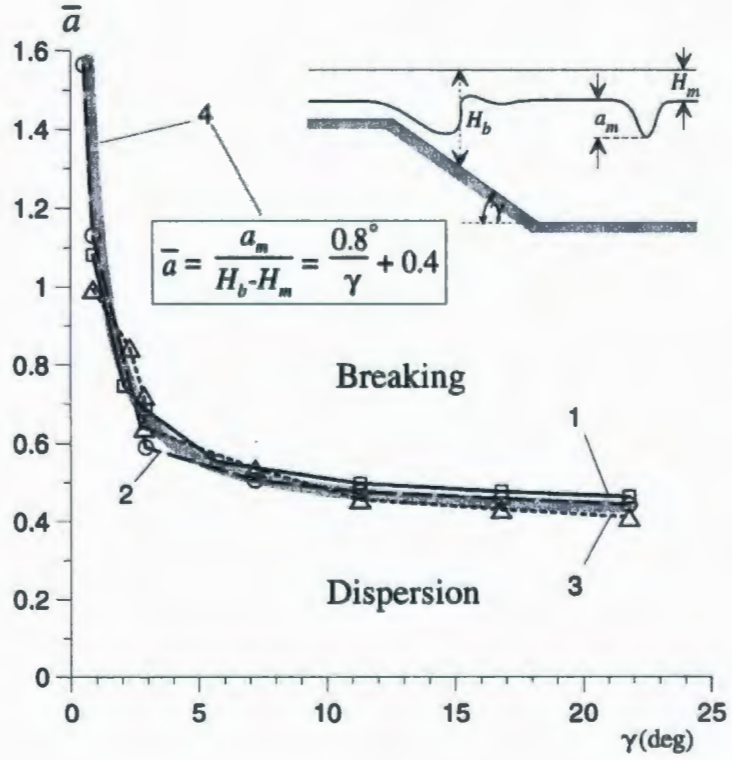

Figure 2.10. Breaking criterion descried by Equation 2.44. Taken from *Vlasenko and Hutter* [2002a]

small amplitudes.

A number of laboratory experiments were conducted to investigate the properties and behaviour of an ISW interacting with a sloping topography. *Wallace and Wilkinson* [1988], *Helfrich* [1990], *Helfrich* [1992] studied the breaking and runup of periodic IWs in a two-layer fluid on a uniform slope. The shoaling and breaking of IWs over the slope was also investigated for the continuous stratification by *Kao et al.* [1985]. They found that the onset of the wave breaking is governed by shear instability, which is initiated when the local gradient Richardson number is less than $1/4$.

Laboratory experiments of *Michallet and Ivey* [1999] used dye to visualize the process of solitary wave breaking on a linear slope. Unlike conclusion of *Kao et al.* [1985], they found that the breaking is initiated by the gravitational instability at the rear of the wave.

When an internal solitary wave interacts with a slope, some fraction of its energy will be lost to dissipation (sidewall, interfacial, bottom), some fraction will go to irreversible mixing (though breaking), some energy will be reflected back to the source. Recently *Bourgault and Kelley* [2007] used nonhydrostatic numerical simulations to answer the question what fraction of energy of an incident solitary wave, (E_0), will be reflected back, E_R. They found that the reflectance $R = E_R / E_0$ is close to what *Michallet and Ivey* [1999] measured in laboratory experiments provided that sidewall friction is taken into account. Their values are significantly higher than ones found by *Helfrich* [1992]. *Bourgault and Kelley* [2007] proposed a simple parametrization for the reflectance of ISW on smooth uniform slopes:

$$R = 1 - e^{-\xi/\xi_0}, \tag{2.45}$$

where ξ is the Iribarren slope parameter or the Iribarren number, defined as the ratio of the bottom slope, s, to the internal wave slope a/L_w:

$$\xi = s/\sqrt{a/L_w} \tag{2.46}$$

and $\xi_0 = 0.78 \pm 0.02$ from the best fit.

2.4.2 Boluses

It has been generally accepted that ISWs can have both signs of polarity. *Keulegan* [1953] showed theoretically that in a two layer fluid the disturbance of the interface can be negative (wave of depression) if the depth of the upper layer h_1 is bigger than the depth of the lower layer h_2 and positive (wave of elevation) if $h_1 < h_2$. Based on this, *Kaup and Newell* [1978] proposed that a wave of depression can switch its polarity while moving through the turning point. This idea led to a long discussion about such a possibility. *Helfrich et al.* [1984] showed numerically that a single wave of depression is transforming into a number of waves of reversed polarity. It was confirmed with laboratory experiments by *Wallace and Wilkinson* [1988] who reported on the generation of approximately periodic train of internal waves of elevation that are produced as the result of interaction of a single wave of depression with a slope. They described the resultant ISWs of elevation as features having circular shape and

sometimes recirculating cores, see Figure 2.11. Similar features were observed in coastal waters of California by *Emery and Gunnerson* [1973] who introduced the term "bolus" for such waves of elevation which emphasizes their circular shape characteristics.

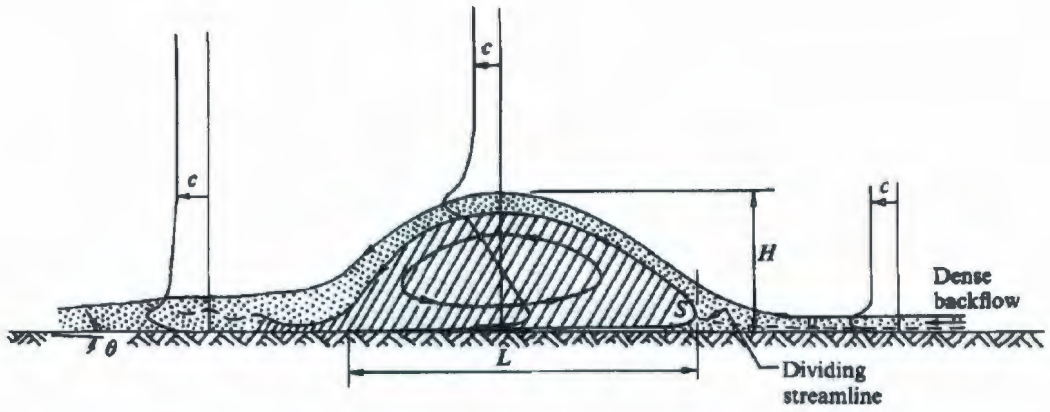

Figure 2.11. Sketch of the bolus internal structure and associated velocity profiles, made on the basis of laboratory experiments (Taken from *Wallace and Wilkinson* [1988]). Backflow of dense fluid going on top of the bolus and closed streamlines inside the bolus are important features that should be noted.

At the same time, the majority of field observations describe large amplitude IWs of depression. There are very limited observations of the waves of elevation and transition of the wave of depression through the turning point. *Orr and Mignerey* [2003] presented acoustic flow visualization of the conversion of the packet of ISWs of depression into waves of elevation near the South China Sea shelf break in the Luzon Strait. The amplitudes of the leading waves of depression typical to this region are about 70 m. They noted that the conversion is accompanied by the presence of the shear instabilities at the interface between layers and signs of mixing in the lower layer. The amplitudes of the larger instabilities were about 40 m and widths were 100 - 150 m. There were also small instabilities with amplitudes 1.5 - 2 m. However, only the beginning of the conversion process was observed and there were no attempts to systematically study properties of the internal waves of elevation.

Klymak and Moum [2003] presented observation of the internal waves of elevation propagating shoreward along a near-bottom pycnocline over the Oregon continental shelf. The

backscatter image was compared to the solution of the fully-nonlinear soliton model (Long equation), *Long* [1956], [*Lamb*, 2002]. Based on the theoretical nonlinear fit the estimation of the IWs energy was made. *Klymak and Moum* [2003] estimated the energy dissipation rate to be too small and hypothesized that the wave of elevation will eventually break up on the slope. They also proposed that the observed intensification of the acoustic signal inside the bolus may be attributed to denser fluid trapped inside the region with closed circulation. For lack of density measurements inside the bolus, they rely instead on the solution of the Long equation which yielded closed streamlines. However, the main assumption used for the derivation of the Long equation is that all streamlines should originate far upstream and thus the physically meaningful solution excludes the existence of regions with closed streamlines [*Davis*, 1969; *Davis and Acrivos*, 1967]. Citing *Davis* [1969], serious disadvantage "is that the solutions obtained from Longs model often indicate both regions of closed streamline flow, which are inconsistent with the model itself, and regions in which the density increases with height, a configuration which is likely to be unstable." Thus such solution may not be used as a proof of existence of trapped cores inside the bolus.

Hosegood and van Haren [2004] published observations of internal waves of elevation in the Faeroe-Shetland Channel. They report on the propagation of a train of the high frequency (5 - 20 min) ISWs with a steep leading edge of amplitude $\mathcal{O}(10\ \mathrm{m})$. Their CTD and microstructure measurements indicate that boluses can result in the short-term maximum of the vertical diffusivity, $K_z \sim \mathcal{O}(10^{-1}\ \mathrm{m^2 s^{-1}})$. They, however, claim that the long-term $K_z \sim \mathcal{O}(10^{-4}\ \mathrm{m^2 s^{-1}})$, implying that the boluses are not important for sustaining deep-sea mixing.

Scotti and Pineda [2004] reported about observation of large ($a \sim 12\,\mathrm{m}$) and steep near-bottom waves of elevation. Important distinction of these waves were the presence of regions of closed circulation (trapped core), (Figure 2.12). They speculated that trapped cores will greatly enhance shoreward transport of water, plankton and contaminants.

Derzho and Grimshaw [1997] proposed an asymptotic solution of the Boussinesq equations allowing for an internal wave of depression to contain a trapped core with uniform vorticity. The possibility of existence of trapped cores inside a wave of depression was demonstrated through nonhydrostatic numerical simulations by *Lamb* [2002]. It was shown that formation of trapped cores can be facilitated by the effect of the constant background

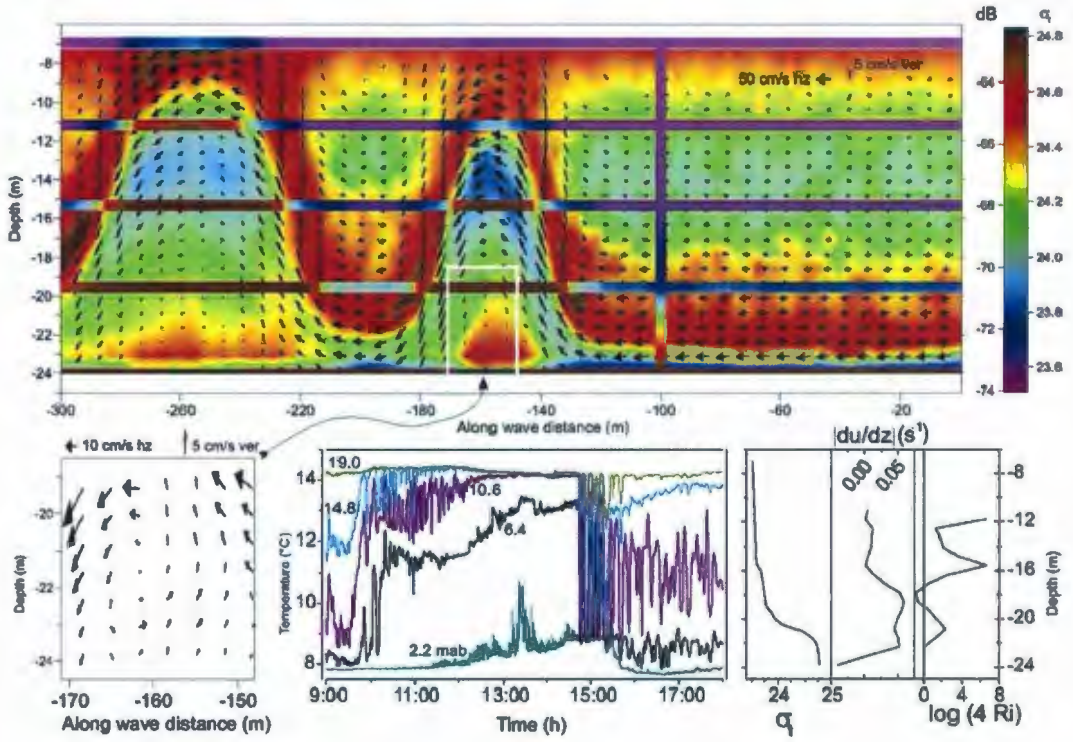

Figure 2.12. Observation of large ($a \sim 12$ m) and steep near-bottom waves of elevation made by *Scotti and Pineda* [2004]. Region with closed circulation is highlighted by a white rectangle on the upper panel and details of the velocity vectors are shown on the bottom left panel. Bottom middle panel presents the temperature records over the period of the observations. Right bottom panel shows the inferred density (left), magnitude of shear (center) and gradient Richardson number (right) just before the arrival of the first wave.

current during wave shoaling. Beside mention of potential influence of waves with trapped cores for transport and speculations about importance for biological productivity or pollutant spreading, very few papers provide either quantitative results or systematic research on properties of waves with trapped cores.

Venayagamoorthy and Fringer [2007] considered shoaling of progressive internal waves in the continuously stratified fluid. Waves were forced at the left boundary using the velocity corresponding to the first mode internal wave with the amplitude U_0 and were shoaling on a linear slope forming circular surges of dense water. Despite of the difference in formulation of physical problem, boluses formed were similar to ones generated by solitary

waves, (Figure 2.13). Internal waves in the continuous stratification are characterized by

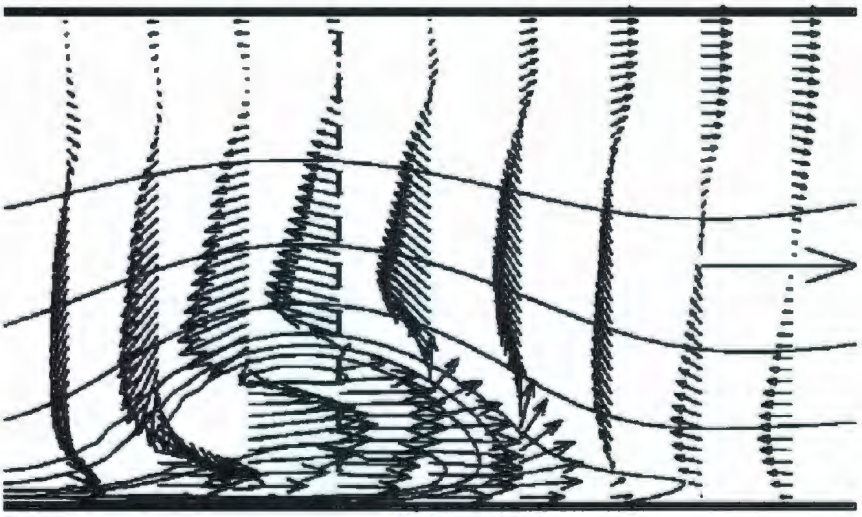

Figure 2.13. Velocity vectors and density contours inside a bolus formed as a result of the interaction of mode 1 internal wave with a linear slope in continuously stratified fluid. Results of numerical simulations by *Venayagamoorthy and Fringer* [2007]).

two nondimensional numbers: the Froude number $Fr = U_0/c_{ph}$, where c_{ph} is the linear first-mode internal wave speed, and the ratio γ/s, where γ is the topographic slope and s is the slope of the internal wave beam characteristic. Following *Legg and Adcroft* [2003], *Venayagamoorthy and Fringer* [2007] assumed that the necessary condition for the development of boluses is that the Froude number of the reflected wave should exceed 1. Analysis of the reflection of IWs based on linear inviscid theory led to the conclusion that the formation of boluses in the continuously stratified fluid can occur only in a certain range of $[Fr, \gamma/s]$ parameter space:

$$\frac{\gamma}{s} = \frac{Fr^{-1/2} + 1}{Fr^{-1/2} - 1}. \tag{2.47}$$

This finding differs significantly from the case with two-layer stratification. *Helfrich et al.* [1984] showed that in this case an internal wave of depression is always transforming in at least one wave of elevation. *Venayagamoorthy and Fringer* [2007] also stated that boluses formed in the linearly stratified fluid are propagating essentially as gravity currents. *Maxworthy et al.* [2002] performed laboratory experiments of gravity currents propagating

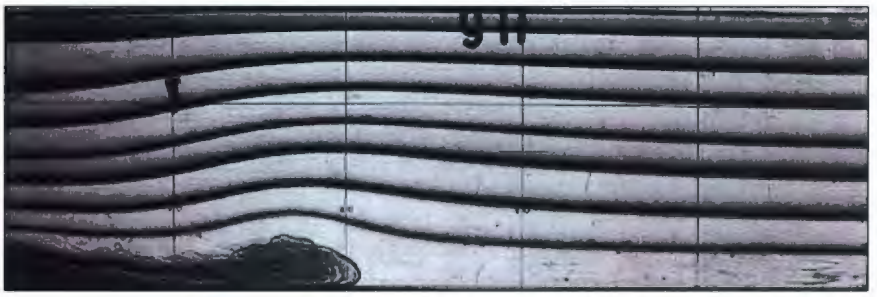

Figure 2.14. An example of the gravity current head propagating over a flat bottom in a linearly stratified fluid. Reproduced from the laboratory experiments of *Maxworthy et al.* [2002]. Note similarity to the bolus from the numerical simulations of *Venayagamoorthy and Fringer* [2007].

in a linearly stratified fluid. Noting certain similarities with internal solitary waves they tested the agreement of their results with weakly nonlinear KdV theory. They found agreement to be poor.

2.4.3 Mass transport

One of the reasons for studying ISWs is their effect on the vertical exchange of nutrients and heat near the shelf edge [e.g. the Scotian Shelf *Sandstrom and Oakey*, 1995]. ISWs may also contribute significantly to the transport rates in the along shore direction [e.g. *Bogucki et al.*, 1997]. *Huthnance* [1995] has suggested that the transport effect of a typical ISW packet can be the same order of magnitude as other shelf edge processes, such as slope current meanders and upwelling.

It is well-known that progressive surface waves result in a small drift of surface particles (Stokes drift). Using numerical experiments *Lamb* [1997] showed that propagation of a nonlinear ISW can also result in a finite displacement of suspended particles on the surface, where the velocities generated by the ISW are the highest. The displacement of the particles closest to the interface, however, is small because of a small velocity induced by the internal wave.

Inall et al. [2001] presented observations of ISW packets on the Mallin shelf and compared mass transport caused by ISW to the results derived from the weakly nonlinear KdV

theory. They derived an equation which connects the mass transport to the displacement of the interface, depths of the layers and long wave speed. For the lower layer it reads:

$$Q_2 = c_0 \left(\eta - \frac{3(h_2 - h_1)}{4\, h_1\, h_2}\, \eta^2 \right) + \frac{h_1\, h_2}{6\, c_0}\, \frac{\partial^2 \eta}{\partial t^2}, \tag{2.48}$$

Figure 2.15 shows the mass transport given by Equation 2.48. It consists of three terms: linear, non-linear and dispersion. When these terms are integrated to find the depth-integrated mass transport, the dispersion term becomes zero but the linear and nonlinear terms do not. The transport in the upper layer has the same absolute value as Q_2 but is opposite in

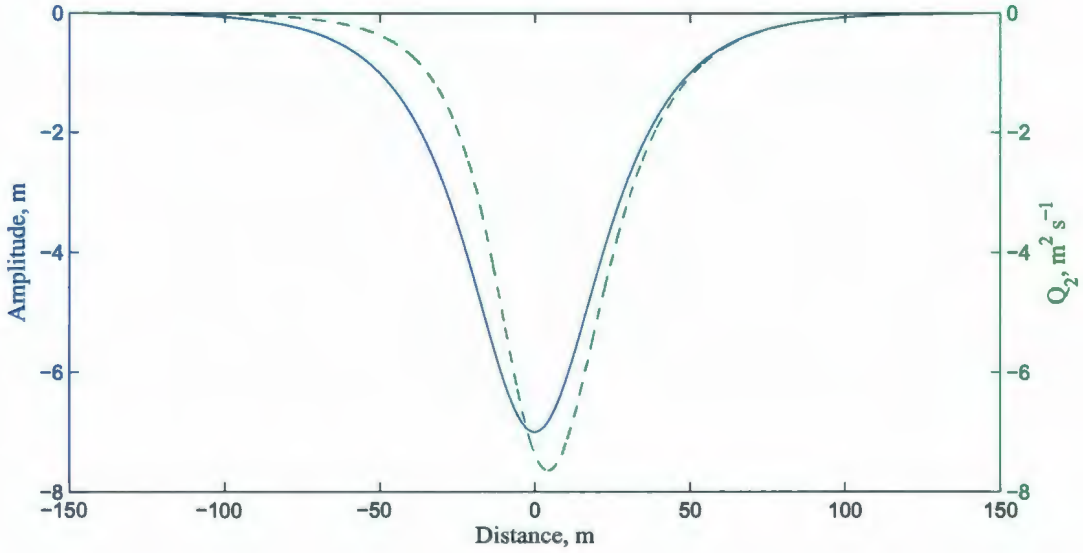

Figure 2.15. Vertical displacement of the interface (blue solid line) and mass transport in the lower layer Q_2 induced by the ISW of depression with amplitude $a = 7$ m calculated from Equation 2.48 (green dashed line).

the direction. For a wave of depression, the transport in the upper layer is pointing in the same direction as wave's phase speed, while Q_2 is in the direction opposite to the wave. *Inall et al.* [2001] found that the depth-integrated mass flux Q_2 resulted from the wave train consisting of several ISWs of depression was dominated by the linear term $c_0\eta$, so has a form similar to the depression of the isotherm observed using thermistor chains.

Pritchard and Weller [2005] used Equation 2.48 to estimate mass transport flux from wave-train consisting of 7-8 waves of elevation with amplitudes $\mathcal{O}(15$ m) and periods

$\mathcal{O}$(6.5 min) observed on the New England continental shelf. They also found that Q_2, which was now directed toward the shore, had a largest contribution form the linear term.

Butman et al. [2006] performed a field experiment in Massachusetts Bay to assess the role of large-amplitude internal waves in resuspending bottom sediments. They observed that bottom currents induced by packets of 5–10 waves with periods of 5–10 min and wavelengths of 200–400 m were sufficiently strong to cause sediment resuspension. The beam attenuation increased by several times after the arrival of the ISWs packet and remained elevated for 1–2 h. Figure 2.16 shows the location of this field study, grey dotted line indicate the area of ISWs activity and arrows shows the direction of the bottom transport which was inferred from the beam attenuation measurements. In accordance with Equation 2.48 internal solitary waves of depression propagating toward the shore resulted in induced transport which was directed offshore.

On the other hand, internal waves of elevation or boluses have reversed polarity and thus their depth integrated transports are oriented offshore in the upper layer and onshore in the lower layer, (Figure 2.17). This makes them a good candidate for the mechanism of onshore transport of cold nutrient-rich bottom water and suspended sediments.

Recently, *Bourgault et al.* [2008] investigated turbulence and transport of subpycnocline water caused by boluses. The field study took place in St. Lawrence estuary. Since it is not possible to use Equation 2.48 in field measurements, they calculated mass flux of subpycnocline water at one point on a slope, x_0, using

$$F_x(x_0,t) = \int_0^H \delta(\rho_s)\rho(x_0,z,t)u(x_0,z,t)\,dz, \tag{2.49}$$

where

$$\delta(\rho_s) = 1 \quad \text{if } \rho > \rho_s,$$

$$\delta(\rho_s) = 0 \quad \text{if } \rho < \rho_s.$$

Here ρ_s = 1017 kg m^{-3} represents the density of fluid originating from below the pycnocline, $u(x,z,t)$ is the horizontal velocity induced by internal waves. As boluses were moving pass the chosen point x_0, the time series of the mass flux $F_x(t)$ was recorded. The

time-integrated mass transport can be calculated as

$$M = \int_{t_1}^{t_2} F_x(t)\, dt, \tag{2.50}$$

where time interval $[t_1\ t_2]$ can be chosen to contain the input from each individual bolus or to contain the full wavetrain of boluses.

2.4.4 Coastal mixing induced by solitary internal waves

It was noticed during numerous observations [*Kunze and Smith*, 2003; *Munk and Wunsch*, 1998; *Nash et al.*, 2004; *Wunsch and Ferrari*, 2004] that at some locations mixing rate is much higher compared to the values observed in the abyss. Several regions of enhanced mixing have been described, for example around seamounts [*Lueck and Mudge*, 1997], over rough abyssal topography [*Ledwell et al.*, 2000; *Polzin et al.*, 1997], in submarine canyons [*Lien et al.*, 2001], and in tidal channels [*Lu and Lueck*, 1999; *Lu et al.*, 2000]. Observations of *Garabato et al.* [2004] in the Southern Ocean using the method proposed by *Polzin et al.* [2002] revealed remarkably intense enhanced turbulent mixing over rough topography. Common mixing rates above complex bathymetry exceeded background values by a factor of 10 to 1000.

This mixing is believed to be at least partially triggered by internal wave breaking events occurring over sloping bottoms [*Garrett*, 2001; *Munk*, 1966; *Munk and Wunsch*, 1998]. This hypothesis is supported by observations [*Boegman et al.*, 2005; *Gregg*, 1987], laboratory experiments [*Helfrich*, 1992; *Michallet and Ivey*, 1999], and numerical simulations [*Slinn and Riley*, 1996]. However, the magnitude of mixing caused by breaking IWs still remains an open question.

Estimating the local rate of the vertical diffusion coefficient from turbulence measurements, *Osborn* [1980] argued that in a stably stratified ocean, the turbulent kinetic energy is produced mainly by the shear generated by breaking IWs. While most of the turbulent kinetic energy is dissipated by viscous friction at a rate ε, a fraction Γ goes to vertical mixing of the fluid density. This fraction of the turbulent kinetic energy available to actually mix the fluid is called mixing efficiency.

In the laboratory experiments, *Helfrich* [1992] and *Michallet and Ivey* [1999] measured

mixing efficiency of a solitary interfacial IWs modeled in a two-layer system. Mixing efficiency is introduced as a ratio

$$\Gamma = \frac{\triangle E_p}{E_0 - E_R} = \frac{\triangle E_p}{E_0} \frac{1}{1-R}, \tag{2.51}$$

where $\triangle E_p$ is the potential energy increase after the breaking of IW, E_0 is the energy of the incident IW and E_R is the energy of the reflected wave, R is the reflectance coefficient. *Michallet and Ivey* [1999] found that a breaking IW can contribute up to 25% of its energy to vertical mixing. However, *Helfrich* [1992] found no significant dependence of the mixing efficiency on the external parameters, such as characteristic slope length L_S and characteristic wavelength L_W, while *Michallet and Ivey* [1999] report a peak at $L_W/L_S = 0.5$.

As formula 2.51 suggests, the mixing efficiency for a given ISW depends on the energy of incident wave, E_0. Recently, there has been a surge of renewed interest in estimating the energy content of ISWs and associated energy fluxes both from theoretical point of view (*Scotti et al.* [2006] and *Lamb* [2007]) and in the field measurements (*Klymak and Moum* [2003], *Scotti and Pineda* [2004], *Scotti et al.* [2006], *Moum et al.* [2007]). The total energy of the ISW in incompressible fluid is partitioned into kinetic and potential parts. Kinetic energy density is given by

$$ke = \frac{1}{2}\rho(x,z)\left(u^2(x,z) + w^2(x,z)\right). \tag{2.52}$$

The volume integral, evaluated over the volume of the ISW will then give the value of the kinetic energy associated with the wave:

$$KE = \int_V ke\, dV. \tag{2.53}$$

The potential energy per unit volume is

$$pe = g\,\rho(x,z)\,z. \tag{2.54}$$

The potential energy of the volume containing the ISW is thus

$$E_p = \int_V pe\, dV. \tag{2.55}$$

Since the full potential energy is one order of magnitude large than the kinetic energy, they are not suitable for comparison. Another reason why the full potential energy should be substituted by some another quantity comes from the realization that most of the fluid column is stably stratified and only the part of fluid that is been displaced by the wave contains the useful measure of the potential energy associated with the wave. The idea was formulated by *Margules* [1909] and developed by *Lorenz* [1955]. The part of the potential energy which is available for conversion to other forms of energy is called Available Potential Energy (APE) and is usually defined as the difference between potential energy of the state under consideration and some suitably defined reference state. In many cases (especially in observations) the reference state is chosen to be the state with background stratification, *Reid et al.* [1981]. Another way to choose the reference state is to adiabatically resort density profile, $\rho_{sort}(z)$, *Winters et al.* [1995]. This state corresponds to the minimum of potential energy, E_p^{ref}, because no other rearrangement of density can lower the potential energy of the fluid. The APE is then

$$APE = E_p - E_p^{ref} = g \int_V (\rho(x,z) - \rho_{sort}(z))\, z\, dV. \tag{2.56}$$

Holliday and McIntyre [1981] pointed out several problems with the form of Eq. 2.56. First of all, the expression 2.56 is not sign-definite and thus should be used with caution for situations where differently-signed contributions may cancel each other. *Holliday and McIntyre* [1981] have proposed a different APE energy density:

$$ape = -\int_0^{\xi} g\, \widetilde{\xi} \rho_0'(z - \widetilde{\xi})\, d\widetilde{\xi}, \tag{2.57}$$

where $\xi(\mathbf{x}, \mathbf{t})$ is the vertical distance that the fluid element at $(\mathbf{x}, \mathbf{t})$ has moved from its original, undisturbed position in the background density profile $\rho_0(z)$ and prime denote the differentiation in z. As it is clear, for stable stratification $-\rho'(z) > 0$ for all z and therefore 2.57 is always positive. *Holliday and McIntyre* [1981] have shown the equivalence of this

two formulations by Taylor expansion of $\rho_0'(z-\widetilde{\xi})$ about $z=\xi$. It then follows that the volume integral of 2.57 equals to Eq. 2.56.

The second problem in the definition 2.56 is that it is global. In order to find APE energy density at a specific location, the whole fluid in the domain under consideration should be sorted to the lowest potential energy state. Therefore using 2.56 APE is well defined for closed domains and in situations when one is interested in APE of the whole region. Difficulties appear when one wish to estimate the APE of a single isolated feature of a flow, such as ISW, front or an eddy.

Hebert [1988] was first to address this issue. He argued that the use of the background (far-field) density profile as a reference state is justified only for the truly isolated feature in the infinitely wide basin. On the other hand, when one is calculating APE in the domain of the finite size, the background density structure at infinity is obviously not accessible. That is why APE is calculated using the sorted density $\rho_{sort}(z)$ as the reference. However, the sorted density will depend on the extents of the domain in which the sorting is taking place. As the result, APE calculated in the domain of the finite size will always have an offset corresponding to the difference between sorted density profile and far-field background density profiles. As the basin becomes large, Hebert suggested that the sorted density profile will approach the far-field density structure at infinity and APE will reach asymptotically the constant value which he denoted as true APE of the isolated feature.

Recently, *Lamb* [2008] have revisited the problem and, using a simple toy problem, reached the same conclusion that in order to get the correct APE of the isolated feature, one needs to extend the domain to infinity. However, it should be pointed out that both in *Hebert* [1988] and in *Lamb* [2008] the examples used to show this idea are symmetric. As it will be shown latter, when the isolated feature is non-symmetric or when density profiles on both sides of the isolated feature are different, the APE is not converging to asymptote but rather tends to infinity as the domain is extended. Therefore this method should be used with care.

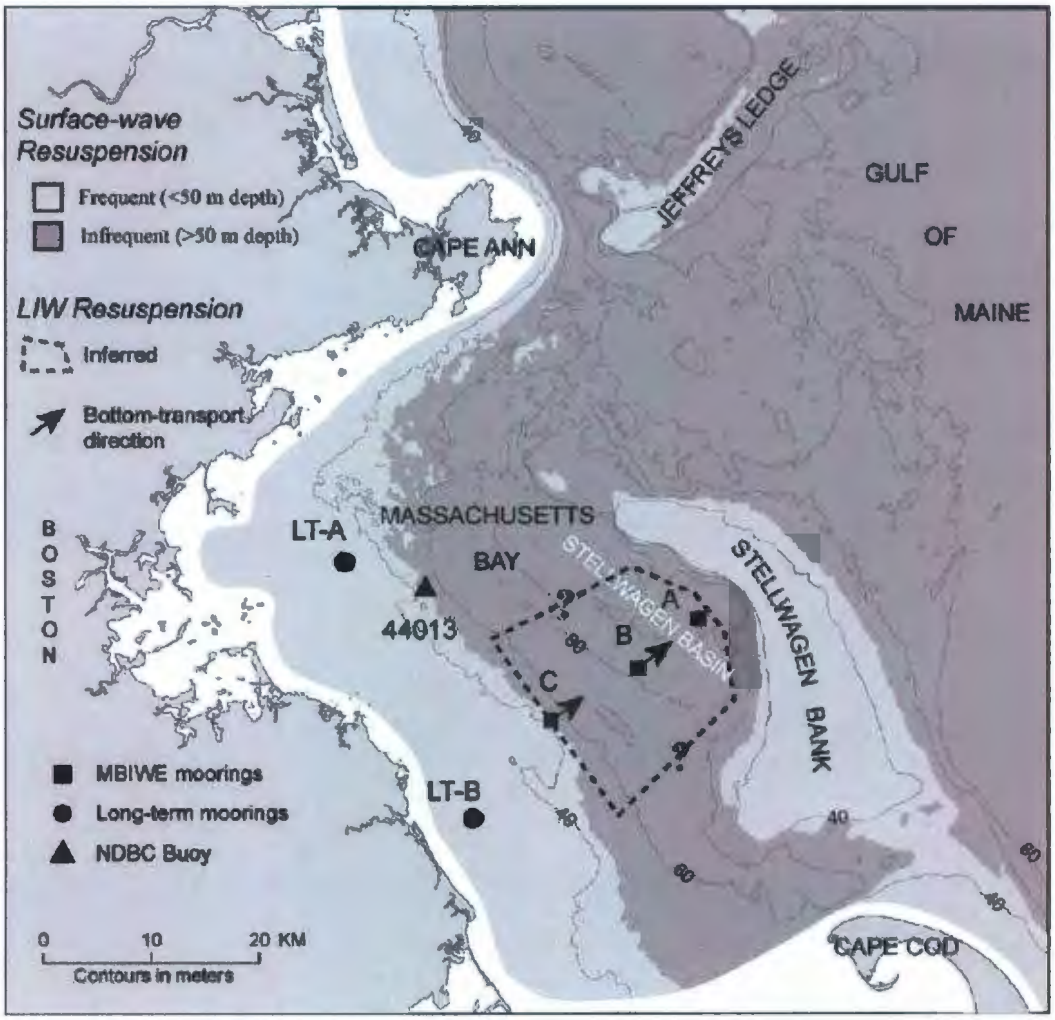

Figure 2.16. Map of the field study and arrows indicating the direction of mass transport induced by shoaling ISWs of depression. Taken from *Butman et al.* [2006].

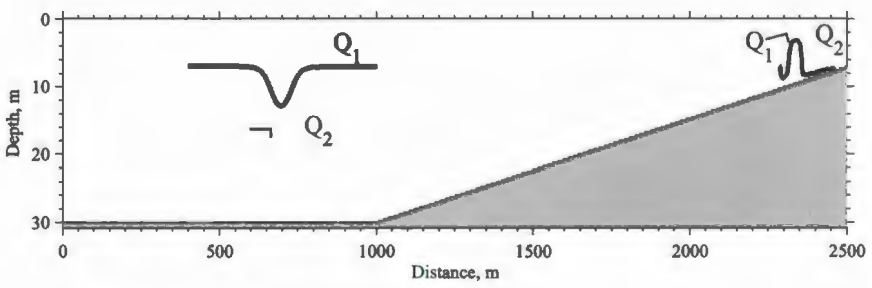

Figure 2.17. Schematic diagram of an internal wave of depression and elevation with corresponding transport directions in the upper and lower layers. Both wave are propagating to the right.

Chapter 3

Methods

3.1 Field work

The current research partially relies on the results of a field experiment carried out in the St. Lawrence Estuary during 14 days in August - September 2004 near the shore of Ile-aux-Lièvres Island as part of St. Lawrence Estuary Internal Wave Experiment (SLEIWEX) project.

The choice of this particular place of study is motivated by several reasons. According to remote and *in situ* observations [*Bourgault and Kelley*, 2003; *Bourgault et al.*, 2005] the site has a high and predictable IW activity and shows the manifestation of IW boundary collisions. These studies suggest that there is a certain possibility of IW observations during the full course of their evolution, from generation to the final dissipation stage.

A detailed description of the geography of the region and background oceanographic conditions can be found in *Bourgault and Kelley* [2003] and references therein. The location and bathymetry of the area of interest are shown in Figure 3.1.

Bidirectional data collection was conducted by using both bottom mounted upward-looking and towed downward-looking instruments. Two 600 kHz and one 1200 kHz upward-looking RD Instruments broadband acoustic Doppler current profilers (ADCPs) were moored on the slope along a line perpendicular to the shore at depths of 39, 23, and 12 meters. These instruments recorded the backscatter intensity and the three-dimensional currents in the water column and were set to record 7 s, 15 s, and 10 s ensemble averages with 1.00 m, 0.75

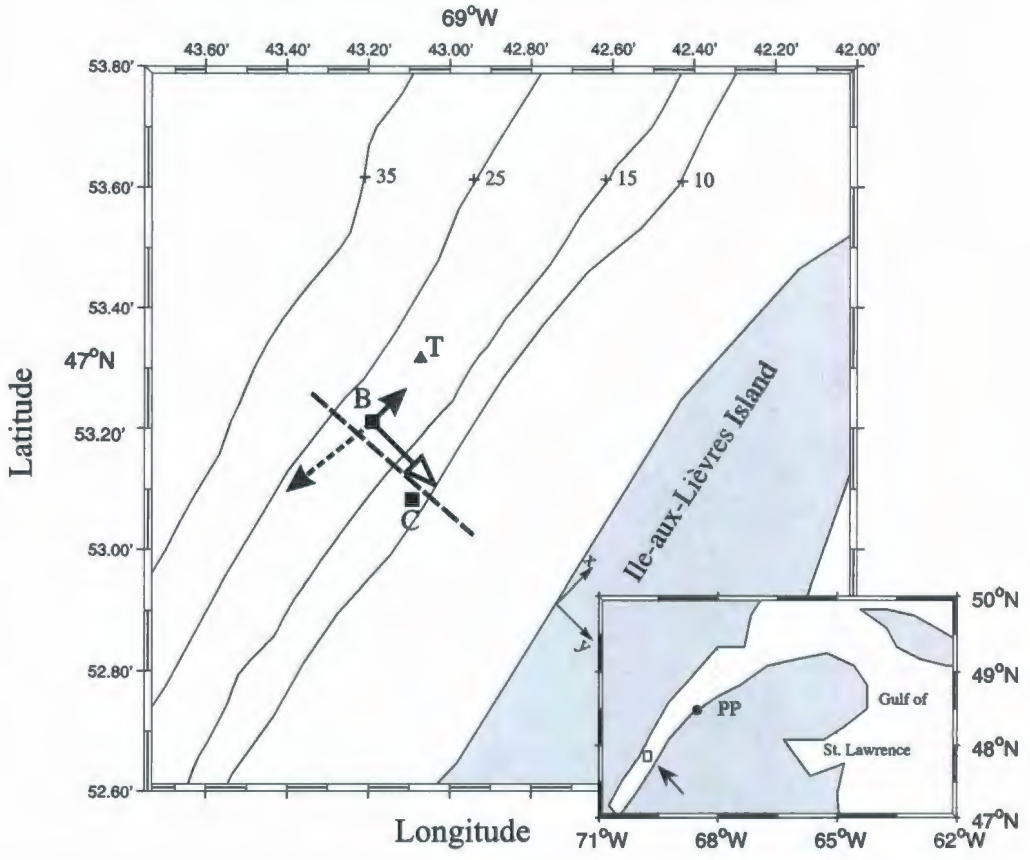

Figure 3.1. The map of the observational region. The dashed line shows the average transect along which towed measurements were collected. The axis system is indicated with its origin at the island edge. The squares mark Moorings B and C and the triangle marks the thermistor and CT chain. The mean surface current is indicated with the solid vector, while the dashed vector represents the mean at 13 m depth, below the pycnocline. The open arrowhead vector indicates the phase speed ($c = 0.6$ m s^{-1}) and direction of the leading wave of the wavetrain (i.e. the wave on the first panel of Figure 4.1). The observational region is marked as a square in the inset. Pointe-au-Père tidal gauge is marked as PP on the map. *Note:* The depths in the figure are taken from the Canadian Hydrostatic Service bathymetric chart 1235 and are reduced to the lowest normal tide (LNT). The actual depths during the observational period were a few meters above the LNT.

Table 3.1. Mooring details for ADCPs and the thermistor chain

Moorings	Inst. Freq. kHz	Location Lon/Lat	Depth, m	Bin size, m	Ensemble interval, sec
A	614.4	47° 53.522N / 69° 43.418W	39	1.00	7.0
B	614.4	47° 53.176N/ 69° 43.220W	23	0.75	15.0
C	1228.8	47°53.0.58 N/ 69°43.111W	12	0.40	10.0
T	-	47°53.316 N/ 69°43.072W	22	2.00	150.0

m, and 0.40 m vertical bin sizes, respectively. Mooring C also recorded the near-bottom temperature. The mooring configuration enables us to collect data at various stages of IWs evolution from the undisturbed phase to the transition to waves of elevation and breaking. The main characteristics of the moorings and their locations are presented in the Table 3.1. Deployment site is shown in Figure 3.1.

Surface sampling was carried out from a 25-foot vessel. One Biosonics narrow-beam echosounder with two transducers with frequencies 199 kHz and 418 kHz were mounted on a towed body along with an 300 kHz ADCP. Towing speeds were typically 1.5 - 2.5 m/s. Internal waves detected on the echosounders were associated with visible bands on the sea surface, and the latter were used to maintain a steaming direction orthogonal to the wave propagation direction. Horizontal position was determined to within 5 m with a Global Positioning System (GPS) unit.

A coordinate system is defined relative to the wave propagation direction (see Figure 3.1). The position associated with each echosounding measurement is then adjusted for the Doppler shift by remapping the recorded positions x' of every ping with

$$x = x' - c(t - t'), \tag{3.1}$$

where t is time, t' is the time when the wave trough/crest was observed and c is the wave phase velocity determined by the distance the wave trough/crest propagated between two consecutive transects. Visual inspection of the scattering layers on the Doppler-adjusted echogram yields $\eta(x)$, the wave interfacial displacement relative to the background level. The amplitude is computed as $a = \max(\eta)$.

Over one hundred transects perpendicular to the shore up and down the slope were made per day from 25 August to 2 September (weather permitting) to detect internal wave manifestation. When an IW was located the vessel closely followed the chosen wave. This yielded the detailed temporal description of the evolution of the IW propagating on the slope. The small size of the vessel enabled us follow into waters as shallow as 5 m depth and thus to monitor the whole wave evolution until the full dissipation.

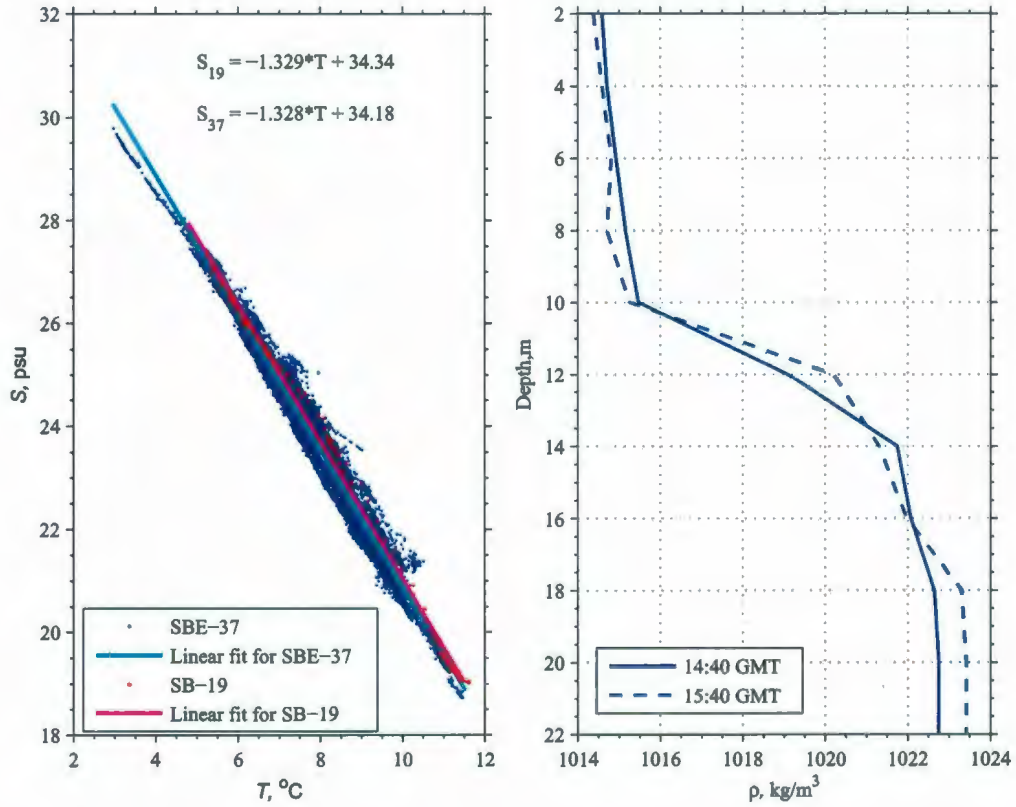

Figure 3.2. TS-diagram (left panel) obtained from two SeaBird-19 casts made around 15:00 GMT on 26 Aug 2004 near T-mooring (red dots) and from SBE-37 sitting at 6 m depth on the thermistor line (blue dots). Equations on the top give the linear fit for density profiles (right panel) inferred from the data collected by thermistors at 14:40 GMT and 15:40 GMT on 26 Aug. 2004.

Two conductivity-temperature-depth (CTD) recorders (SeaBird-19 and SeaBird-25, by Sea-Bird Electronics, Inc) were used occasionally to profile the temperature and salinity structure. A vertical Minilog-8 bit Vemco thermistor chain was moored about 450 m away from the mooring C and about 250 m from the mooring B (see Figure 3.1 for the exact posi-

tion) and was used for additional evaluating of water stratification. The thermistor line held eleven evenly spaced at 2 m intervals sensors with a sampling interval of 2.5 min. Additionally, for calibration purposes, two fast-response conductivity-temperature (CT) recorders (SBE-37, by Sea-Bird Electronics, Inc) with a sample interval of 15 s were fastened to thermistors at the depth of 2 and 18 m respectively (i.e. above and below the pycnocline, expected to be around 10 m depth). The response time of the thermistors was of the same order as the wave period, $\mathcal{O}(100$ s), so their sole use was in establishing the background temperature stratification. Water salinity was derived from conductivity and temperature measured by the CTDs. Similar tight linear dependence between temperature and salinity (correlation coefficient $R = 0.95$) (see Fig. 3.2a), acquired by the SeaBird-19 casts on Aug 26 and by the SBE37 during the two-week data collection on the thermistor line allowed us to infer salinity from temperature measurements obtained from thermistors. From temperature and salinity the density stratification is then calculated based on the equation of state for seawater.

A typical density structure is shown in Figure 3.2b. It can be concluded that the stratification in the area of interest is close to a two-layer fluid.

3.2 Numerical simulations

Idealized 2D numerical experiments were carried out in order to investigate propagation of internal waves and dynamics of their interaction with sloping boundaries. The non-hydrostatic model of *Bourgault and Kelley* [2004] was used. It solves laterally averaged 2D Navier-Stokes equations with the Bousinesq approximation ($\triangle\rho/\rho << 1$) and a free surface. The governing momentum equations for the model are expressed as:

$$\frac{\partial u}{\partial t} + u\frac{\partial u}{\partial x} + w\frac{\partial u}{\partial z} = -\frac{1}{\rho_0}\frac{\partial p}{\partial x} + \frac{\partial}{\partial x}\left(A_h\frac{\partial u}{\partial x}\right) + \frac{\partial}{\partial z}\left(A_v\frac{\partial u}{\partial z}\right) \tag{3.2}$$

$$\frac{\partial w}{\partial t} + u\frac{\partial w}{\partial x} + w\frac{\partial w}{\partial z} = -\frac{1}{\rho_0}\frac{\partial p}{\partial z} + g\frac{\rho}{\rho_0} + \frac{\partial}{\partial x}\left(A_h\frac{\partial w}{\partial x}\right) + \frac{\partial}{\partial z}\left(A_v\frac{\partial w}{\partial z}\right) \tag{3.3}$$

along with the continuity equation:

$$\frac{\partial u}{\partial x} + \frac{\partial w}{\partial z} = 0 \tag{3.4}$$

and the governing equation for a passive tracer C:

$$\frac{\partial C}{\partial t} + u\frac{\partial C}{\partial x} + w\frac{\partial C}{\partial z} = \frac{\partial}{\partial x}\left(A_h \frac{\partial C}{\partial x}\right) + \frac{\partial}{\partial z}\left(A_v \frac{\partial C}{\partial z}\right). \tag{3.5}$$

Here $u(x,z,t)$ and $w(x,z,t)$ are horizontal and vertical velocities respectively, $C(x,z,t)$ is the concentration of any scalar, $p(x,z,t)$ is pressure and A_h and A_v are coefficients of horizontal and vertical eddy viscosity defined through *Smagorinsky* [1963] parametrization as

$$A_h = A_v = \begin{cases} (C_s\Lambda)^2\sqrt{2\mathcal{S}^2 - N^2}, & \text{if } 2\mathcal{S}^2 > N^2 \\ 10^{-6}\ \mathrm{m^2 s^{-1}}, & \text{otherwise,} \end{cases}$$

In this parametrization $C_s = 0.2$ is the *Smagorinsky* [1963] coefficient, $\Lambda = (\Delta x\,\Delta z)^{1/2}$ is a length scale of unresolved eddies, $\mathcal{S}$ is the velocity strain defined as

$$\mathcal{S}_{ij} = \frac{1}{2}\left(\frac{\partial u_i}{\partial x_j} + \frac{\partial u_j}{\partial x_i}\right)$$

The process of the dissipation of wave energy at the seabed may be modeled by the action of a stress

$$\vec{\tau} = -C_d \rho \mathbf{u_b}|\mathbf{u_b}|, \tag{3.6}$$

where $\mathbf{u_b}$ is the water velocity, just above the bottom boundary layer, *Kundu* [1990]. The coefficient of bottom drug C_d may be expected to vary slowly with flow conditions and usually is taken to be a constant.

Note that governing equations 3.2 - 3.2 were simplified by setting the channel width $B(x)$ as a constant. General form of laterally-averaged equations and the details of the numerical scheme can be found in the original paper of *Bourgault and Kelley* [2004].

3.2.1 Model setup

There are $N = 6$ free parameters that define the problem of the ISW shoaling on the linear slope. The Buckingham's Pi Theorem allows one to connect them using functional relationship:

$$f(\Delta\rho,\, a,\, h_1,\, H,\, \Delta h,\, s) = 0. \tag{3.7}$$

Here $\triangle\rho$ is the density difference between top and bottom layers, a is the amplitude of the incident ISW, h_1 and H are depthes of the top layer and the total water depth correspondingly, $\triangle h$ is the width of the interface between layers and s is the angle of the sloped part of the bottom. It can be easily shown that the dimensional matrix constructed of the dimensional units of parameters in 3.7 has the rank $r = 2$. This means that the number of nondimensional parameters determining the problem is $N - r = 4$. The proper choice of the cycling variables gives the following nondimensional parameters:

$$\Pi_1 = \frac{\triangle\rho}{\rho}, \tag{3.8}$$

$$\Pi_2 = \frac{h_1}{h_2}, \tag{3.9}$$

$$\Pi_3 = \frac{a}{H}, \tag{3.10}$$

$$\Pi_4 = s, \tag{3.11}$$

This possible choice of independent parameters was given, for example, in *Helfrich* [1992]. At the same time, the Iribarren number, ξ, defined by Eq. 2.46, is an empirical surf parameter derived for surface waves based on the results of laboratory and field studies. It contains the ISW wave length, which is not an independent parameter of the problem, since it depends on the amplitude of the wave. As such, Irribaren number cannot be obtained from the formal application of the Buckingham's Pi Theorem, as it would be required to use some knowledge of underlying physical laws, which exact form we wish to study.

All numerical experiments were set up with a similar geometry presented in Figure 3.3. An internal wave starts over the flat portion of the domain and propagates towards the linearly sloping part. Horizontal grid used in the numerical simulations had constant spacing $\triangle x = 4$ m in the flat bottom region for series A-C and $\triangle x = 10$ m for series D-E and decreased gradually to $\triangle x = 0.25$ m on the slope for series A-C and to $\triangle x = 0.1$ m on the slope for series D-E. Vertical grid spacing was constant for series A-C, $\triangle z = 0.25$ m. Vertical grid spacing for series D and E was constant $\triangle z = 0.1$ m in the upper 15 m of the

fluid column and than increased gradually to $\triangle z = 0.25\,\mathrm{m}$. The model uses an adaptive time step with a restriction that the Courant-Freidrichs-Lewy (CFL) stability criteria for convective flows is satisfied.

Initial background density had a two-layer stratification:

$$\rho_b = \rho_0 + \frac{\triangle\rho}{2}\left[1 + \tanh(\frac{z - z_0}{\triangle h})\right], \tag{3.12}$$

where $\rho_0 = 1020.0\,\mathrm{kg/m^3}$ is a constant reference density, z_0 is the position of the interface and $\triangle h$ is the width of the interface. $\triangle\rho$ was set to 6 kg/m^3 for all runs such that the density of the lower layer was 1017 kg/m^3 and the density of the top layer was 1023 kg/m^3. This stratification was close to one observed in our field study.

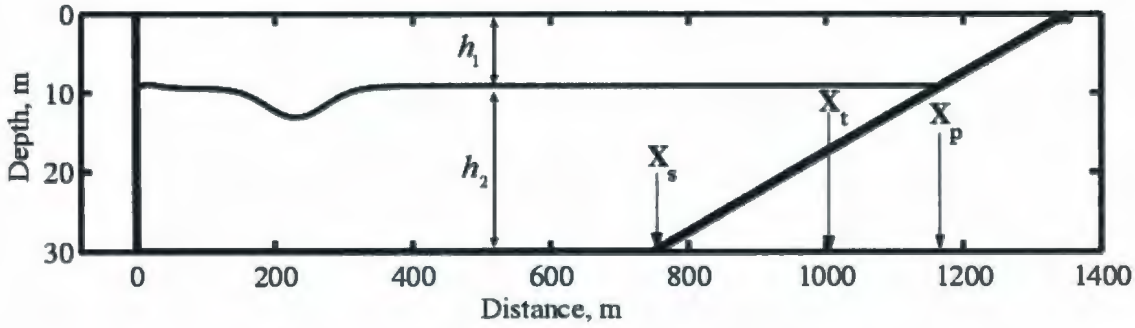

Figure 3.3. Setup of numerical experiments. Special points of interest are: X_s is the beginning of the slope, X_t is the turning point, X_p is the point of the interface-slope intersection.

Over 60 numerical experiments were carried out using various stratifications, incident waves amplitudes and angles of slopping bottom (Table 3.2). Series A-C were performed with the stratification having $h_1 = 7\,\mathrm{m}$ and $\triangle h = 10\,\mathrm{m}$. Series D and E have $h_1 = 9\,\mathrm{m}$ and $\triangle h = 5\,\mathrm{m}$. The total depth of the water column was taken to be $H = 30\,\mathrm{m}$ for all simulations. Figure 3.3 is a definition sketch showing relevant parameters, such as the beginning of the slope, X_s, position of the turning point, X_t, and the position of the bottom-interface intersection X_p.

Table 3.2. Parameters of the numerical simulations Iribarren number (Equation 2.46) represents the incident wave of depression.

Num. exp. ♯	Slope angle, rads	IW amplitude, m	h_1/H,	$\triangle h/H$,	Iribarren number
A: 1 -10	0.05 - 0.083	1.3	0.23	0.35	0.05 - 0.20
B: 11-20	0.024 - 0.14324	3.3	0.23	0.35	0.08 - 0.35
C: 21-30	0.0267 - 0.19	4.0	0.23	0.35	0.04 - 0.30
D: 31-40	0.0077-0.096	6.0	0.23	0.35	0.02 - 0.25
E: 41-50	0.0077-0.096	6.0	0.30	0.17	0.02 - 0.25

3.2.2 Model initialization

The model was initialized using the approach described in *Vlasenko et al.* [2000]. Initial distributions of the density and velocity fields were calculated from the weakly nonlinear KdV theory. A corresponding initial wave is allowed to evolve freely over the flat bottom. A weakly nonlinear wave does not fulfill the system of nonlinear equations which are solved numerically by the model. Ensuing adjustment process involves the transformation of a weakly nonlinear wave into a fully nonlinear one and the generation of a dispersive train of small amplitude waves behind it. The wave decrease in the amplitude by $5 - 10\%$ depending on the initial amplitude. Having the bigger phase speed than the rest of the dispersive trail, the leading wave propagates freely and after some time a fully nonlinear internal wave becomes solitary. This wave is then used as an initial condition for subsequent numerical experiments. A weakly nonlinear ISW is computed from solutions of the KdV or the Gardner equations (see *Ostrovsky and Stepanyants* [2005] for details and parameters):

$$\eta(x,z,t) = a\psi(z)\mathrm{sech}^2\left(\frac{x-ct}{L}\right), \tag{3.13}$$

$$\eta(x,z,t) = -\psi(z)\frac{\alpha}{\alpha_1}\frac{\nu}{2}\left[\tanh\left(\frac{x-ct}{L}+\phi\right) - \tanh\left(\frac{x-ct}{L}-\phi\right)\right], \tag{3.14}$$

where a is the wave amplitude, L is a characteristic length scale of the wave. $\psi(z)$ is the vertical structure function found from the numerical solution of the Sturm-Liouville boundary value problem:

$$\psi'' + \frac{N^2}{c^2}\psi = 0, \tag{3.15}$$

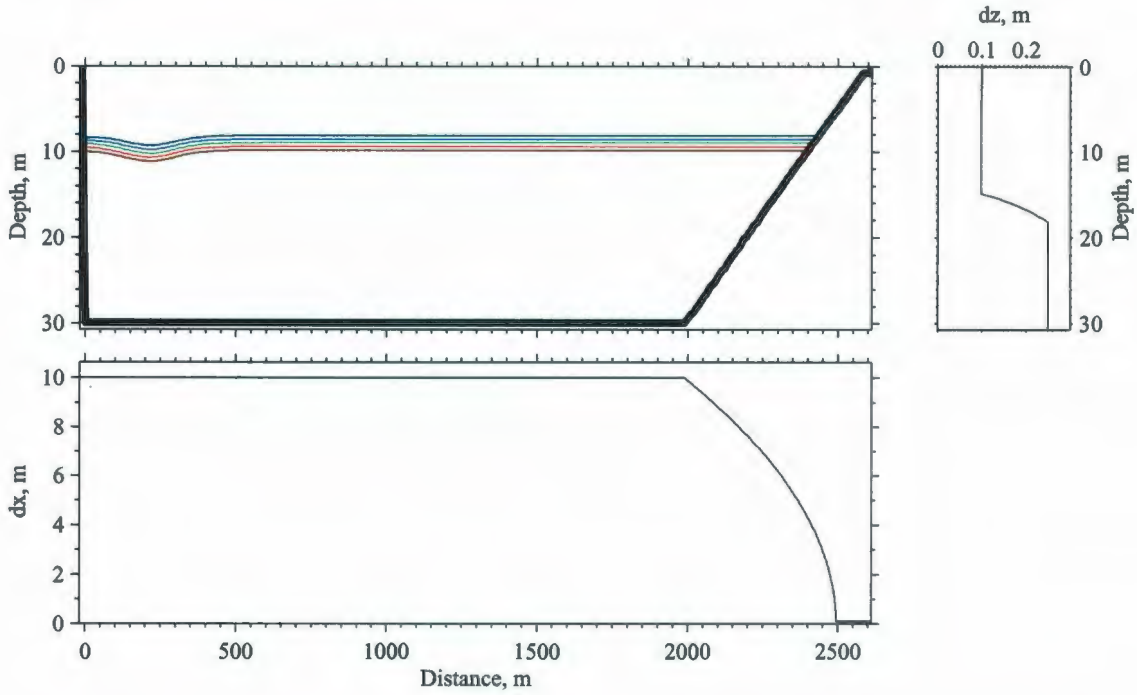

Figure 3.4. Sketch of numerical simulation setup. Initial fully nonlinear wave is located on the left of the flat-bottom section of the domain. A linear slope is located on the right and extend to the the depth 0.75 m. Vertical grid spacing with dz_{min} = 0.10 m in the upper 15 meters dz_{max} = 0.25 m in the lower 15 meters is shown on the right panel. Horizontal

$$\psi(z=0) = \psi(z=H) = 0,$$

where $N(z)$ is the buoyancy frequency and c is the unknown eigen-value of the nonlinear phase speed of the internal wave. Figure 3.5 shows an example of the velocity and density contours used to initialize the model.

This way of initialization has an advantage of being numerically efficient but also has a disadvantage. The amplitude and phase speed of weakly nonlinear interfacial waves have an upper bound, which was found for the case of the KdV soliton by *Amick and Turner* [1989]:

$$a_{max} = \frac{h_1 \rho_2^{1/2} - h_2 \rho_1^{1/2}}{\rho_1^{1/2} + \rho_2^{1/2}}, \tag{3.16}$$

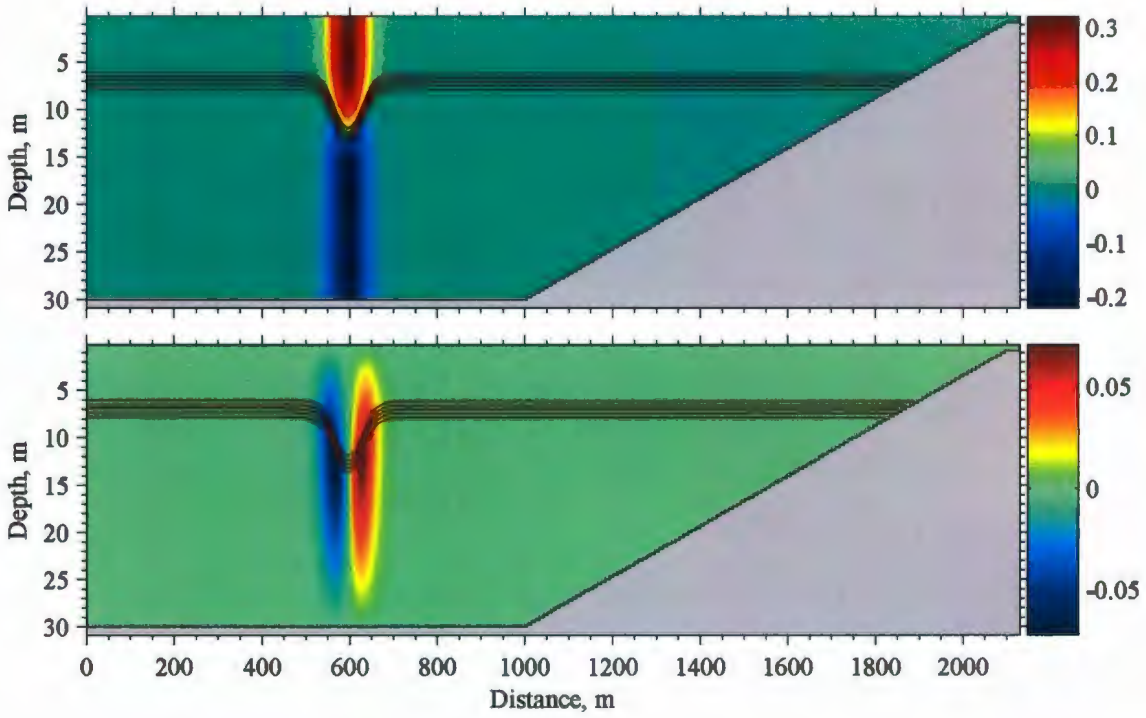

Figure 3.5. Horizontal (top) and vertical (bottom) components of the velocity and density contours used to initialize the model. Color bars are in m/s.

$$c_{max} = \frac{g(h_1 + h_2)(\rho_1 - \rho_2)}{\rho_1^{1/2} + \rho_2^{1/2}}. \tag{3.17}$$

It is not possible to initialize the model with a wave larger than this upper bound. For the case $h_1 = 7.00\,\mathrm{m}$, $h_2 = 23.00\,\mathrm{m}$ and $\rho_1 = 1017\,\mathrm{kg/m^3}$, $\rho_2 = 1023\,\mathrm{kg/m^3}$ the maximum displacement of isopycnals is $\eta_{max} = 7.98\,\mathrm{m}$ and the maximum phase speed is $c_{max} = 0.66\,\mathrm{m/s}$.

All runs were initialized with a passive tracer occupying the lower part of the domain below the pycnocline. This passive tracer will be used to investigate the transport properties of internal waves. The initial distribution of tracer is shown in Figure 3.6.

Results of experiments on interaction of internal solitary waves with the slope are classified using the Iribarren number defined by Equation 2.46. The half-length of the observed

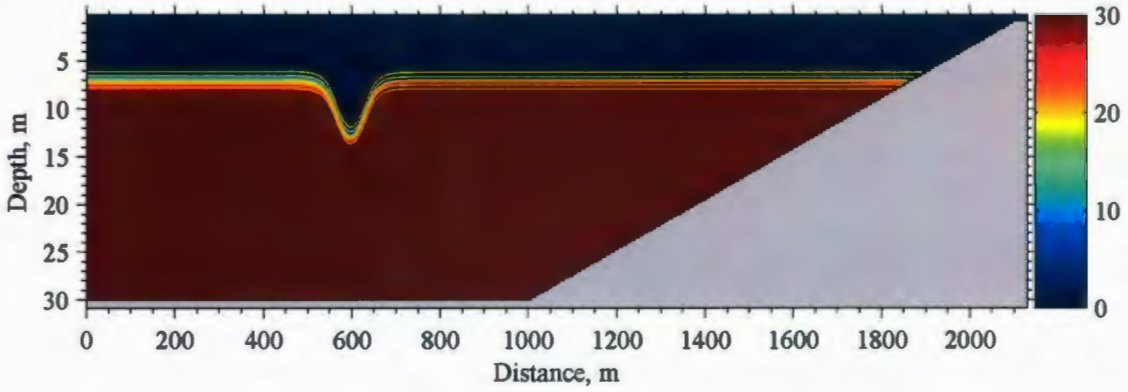

Figure 3.6. Initial distribution of a tracer used for mass flux calculations.

internal waves was estimated using the expression:

$$L = \frac{1}{2a}\int_{x_1}^{x^2} \eta(x)dx, \tag{3.18}$$

where the interval $[x_1\ x_2]$ includes the entire wave (*Vlasenko et al.* [2000], *Bourgault and Kelley* [2004]; *Bourgault et al.* [2007]).

The total energy of an incident wave of depression as well as boluses is partitioned between the kinetic and available potential energies. The depth integrated kinetic energy (KE) per unit wave width is defined as

$$KE = \frac{1}{2}\rho_0 \int_{x_1}^{x_2}\int_0^H \left(u^2 + w^2\right) dz\, dx, \tag{3.19}$$

the depth integrated available potential energy (APE) is defined as

$$APE = g\int_{x_1}^{x_2}\int_0^H (\rho - \overline{\rho})\ z\, dz\, dx, \tag{3.20}$$

Mass displaced by a solitary wave can be defined as

$$M_w = \int_{x_1}^{x_2}\int_0^H (\rho - \rho_b)\ dz\, dx. \tag{3.21}$$

Here $\overline{\rho}$ is a sorted dynamically stable density profile corresponding to the minimum potential energy state and ρ_b is the undisturbed density profile. Mass of the internal solitary

wave in the form given by 3.21 was introduced by *Lamb* [1998]. Limits $[x_1\, x_2]$ are chosen to include the whole wave in such a way that the mass and energy of the ISW converged to constant values independent of the horizontal limits, (Figure 3.7):

Typically it is enough to calculate KE and APE energies of an incident wave with the horizontal limits $[-8\,L,\ 8\,L]$. For boluses, however, to calculate their mass and energies the horizontal limits have to be chosen as $[-L_b\ L_b]$ because of the strong spatial localization of these features. Here L_b is the characteristic length of a bolus.

Now we compare the resultant fully nonlinear waves used as initial conditions in numerical computations with the KdV solitons used at the beginning of the initialization procedure. While the final amplitudes of nonlinear ISWs reduce during transformation by 5-10 %, wavelengths become larger. Figure 3.8 shows the KdV relationship between the ISW characteristic wavelength and amplitude and how fully nonlinear ISWs compare to the KdV theory. The wave with the amplitude $a = 1.3$ m compares with the KdV equations very well. The wavelength estimated from the numerical model is $L = 41.20$ m, while KdV theory wave-length is $L_{KdV} = 41.1$ m. Energies also compares well with each other: $E = 5.4$ KJ/m estimated for fully nonlinear wave and $E_{KdV} = 4.9$ KJ/m for the KdV case. For waves with amplitudes $a = 3.5$ m and $a = 6.0$ m the agreement is getting poor. Wavelengths differ from the KdV estimates by 1.5 and 2 times correspondingly.

Figure 3.9 indicates the dependence of mass displaced by an incident wave of depression M_w on the amplitude of the wave. As can be seen, the mass depends linearly on the amplitude of the wave for small waves (dotted line in Figure 3.9) with amplitudes from a = 1.3 m to a = 5.0 m. For larger waves the mass displaced by the wave grows significantly. This agrees well with the eKdV theory which predicts that as the amplitude of the wave approaches to the limiting value defined by Equation 3.16 and shown in Figure 3.9 as a dashed vertical line, the wave broadens and thus its mass grows. This was observed by *Grue et al.* [1999] both in the laboratory and in a numerical solution of the two-layer fully nonlinear model.

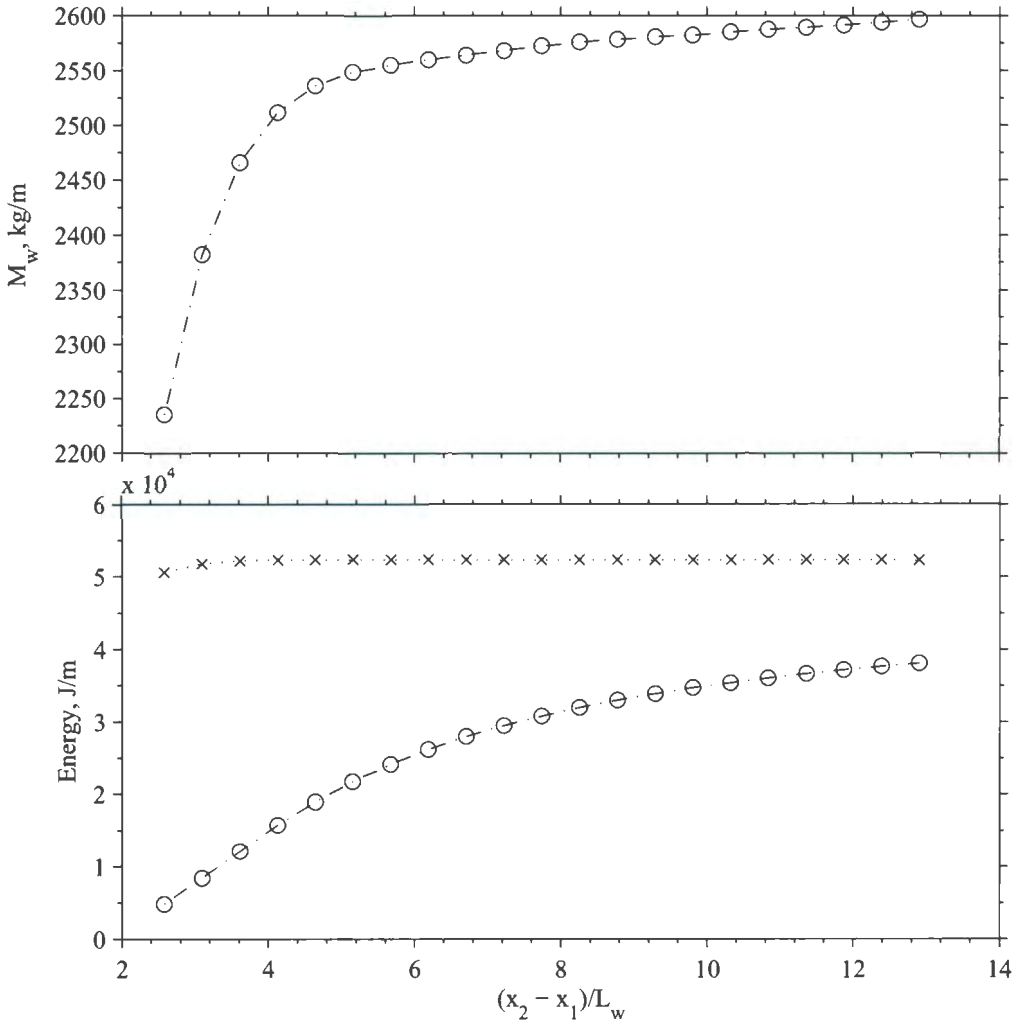

Figure 3.7. Mass of fluid displaced by the wave of depression (top panel), kinetic energy ('x') and available potential energy ('o') (bottom panel) calculated using different horizontal limits expressed in the terms of an ISW wavelength.

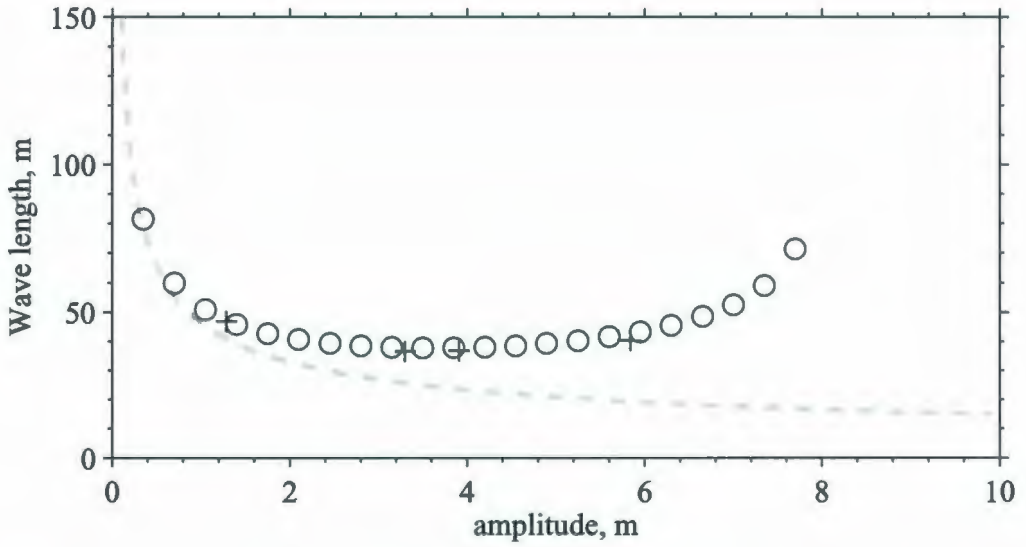

Figure 3.8. The wavelengths and amplitudes of the initial KdV solitons with which the numerical simulations were started and fully developed nonlinear waves calculated using non-hydrostatic model ('+'). The wavelength and amplitude of the initial KdV solitons related through Equation 2.19 is shown as a dashed line. Open circles are waves calculated using fully nonlinear two layer model.

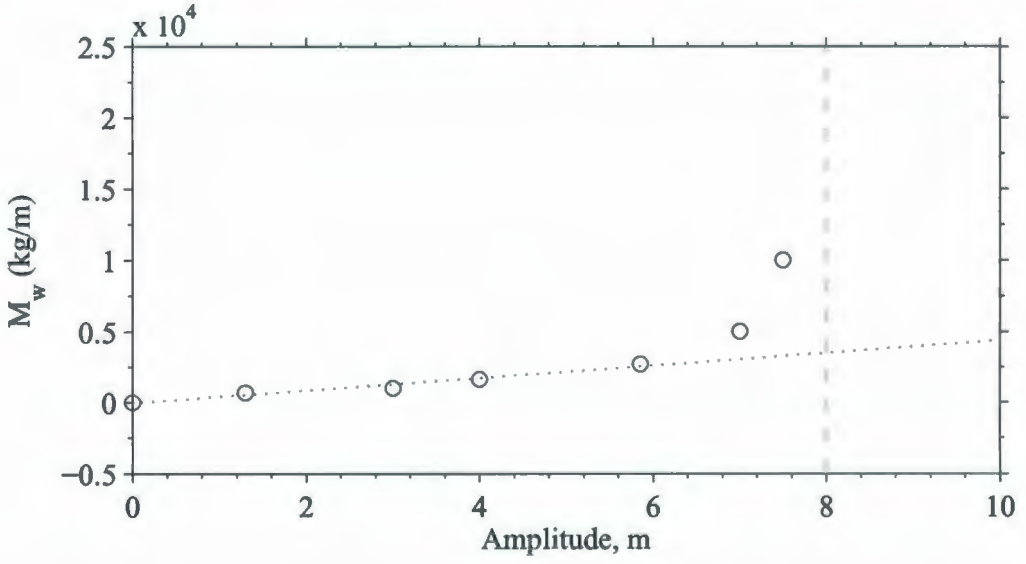

Figure 3.9. Dependence of mass associated with an incident wave of depression on the amplitude of the wave. Dotted line represents the linear fit for low values of amplitude values. The vertical dashed line is the maximum amplitude which ISWs can attain in a two-layer system (Equation 3.16).

Chapter 4

Observations of shoaling internal waves on a natural slope

In this section we describe in detail the results of our observation of ISW packet shoaling made on August 26, 2004. In this observation a train of ISWs was encountered impinging the slope. This allowed to track the shoaling of the leading wave of depression and its transformation into the set of boluses, of which only the first one is followed. The bolus became unrecognizable on the echosounder image when the water depth was around 7 meters. This corresponds to the slope-interface intersection point, where depth of the lower layer is becoming zero. Further observation of the leading bolus was not possible due to instrumentations limitations. To study the further stage of the bolus propagation, it is necessary to address to the numerical model, see Section 3.2. Now we first present observations from towed instruments and next we show results from moorings B and C.

4.1 Description of a single event

Figure 4.1 shows a sequence of echograms that captured the evolution of an ISW of depression shoaling over a bottom of quasi-uniform slope $s = 0.05$ as well as the results of the numerical simulation. Bottom topography, background stratification and other parameters used in numerical simulation were the same as in our observation. The only significant difference is that instead of train of ISWs, only shoaling of the leading wave was simulated.

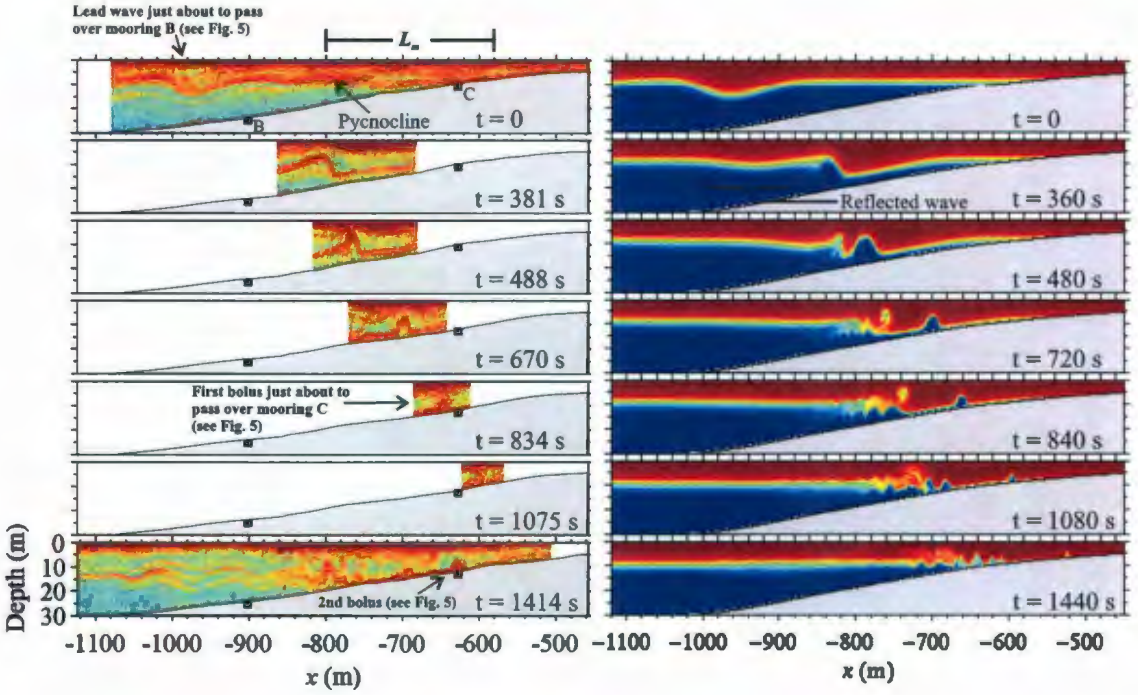

Figure 4.1. Left: Echograms showing the lead wave (top 6 panels) and the full train (bottom panel) impacting the flank of Ile-aux-Lièvres Island. For conciseness, only 7 transects are shown out of 30 collected. The time corresponds to when the wave trough or crests were sampled, except for the bottom panel where it is the median time of the transect. The origin $t = 0$ corresponds to 1436 UTC on 26 August 2004. The background conditions in which this wavetrain evolved were characterized by the density structure and currents shown in Figure 4.2. The depth of the pycnocline and of the maximum vertical shear correspond to the high intensity scattering layer observed at around 9 m depth on the top left panel. Right: Results of a numerical simulation showing changes in the density field induced by the shoaling of an ISW with similar characteristics as the observed ISW.

The background conditions in which this wave evolved were characterized by the density structure and currents shown in Figure 4.2. Density measurements were derived from the thermistor chain record. Calculated buoyancy profile $N^2(z)$ shows a sharp pycnocline at around 7 meters depth. This gives justification of the use of two layer stratification in our numerical simulations. Measurements of horizontal currents from mooring B allowed to estimate the horizontal shear profile, $S^2(z)$ which had a peak just below the pycnocline (Figure 4.2). The Richardson number calculated from Equation 2.37 shows significant ver-

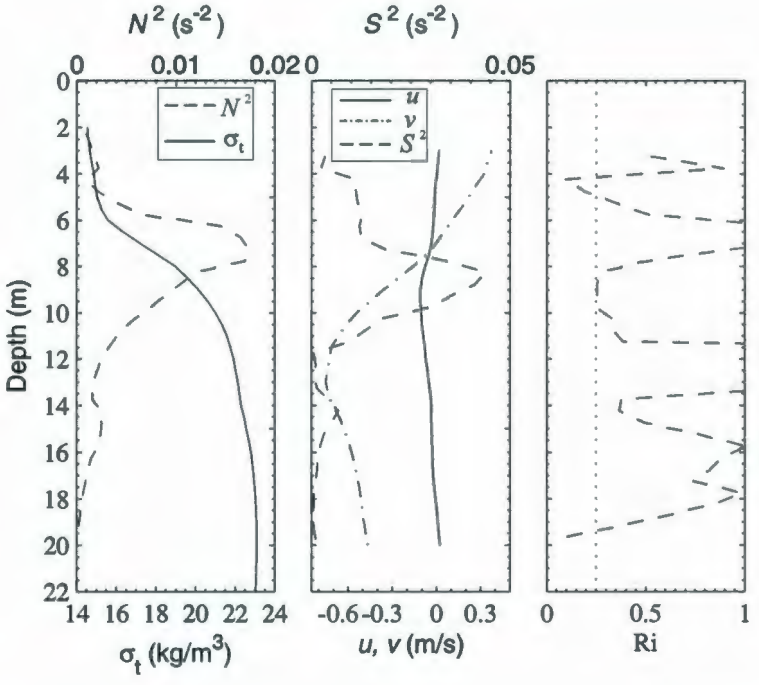

Figure 4.2. Mean density anomaly σ_t, buoyancy frequency squared N^2, horizontal currents u (southeastward) and v (northeastward), shear squared S^2 and gradient Richardson number Ri. The density measurements are from the thermistor-CT chain (triangle on 3.1) and the current measurements are from Mooring B. Note that the gradient Richardson number around the pycnocline was $1/4 < Ri|_{z=-9m} < 1$. These are 5 min averages observed 10 min before the passage of the wavetrain.

tical variability. It is close to its critical value of $1/4$ in the vicinity of the peak in the shear profile 2 meters below the pycnocline and goes below $1/4$ just above the interface. This means that shear instabilities, breaking of internal waves and production of turbulence are possible in these conditions.

As the wave of depression entered the slope region ($t = 0$), it was characterized with amplitude a = 6.5 m and length L = 64.0 m. This corresponds to Iribarren number

$$\xi = \frac{s}{\sqrt{a/L}} = 0.16 \tag{4.1}$$

[*Boegman et al.*, 2005] and is within the range of parameters examined experimentally by

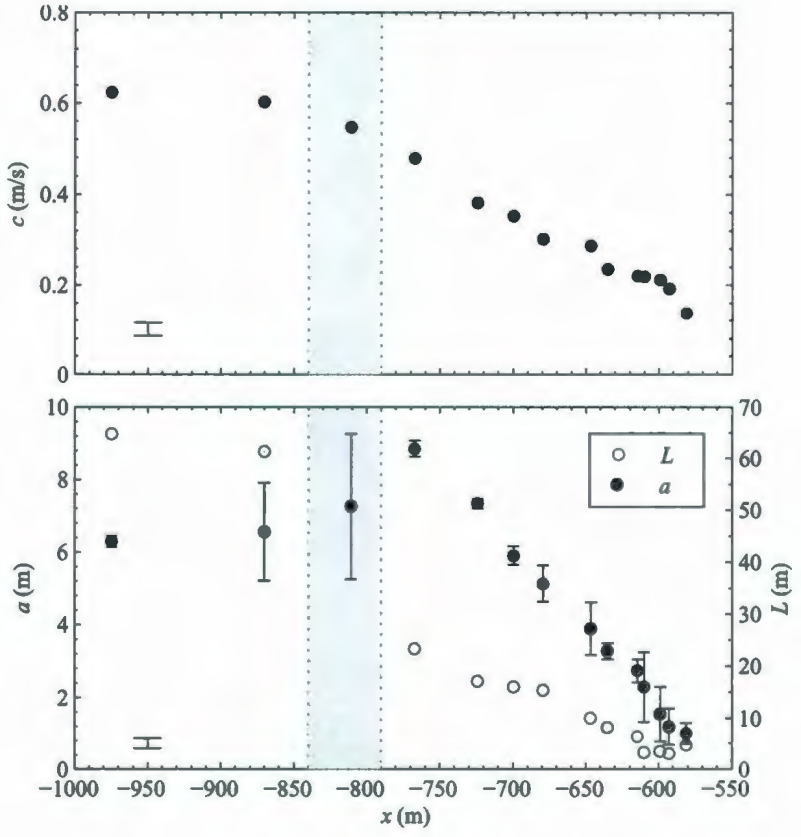

Figure 4.3. (top) The leading wave phase speed c, (bottom) amplitude a and wavelength L as a function of distance from the island. The grey boxes represent the region over which the transition from a wave of depression to a wave of elevation (or bolus) occurred. Errorbars for c and L are shown at the lower left corner of the corresponding panels. The lengthscale was not measured during the transition phase.

Helfrich [1992] for ISW breaking and run-up on uniform slopes.

As the wave propagated up-slope its rear steepened, reaching 50° below horizontal at t = 381 s. By t = 488 s the wave had changed into a wave of elevation. In the terminology of *Helfrich* [1992] and more recently *Venayagamoorthy and Fringer* [2006], we will refer to this feature as a "bolus", keeping in mind that other authors have used the term "wave of elevation" to describe similar features. This transition from a wave of depression to a bolus occurred without recorded evidence of wave breaking or overturning. However, the shadowgraphs of *Helfrich* [1992] for similar shoaling ISWs (see his Figures 3 and 4

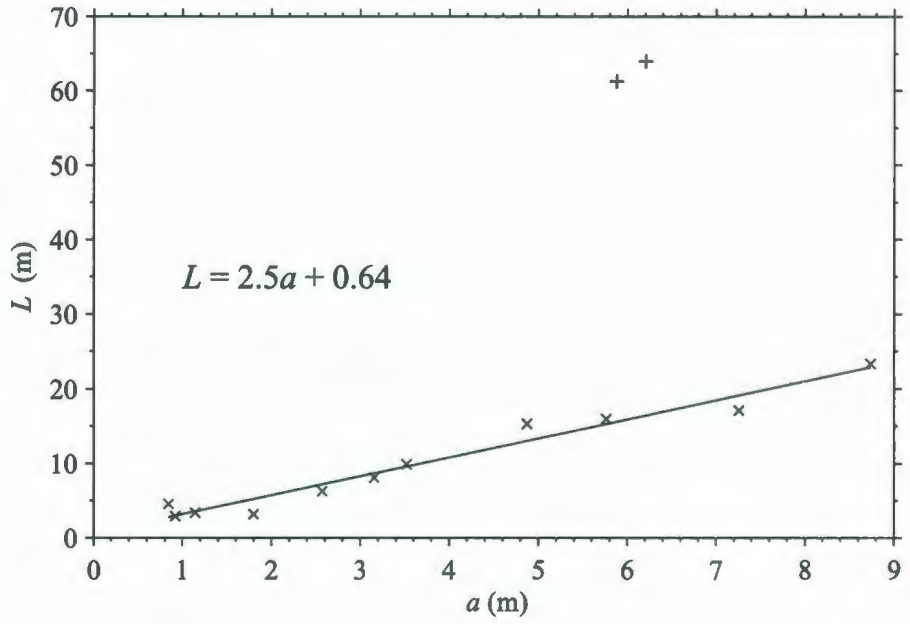

Figure 4.4. Amplitude and wavelength of the IW of depression (+) and the first bolus (x) measured from Figure 4.1

for cases corresponding to $\xi = 0.38$ and $\xi = 0.24$, respectively) show that overturning and mixing occur on the rear face of the incident ISW and behind the first bolus produced during shoaling. *Boegman et al.* [2005] also report similar observations (their Figure 9g-l). This process is also seen in the numerical simulation (Figure 4.1 for $t \geq 480$ s). These laboratory observations and numerical results suggest that overturning likely occurred in the field but was not recorded due to our sampling strategy.

As it continued to move inshore ($t \geq 488$ s), the bolus remained asymmetrical, its front being steeper than its rear, as both its amplitude and horizontal lengthscale decreased. The bolus had almost completely dissipated by the pass at $t = 1075$ s, having traveled a distance $L_m = 230 \pm 10$ m from its site of formation. Along the bolus path, there is no recorded evidence of overturning or shear instabilities as also suggested by the numerical simulation.

The bottom panel of Figure 4.1 shows a slope-wide echogram collected after the leading bolus had dissipated. It reveals that we had sampled the leading wave of a shoaling wave-

train. This echogram shows the spatial structure of the shoaling waves as they approached the slope ($x < -900$ m), changed to boluses ($-800 < x < -700$ m), and then gradually dissipated further up-slope ($x > -750$ m).

Figure 4.3 shows the up-slope variability of the observed phase speed c, amplitude a, and length L of the lead wave of depression and first bolus. They were measured from the echosounder image converted to the depth-range coordinates and corrected for Doppler effect. A semi-automated program for a density contour detection was developed based on the pixel intensity variation technique. Using the amplitude as a free parameter, the length scale was estimated from Equation 3.18. Phase speed was calculated by comparing the wave-crest position on successive echosounder images. The properties remained almost constant prior to the polarity change ($x \leq 850$ m) but decreased rapidly and linearly afterward. Bolus amplitude and length decreased in such a way that the bolus aspect ratio $a/L = 0.4 \pm 0.1$ (Figure 4.4, and by extension the bolus Iribarren number $\xi_b = 0.08 \pm 0.01$, remained constant throughout the up-slope evolution.

Figure 4.5 and Figure 4.6 show the time series of the acoustic backscatter and anomaly currents induced by the passage of the wavetrain over Moorings B and C, correspondingly. The observations at Mooring B are similar to those at Mooring A (not shown) and revealed that the wavetrain was composed of 3 large waves (6 m $< a <$ 8 m) of period $T \simeq 200$ s followed by 12 smaller amplitude waves (2 m $< a <$ 4 m). A close inspection of Figure 4.6 reveals that, by the time the wavetrain reached Mooring C, 270 m further upslope, it had disintegrated into 18 ± 1 boluses. These boluses are characterized as irregularly spaced, near-bottom and short-duration signals of the density (superimposed on a longer timescale depression of the pycnocline), backscatter intensity and currents u', v' and w'. The bolus-induced density fluctuations of around 2 kg m^{-3} indicate that they transport dense water upslope. This upslope transport of dense water by the boluses is also seen in the numerical results. The timescale of the wavetrain shoaling event $T_m \simeq 5000$ s is taken as the period between the time the leading wave entered the slope region (t = 0) and the time the last bolus went over Mooring C.

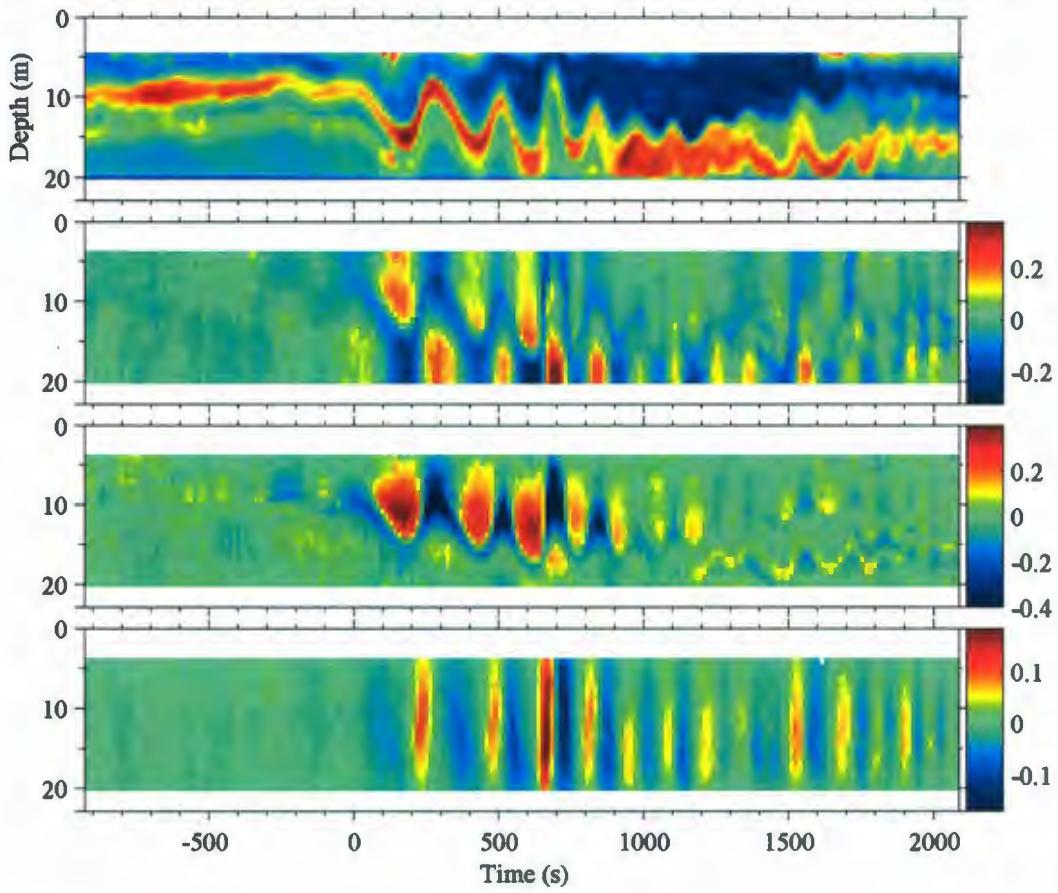

Figure 4.5. Acoustic backscatter intensity (in relative units), horizontal u, v and vertical w (positive up) wave-induced currents at Mooring B. The prime indicates that the variables have been highpass filtered using a fourth-order Butterworth filter with a cutoff frequency of 10^{-3} s^{-1}. Velocity range in m/s is represented by color bars to the right.

4.2 Energy and wave phase speed observation

The energy, per unit of crest length, of the three leading solitary-like waves impacting the slope was estimated to be $E_0 = 230 \pm 40$ kJ m^{-1}. This value was inferred by combining velocity data from the ADCP at Mooring A with a normal mode structure of the waves using the density profile shown in Figure 4.2. The energy E_0' of the smaller amplitude trailing waves was more difficult to determine, given their complex signal. An order of magnitude

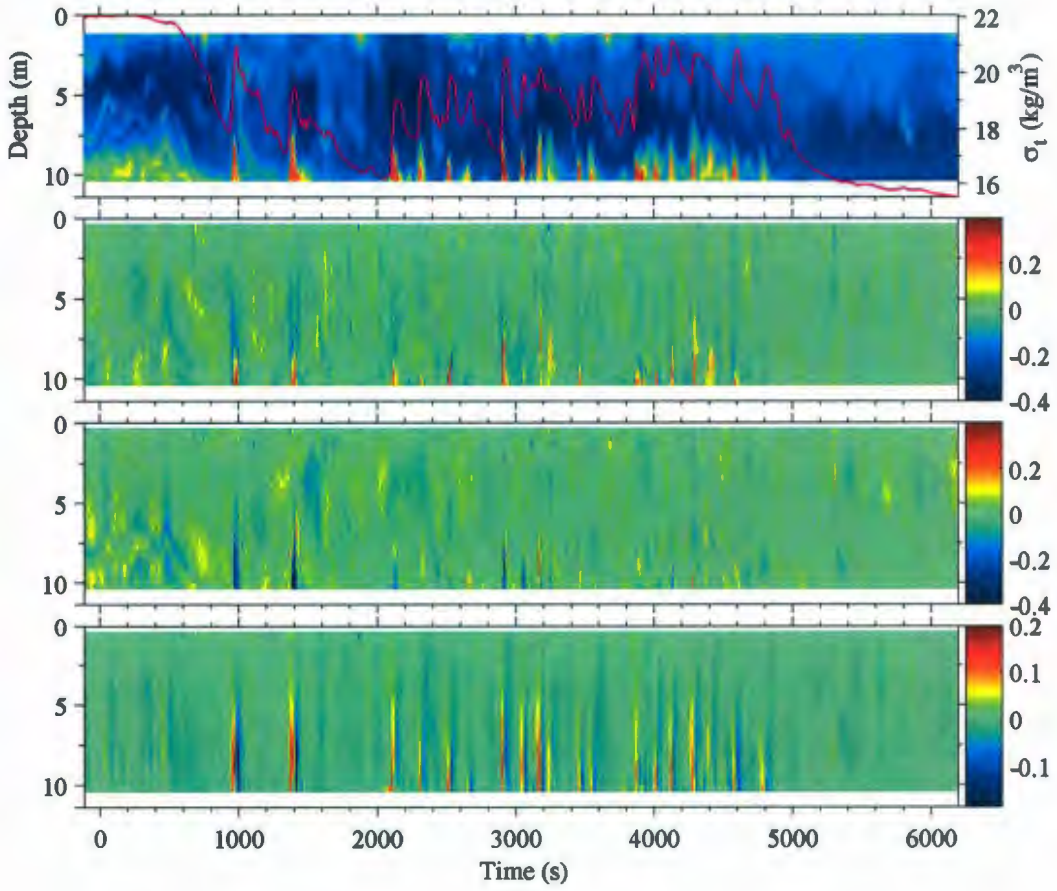

Figure 4.6. Acoustic backscatter intensity (in relative units), horizontal u', v' and vertical w' (positive up) wave-induced currents at Mooring C. The prime indicates that the variables have been highpass filtered using a fourth-order Butterworth filter with a cutoff frequency of 10^{-3} s^{-1} The near-bottom density anomaly σ_t shown as the magenta curve on the top panel. Velocity range in m/s is represented by color bars to the right.

calculation based on two-layer linear wave theory [*Kundu*, 1990] gave $E_0' \sim 100$ kJ m^{-1}.

Figure 4.7 shows the upslope decay of the energy of the leading ISW of depression and the first bolus. The energy of the ISW of depression remained constant up to transition point. After the transition, the energy of the first bolus decreased from 10^5 J/m to 10^2 J/m in less then 150 meters.

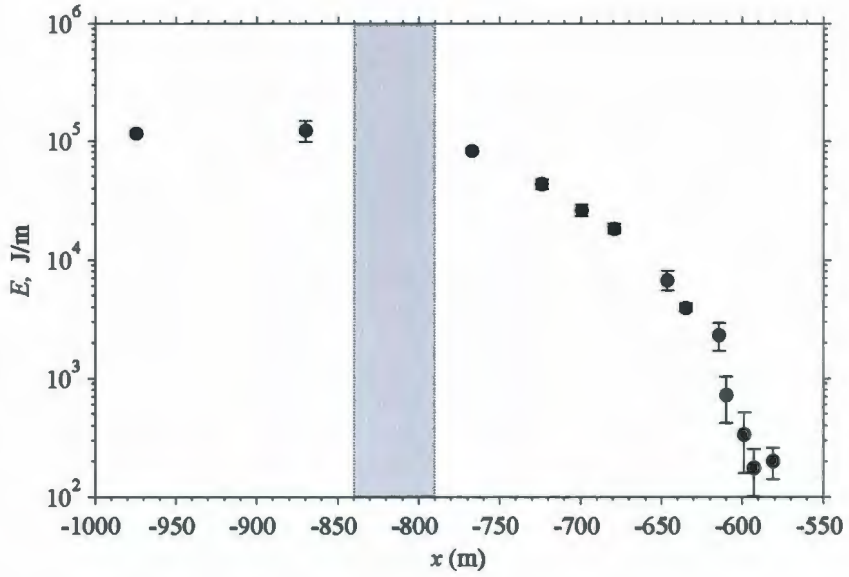

Figure 4.7. Energy of the leading wave of depression and first bolus as function of distance traveled. Gray area corresponds to the vicinity of the transition point.

The fraction of E_0 that reflected at impact was estimated using parametrization for the reflectance given by Equation 2.45 proposed by *Bourgault and Kelley* [2007] for uniform slopes and normally incident ISWs. Using $\xi = 0.16$ gives reflectance coefficient $R = 0.19$. The reflected portion of the incoming wavetrain could not be unambiguously extracted from the mooring observations but is clearly seen in the numerical simulations for the case of a single impinging ISW (Figure 4.1).

From laboratory experiments on shoaling ISWs, *Helfrich* [1992] found that a fraction $\Gamma = 0.15 \pm 0.05$ of the unreflected wave energy is lost to irreversible turbulent mixing in the slope region during the shoaling process, independently of the Iribarren number ξ . In a similar experiment, *Michallet and Ivey* [1999] found a dependance of Γ on ξ: for $\xi = 0.2$ (i.e. their lowest value examined) they found $\Gamma = 0.07 \pm 0.01$ (see *Boegman et al.* [2005] for a re-interpretation of the *Michallet and Ivey* [1999] measurements in terms of ξ). Applying these results to our field site suggests that the impact of the 3 leading waves on the slope increased the mean potential energy of the system by $\Delta P = \Gamma E_0(1 - R) = 27 \pm 17$

kJ m^{-1}. Assuming that the mixing took place over the length L_m and over the timescale T_m yields a buoyancy flux per unit area $J = \Delta P/(T_m L_m) = 0.023 \pm 0.015$ W m^{-2}. We did not attempt to quantify the mixing caused by the trailing waves so the above estimate of the wavetrain-induced buoyancy flux should be considered a conservative lower bound.

4.3 Comparison of observations with solitary wave models

In this section we compare both internal solitary waves of depression and elevation to number of available solitary wave models, such as weakly nonlinear KdV theory, extended KdV theory and fully nonlinear two layer theory by *Grue et al.* [1999].

Internal waves of depression observed on 26 of August 2004 are compared both with KdV (Equation 2.14) and fully nonlinear model (Equations 2.35 and 2.36). The amplitude of the wave of depression as well as depths of the upper and lower layers are measured directly from the echosounder image and used as free fitting parameters. Visual inspection shows a reasonable agreement in profiles, although the KdV theory underestimates the wavelength (Figure 4.8). The wavelength computed using Equation 2.19 from the KdV theory is $L_w = 22.5$ m compared to $L_w = 32$ m retrieved from the backscatter image. Phase speed measured from observations is $c = 0.6$ m/s compared to $c = 0.65$ m/s predicted by the KdV equation. The use of the fully nonlinear theory gives a better fit (Figure 4.8) with values $L_w = 31.5$ m and $c = 0.6$ m/s.

A comparison of waves of elevation is done at two locations. The first one is chosen before the point where the bottom layer disappears and the second one is beyond this point. As seen from Figure 4.9 the KdV theory again underestimates the wavelength of the wave of elevation by almost factor of 2. The fully nonlinear model, on the other hand, does represent the shape of the wave correctly. The phase speed obtained from the fully nonlinear fit $c = 0.3$ m/s also agrees with phase speed of boluses measured in field.

Now let us consider the second further upslope location where theoretical prediction is tested against observations. The depth of the lower layer here is diminishingly small. The KdV theory, same as before, does not pinpoint the shape of the bolus, but so does the fully nonlinear theory. As illustrated in Figure 4.10, the shape of the bolus at this stage is not symmetrical.

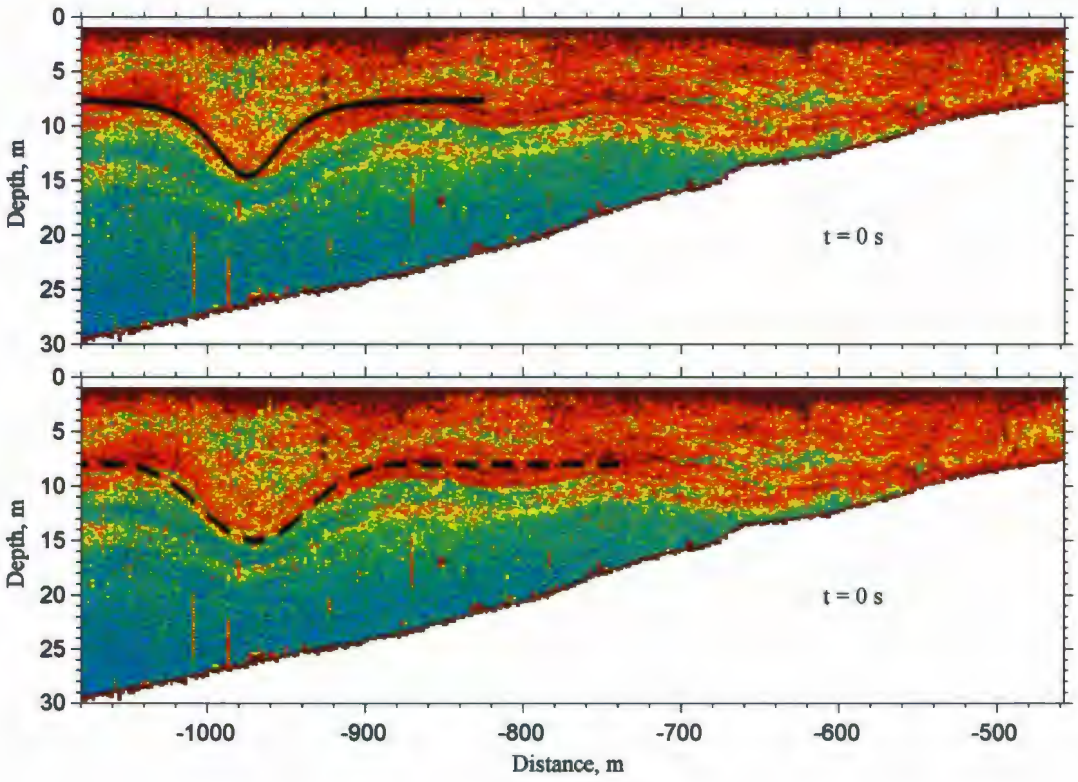

Figure 4.8. Acoustic backscatter intensity of the internal wave of depression with amplitude a = 6 m observed at Mooring A. Top panel is showing the KdV profile calculated from Equation 2.14 using parameters inferred from the echosounder image. Bottom panel shows the fit of the same wave using fully nonlinear model of *Grue et al.* [1999] (Equation 2.35 and 2.36).

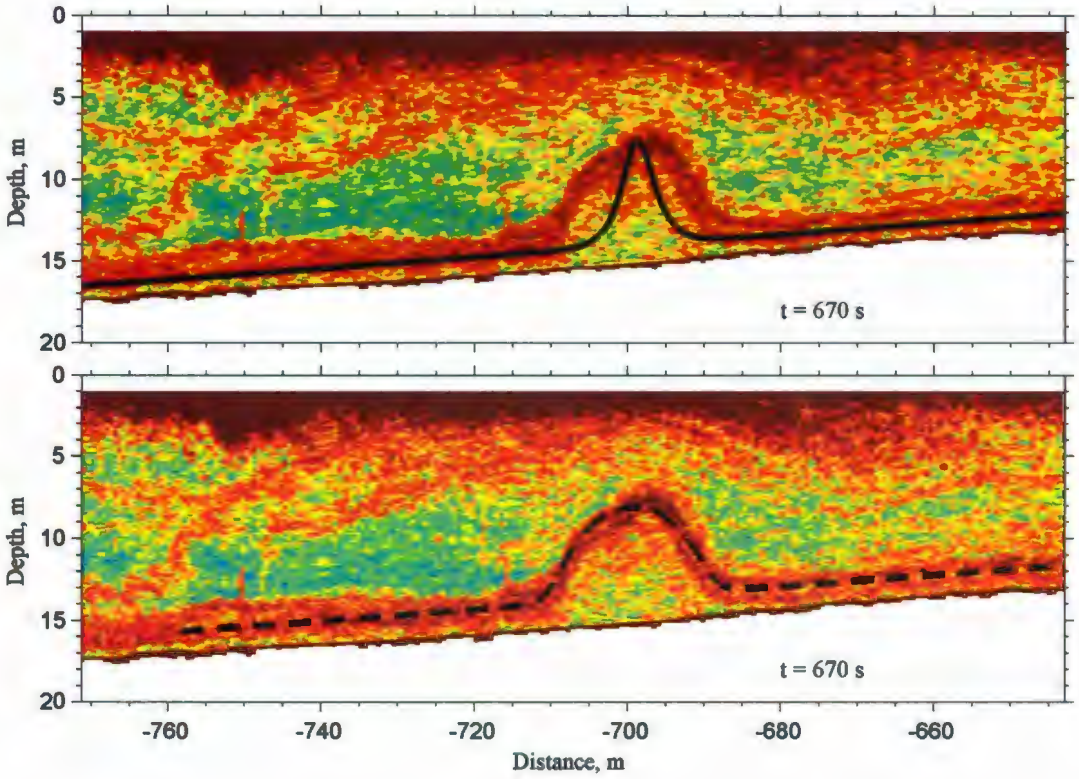

Figure 4.9. Acoustic backscatter intensity of the internal wave of elevation with amplitude a = 4.8 m observed at Mooring C. Top panel is showing the KdV profile calculated from equation 2.14 using parameters inferred from the echosounder image. The bottom panel shows the fit of the same wave using fully nonlinear model 2.35, 2.36 of *Grue et al.* [1999].

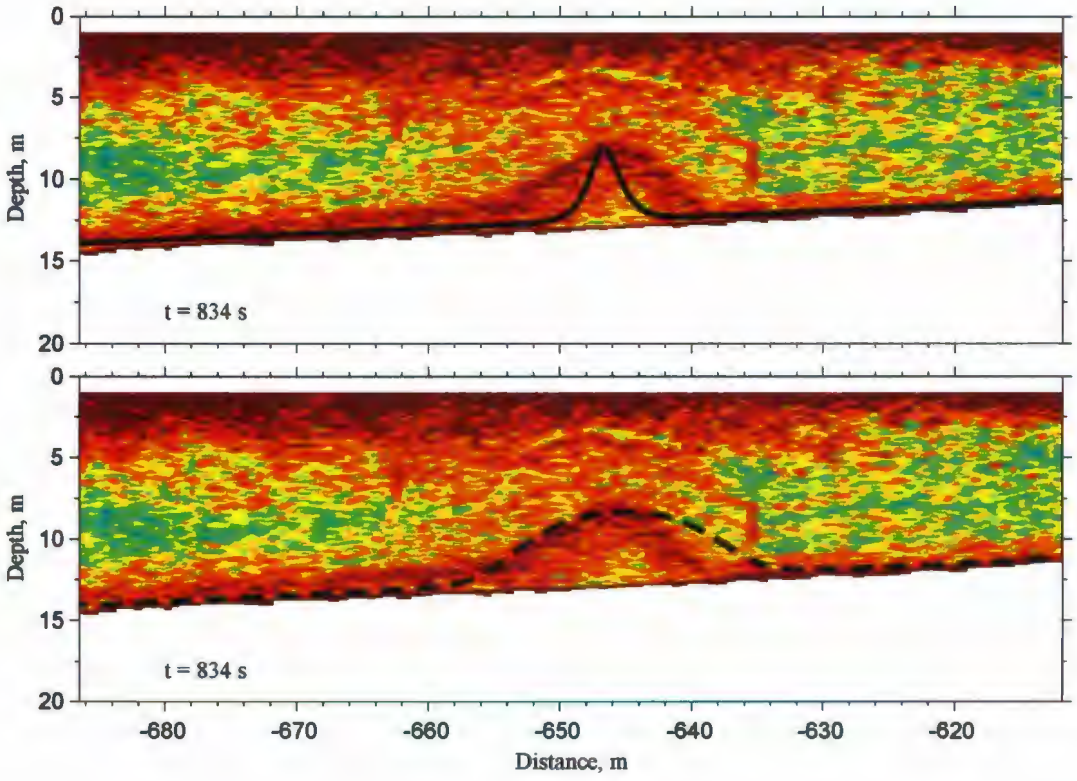

Figure 4.10. As for Figure 4.9 but for the wave of elevation with amplitude $a = 1.5$ m.

4.4 Internal wave climatology

Internal wave temporal distribution and their energetics need to be considered before attempting to quantify IW-induced boundary mixing and planning further field observations. Accordingly, the IW climatology for the SLEIWEX site was constructed using the data collected by moored ADCPs (moorings A, B, and C in Fig. 3.1).

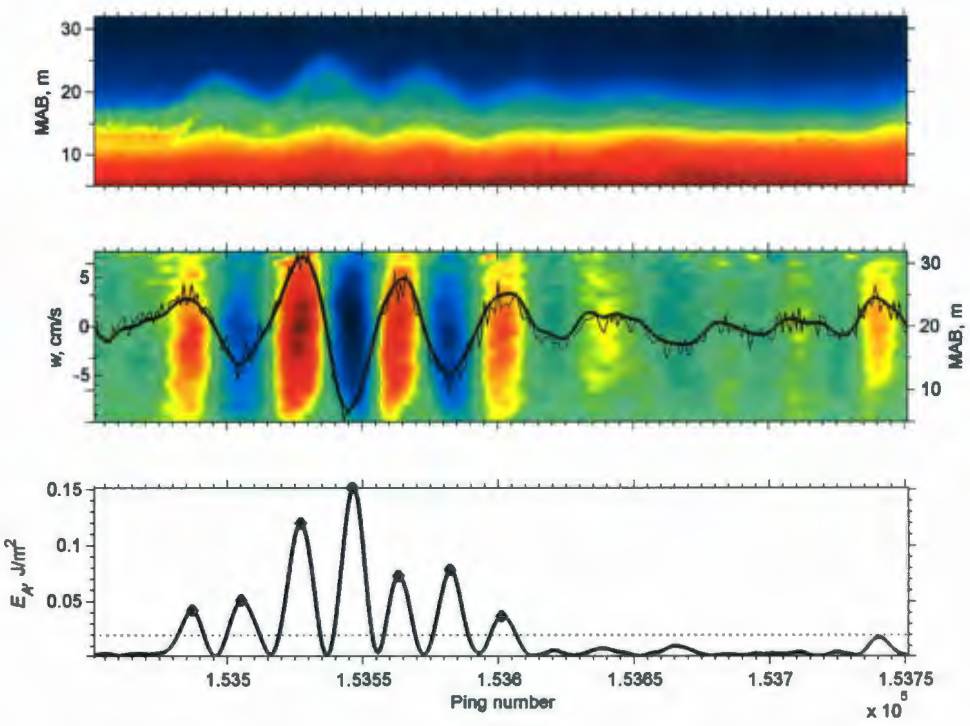

Figure 4.11. Example of an IW event (top panel) retrieval from the backscatter intensity at mooring A, corresponding vertical velocity measurements (middle panel), and the area energy density index as defined in Equation 4.3 (bottom panel). The thin line on the middle panel shows the raw measurements w' around the pycnocline while the thick line shows the filtered measurements w, after the application of the band-pass filter described in the text. The diamonds in the bottom panel indicate the automatically detected peaks E_A. Peaks below the threshold value indicated by the dashed line are disregarded from the analysis.

The fundamental quantity for estimating the vertical mixing caused by IWs is the total energy of incident internal waves E_0 given by $E_0 = KE + APE$. Assuming equipartition between kinetic and potential energy, the total energy in the KdV approximation can be

expressed as [see e.g. *Bourgault and Kelley*, 2003]:

$$E_0 = 2E_P = 2E_K = \frac{4}{3}\Delta\rho g a^2 L_w, \tag{4.2}$$

where $\Delta\rho$ is the density difference between top and bottom layers, a is the IW amplitude, and L_w is the half-length of an IW. Extracting the IW wavelength from single site ADCP measurements cannot be done without assumptions on wave phase speed. It is therefore expeditious to introduce such a quantity that makes the energy estimation more feasible task to perform. The proposed energetic variable is *the area energy density* :

$$E_A = E_0/L_w \sim \int_0^H \rho_0 w^2(z,t)\, dz \ \text{(in units of } \mathrm{J\,m^{-2}}) \tag{4.3}$$

where w is the vertical velocity of an IW measured approximately at the depth of the pycnocline. Note that Equation 4.3 does not represent the actual kinetic energy density because it does not take into account the wave-induced horizontal velocity u. The quantity E_A, although having units of area energy density, is really an index of IW activity.

Visual examination of ADCP backscatters and corresponding vertical velocity (w) measurements reveal that IWs have pronounced manifestation in w acquired at the pycnocline depth as illustrated in Figure 4.11.

For proper peak detection, a Butterworth band - pass filter with cutoff frequencies of 1/90 Hz and 1/1800 Hz was used to remove the low frequency tidal signal and high-frequency noise from the raw vertical velocity measurements $w'(z,t)$. The effect of this filter is illustrated on the middle panel of Figure 4.11.

The filtered vertical velocity $w(z,t)$ was used to produce a time series of the area energy density according to Eq. 4.3 (see bottom panel of Figure 4.11). Peaked values were then automatically detected from the E_A time series and the time of their occurrence relative to the closest time of low water (LW) at the Pointe-au-Père tidal gauge (not local tide) was determined. Since two peaked values are found per wave event (see Figure 4.11), only the average value was kept. Peak values lower than 0.02 $\mathrm{J/m^2}$ were disregarded from the analysis. This value was chosen visually by examining a few individual cases. The climatology pattern is not sensitive to the choice of this threshold value, but the absolute

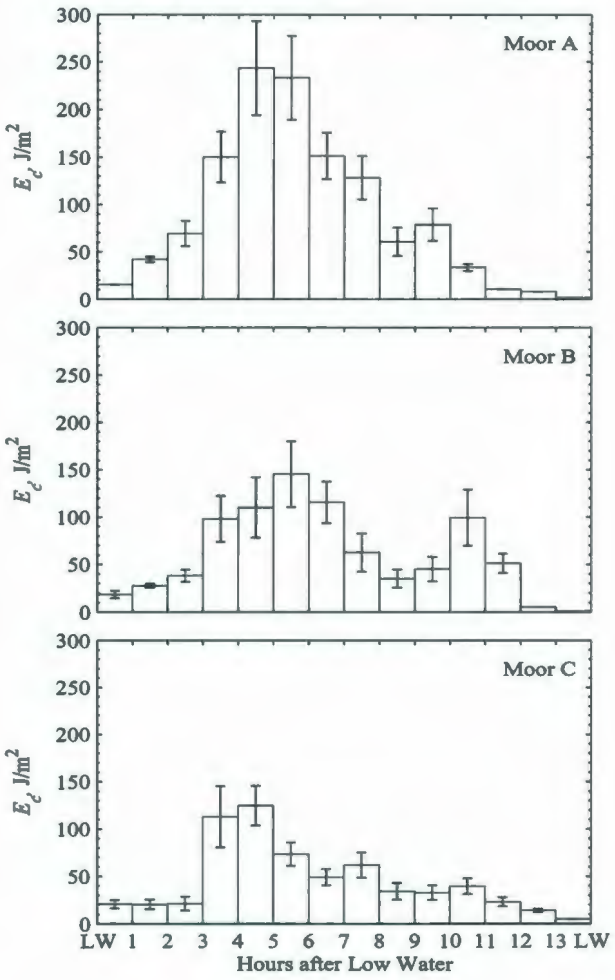

Figure 4.12. The IW climatology at moorings A (top), B (middle) and C (bottom). Error bars show the mean absolute deviation. The time of low water is relative to the Pointe-au-Père tidal gauge station.

values are.

Since the IWs at the SLEIWEX site are thought to be semi-diurnally-driven by the tides [*Bourgault and Kelley*, 2003], the climatology will provide nE_A as a function of the tidal phase (i.e. time relative to low water), where n is the total number of IW occurrences within a given time interval. An interval of one hour was chosen for easier comparison with the atlas of tidal current [Government of Canada, 1997]. As a reference point for tidal time measurements, the Pointe-au-Père tidal gauge station was chosen (see Fig. 3.1 for the location)

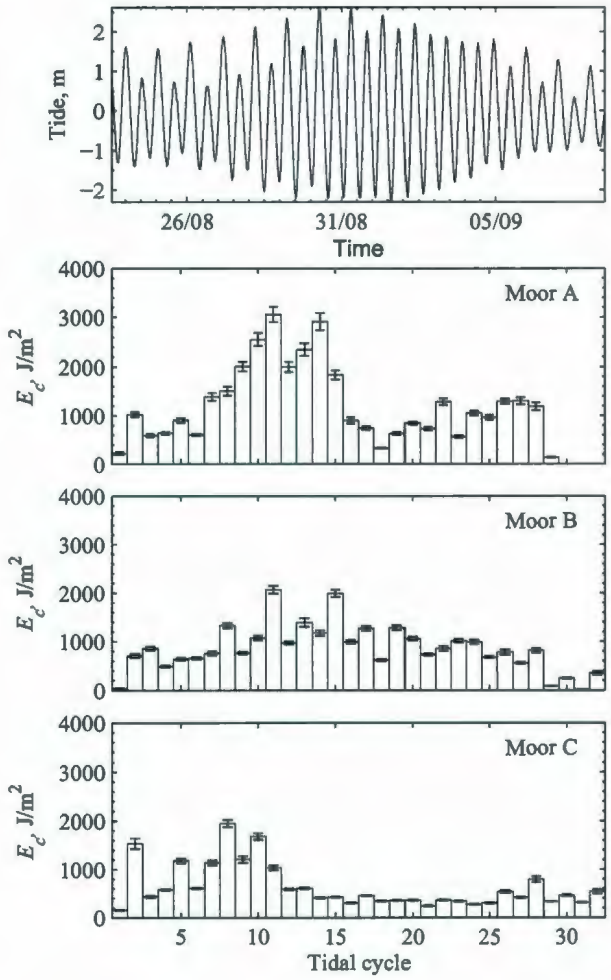

Figure 4.13. The neap-spring variability in IW energy at moorings A (second panel), B (third panel) and C (bottom panel). The top panel shows the observed surface tide during the sampling period.

The distribution of the IW area energy density as function of semi-diurnal tides (or the hourly semi-diurnal climatology) was computed as

$$E_C = \frac{1}{N} \sum_{1}^{N} \left(\sum_{0}^{n} E_A \right), \tag{4.4}$$

where n is the number of identified occurrence of a wave event within a given hour interval relative to LW (there are 13 of these hourly intervals) and N is the total number of semi-diurnal cycles of the sampling period ($N = 29$ for Mooring A and $N = 32$ for Moorings B

and C).

Figure 4.12 shows the hourly semi-diurnal climatology E_C for moorings A, B and C. At Mooring A, there is a peak in E_C between 3 and 7 hours after low water at the Pointe-au-Père station (LW hereafter). This peak is also observed at Mooring B but is less energetic. This is consistent with the hypothesis [*Bourgault and Kelley*, 2003] that IWs predominantly propagate from Mooring A to Mooring B with dissipation taking place in between. At Mooring B there is another peak, not as clearly observed at Mooring A, between 10 and 11 hours after LW. Finally, Mooring C shows a pattern similar to Moorings A and B with a peak between 3 and 6 hours after LW. The IW energy at Mooring C is less than Moorings A and B, consistent again with shoreward propagating IWs.

To determine IW distribution during spring and neap tides, the total IW area energy density *per tidal cycle* (not per hour as previously) for the three moorings was computed (there are around 30 semi-diurnal tidal cycles over the sampling period). Figures 4.12 - 4.13 shows the results of this analysis. The results indicate that IWs are more important during the transition from neap to spring tide. Since only one neap-spring cycle has been examined here we cannot conclude whether this is a general pattern or just a coincidence.

In conclusion, it may be said that if the *area energy density index* as defined in Equation 4.3 is representative of the total IW energy at the SLEIWEX site then the obtained climatology indicates that the IWs are tidally-driven and predominantly appear between 3 and 7 hours after LW at Pointe-au-Père. During the sampling period the IWs were more energetic during the transition from neap to spring tide.

Chapter 5

Numerical simulation of shoaling internal waves

5.1 Grid sensitivity study

When a set of equations is solved numerically with a finite difference method, it is a matter of a compromise between the grid size used in calculations and a reasonable time for execution. Ideally there is a small enough grid size for which further refinement of the grid does not change the solution. In this case numerical simulation results are considered to be grid independent.

Figure 5.1 represents a shoaling internal wave with initial amplitude a = 4 m. Three panels represent results of numerical runs with the same vertical resolution Δz = 0.25 m and different horizontal grid sizes Δx = 1 m (top), Δx = 0.5 m (middle) and Δx = 0.25 m (bottom). Several boluses formed during a shoaling process propagating up-slope. Comparison of the top and bottom panels shows that the speed of the leading bolus is not captured correctly by the simulations with the low horizontal resolution, while for runs with Δx = 0.5 m and Δx = 0.25 m the position of the bolus head is practically coinciding.

Figure 5.2 shows internal wave density contours obtained from three numerical runs with both identical geometry and initial conditions but with different vertical resolutions. The presented simulations have resolutions $\Delta z = 1.0$ m, $\Delta z = 0.5$ m, $\Delta z = 0.1$ m from top to bottom. It is clear that for the correct representation of internal wave shoaling

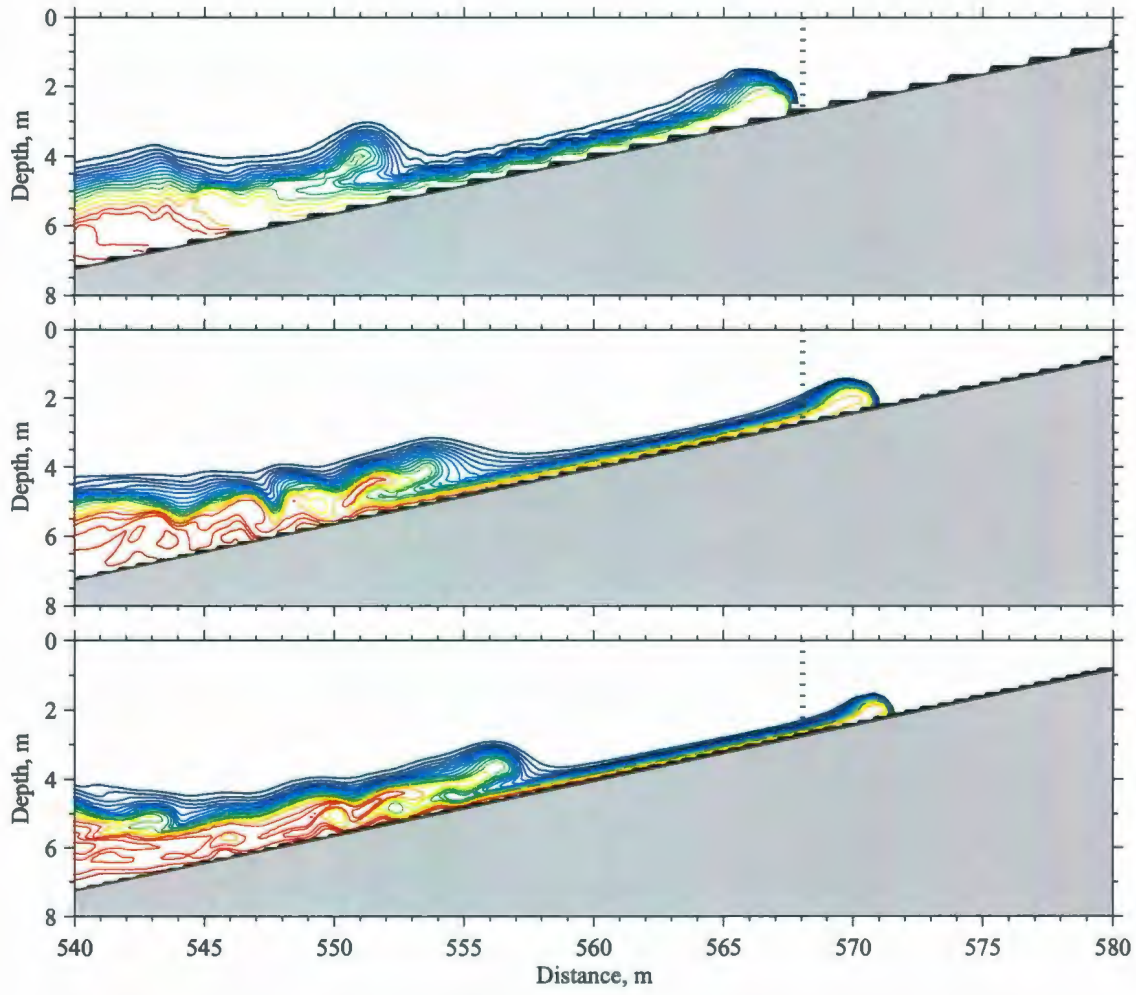

Figure 5.1. An example of wave evolution obtained from numerical runs with identical geometry and initial conditions but with different horizontal grid resolutions of $\Delta x = 1$ m (top), $\Delta x = 0.5$ m (middle) and $\Delta x = 0.25$ m (bottom). The color contours represent the density field. The vertical dashed line marks the position of bolus head for $\Delta x = 1$ m.

and mixing on the sloping topography it is necessary to have adequate vertical resolution. The numerical results with finer vertical resolution show that the transition of the waves of depression into waves of elevation is accompanied by many more irregular features in the density field along the pycnocline. This results in more mixing than predicted by the low vertical resolution simulations.

In the present study, the mass transport of dense water brought above the pycnocline was calculated using numerical simulations with the same vertical resolution of $\Delta z = 0.25$ m

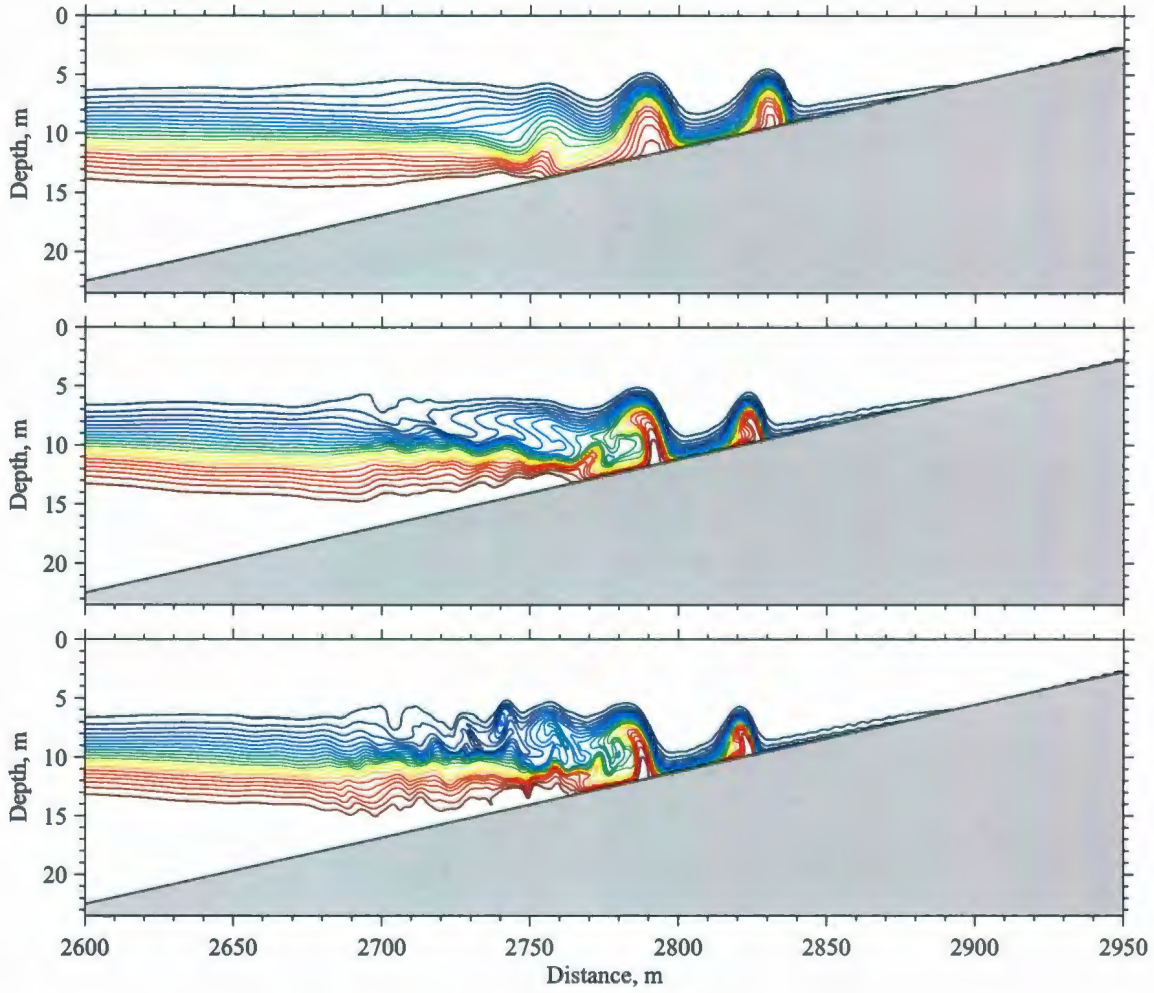

Figure 5.2. An example of wave evolution obtained from runs with identical geometry and initial conditions but with different vertical grid resolutions of $\Delta z = 1$ m (top), $\Delta z = 0.5$ m (middle) and $\Delta z = 0.25$ m (bottom). The color contours represent the density field.

and different horizontal resolution.

The amount of water brought above the pycnocline strongly depends on the horizontal resolution. Saturation is reached only for values of $\Delta x = 0.25$ m or less (Figure 5.3). In all numerical simulations presented in this study the horizontal resolution is chosen to be either $\Delta x = 0.25$ m (for runs with gentle slopes) or $\Delta x = 0.1$ m (for runs with steeper slopes).

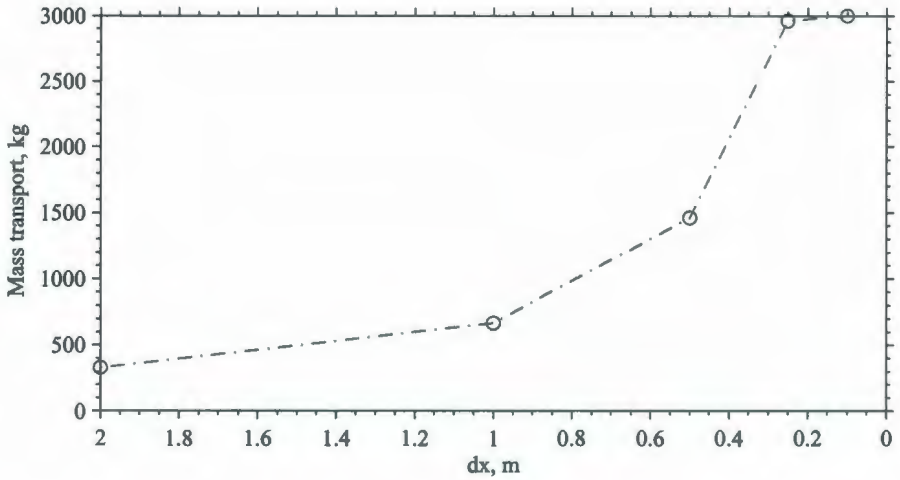

Figure 5.3. The total mass of the sub-pycnocline water brought above the slope - pycnocline intersection (point X_p in Figure 3.3) by all boluses calculated from numerical simulations used for the grid sensitivity study. All runs have the same vertical resolution with Δz = 0.25 m and horizontal resolutions Δx = 2, 1, 0.5, 0.25, 0.1 m.

5.2 Terms in the governing equations

Now let us have a closer look at physical forces affecting wave behaviour. One way to estimate the importance of various physical processes governing wave evolution (*i.e.* advection, viscosity) is to consider the input of the individual terms in the full set of nonlinear equations 3.2 - 3.3. The first term on the right-hand side of Equation 3.2 equal to the negative of the pressure gradient represents the pressure force. The second term equal to the Laplacian of the velocity multiplied by the eddy viscosity is the viscous force. According to the Smagorinsky-type parametrization [*Bourgault and Kelley*, 2004], horizontal and vertical eddy coefficients A_h and A_v can be chosen equal to each other if the horizontal and vertical resolutions are comparable.

It can be shown that the instantaneous fluid acceleration $\partial u/\partial t$ and advection terms $u\,\partial u/\partial x$ and $w\,\partial u/\partial z$ are dominant over viscous terms. A measure of relative importance of advection over viscosity can be estimated by calculating the Reynolds number. While there are different ways to introduce it, an estimate of the turbulent Reynolds number R_t is

$$Re_t = \frac{\varepsilon}{\nu N^2}, \tag{5.1}$$

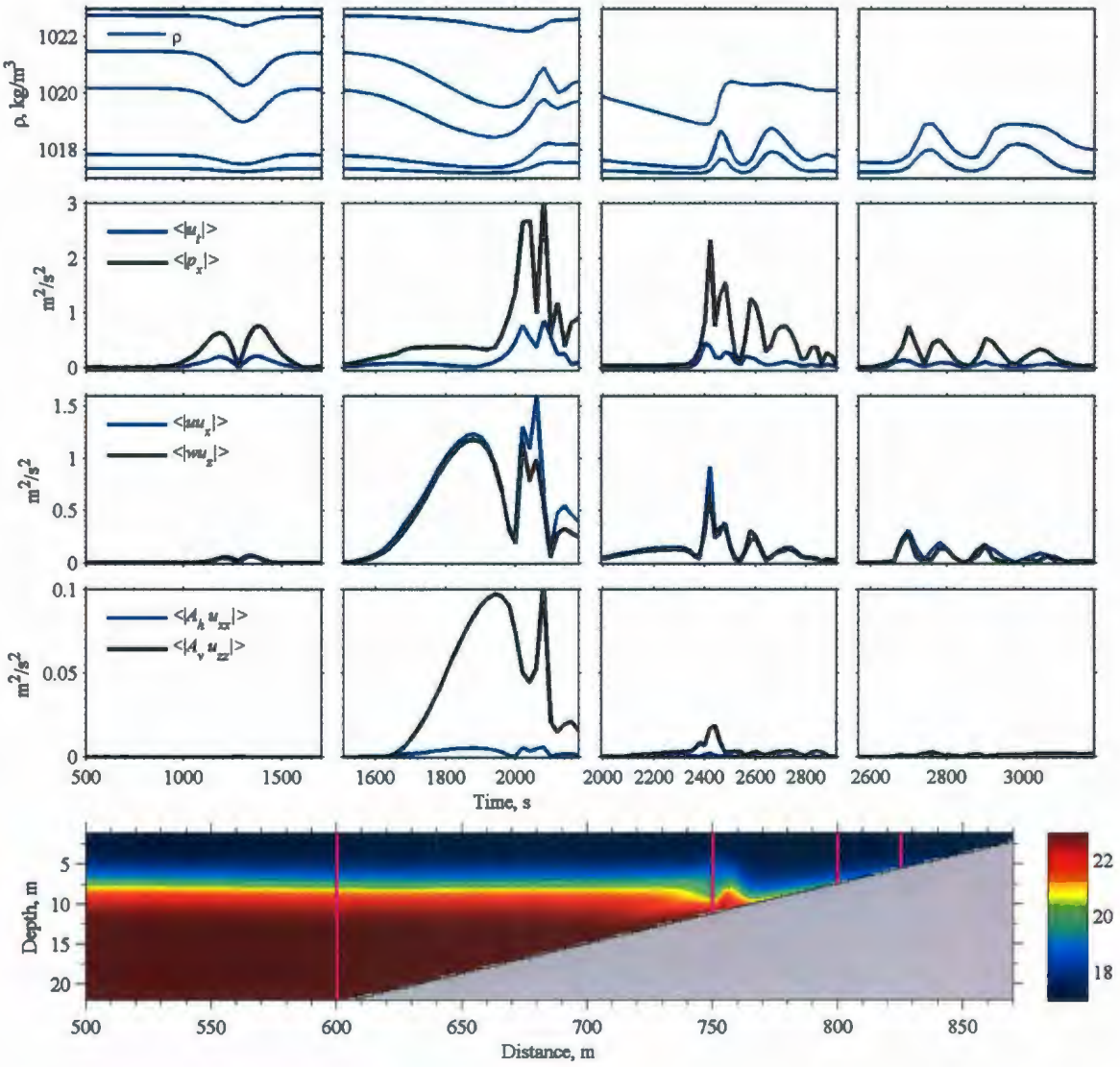

Figure 5.4. Time series of the depth-integrated terms in the the horizontal momentum equation (Equation 3.2) at different locations on the slope. Row 1 represents density contours recorded at the corresponding points. Row 2 shows the depth integrated acceleration and pressure-gradient terms. Row 3 is the depth integrated advection terms. Row 4 is the depth-integrated viscous terms. The bottom panel represents the snapshot of the density field with superimposed pink vertical lines which indicate the locations where the depth integrated terms were calculated. The initial amplitude of a shoaling wave is $a = 1.3$ m.

where ε is the turbulent kinetic energy dissipation rate, N is the buoyancy frequency and ν is viscosity [*McPhee-Shaw and Kunze*, 2002]. Using the estimates from the literature, $\varepsilon = 0.5 - 1.5 \cdot 10^{-4}$ m^2 s^{-3} for high amplitude waves and $0.6 - 1.6 \cdot 10^{-5}$ m^2 s^{-3} for small

amplitude waves and $N^2 \sim 0.02$, Re_t is estimated to be in the range $\sim 10 - 50$. This indicates that when the ISW propagates over the flat bottom, viscous effects are insignificant. The Reynolds number corresponding to the transition from laminar to turbulent regimes depends strongly on the particular type of flow under study (due to different characteristic length of the flow) and has to be determined experimentally. Visual inspection of the flow suggests that for this value of Reynolds number the ISWs are mostly laminar. The better indicator of the presence of turbulence in shear flows is the Richardson number defined by Equation 2.37. *Bogucki and Garrett* [1993] showed that Ri associated with a wave of depression depends on wave amplitude and can go below the critical value of $1/4$, thus indicating the possibility of shear instability and turbulence.

We find it advantageous to consider depth-integrated evolution equations for the fluid acceleration at a fixed point in the flow. Figures 5.4 - 5.7 present the time series of depth-integrated inputs of different terms in the horizontal and vertical momentum equations 3.2 and 3.3. Four locations representing different stages of wave evolution are chosen for the description of terms during shoaling event of a small amplitude wave with $a = 1.3$ m (Figures 5.4 and 5.5) and a large amplitude wave with $a = 6$ m (Figures 5.6 and 5.7). The first location is taken in the region where a wave of depression travels over the flat bottom, the second and the third depict transition from a wave of depression into wave of elevation, and the last one is in a region where a formed bolus propagates upslope. Figures are organized as follows. Four columns correspond to four locations along the slope shown by pink vertical lines on the bottom panel. The first row of panels shows the density contours recorded at the chosen locations. The second row of panels represents time series of the depth-integrated absolute values of the acceleration terms ($\langle|u_t|\rangle$ for horizontal component and $\langle|w_t|\rangle$ for vertical component equation) as well as corresponding depth-integrated absolute values of the pressure-gradient terms ($\langle|p_x|\rangle$ and $\langle|\rho_0^{-1}p_z|\rangle$). Here $\langle|...|\rangle = \int_0^H |...|\, dz$. The third row of panels shows the depth integrated absolute values of the advection terms ($\langle|u\,u_x|\rangle$, $\langle|w\,u_z|\rangle$ and correspondingly $\langle|w\,u_x|\rangle$ and $\langle|w\,w_z|\rangle$ for vertical component). Finally, the fourth row of panels presents the time series of the depth-integrated absolute values of the viscous terms. The bottom panel gives an example of a density field snapshot along with the positions indicated by vertical lines where time series of depth-integrated terms were recorded.

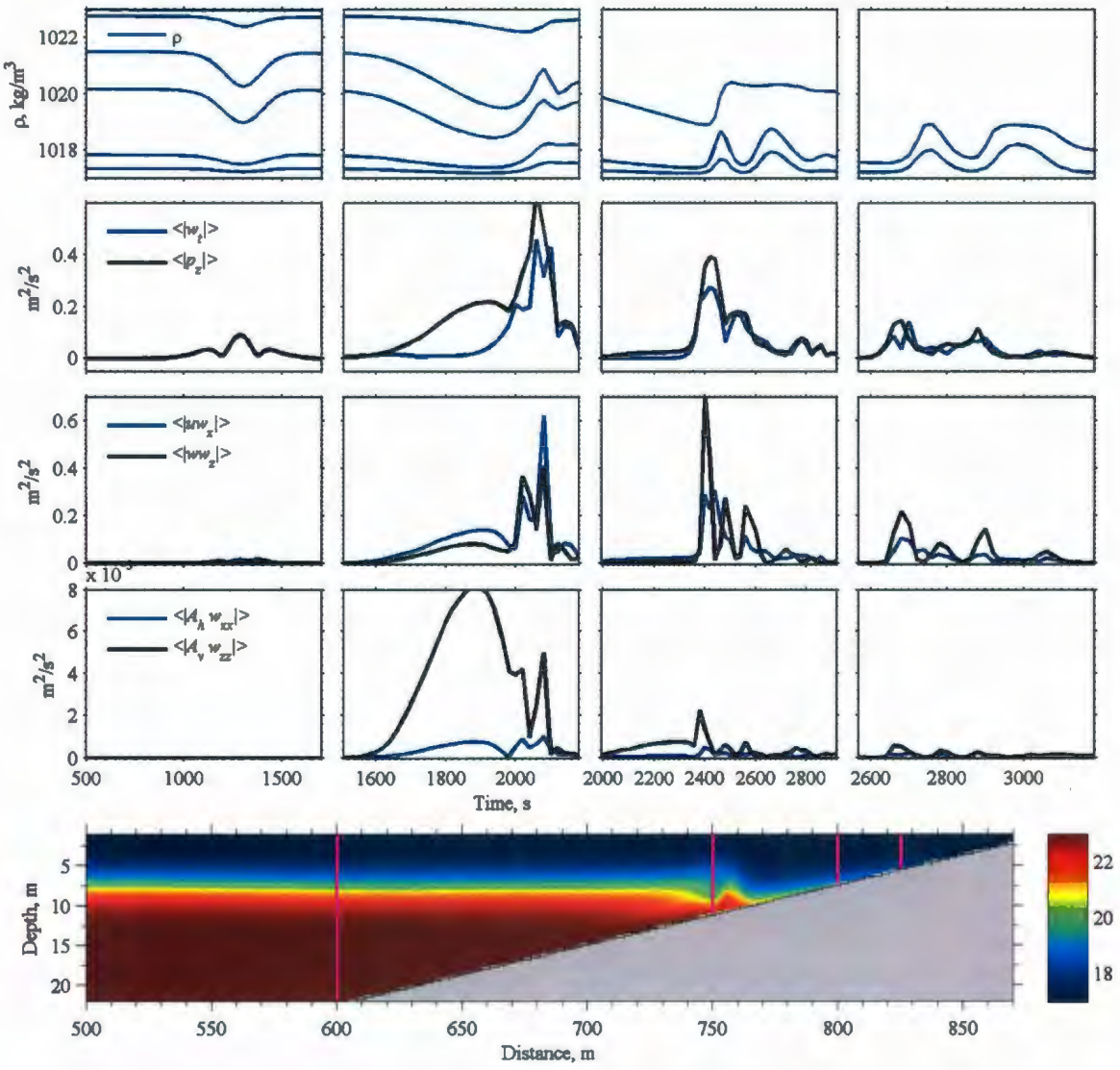

Figure 5.5. As for Figure 5.4 but for the terms in the vertical momentum equation (Equation 3.3).

For a solitary wave of depression two most significant components in the Navier-Stokes equation are instantaneous acceleration and pressure gradient (seconds row panels in Figures 5.4 - 5.7). In other words, the vertical acceleration dw/dt is sustained mostly by the vertical pressure gradient dp/dz. If the absolute values of depth-averaged pressure gradient and acceleration terms can be as large as 0.2 inside the wave of depression of 1.3 m then advection terms can reach only 0.07, depth-average of viscous terms are of the order of $10^{-4} \div 10^{-7}$.

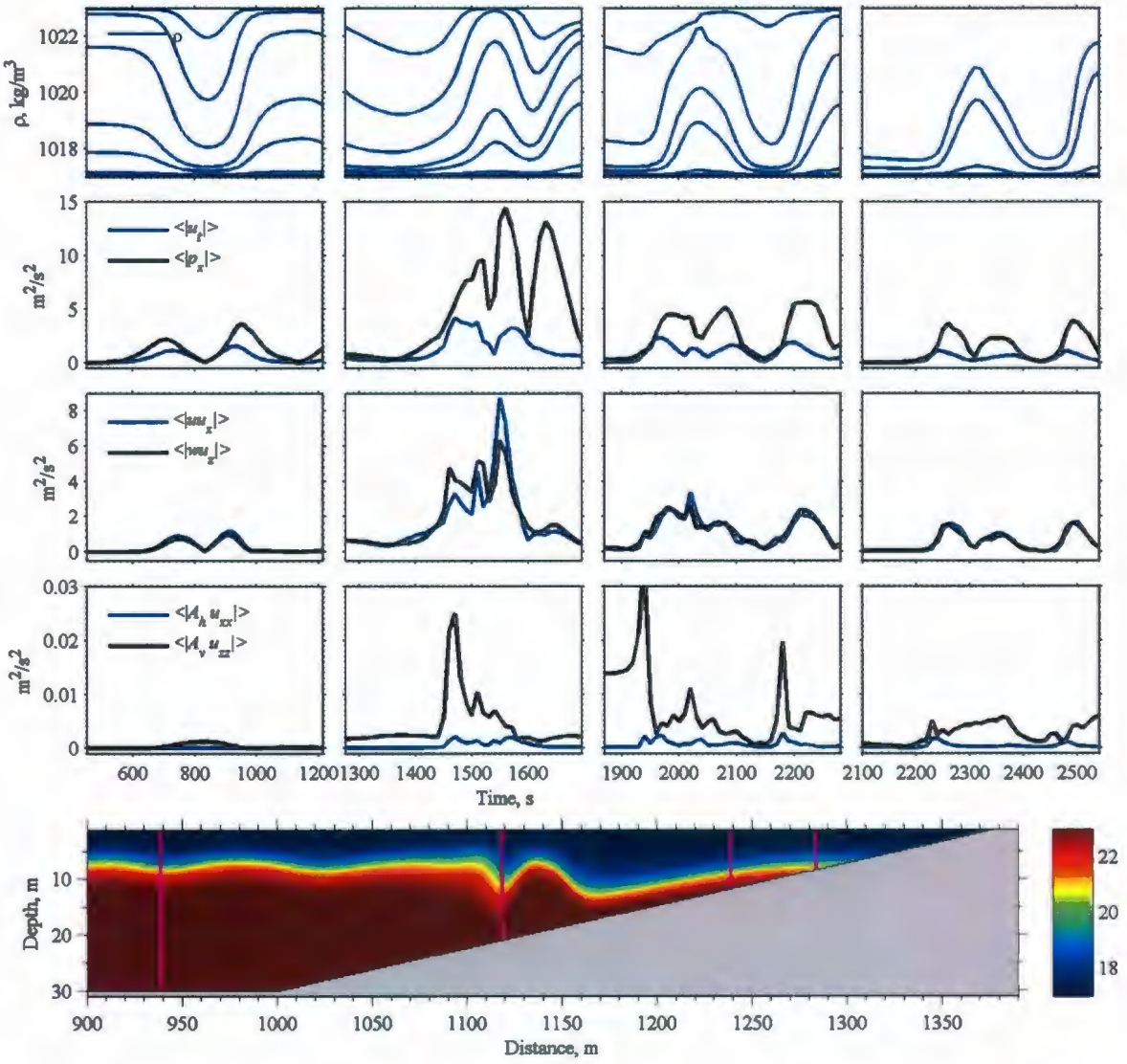

Figure 5.6. Time series of the depth-integrated terms in Equation 3.2 calculated during a shoaling event of a large amplitude wave $a = 6.0$ m. For details see Figure 5.4.

As the wave approaches the slope, it creates a backflow down the sloped boundary. This is reflected in the significant increase of the advection terms (third row panels in Figures 5.4 - 5.7). Although all depth-integrated terms increase in value, their ratio changes as well. The ratio of the acceleration term $< |u_t| >$ to the viscous term $< |A_v\, u_{zz}| >$ in the horizontal momentum equation decreases by a factor of two. The importance of the advection terms is reflected by the increase of their ratio to the acceleration terms from 0.35 to 4 during wave propagation from location 1 to location 2 (Figure 5.4, the third row). The

only terms which maintain the constant ratio between each other are the acceleration and pressure-gradient terms, with the unchanged ratio equal to 0.2 (Figure 5.4, second row). This means that in all cases the pressure disturbance is driven by the local vertical acceleration of fluid.

It was noticed since early laboratory experiments on shoaling ISWs that the back-flow goes above the bolus and brings the lighter fluid from the location above the slope over top of the denser fluid inside the bolus. Thus, for boluses, the interplay of terms in Equations 3.2 - 3.3 is somewhat different. Now advection terms are comparable in magnitude with depth-integrated pressure and acceleration terms or exceed them. For example, $< |u_t| >$ = 0.45 and $< |u\,u_x| >$ = 0.90. When a wave of depression undergoes the transformation into train of waves of elevation, high velocity gradients are induced when the wave front is approaching vertical. This explains the peak in the viscous terms visible in Figures 5.4 - 5.7. High velocities close to the boundary, persist for the fully developed bolus, with depth-integrated viscous terms of the order $\mathcal{O}(0.01)$.

While the bolus propagates upslope and dissipation removes its energy, all depth integrated terms are getting smaller. Acceleration and pressure gradient terms are still dominant, with the depth-integrated advection terms smaller but of the same order, while viscous terms are negligible.

It is interesting to compare the time series between small and large amplitude internal waves, Figures 5.4 and 5.6. The description of the time series of the depth-integrated terms for the horizontal momentum equation for large-amplitude wave with $a = 6$ m is analogous. First of all, for the larger wave the pressure gradient term is much larger than the acceleration term. For the case of the wave shoaling (second column in Figures 5.6) $< |p_x| >$ is 3.5 lager than $< |u_t| >$. The same ratio also holds for the small-amplitude wave. Second, as for the small wave, the advection and viscous terms are getting much more important during the shoaling of the wave. The depth-integrated viscous terms for the large wave play an important role when the bolus is developed, while the depth-integrated viscous terms for the small wave decreased by factor of 10.

After the wave of depression transforms into a series of boluses, velocity gradients are getting smaller, which is reflected in the decrease of the advection terms (third and fourth columns in Figures 5.4 - 5.7). However, they exceed the input from the acceleration terms.

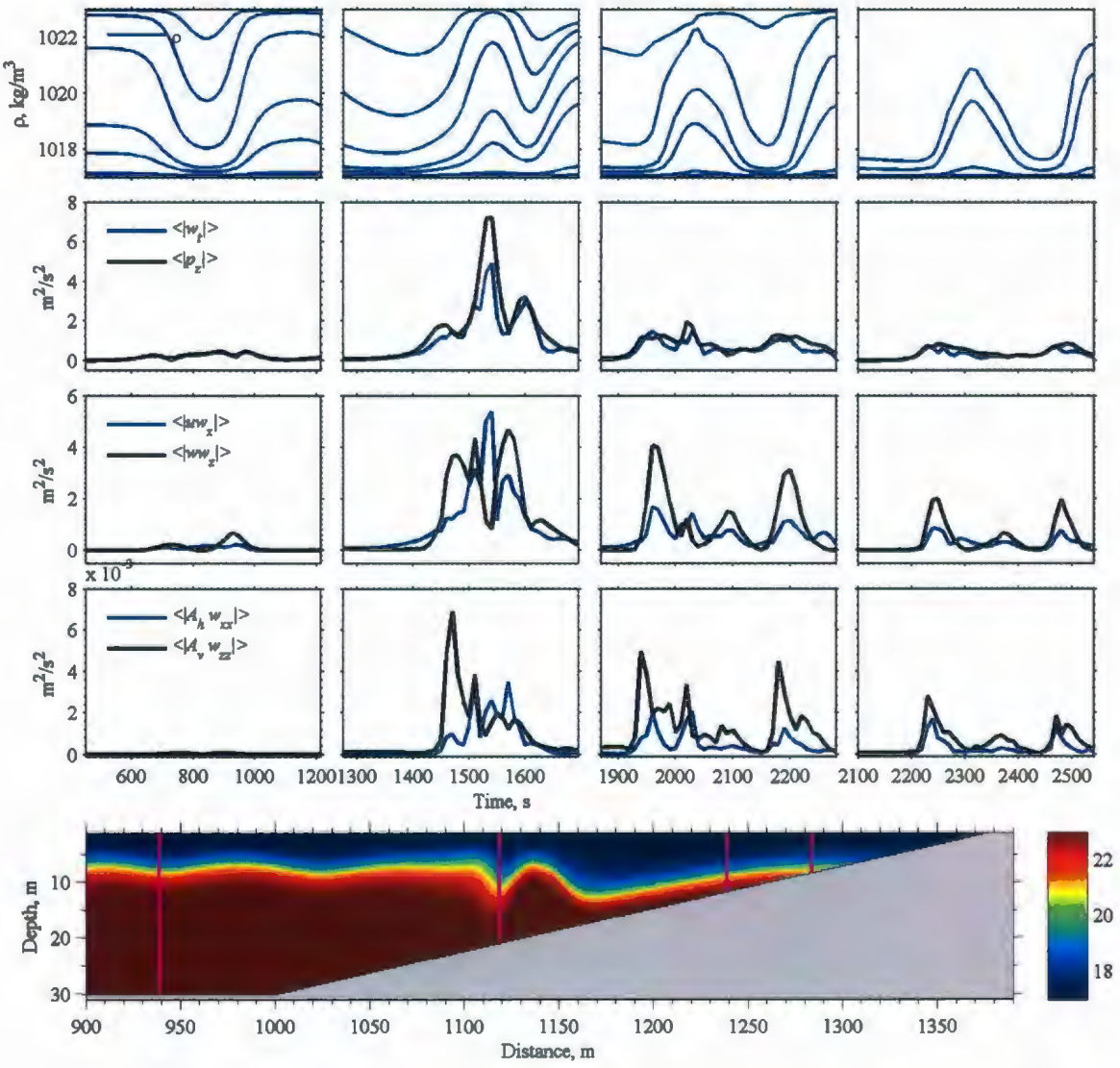

Figure 5.7. Same as for Figure 5.6 but for terms in equation 3.3.

Viscous terms for boluses are also getting smaller, as the wave-induced velocities vanish. It is still worth noting that viscous effects play an important role during the wave transition (second columns in Figures 5.4 - 5.7).

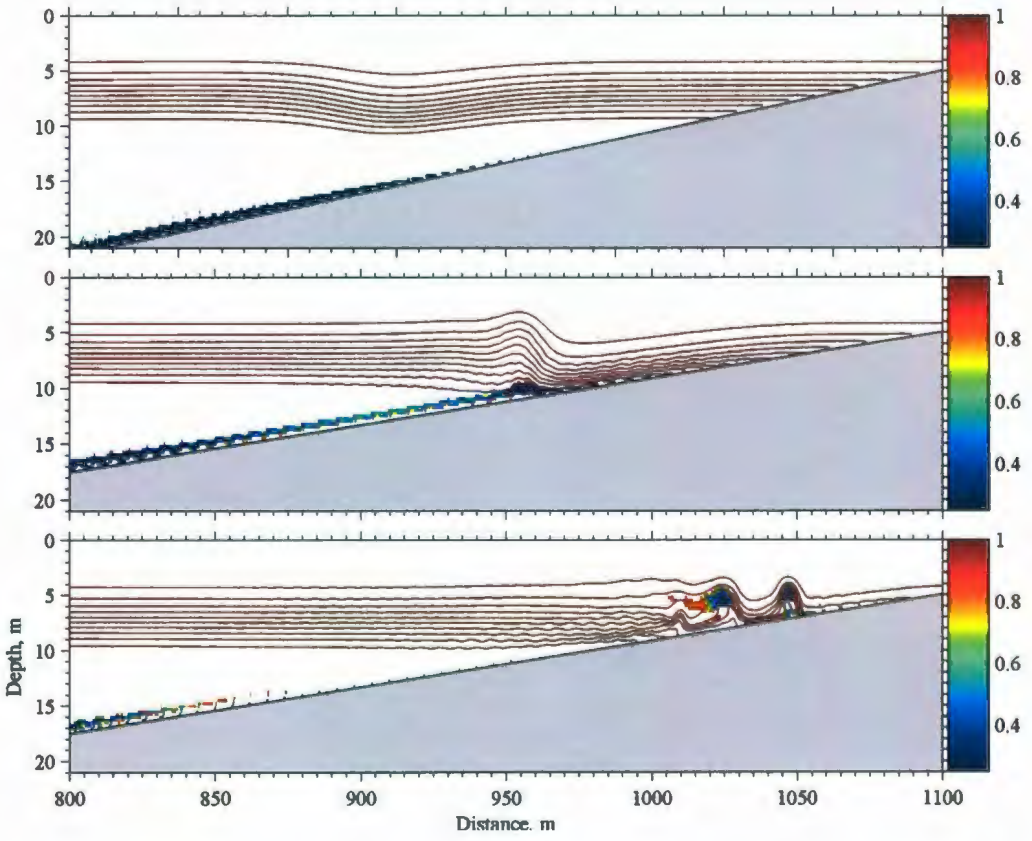

Figure 5.8. The Richardson number (colored regions) superimposed on contour plots of the density field. Richardson number values that exceed the limits of the color bars (> 1) appear white. The initial amplitude of a shoaling internal wave is 1.3 m, the slope angle is 2.4 degrees. Time on panels from the top to the bottom: $t = 500, 1500, 2000, 2500$ s.

5.3 Interaction with a slope

An internal solitary wave propagating towards a sloping bottom experiences several stages of evolution. The first one is deep water propagation. It is characterized by adiabatic changes in wave characteristics allowing the wave to propagate without change over large distances [*Vlasenko et al.*, 2005]. After the moment an ISW passes the point of the beginning of the slope, X_s, (Figure 3.3) its evolution is no longer adiabatic because of its strong interaction with the bottom.

Shoaling can take the form of a gradual transformation of an ISW into a train of internal waves of elevation. For a certain combination of parameters (typically for large amplitude waves) shoaling may take an abrupt form when an incident ISW transforms into a number of waves of elevation through breaking . Breaking can be defined as the appearance of inversions in the density profile [*Bourgault and Kelley*, 2003].

According to the criterion proposed by *Vlasenko and Hutter* [2002a] the total depth of the fluid column at the point of breaking, H_b, the amplitude of the incident wave, a_m, the depth of the density contour of maximal depression, H_m, and the topographic slope, s, are connected through the relationship given by Equation 2.44. The depth of the density contour with the maximal depression coincides with the depth of the maximum of the density structure function defined by Equation 2.10. This, however, is true only for small weakly nonlinear waves [*Vlasenko and Hutter*, 2002a]. For large amplitude waves, H_m has a shifted location and this shift depends on the wave amplitude. In the present study H_m is calculated for each case by taking the difference between the density profile at the wave crest and an undisturbed density profile at a place far from the wave.

As an example, let us apply the criterion given by Equation 2.44 to a small ISW with amplitude $a = 1.3$ m shoaling over a slope of $\gamma = 2.4$ degrees. The depth of the density contour with the maximal depression was measured to be $H_m = 8.3$ m. The total depth of fluid at the breaking location is then calculated to be $H_b = 10$ m. The incident wave transforms into a train of three boluses at the transition point, X_t, where the depth of fluid is 14 m. Numerical simulations show no indication of breaking or instabilities, neither during wave transformation, nor inside formed boluses (Figure 5.8). In this case the ISW with amplitude $a = 1.3$ m and Iribarren number $\xi = 0.3$ experiences a smooth transition

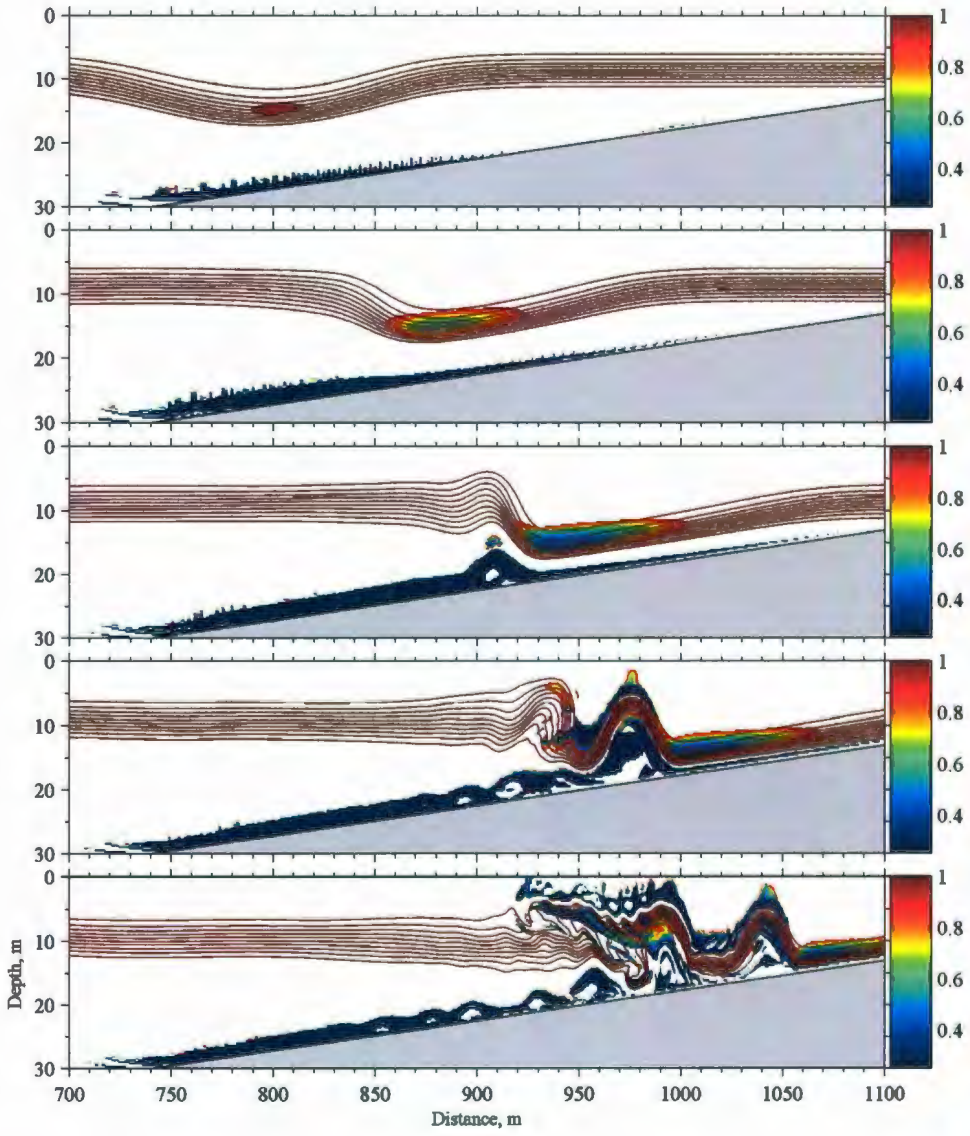

Figure 5.9. The Richardson number (colored regions) superimposed on contour plots of the density field. Richardson number values that exceed the limits of the color bars (> 1) appear white. The initial amplitude of a shoaling internal wave is 6 m, the slope angle is 2.4 degrees. Time on panels from the top to the bottom: $t = 100, 1000, 1200, 1400, 1600, 1800$ s.

into a wavetrain of boluses and each bolus experiences a smooth decay.

Another way to explore the ISW breaking is to plot the Richardson number defined by Equation 2.37. Figure 5.8 shows the Richardson number for the same shoaling ISW with

amplitude $a_0 = 1.3$ m. The Richardson number is well above 1 (shown in white) everywhere in the fluid interior due to small vertical velocity gradients. However, close to the bottom the strong shear generated by the shoaling wave causes the Richardson number to lower to 0.5, in accordance with *Bogucki and Garrett* [1993]. This value is still higher than the critical Richardson number $\mathrm{Ri}_{\mathrm{cr}} = 1/4$ below which the development of instabilities and turbulence is possible in the stratified shear flows. This agrees with the absence of instabilities in the density contours.

Now let us take up the case of a larger internal wave shoaling. Figure 5.9 shows the Richardson number and density contours for a shoaling ISW with amplitude $a_0 = 6$ m over a slope of $\gamma = 2.4$ degrees. It can be noted that the Richardson number in this case is low not only in the bottom boundary layer, but also inside the wave close to its trough. In this situation the wave breaks and small scale instabilities appear on the rear end of wave (Figure 5.9d, e). Equation 2.44 (Vlasenko's criterion) predicts the depth at which the breaking occurs to be $H_b \approx 18$ m. This value agrees well with the depth that can be inferred from Figure 5.9. Boluses formed in this case are themselves capable of lowering the Richardson number below the critical value inside their cores and around their crests, as is clear from Figure 5.9. This suggests that boluses may play a significant role in mixing.

5.4 Bolus development and up-slope propagation

Here we investigate bolus properties using as a case study the incident wave of depression with the initial amplitude $a_0 = 4$ m. In the vicinity of the turning point the ISW becomes steeper and transforms into a number of waves of elevation. These waves are propagating up-slope, bringing the dense water from below the pycnocline into the above-pycnocline region.

Figure 5.10 presents the full course of the first bolus development. The distance traveled by the bolus is expressed relative to the point X_p due to the importance of this point, as will be shown later. Visual inspection of the evolution of the first bolus with time shows that it can be divided into three stages. Figure 5.10a,b shows the formation of the bolus. Small instabilities appearing close to the bottom (Figure 5.10b) persist inside the bolus core but do not lead to the breaking of the wave. They are probably similar in nature to the ini-

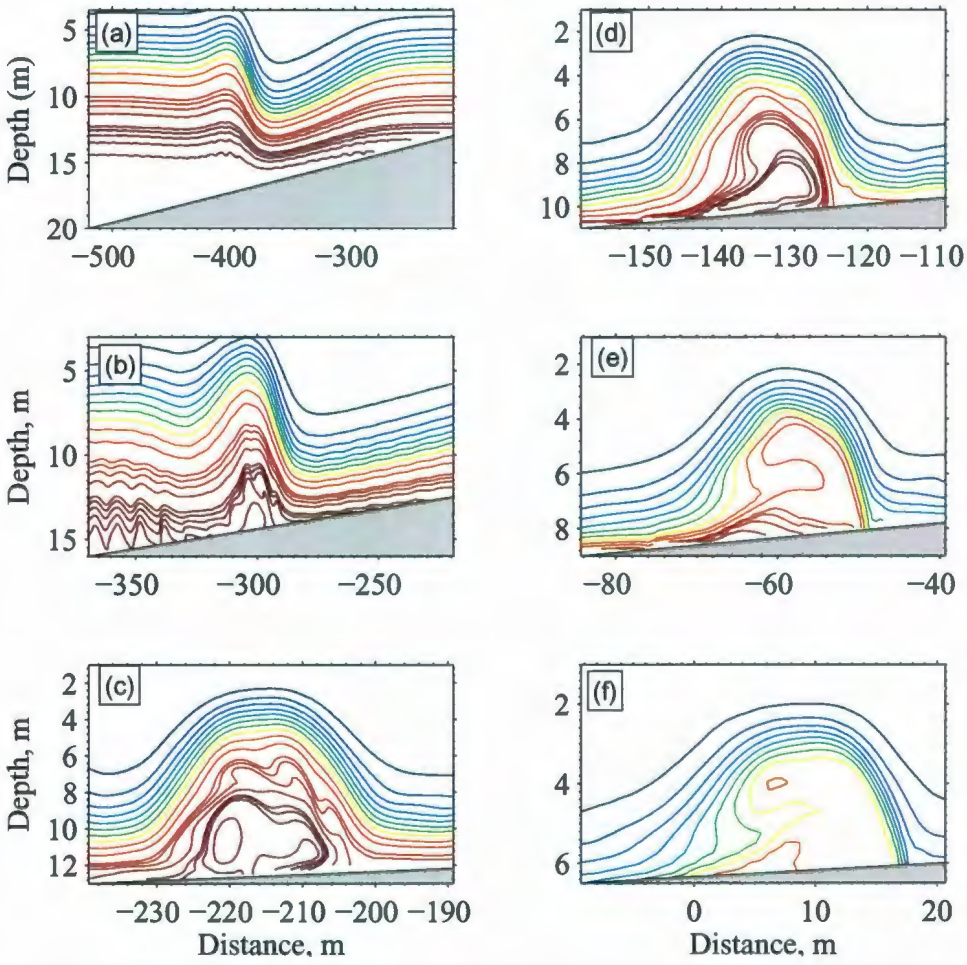

Figure 5.10. Evolution of the first bolus. The contours on the plots are of the density field. The amplitude of the incident wave of depression is $a = 4$ m. The Iribarren number for this case is 0.085. Time on panels is t =1200 s (a), t = 1500 s (b), t = 1800 s (c), t = 2100 s (d), t = 2400 s (e), t = 2700 s (f). The distance is relative to the point X_p.

tial disturbances required for the growth of the Kelvin-Helmholtz (KH) billows reported by *Moum et al.* [2003] for IWs of depression. The horizontal scale of these features is approximately 3.5 m and agrees with the scale of KH billows observed in the ocean thermocline by *Li and Yamazaki* [2001]. Growth of the initial disturbances can lead to the bolus breakup further upslope. This scenario of the bolus' fate was suggested by *Klymak and Moum* [2003] based on the low energy decay rate. However, for the parameters used in the present study, the disturbances inside the bolus wither away and the bolus propagates onshore ex-

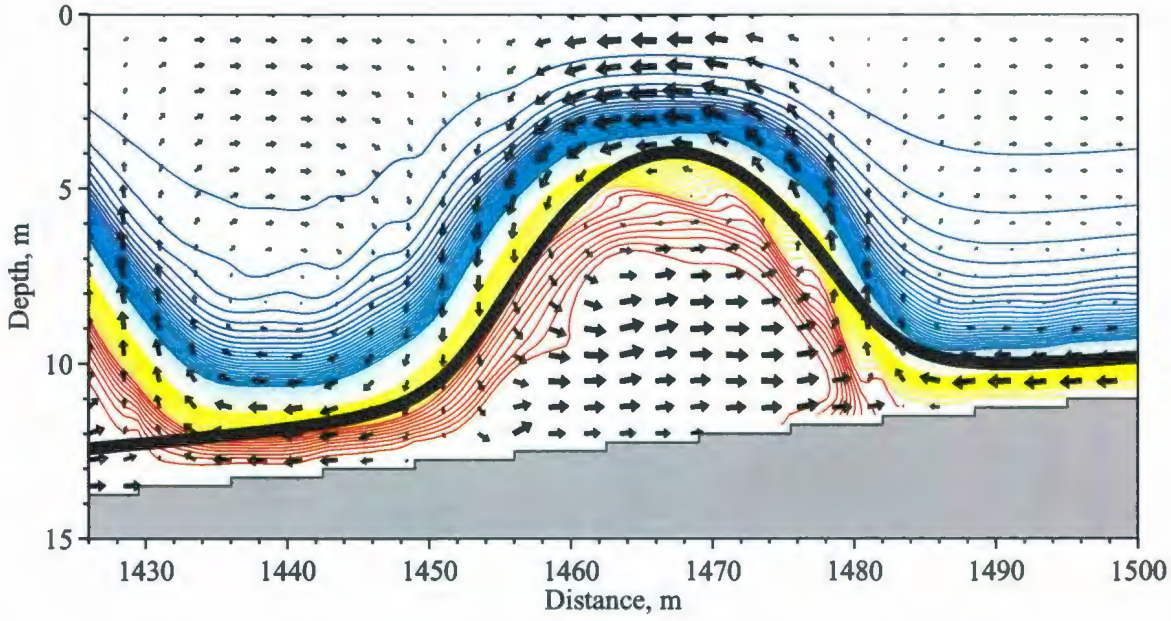

Figure 5.11. Density contours and velocity vectors of the first bolus shortly after the formation. The black solid line is a fit obtained from the two-layer fully nonlinear model of *Grue et al.* [1999]. The amplitude of the bolus is $a = 4.92$ m. Depth of the lower layer is $h_2 = 1.27$ m and of the upper layer $h_1 = 11.2$ m.

periencing a smooth decay. Finally, a fully developed bolus is formed (Figure 5.10c).

The second stage, shown in Figure 5.10c-d, is characterized by a well developed bolus with the shape of a solitary wave of elevation. At this stage, bolus characteristics are well comparable with ISWs computed using a fully nonlinear interfacial theory by *Grue et al.* [1999], as presented in Figure 5.11. The phase speed of the bolus in Figure 5.11 obtained from the fit is 0.39 m/s which compares well with $c = 0.36$ m/s obtained from the numerical simulations.

Figure 5.12 shows the relationship between the characteristic length and amplitude of the leading bolus. Bolus length and amplitude were calculated from different numerical runs at the locations where depths of the upper and lower layers are $h_1 = 11.2$ m and $h_2 = 1.2$ m, correspondingly. Comparison with the KdV relationship (grey curve) and the fully nonlinear model shows that small boluses with amplitudes $a < 0.4$ m can potentially be well described by both theories. Such small boluses, however, are not observed during

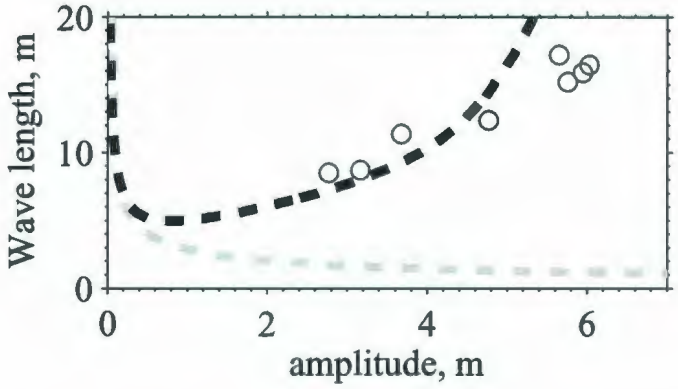

Figure 5.12. The relationship between characteristic length and amplitude of the leading bolus. Open circles represent results of different numerical simulations for the location where depths of the lower and upper layer are $h_2 = 1.27$ m and $h_1 = 11.2$ m. Grey dashed line shows the KdV dependence and the black dashed line is the dependence obtained from the fully nonlinear two-layer model with the same parameters.

the present study owing to resolution limitation. Boluses with amplitudes 0.4 m $< a <$ 5 m are substantially broader than the KdV solitons, but the fully nonlinear model is shown to be a valid model, as supported by Figure 5.11. There are, however, larger amplitude boluses with $a > 5$ m which can not be described by either of the presented theories. The fully nonlinear model overestimates the bolus widths predicting much broader boluses than the ones obtained from the numerical simulations. This is explained by viscous effects which are neglected in both weakly and fully nonlinear two-layer theories.

As another verification of the bolus nature and their relation to solitons we consider the overtaking collision between two boluses moving along the slope in the same direction. Being dispersive waves, boluses of different amplitudes propagate with different speeds proportional to their amplitude, as described by Equation 2.17.

As a result, a bolus with a larger amplitude moves faster than a bolus with a smaller amplitude. Figure 5.13 shows two boluses with amplitudes $a = 4.5$ m and $a = 3.5$ m and their overtaking collision. The weakly nonlinear KdV theory predicts that the taller and faster wave catches up to the slower soliton, interacts with it and then passes the smaller soliton. After the interaction, properties of both solitons are unchanged and the shapes are undistorted. This type of interaction is called elastic. Referring to Figure 5.13 it can be

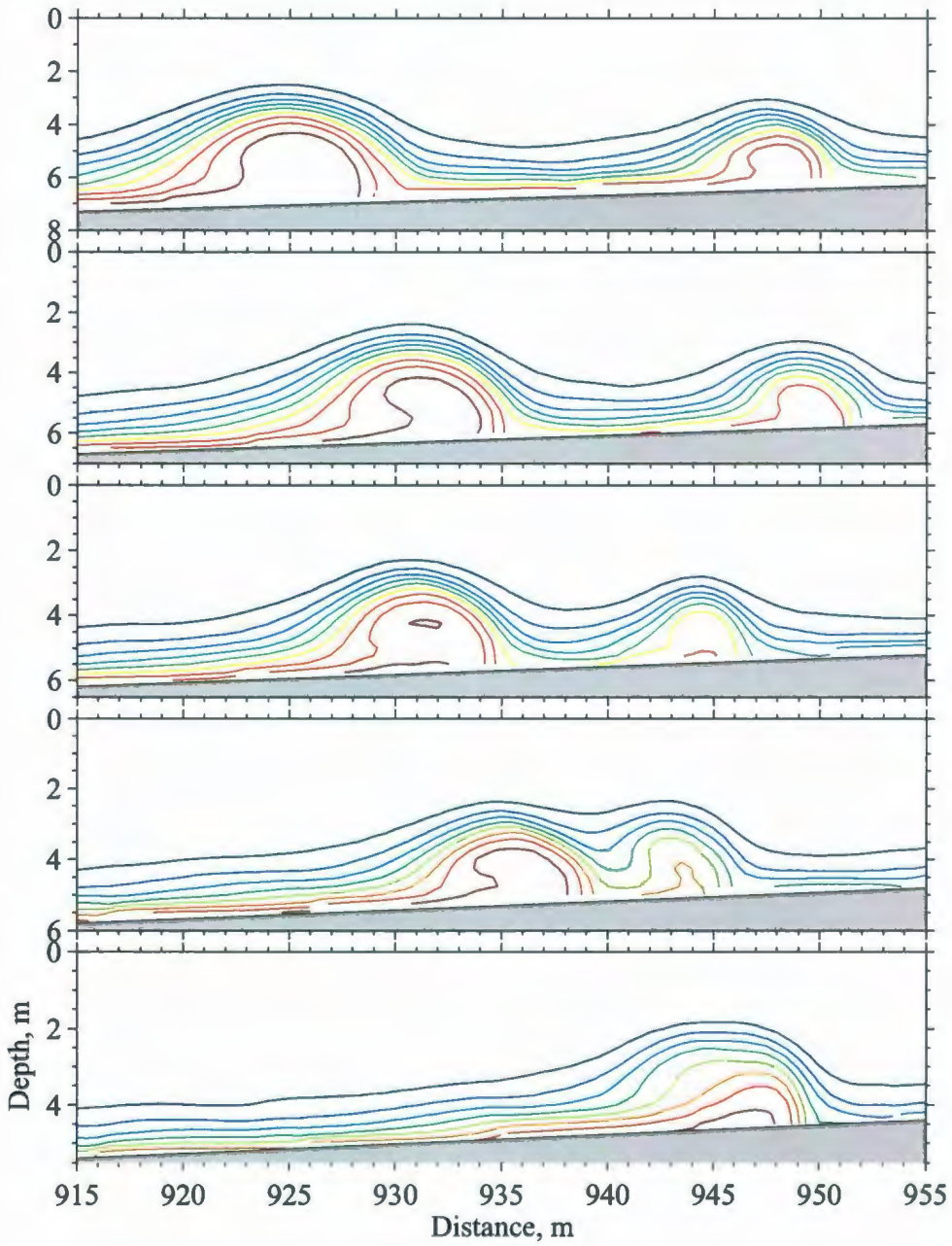

Figure 5.13. Inelastic overtaking collision between two boluses with amplitudes $a = 4$ m and $a = 3$ m. As a result a single bolus is formed with amplitude $a = 2.8$ m.

observed that two boluses interact in an inelastic manner. As a result of this interaction a single bolus of amplitude $a = 3.0$ m is formed. One can draw the conclusion that boluses, despite similarities with solitary waves, do not behave like solitons.

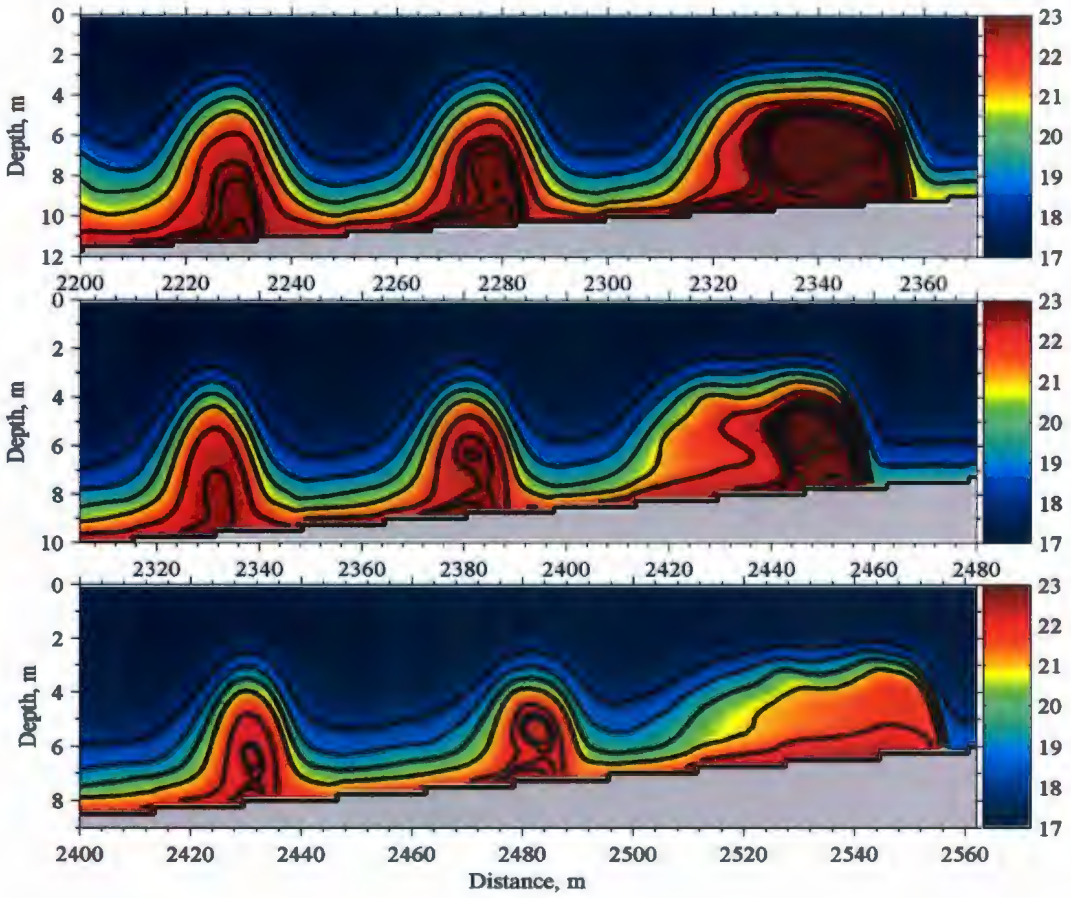

Figure 5.14. Density contours $\sigma_t = \rho - 1000$ of the first three boluses with trapped cores formed during a large ISW ($a_0 = 6$ m) shoaling over a gentle slope of 0.85 degrees. Time on panels (from the top to the bottom) 4200 s, 4600 s and 5000 s, correspondingly. The color bar indicates the density scale in kg/m^3.

To finish the discussion about the bolus nature, we return to Figure 5.10e - f to describe the final stages of the bolus evolution. Close to the point X_p where the depth of the lower layer is becoming zero, the shape of the bolus is changing. The bolus loses its symmetry and steepens on the front end. The strain rate defined by Equation 2.42 is calculated for the panel (e) of Figure 5.10 to reach 15. This means that the density contours at the front of the bolus are compressed compared to the density contours at the rear of the bolus. The bolus retains such an asymmetrical form until its full dissipation. In this form bolus is close in

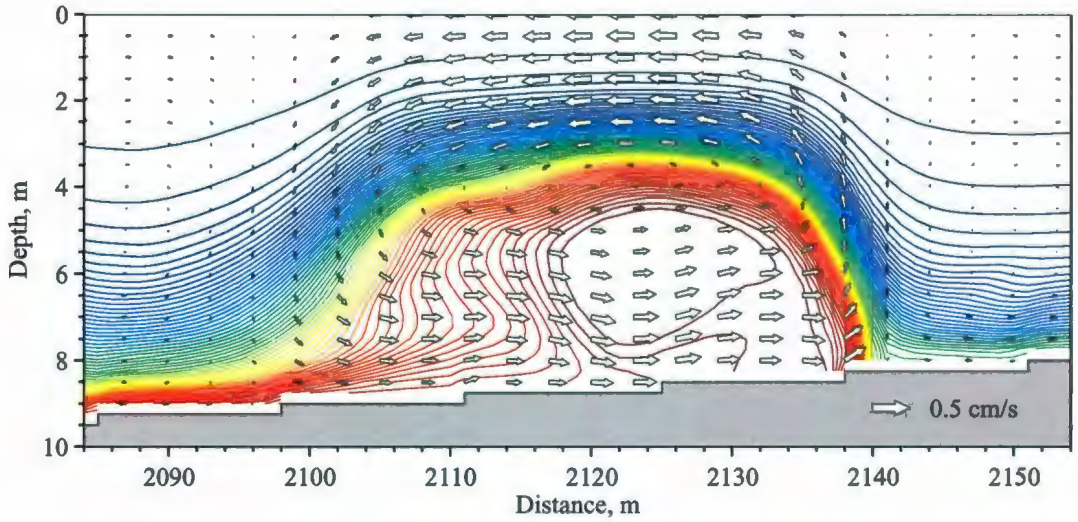

Figure 5.15. Density contours and superimposed velocity vectors of the leading bolus from Figure 5.14 showing details of trapped core in the stationary reference frame.

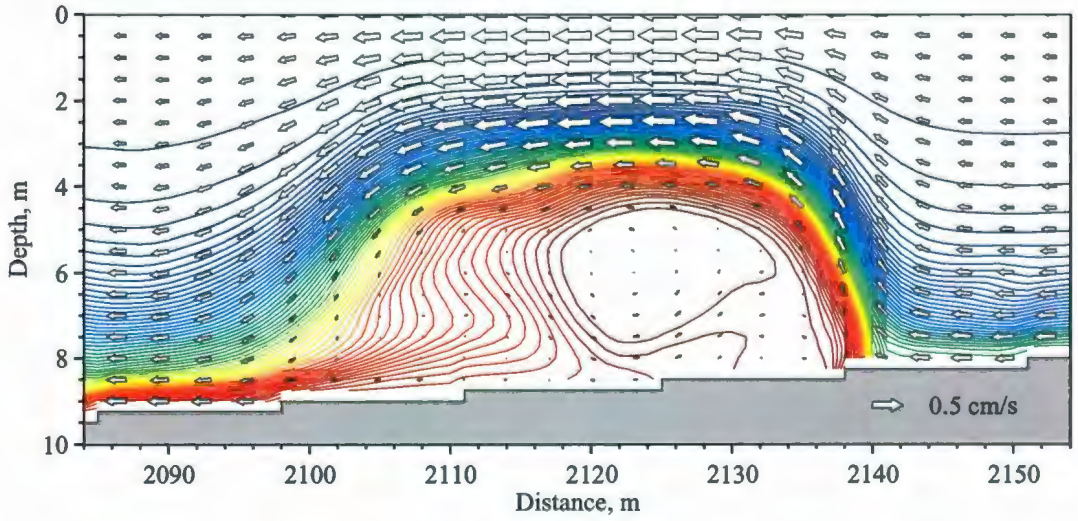

Figure 5.16. Density contours and superimposed velocity vectors of the leading bolus from Figure 5.15 showing details of trapped core in a co-moving reference of frame.

shape to the head of gravity current, with example shown in Figure 2.14. However, lacking the theoretical basis for the description of gravity currents even on a flat bottom, it is hard

to perform a comparison with bolus properties propagating over linear slopes.

It is interesting to note differences in the structure between boluses produced by a solitary wave (Figure 5.10) and boluses generated by progressive internal waves in the continuously stratified fluid (Figure 2 of *Venayagamoorthy and Fringer* [2007]). Unlike the case with the continuous stratification where the formation of boluses is only allowed by the criterion 2.47, internal solitary waves propagating in the two-layer fluid always transform into at least one bolus. This is supported by theoretical and numerical solution of the extended KdV equation [*Helfrich et al.*, 1984; *Knickerbocker and Newell*, 1980]. Another difference is the shape of boluses. In the continuous stratification, generated boluses are always in the gravity current mode [*Venayagamoorthy and Fringer*, 2007, see their Figure 2 and Figure 14]. The connection between internal wave modes and gravity current modes of the fluid flow along a sloping bottom is discussed by *Maxworthy et al.* [2002].

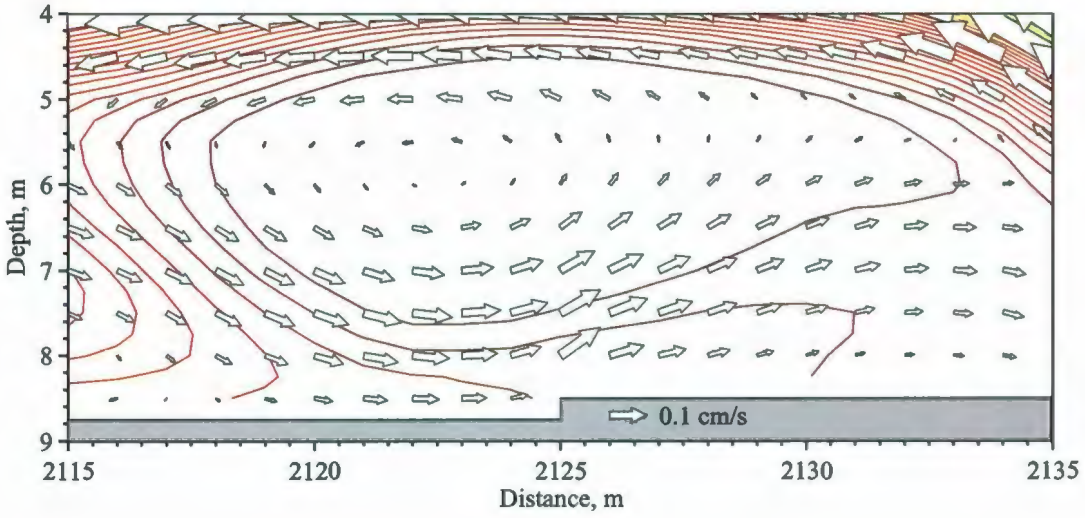

Figure 5.17. Zoom of the trapped core inside the bolus shown in Figure 5.16 Velocity vectors show closed circulation inside the bolus.

Boluses generated by the transition of an IW of depression retain solitary wave form for the period of time before passing the point where the lower layer depth becomes zero.

5.4.1 Boluses with trapped cores

Figure 5.14 represents a series of three boluses formed by a shoaling ISW with amplitude $a = 6.00$ m over a gentle slope of $\gamma = 0.85$ degrees. The initial amplitudes of these boluses soon after their formation were approximately the same $a = 7.00 \pm 0.50$ m. These boluses have the ratio of amplitude to depth of the upper layer $a / h_1 \approx 1$ and are not rank ordered in terms of the amplitude. In this simulation, the closed density contours are developed inside all formed boluses, only three of which are shown. They persist inside the boluses for at least 30 minutes during which boluses have traveled ~ 300 m upslope. Boluses with trapped cores as proposed by *Scotti and Pineda* [2004] are effective in transporting dense fluid and nutrients up the sloping bottom.

Mechanism of the trapped core formation proposed by *Lamb* [2002] and *Derzho and Grimshaw* [1997] implies that breaking of an internal wave with an amplitude larger than the critical value for a given depth (Equation 3.16) leads to overturning of density contours and trapping of mixed fluid inside the region with closed contours. According to *Derzho and Grimshaw* [2007]: "Overturning occurs at a certain finite critical wave amplitude at which the horizontal velocity approaches zero in a frame of reference moving with the wave, that is, a local critical point appears inside the flow. Above this critical amplitude the critical point may evolve into a trapped vortex core that moves with the wave."

Here we explain how similar mechanism can lead to the formation of boluses with trapped cores without involvement of breaking process. As an ISW transforms from a wave of depression to a number of waves of elevation, a backflow down the slope is created upstream the ISW. The strength of this flow depends on the amplitude of the impinging wave and on the topographic slope. A newly formed bolus propagates in a still stratified fluid with local depths of lower and upper layer h_1 and h_2. Depending on the slope angle, depths of the lower and upper layers at the particular location may be such that the formed bolus will be of the maximum amplitude supported by this stratification. Following *Grue et al.* [2000], in the wave of the maximal amplitude the maximum induced velocities are close to the bolus phase speed. In this situation, a local critical point appears in the flow. In the reference frame moving with the bolus phase speed, this critical point is a stagnation point where the fluid velocity is zero. The stagnation point then may develop into the stagnant

region with closed streamlines (Figure 5.17). In the presence of the back-flow generated by a shoaling wave, the stagnation point may appear even if the bolus is not of the maximal amplitude and far from the breaking limit. The formation of the trapped core is thus connected to the topographical slope and on the strength of the backflow which depends on the amplitude of the incident wave. Referring to Figure 5.36 these conditions are satisfied when the Irribaren number of an incident wave is less than 0.2.

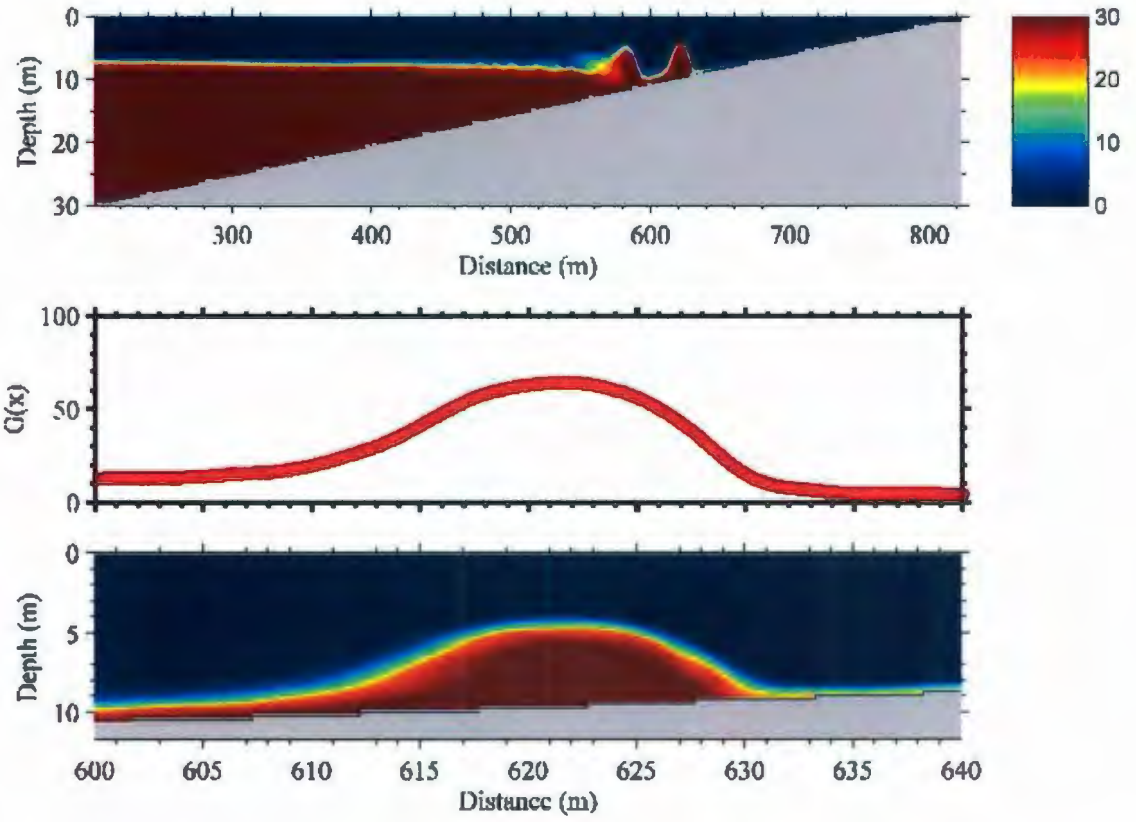

Figure 5.18. Position of the first bolus (a), distribution of the vertically intergraded tracer (b) and tracer contours (c).

Figure 5.15 displays density contours of the leading bolus along with the velocity vectors inside the trapped core. It is made in a stationary coordinate system fixed to the bottom. To show the closed circulation inside the bolus trapped core it is necessary to switch into a co-moving coordinate system moving along with the bolus phase speed (Figure 5.16).

It is interesting to note that the circulation inside the bolus core is rather weak compared to the strong off-shore back flow going above the bolus, in agreement with the laboratory experiments of *Wallace and Wilkinson* [1988] and *Helfrich* [1992]. Figure 5.17 shows the detailed closed circulation inside the bolus trapped core. This is in agreement with the velocity vectors observed by *Scotti and Pineda* [2004] in their field study (see Figure 2.12).

Tracking and measuring of the bolus dimensions are done by following a passive tracer placed below the pycnocline. *Venayagamoorthy and Fringer* [2007] used the densest fluid contour for measuring their boluses. This choice is not suitable for the present study, because of the geometry used for numerical simulation. Fluid runoff down the slope, bolus decay due to the friction in the bottom boundary layer, and mixing of fluid inside the bolus during upslope propagation will lead to the decrease in the maximum value of the density inside the bolus. After some time of upslope propagation, the bolus will not contain the densest fluid from below the pycnocline. That is why a particular density contour can not be used for bolus tracking. Instead, the bolus position, amplitude and characteristic length are calculated by measuring the amount of a passive tracer (which represents the dense water from below the pycnocline) that is trapped inside the bolus. Figure 5.18b shows the vertically integrated distribution of the tracer C:

$$G(x) = \int_0^H C(x,z)dz. \tag{5.2}$$

Figure 5.19 (top panel) shows position of the first and second boluses as a function of time. The second bolus is faster than the first one and overtake events are sometimes observed. The phase velocity of both boluses changes linearly before point X_p. After the point X_p, it only slightly deviates from the linear law, Figure 5.19 (bottom panel).

Trapped cores are formed inside both boluses (and also third bolus, see Figure 5.14) at times $t_1 = 4720$ s and $t_2 = 4800$ s. This corresponds to the positions -50.50 m and -80.50 m on the slope relative to the point X_p. Trapped cores persist inside boluses till the final dissipation. This indicates that trapped cores can travel over 200 meters up the slope. The maximum density inside the trapped cores is shown in Figure 5.20. It is clearly seen that the boluses transport the dense subpycnocline water with the density ρ_2. The maximum density inside boluses decreases linearly with the distance traveled by boluses.

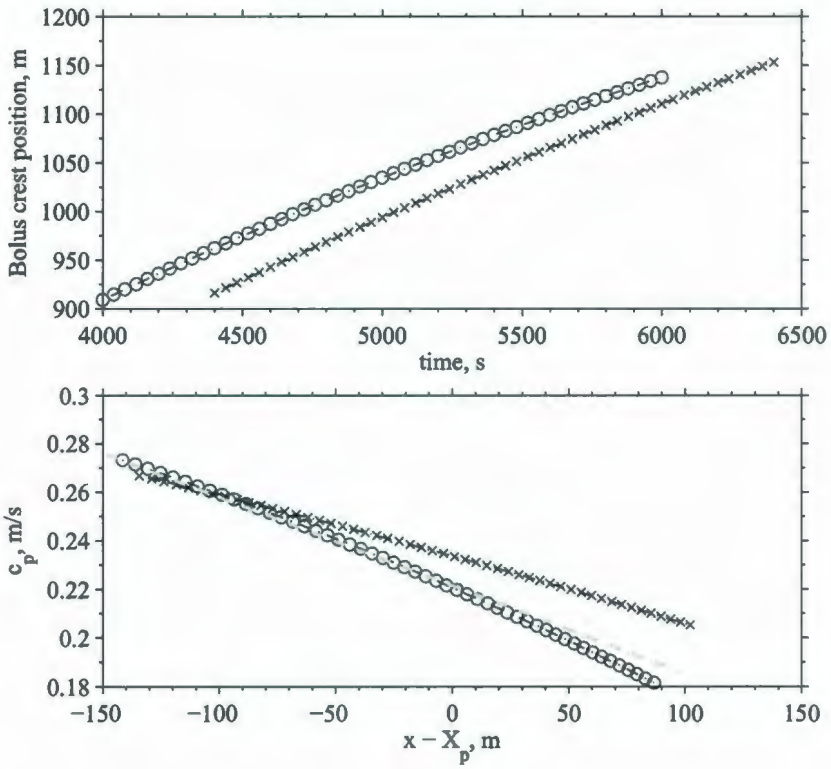

Figure 5.19. Wave-crest positions as function of time (top), and phase speed as function of distance traveled (bottom) for the first (o) and second boluses (x). The distance is expressed relative to the point where the second layer is absent, X_p.

The rate of the maximum density decrease is the same for both boluses which means that the mechanism of the decay is the same and does not depend on the particular bolus properties.

5.4.2 Decay of boluses

Figure 5.21 shows how the amplitude and characteristic length of the first bolus change as it propagates upslope. The amplitude and characteristic wavelength of the bolus decay linearly such that the aspect ration of the bolus is almost constant and equal to 0.6. After the boluses pass the point X_p the aspect ratio decays and reaches 0.4. The last stage of the bolus decay is marked by rapid decay in wavelength and thus aspect ratio again rises to its original value.

An important nondimensional number for ISWs is the ratio of the local phase speed to

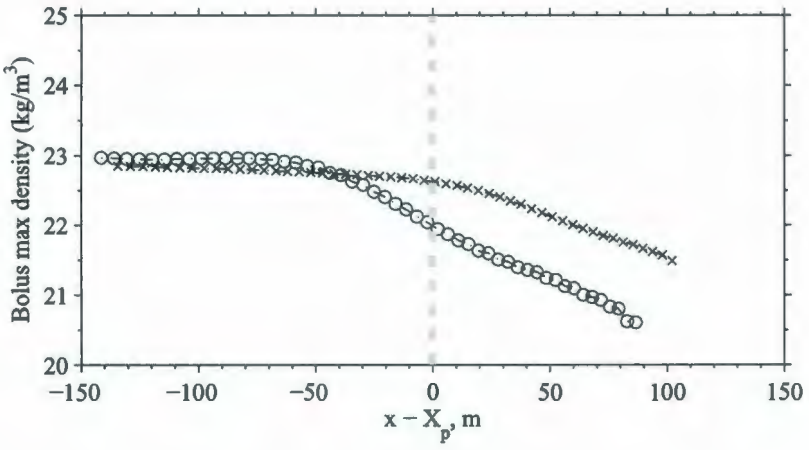

Figure 5.20. The maximum density inside the trapped cores of the first (o) and second boluses (x) shown in Figure 5.19 as a function of the distance traveled by boluses relative to the slope-pycnocline intersection point X_t shown as vertical dashed line.

the maximum horizontal velocity inside the wave U_{max}/c_p [*Lamb*, 2003]. If somewhere inside the wave the orbital velocity is larger than the phase speed of the wave, *i. e.* the ratio $U_{max}/c_p > 1$, the convective instability and overturns are possible. Let us plot this ratio for the first two boluses considered here, Figure 5.22. As can be seen, the ratio for both boluses is larger than unity and grows from 1.1 to 1.45 for the leading bolus and to 1.2 for the second bolus. This means that the convective instabilities are likely inside the bolus trapped cores and indeed happen as is evident from Figure 5.14.

Now we consider the energy of the two first boluses. The first bolus has initial energy 15 KJ/m which is approximately half of the energy of the incident IW of depression ($E_0 = 30.53$ KJ/m), the second bolus has the initial energy of around 7.00 KJ/m. After the short growth during the transition phase, energies of the first and second boluses decrease linearly with distance traveled by a bolus with rates 100 W/m and 66.80 W/m correspondingly (Figure 5.23, top panel). After boluses pass the point where the lower layer is absent, (X_p), the decay rates change and the energy of the boluses decreases linearly again with the rate of 36.60 W/m. *Klymak and Moum* [2003] calculated the rate of bolus decay from chameleon profiles and from observations of near bottom velocities to be $1 - 2$ W/m and

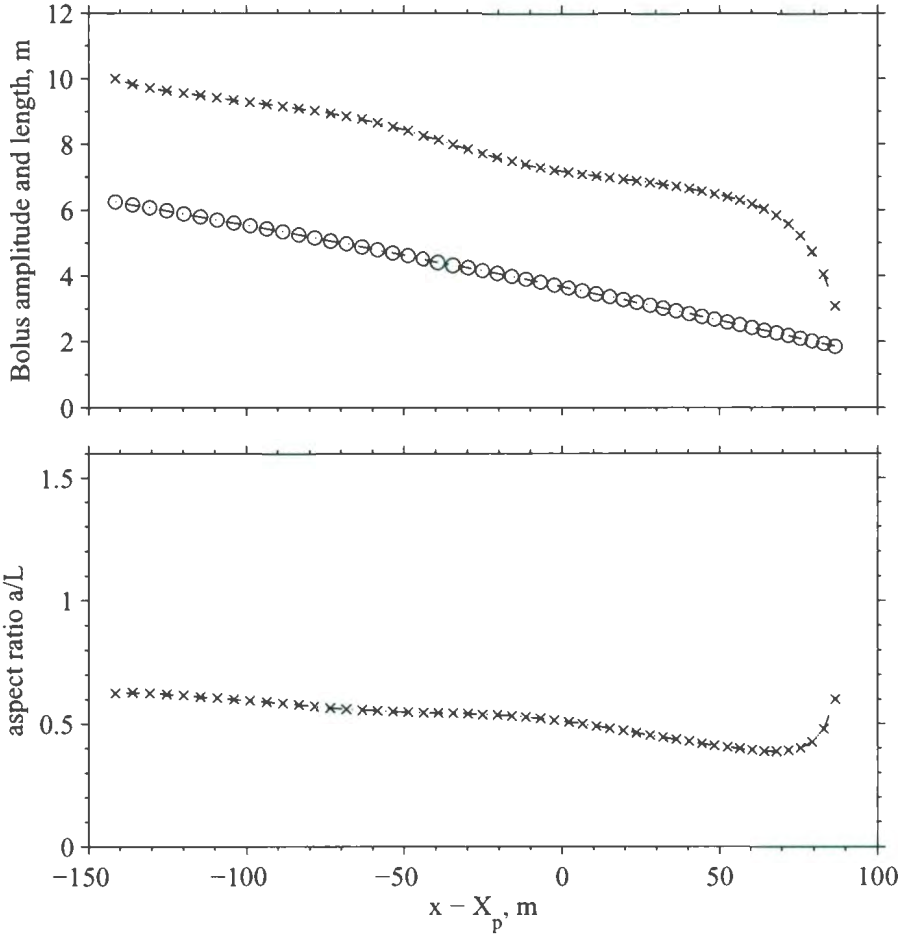

Figure 5.21. The amplitude (o) and characteristic length (x) of the first bolus as a function of distance traveled (top panel). The aspect ratio of the first bolus as a function of distance traveled (bottom panel).

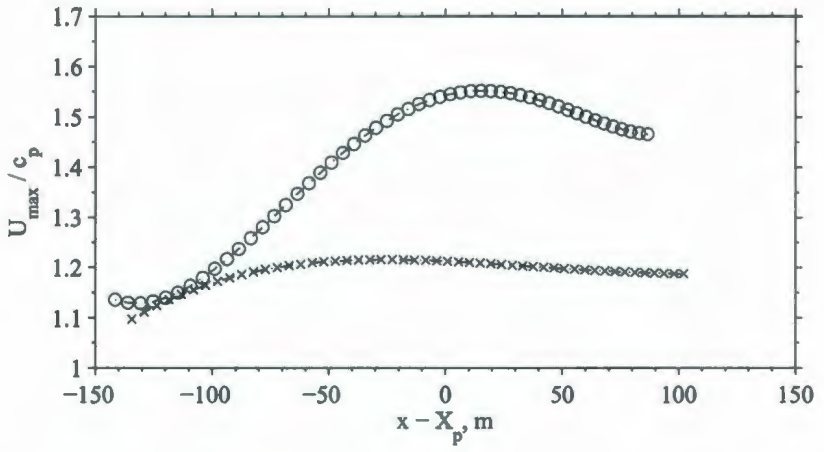

Figure 5.22. The ratio of the maximum velocity inside the bolus core to the local phase speed of the first (o) and second bolus (x) as a function of the distance traveled.

concluded that it is too low for the bolus to dissipate before reaching the shore and thus the bolus should break at some location further upslope. Here, the numerical simulations show that the energy decay rate of both boluses is significantly larger than that estimated by *Klymak and Moum* [2003]. Both boluses dissipate completely without breaking in agreement with our field observations presented in the previous chapter.

The ratio between the kinetic and available potential energies of the first bolus is shown in Figure 5.24. It is close to 1.2 at the beginning and remains constant for both boluses up to the point X_p. After the the point X_p the ratio increases to 5 for the first bolus and to 15 for the second bolus. *Lamb* [2007] investigated the energy partition in internal waves of depression and found that KE/APE ratio is close to unity for weakly nonlinear waves and ranges from 1.2 to 1.4 for strongly nonlinear waves. *Klymak and Moum* [2003] observed waves of elevation propagating up the Oregon shelf and estimated the ratio KE/APE at one location on a slope in the range $1.8 - 2$.

It is interesting to note that the linear decay of the amplitude, wavelength and phase speed was observed in the field study of *Bourgault et al.* [2007] where the leading bolus was tracked. The constancy of the bolus aspect ratio was also documented during this study. The change in the energy decay rates and bolus aspect ratio after the bolus passes

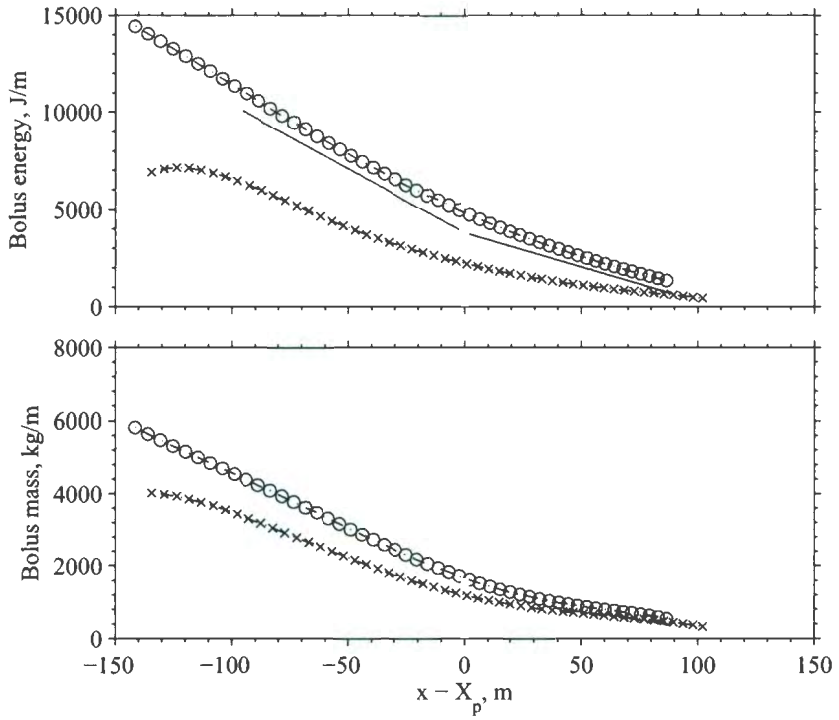

Figure 5.23. The energy (top) and mass (bottom) of the first (o) and second (x) boluses as a function of the distance traveled. The distance is expressed relative to the point X_p where the second layer is absent (also shown as a vertical dashed line). The straight lines on the top panel are the best fits for the energy decay rate before and after passage of the point X_p.

the point where the lower layer had vanished, X_p, was not observed because this point was not reached during the field study owing to instrumentation limitations.

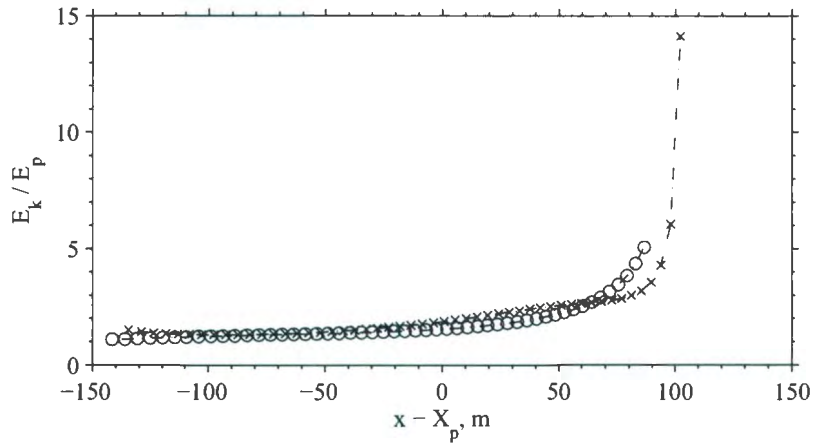

Figure 5.24. The ratio of the kinetic and available potential energy for the first (o) and second bolus (x) as a function of the distance traveled.

The portion of the incident wave energy which is transmitted towards the slope can be estimated using the parametrization proposed by *Bourgault et al.* [2007]. For the case of the incident wave characterized by the Iribarren number $\xi = 0.1$ the reflectance coefficient estimated from Equation 2.45 is $R = 0.3$.

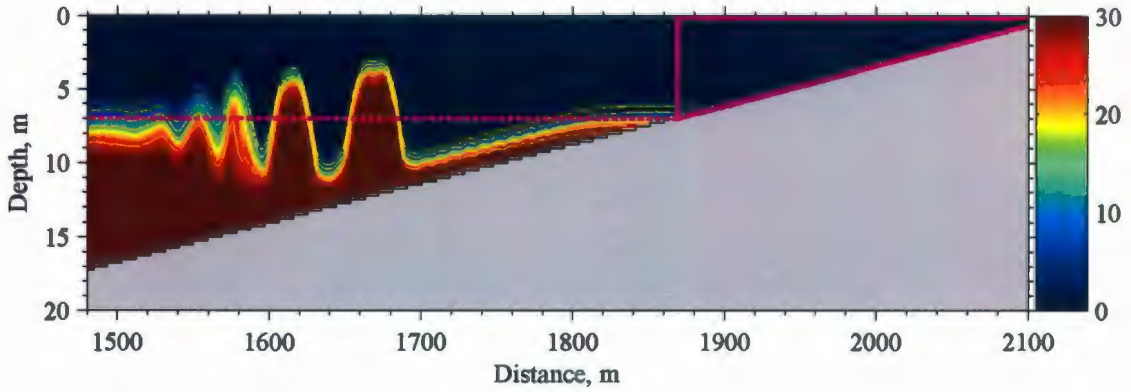

Figure 5.25. Sketch illustrating the area above the pycnocline which is used to calculate the mass of the subpycnocline water.

5.5 Available potential energy of ISWs as isolated features

In the previous section we have considered the energy of internal waves of depression and elevation. We showed that for both ISWs of depression and for boluses, the total energy decays linearly with the horizontal distance. This result is supported by our field observations [*Bourgault et al.*, 2007]. Recently, there has been a renewed interest is describing the energy content of a given ISW [*Moum et al.*, 2007]. The total energy is usually partitioned into kinetic and potential parts. As it was discussed in Section 2.4.4, not all potential energy is available for conversion to other forms of energy. Several studies have developed the concept of available potential energy (APE), [*Shepherd*, 1993, see for example], i.e. the part of potential energy that is available to other physical interactions. It follows that a much more useful invariant associated with the internal solitary waves is the pseudo-energy defined as the sum of kinetic and available potential energies [*Lamb*, 2007; *Shepherd*, 1993].

The definition of APE is well settled for large basins with closed or semi-enclosed boundaries. This assumes no mass flux across these boundaries. However, when the scale of the flow is small, it turns out that to calculate APE is harder because the background or reference state is not unique. Even more, the boundaries of the domain chosen for calculations are rather arbitrary. *Hebert* [1988] and recently *Lamb* [2007] considered that

in order to get the correct estimate of the APE of an isolated feature of the flow, one need to assume that the density structure outside the feature extents to infinity. Using symmetric density fields they suggest that the APE of the isolated feature is asymptotically reaching the constant 'true' APE value when the domain is extended to infinity. Here we present some theoretical considerations that show that this is not always the case. We elaborate on APE calculation for features which have non-symmetric density structure, with an objective to apply the same reasoning to ISWs of elevation propagating up the slope.

Below we consider a two-dimensional incompressible fluid which stably stratified background state is characterized by zero velocities and horizontally uniform density field $\rho_b(z)$. Let us introduce an "isolated feature" with the density field $\rho_w(x,z)$ that occupies the region $[-L_0, \quad L_0]$.

Let ρ be the density of the fluid in the physical space under consideration and $\widetilde{\rho}_L$ be the reference density, sorted within specified horizontal limits $[-L, \ L]$. Then

$$APE_L = E_p - E_p^{ref} = \int_V \rho\, g\, z\, dV - \int_V \widetilde{\rho}_L\, g\, z\, dV = g \int_V (\rho - \widetilde{\rho}_L)\, z\, dV. \tag{5.3}$$

This expression can be presented in a slightly different form using the available potential energy density defined as in *Lamb* [2008] (Equation 1.1):

$$APE_L = \int_V E_w dV, \qquad E_w = \rho_w\, g\, z, \tag{5.4}$$

where $\rho_w = \rho - \widetilde{\rho}_L$.

A convenient way to calculate a sorted reference density field was proposed by *Winters et al.* [1995]. Using the relationship $\widetilde{\rho}_L(z) = \rho(x, z^*)$, where $z^*(x,z)$ is the vertical position in the reference state of a fluid parcel at position (x,z) they presented APE in the following form:

$$APE_L = E_p - E_p^{ref} = g \int_V \rho(x,z)\,(z - z^*)\, dV. \tag{5.5}$$

To find the sorted density field (or alternatively z^*) associated with the state with minimum potential energy, the fluid is considered to consist of elementary volumes. Then the standard sorting algorithm can be applied to a one-dimensional array of fluid volumes and

as the result a monotonically increasing density vector is obtained. The original domain is then filled with these density values with the heaviest elements on the bottom and lighter elements on the top.

5.5.1 Hebert's symmetric example

Now we consider an example given in *Hebert* [1988]. Using a simple toy problem, he shows that the choice of limits plays a significant role for calculating APE of an isolated feature of the flow. In his example Hebert considered a region of fluid with constant buoyancy frequency N_0^2 imbedded into the region of different constant buoyancy frequency N^2. We will re-estate his result but for simplicity will consider just regions of constant densities. Figure 5.26 shows sketch of the Hebert's example on top panels, current example on the bottom panels. The "feature" of the flow is presented by the region with constant density ρ_0 of the length $2\,L_0$ surrounded from both sides by equal amount of fluid with constant density ρ such that the total length of the domain is $2\,L$. The sorted reference state has density $\widetilde{\rho}_L$. We will assume that the feature is denser than the surrounding far-field density, $\rho_0 > \rho$.

After adiabatic redistribution no other densities will be present in the sorted field except those that exist in the original state. Using mass conservation, the interface between layers, z^*, can be found:

$$4\,(L - L_0)\,h_0\rho + 4L_0h_0\rho_0 = 2L\left(\int_{-h_0}^{z^*}\rho_0\,dz + \int_{z^*}^{h_0}\rho\,dz\right) \tag{5.6}$$

Solving this equation for z^* gives

$$z^* = h_0\left(\frac{2L_0}{L} - 1\right). \tag{5.7}$$

The limiting cases are:

$$\text{(a)} \qquad \text{when} \quad L \to L_0 \qquad \frac{2L_0}{L} \to 2 \quad \text{and} \quad \mathrm{z^* \to h_0},$$

which means that the whole domain will be occupied by the fluid with density ρ_0;

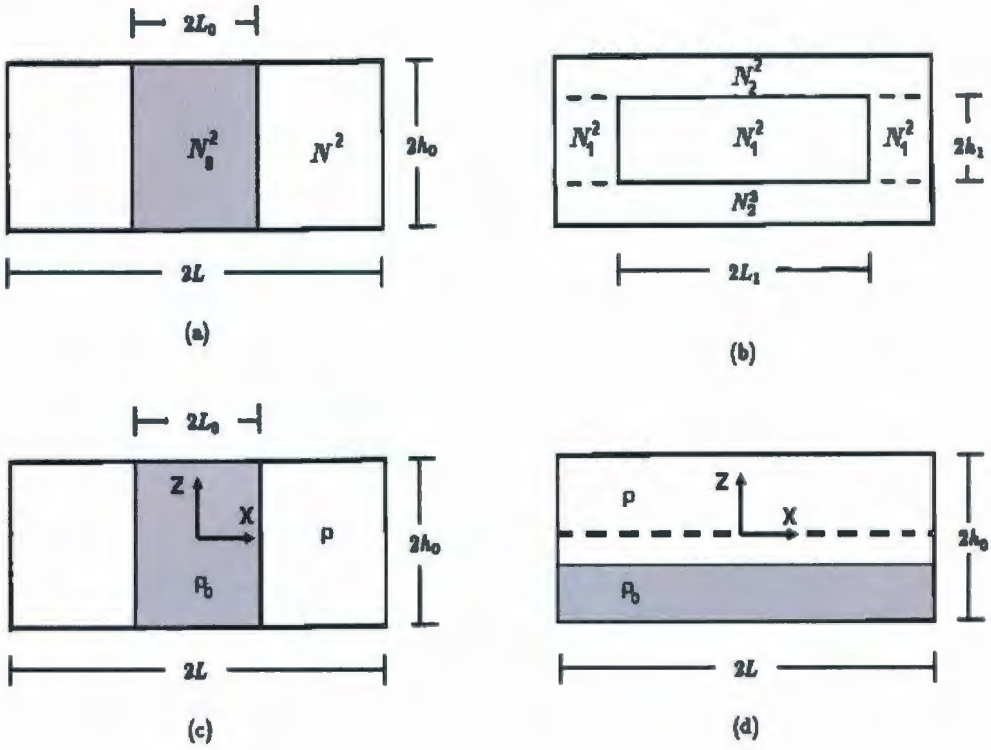

Figure 5.26. Sketches of the examples of APE calculation for a simple isolated feature. Panels (a) and (b) show the density in physical and reference states used by *Hebert* [1988]. Panels (c) and (d) represent density in physical and reference states used in the example below.

$$\text{(b)} \qquad \text{when} \quad L \to \infty \qquad \frac{2L_0}{L} \to 0 \quad \text{and} \quad z^* \to -h_0,$$

which means that the whole domain will be filled with the fluid of density ρ. Using Equation 5.3 the APE can be calculated as the difference in potential energies between the state under consideration and a sorted reference state. The coordinate system (centered in the middle of the isolated feature) is chosen in this example such that the potential energy of the original state is zero:

$$E_p = 2\,(L - L_0)\,g \int_{-h_0}^{h_0} \rho\, z\, dz + 2\,L_0\,g \int_{-h_0}^{h_0} \rho_0(x,z)\, z\, dz =$$

$$= 2\,(L - L_0)\,g\,\rho \left(\frac{h_0^2}{2} - \frac{(-h_0)^2}{2} \right) + 2\,L_0\,g\,\rho_0 \left(\frac{h_0^2}{2} - \frac{(-h_0)^2}{2} \right) = 0. \qquad (5.8)$$

The potential energy of the sorted reference state is then

$$E_p^{ref} = 2\,L\,g \int_{-h_0}^{z^*} \rho_0\, z\, dz + 2\,L\,g \int_{z^*}^{h_0} \rho\, z\, dz =$$

$$= 2\,L\,g\,\rho_0 \left(\frac{(z^*)^2}{2} - \frac{(-h_0)^2}{2} \right) + 2\,L\,g\,\rho \left(\frac{h_0^2}{2} - \frac{(z^*)^2}{2} \right) = g\,\delta\rho\,h_0^2\,L_0 \left(\frac{L_0}{L} - 1 \right), \quad (5.9)$$

where $\delta\rho = \rho_0 - \rho > 0$. Therefore the APE is

$$APE = E_p - E_p^{ref} = -E_p^{ref} = g\,\delta\rho\,h_0^2\,L_0\,(1 - L_0/L)\,. \quad (5.10)$$

This result is similar to the one obtained by *Hebert* [1988] in his example with continuous stratification, which reads

$$APE_G = \frac{2}{3}\rho\,h_0^3\,L_0\,N^2\,\left(1 - N_0^2/N^2\right)\,(1 - L_0/L)\,. \quad (5.11)$$

It follows from both Equations 5.10 and 5.11 that when the feature fills the extent of the domain

$$L \to L_0 \qquad L_0/L \to 1 \qquad APE \to 0.$$

On the other hand, if the domain containing the feature is extended to infinity:

$$L \to \infty \qquad L_0/L \to 0 \qquad APE \to g\,\delta\rho\,h_0^2\,L_0,$$

the APE of the isolated feature approaches a constant value. This example shows that when one is interested in calculating APE of a single isolated feature of the flow, extents of the domain should be chosen with care.

5.2.2 Modified asymmetric case of Hebert's example

The example shown above is symmetric, the isolated feature is surrounded from both sides by equal amount of fluid of equal density. What if we do not have exactly the same density on both sides of the feature? Let us analyze the following modified example. We consider the same geometry and the same feature but now it is surrounded by fluid with different

densities ρ_1 and ρ_2. We shall assume that $\rho_1 < \rho_0 < \rho_2$ and keep all density constant for simplicity. The sketch of this example is shown in Figure 5.27.

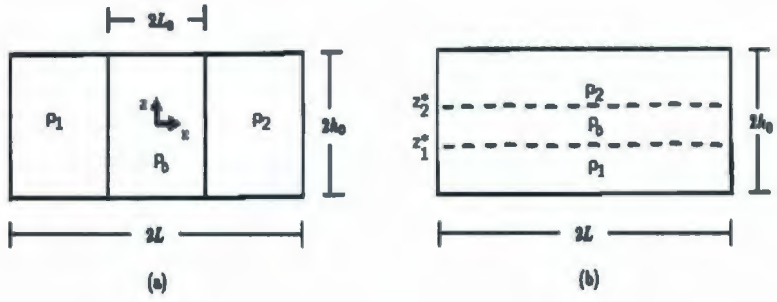

Figure 5.27. Sketch of the modified Hebert's example for APE calculation of a simple isolated feature.

The vertical positions of the interfaces between layers with different densities, z_1^* and z_2^*, corresponding to the state with the minimum potential energy may be found again from the conservation of mass during adiabatic redistribution:

$$(L - L_0)\,2h_0\,\rho_1 + 2\,L_0\,2h_0\,\rho_0 + (L - L_0)\,2h_0\,\rho_2 =$$

$$= 2L\int_{-h_0}^{z_1^*} \rho_2\,dz + 2L\int_{z_1^*}^{z_2^*} \rho_0\,dz + 2L\int_{z_2^*}^{h_0} \rho_1\,dz. \tag{5.12}$$

Solving for z_1^* and z_2^* gives

$$z_1^* = -h_0\,(L_0/L) \tag{5.13}$$

$$z_2^* = h_0\,(L_0/L). \tag{5.14}$$

When $L_0/L \to 0$ (that is, when the isolated feature shrinks in size) fluid with density ρ_1 tends to occupy the upper half-space, while fluid with density ρ_2 - the lower half-space. Alternatively, when $L_0/L \to 1$ the domain is filled entirely with fluid of density ρ_0.

As in the previous example, the potential energy of the initial state under consideration is zero. It can be shown that the potential energy of the reference state

$$E_p^{ref} = 2L\int_{-h_0}^{z_1^*} \rho_2\,z\,dz + 2L\int_{z_1^*}^{z_2^*} \rho_0\,z\,dz + 2L\int_{z_2^*}^{h_0} \rho_1\,z\,dz \tag{5.15}$$

and the APE is

$$APE = -E_p^{ref} = g\,L\,h_0^2\,(\rho_1 - \rho_2) + g\,\frac{L_0^2 h_0^2}{L}\,(\rho_2 - \rho_1)\,. \tag{5.16}$$

Now as we can see Equation 5.16 consists of two terms. The second term depends inversely on the domain width L and will decay as the domain is extended to infinity. The first term, however, depends on L linearly. Thus the limiting cases are:

$$\text{(a)} \qquad \text{when} \quad L \to L_0$$

$$\frac{L_0}{L} \to 1 \quad \text{and} \quad APE \to g\,L_0\,h_0^2\,(\rho_1 - \rho_2) + g\,L_0\,h_0^2\,(\rho_2 - \rho_1) \to 0.$$

$$\text{(b)} \qquad \text{when} \quad L \to \infty$$

$$\frac{L_0}{L} \to 0 \quad \text{and} \quad APE \to \infty.$$

Let us explain in details why APE goes to zero when $L \to L_0$ in both examples from Section 5.5.1 and 5.5.2 as well as in Hebert's example. If the "isolated feature" represented by a region of constant density (or by a stably stratified region with the constant buoyancy frequency as in Hebert's example) occupies the whole domain, no adiabatic sorting of the density field can lower its potential energy. Thus in all these examples when $L \to L_0$ the state under consideration and the reference state will be identical. So the difference between potential energies of the initial state and sorted state will be zero. But what if the feature is something more complicated than a region of constant density or a region with a stable stratification with the constant buoyancy frequency? In this case APE of the feature even with $L = L_0$ will not be zero. And, as it was shown in the example above, if the far-field density profiles are not trivial, APE will not converge to any reasonable value when the domain is extended to infinity.

5.5.3 Lamb's symmetric example

Recently, *Lamb* [2007] revisited the problem and, following *Hebert* [1988] showed that the APE of the "isolated feature" depends on the limits of integration. However, again like

Hebert, he considered a symmetric situation with a constant far-field density profile. A two layer fluid with densities ρ_1 and $\rho_1 + \triangle\rho$ contains an isolated feature presented by a quare well centered at zero. The right hand side of Figure 5.28 (a) shows the sketch of the Lamb's example. While Lamb performed his calculations only in the positive horizontal half-space, his example is actually half of the symmetric case depicted in Figure 5.28.

Let us choose the coordinate system that centers in the middle of the isolated feature and z-axis points upward with zero at the bottom. Mass conservation allows us to find the position of the interface in the reference state, z^*:

$$z^* = z_0 - \frac{\lambda}{L}a. \tag{5.17}$$

This expression shows that when $L \to \infty$ the position of the interface corresponding to the sorted state approaches the position of interface at the far-field. Following *Lamb* [2008] we shall calculate APE using the available potential energy density E_w defined by Equation 5.4. Looking at the density difference between the state under consideration and the reference state, shown in Figure 5.28, we can write the available potential energy density as:

$$E_w(x,z) = \begin{cases} g\triangle\rho z & \text{if} \quad z^* < z < z_0 \quad \text{and} \quad -L < x < -\lambda \\ -g\triangle\rho z & \text{if} \quad z_0 - a < z < z^* \quad \text{and} \quad -\lambda < x < \lambda \\ g\triangle\rho z & \text{if} \quad z* < z < z_0 \quad \text{and} \quad \lambda < x < L \end{cases} \tag{5.18}$$

The volume-integrated APE is then

$$APE = \int_{-L}^{-\lambda}\int_{z^*}^{z_0} g\triangle\rho z\, dx\, dz - \int_{-\lambda}^{\lambda}\int_{z_0-a}^{z^*} g\triangle\rho z\, dx\, dz + \int_{\lambda}^{L}\int_{z^*}^{z_0} g\triangle\rho z\, dx\, dz. \tag{5.19}$$

After some algebra it can be written as

$$APE = 2\,g\triangle\rho L\left(\frac{z_0^2}{2} - \frac{z^*}{2}\right) - 2\,g\triangle\rho\lambda\left[\frac{z_0^2}{2} - \frac{(z_0-a)^2}{2}\right],$$

which after substitution of z^* from 5.17 takes the form:

$$APE = g\triangle\rho\lambda a^2\left(1 - \frac{\lambda}{L}\right). \tag{5.20}$$

Let us examine Lamb's final result for this example (Lamb's Equation 3.15):

$$APE_L = g\frac{\triangle\rho}{2}\left(\lambda a^2 - L a_L^2\right). \tag{5.21}$$

Let us substitute here the expression for a_L, following from the mass conservation $\lambda a = a_L L$ (Lamb's equation 3.8):

$$APE_L = g\frac{\triangle\rho}{2}\left(\lambda a^2 - L\left(\frac{\lambda a}{L}\right)^2\right) = g\frac{\triangle\rho}{2}a^2\lambda\left(1-\frac{\lambda}{L}\right). \tag{5.22}$$

As it follows from the comparison of Equations 5.20 and 5.22, the result of the example presented here differs by a factor of two. Let us consider the limiting cases. When $L \to \infty$, the second term in Equation 5.22 vanishes and APE reaches constant value. On the other hand, when $L \to \lambda$ APE tends to zero. We should emphasize again that this is only because the "isolated feature" is nothing more than a stably stratified region. If we would have a feature with an internal structure, APE calculated within fixed limits $L = \lambda$ won't be zero. More to that, as example 5.1.2 shows, if the density field on both sides of the isolated feature is non-uniform, available potential energy calculated within these limits has more sense than one calculated with the domain been extended to infinity. We shall illustrate this using the same example, but now let us take different far-field density profiles at left and right side of the isolated feature. This is the case when one deals with APE for internal waves of elevation propagating on a slope.

5.5.4 Modified asymmetric Lamb's example

Let us consider the density configuration as shown in Figure 5.29. This figure shows density field of the state under consideration and density difference between this state and sorted reference state. Mass conservation leads to the expression for the interface position in the sorted state:

$$z^* = z_0 - \frac{\lambda}{L}a - \frac{\triangle z_0}{2}\left(1-\frac{\lambda}{L}\right). \tag{5.23}$$

This expression differs from Equation 5.17 by the last term which is zero if the density profiles at both sides are leveled. As it is also clear, this term is linear in L and when $L \rightarrow \infty$ the position of the interface at the reference state $z^* \rightarrow z_0 - \triangle z_0/2$. The available potential energy density in this case can be deduced from Figure 5.29:

$$E_w(x,z) = \begin{cases} -g\,\triangle\rho\,z & \text{if} \quad z_0 - \triangle z_0 < z < z^* \quad \text{and} \quad -L < x < -\lambda \\ -g\,\triangle\rho\,z & \text{if} \quad z_0 - a < z < z^* \quad \text{and} \quad -\lambda < x < \lambda \\ g\,\triangle\rho\,z & \text{if} \quad z* < z < z_0 \quad \text{and} \quad \lambda < x < L \end{cases} \tag{5.24}$$

Thus the APE can be shown is equal to

$$APE = -\int_{-L}^{-\lambda}\int_{z_0-\triangle z_0}^{z^*} g\,\triangle\rho\,z\,dx\,dz - \int_{-\lambda}^{\lambda}\int_{z_0-a}^{z^*} g\,\triangle\rho\,z\,dx\,dz + \int_{\lambda}^{L}\int_{z^*}^{z_0} g\,\triangle\rho\,z\,dx\,dz. \tag{5.25}$$

After some calculations, it takes the form:

$$APE = g\,\triangle\rho\left[a^2\,\lambda - \triangle z_0\,a\,\lambda\right]\left(1 - \frac{\lambda}{L}\right) + g\,\frac{\triangle\rho\,(\triangle z_0)^2}{4}\,L\left[1 - \frac{\lambda^2}{L^2}\right] \tag{5.26}$$

The first term has the familiar form and tends to the constant value when $L \rightarrow \infty$ and tends to zero when $L \rightarrow \lambda$, but the second term needs a special attention. It converges to zero when $L \rightarrow \lambda$, but unlike the first term it depends on L linearly when the extents of the domain go to infinity. So the APE in the limit $L \rightarrow \infty$ does not reach the constant value, but also increases to infinity.

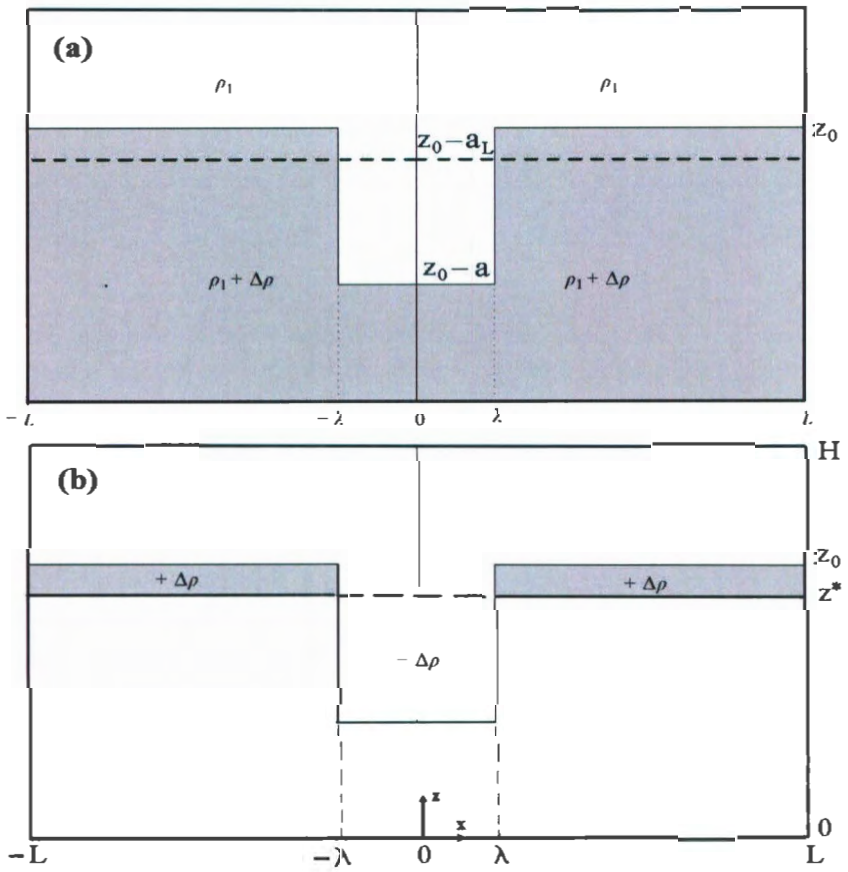

Figure 5.28. Sketch of the symmetric example for calculation APE of simple isolated feature following *Lamb* [2008]. (a) shows the symmetric example, considered originally in *Lamb* [2008]. The two-layer fluid consists of two layers with densities ρ_1 and $\rho_1 + \triangle\rho$ for upper and lower layer respectively. The vertical position of the interface between layers in the sorted reference state, z^*, is shown by the dashed line. This position has an offset, a_L, with respect to the undisturbed density structure z_0. A symmetric isolated disturbance is represented by a square well with amplitude a filled with a fluid with lower density. Panel (b) shows the density difference between the state under consideration and the sorted reference state.

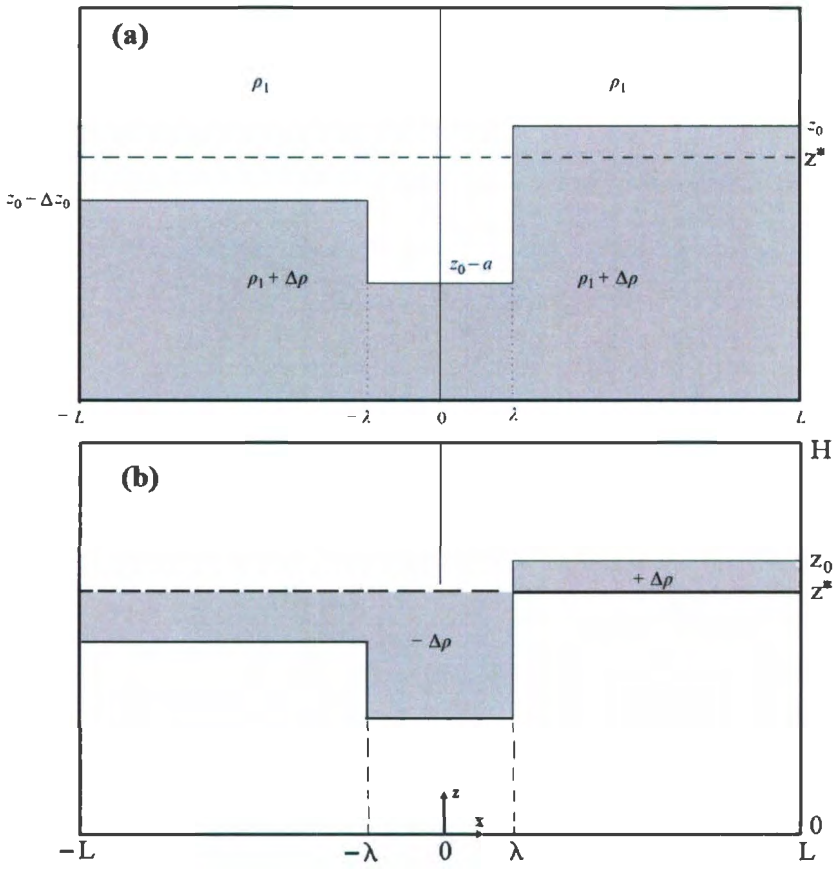

Figure 5.29. Sketch of the modified Lamb's example for APE calculation of simple isolated feature. Description is the same as for Figure 5.28, except the isolated feature is not symmetric.

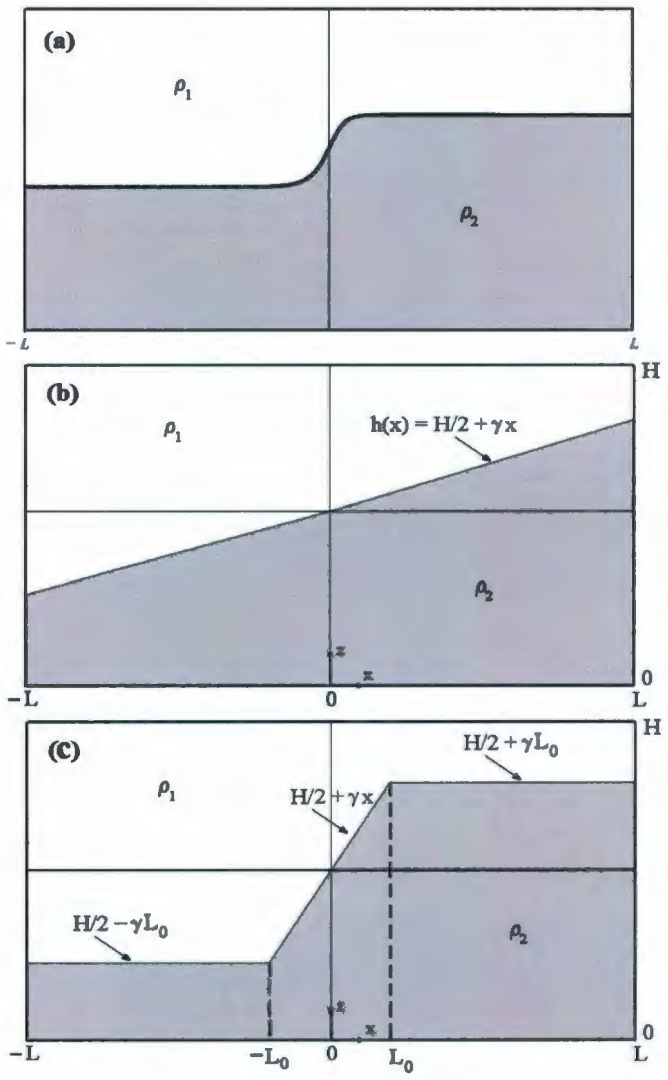

Figure 5.30. Geometry and the density structure used in the example for APE calculation of an internal bore simple model. Panel (a) shows the the sketch of an internal bore in the two-layer fluid. Panel (b) shows the density field of the internal bore approximated by a linear function. Panel (c) shows the full density field under consideration when the extents of the domain tend to infinity. vspace0.5cm

5.5.5 The available potential energy of an internal bore

In all examples presented above, an "isolated feature" did not have internal structure, it was presented either by the region of constant density or constant stratification. Let us consider another example, which is closer to the real oceanic problems. We consider the simplified model of the internal bore. The sketch of this example is shown in Figure 5.30. Panel (a) of this figure shows the sketch of the internal bore in a two layer fluid ($\rho_2 > \rho_1$) in the moving frame of reference, where the flow is stationary. Panel (b) shows the central part of the bore, presented for simplicity as a region with linearly tilted interface. Panel (c) shows the internal bore imbedded into a larger domain. As it is clear form the picture, far-field density profiles on the left and on the right of the bore are different. Let us show that the APE of the internal bore also increases to infinity when the extents of the domain go to infinity.

Let us assume first that the linearly-sloped part of the internal bore occupies the whole domain, Figure 5.30b. The position of the interface in the sorted reference state is located at depth $z^* = H/2$. The potential energy of the sorted reference state is just

$$E_p^{ref} = \frac{1}{4} g\, \rho_1 H^2\, L + \frac{3}{4} g\, \rho_2 H^2\, L, \tag{5.27}$$

Thus the APE in this case is

$$APE = g\, \triangle\rho \frac{\gamma^2 L^3}{3}. \tag{5.28}$$

Let us note that the APE, as in all previous examples, is quadratic in disturbance (here it is an angle of the interface tilt). Now, if the APE, calculated in this fixed horizontal limits does not represent the real value of the APE of the isolated disturbance, as suggested by *Hebert* [1988] and *Lamb* [2008], let us try to extend the horizontal limits by expanding the domain to the left and to the right from the isolated feature. As the result, we will have the

density field shown in Figure 5.30c. The available energy density would be

$$E_w(x,z) = \begin{cases} -g\,\triangle\rho\, z & \text{if} \quad \frac{H}{2} - \gamma\, L_0 < z < \frac{H}{2} \quad \text{and} \quad -L < x < -L_0 \\ -g\,\triangle\rho\, z & \text{if} \quad \frac{H}{2} + \gamma\, x < z < \frac{H}{2} \quad \text{and} \quad -L_0 < x < 0 \\ g\,\triangle\rho\, z & \text{if} \quad \frac{H}{2} < z < \frac{H}{2} + \gamma\, x \quad \text{and} \quad 0 < x < L_0 \\ g\,\triangle\rho\, z & \text{if} \quad \frac{H}{2} < z < \frac{H}{2} + \gamma\, L_0 \quad \text{and} \quad L_0 < x < L \end{cases} \tag{5.29}$$

The volume-integrated APE is then

$$APE = -\int_{-L}^{-L_0}\int_{\frac{H}{2}-\gamma L_0}^{H/2} g\,\triangle\rho\, z\, dx\, dz - \int_{-L_0}^{0}\int_{\frac{H}{2}+\gamma x}^{H/2} g\,\triangle\rho\, z\, dx\, dz +$$

$$+\int_{0}^{L_0}\int_{H/2}^{\frac{H}{2}+\gamma x} g\,\triangle\rho\, z\, dx\, dz + \int_{L_0}^{L}\int_{H/2}^{\frac{H}{2}+\gamma x} g\,\triangle\rho\, z\, dx\, dz. \tag{5.30}$$

Combing the second and the third terms we get

$$APE = -\int_{-L}^{-L_0}\int_{\frac{H}{2}-\gamma L_0}^{H/2} g\,\triangle\rho\, z\, dx\, dz + + \int_{L_0}^{L}\int_{H/2}^{\frac{H}{2}+\gamma L_0} g\,\triangle\rho\, z\, dx\, dz +$$

$$+\int_{-L_0}^{L_0}\int_{H/2}^{\frac{H}{2}+\gamma x} g\,\triangle\rho\, z\, dx\, dz. \tag{5.31}$$

The APE for this case after some tedious calculations is

$$APE = g\,\triangle\rho\gamma^2 L_0^3\left[\frac{L}{L_0} - \frac{2}{3}\right]. \tag{5.32}$$

When $L \to L_0$, the APE does not converge to zero, as in the examples from Sections 5.5.1 and 5.5.3 but, instead, it tends to the constant value which is the value of the APE without extension of the domain:

$$\frac{L}{L_0} \to 1, \quad \left[\frac{L}{L_0} - \frac{2}{3}\right] \to \frac{1}{3} \quad \text{and} \quad \text{APE} \to g\,\triangle\rho\frac{\gamma^2 L^3}{3}.$$

On then other hand, when $L \to \infty$

$$\frac{L}{L_0} \to \infty, \quad \left[\frac{L}{L_0} - \frac{2}{3}\right] \to \infty \quad \textit{and} \quad \text{APE} \to \infty.$$

This example shows that when we are interested in calculating the APE for an isolated feature, the extension of the domain is not giving the correct value unless the feature is symmetric and imbedded into the domain with the same density profiles at both sides of the isolated feature. This can be understood from the following considerations. Let us return to the basic definition of the APE as the difference between potential energies of the state under consideration and the reference state, APE $= E_p - E_p^{ref}$. It is clear that the regions with flat isopycnals do not contribute to the APE, but the difference between potential energies of these regions contribute to the increase in the potential energy of the reference state. Thus the APE increases linearly with the width of the domain. As it follows from examples in Sections 5.5.1 - 5.5.5 the calculations of the APE with the available potential energy density E_w require the use of additional conservation law, namely the conservation of mass during the adiabatic sorting of density. It was discussed by *Shepherd* [1993] and cames from the non-canonical Hamiltonian structure of geophysical fluid dynamics.

5.5.6 Alternative formulations of available potential energy density

As it was already discussed in Chapter 2, the available potential energy density E_w has several disadvantages. We have discussed first two, namely the sign-variable form, depending of the sign of the density difference $\rho - \rho_{sort}$ and global nature of E_w.

Here we shall emphasize another potential drawback. The main ingredient for obtaining the reference state is the sorting of the density profile. In all examples above the assumption been used for the sorting was that it is adiabatic, i.e. the process is fully reversible and no other densities are created during re-stratification. It can be implemented numerically, but may be hard to follow in observations and in laboratory. Here we show that the use of the available potential energy density in the form given by Equation 2.57 may free us from the assumption that the density should be re-arranged in the adiabatic manner. It was noted by *Scotti et al.* [2006] that the derivation of the energy equation for the APE in this form requires only the assumption that the sorted density profile is stable and monotonic and that

$$\min(\widetilde{\rho}) \leq \min(\rho) < \max(\rho) \leq \max(\widetilde{\rho}).$$

Let us consider an example analogous to the one in Figure 5.30b, but now we generalize

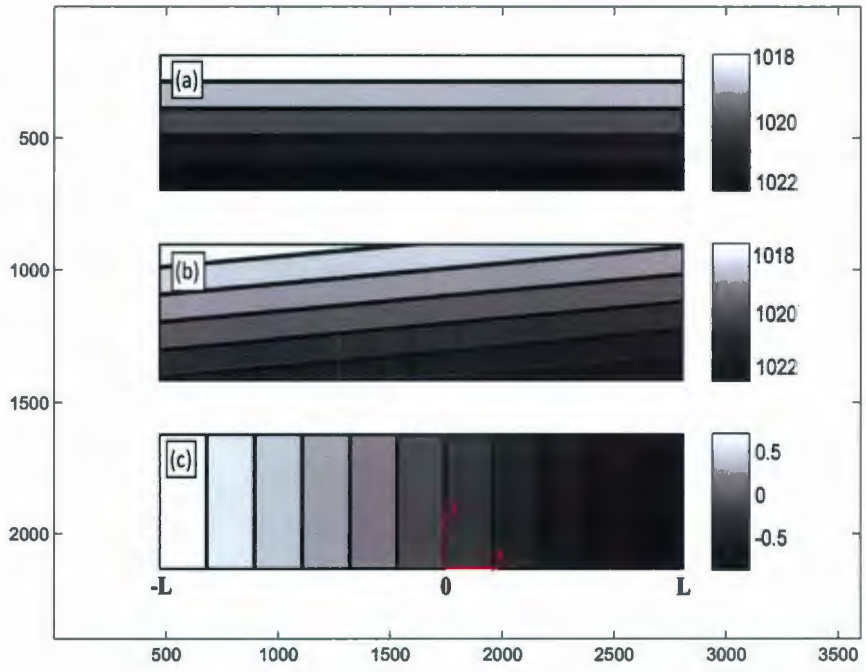

Figure 5.31. Sketch of the example for APE calculation of a simple isolated feature in continuously stratified fluid.

it to the fluid with continuous stratification. Let the background density profile be described by the equation

$$\rho_b(z) = \rho_0 \left(1 + \frac{\alpha\, z}{\rho_0}\right), \tag{5.33}$$

where $\alpha < 0$ is the constant density gradient with depth and ρ_0 is constant. Now let us tilt the fluid by a constant angle β around the line $x = 0$, as shown in Figure 5.31. The density field will take the form

$$\rho(x, z) = \rho_b(z - z^*(x)) = \rho_0 \left(1 + \frac{\alpha\, z + \beta\, x}{\rho_0}\right). \tag{5.34}$$

This example is quite simple because we immediately know the sorted density field, which is $\rho_{sort} = \rho_b$. The mass is also conserved during the density rearrangement. However, as it is also clear that in the density field $\rho(x, z)$ within domain $[(-L \quad L) \times (-H \quad 0)]$ there are regions with densities that are absent in sorted density profile $\rho_{sort}(z)$ (for example with densities $\rho = \rho_b + \alpha\beta x$ when $x > 0$ and densities $\rho = \rho_b - \alpha\beta x$ when $x < 0$). Therefore,

the process that leads from density stratification $\rho(x,z)$ to the horizontally homogeneous density stratification ρ_{sort} can not be considered as adiabatic, because only mixing can reduce the higher values of density present in the original profile.

Nevertheless, we will show that we still can calculate reasonable APE for this case using the available energy density in the form given by Equation 2.57. Following *Lamb* [2008] we present it in slightly different form:

$$E_a = g \int_z^{z^*} [\rho(s) - \rho(x,z)]\, ds, \tag{5.35}$$

where s is a dummy variable and $z^* = z^*(x,z)$ is the vertical distance required to move a fluid particle to reach the position in the reference state. The volume-integrated APE for this case is then

$$APE = g \int_{-L}^{L} \int_{-H}^{0} \left(\int_z^{z^*} [\rho(s) - \rho(x,z)]\, ds \right) dx\, dz =$$

$$= g \int_{-L}^{L} \int_{-H}^{0} \left(\int_z^{z^*} \left[\rho_0 \left(1 + \frac{\alpha\, s}{\rho_0} \right) - \rho_0 \left(1 + \frac{\alpha\, z + \beta\, x}{\rho_0} \right) \right] ds \right) dx\, dz =$$

$$= g \int_{-L}^{L} \int_{-H}^{0} \left(\int_z^{z^*} [\alpha(s - z) - \alpha\beta x]\, ds \right) dx\, dz =$$

$$= g \int_{-L}^{L} \int_{-H}^{0} \left(\frac{\alpha}{2}(z^{*2} - z^2) - \alpha z(z^* - z) - \alpha\beta x(z^* - z) \right) dx\, dz =$$

$$= g \int_{-L}^{L} \int_{-H}^{0} \left(\frac{\alpha}{2}(2\beta x + \beta^2 x^2) - \alpha z \beta x - \alpha \beta^2 x^2 \right) =$$

$$= g\,\alpha\beta H \left(\frac{L^2}{2} - \frac{L^2}{2} \right) - g\alpha\beta \int_{-L}^{L} \frac{H^2}{2}\, dx - \frac{g\alpha\beta H}{2} \left(\frac{L^3}{3} + \frac{L^3}{3} \right) =$$

$$= -\frac{g\,\alpha\beta^2 H L^3}{3}. \tag{5.36}$$

Since $\alpha < 0$, the APE is positive as expected. Equation 5.36 is quadratic in the disturbance (in β) and is similar to the APE for the two-layer case given by Equation 5.28. Therefore

Equation 5.36 shows that it is possible to obtain a valid expression for the APE without assumption of adiabatic sorting when using available energy density given by Equation 5.35.

Finally, we note that there are several other forms of available energy density proposed recently, for example *Tseng and Ferziger* [2001] who proposed to calculate the density of reference state through the probability density function

$$P(\widetilde{\rho}) = \frac{1}{V}\int_V \delta(\widetilde{\rho} - \rho)\, dV, \tag{5.37}$$

which defines the probability to find the density ρ to be inside the interval $\widetilde{\rho}$ and $\widetilde{\rho} + \delta\widetilde{\rho}$. They showed that the height of fluid of density ρ in the minimum potential energy state, $Z_r(\rho)$ can be calculated as

$$Z_r(\rho) = H\int_{\rho}^{\rho_M} P(\widetilde{\rho})\, d\widetilde{\rho}, \tag{5.38}$$

where ρ_M is the maximum density in the density profile. As the result, the reference potential energy can be expressed as

$$E_p^{ref} = g\,A\int_0^H \rho(Z_r) Z_r\, dZ_r, \tag{5.39}$$

where A is the horizontal cross section of the domain. The APE can be then calculated by subtracting Equation 5.39 from the total potential of the fluid.

5.5.7 APE of ISWs of depression and boluses

Let us now apply the method for calculation of APE to internal solitary waves. We will calculate APE with and without the spreading out the extents of the domain. First we present the derivation of the APE for internal solitary waves in two-layer fluid. This will give us a useful number for comparison. We assume that the wave of amplitude a_0 propagates in two-layer fluid with depths of the top layer h_1 and the bottom layer h_2 and densities ρ_1 and ρ_2, correspondingly. The total depth of the fluid is $2\,h_0$ and the horizontal extents occupied by the wave are $2\,L_0$. The density difference between layers is $\triangle\rho = \rho_2 - \rho_1 > 0$. Let us place the coordinate system at the interface between layers. The sorted reference state for this system will be the system of two horizontal homogeneous layers. It can be shown that,

for such coordinate system, centers of mass of each layer in the reference state are located at half-depths and thus the reference potential energy is easily derived to be

$$E_p^{ref} = g\left[\frac{\rho_1 h_1^2}{2} - \frac{\rho_2 h_2^2}{2}\right] 2\,L_0. \tag{5.40}$$

The total potential energy of the ISW under consideration is

$$E_p = g\int_{-L_0}^{L_0}\int_{-h_2}^{\eta(x)} \rho_2\, z\, dx\, dz + g\int_{-L_0}^{L_0}\int_{\eta(x)}^{h_1} \rho_1\, z\, dx\, dz =$$

$$= \frac{g(\triangle\rho)}{2}\int_{-L_0}^{L_0} \eta^2(x)\, dx + E_p^{ref}. \tag{5.41}$$

The available energy density is then

$$APE = \frac{g(\triangle\rho)}{2}\int_{-L_0}^{L_0} \eta^2(x)\, dx. \tag{5.42}$$

If one substitute $\eta(x) = a_0\,\mathrm{sech}^2(x - ct/L)$ Equation 5.42 in the limit $L_0 \to \infty$ will lead to the familiar formula 4.2 [see e.g. *Bourgault and Kelley*, 2003] for the half of the total energy of the solitary wave:

$$APE = E_0/2 = \frac{4}{3}\Delta\rho g a^2 L_w. \tag{5.43}$$

We now proceed from the simple theoretical examples for calculation of the APE for ISWs of depression and boluses obtained in numerical simulations. We shall take first an ISW of depression with $a_0 = 6$ m far from the slope. The distance between the wave crest and the beginning of the slope is 300 meters which is approximately 10 times larger than the the half-length of the wave. The displacements induced by the wave decay away from the wave crest and therefore density profiles taken on both sides of the wave are almost identical. We expect this case to be similar to the symmetrical examples presented by *Hebert* [1988] and *Lamb* [2008]. Indeed, Figure 5.32 shows that APE of the wave of depression converges rapidly to a constant value as we extend the domain.

On the other hand, as the middle panel in Figure 5.33 shows, when we extend the

domain in the case of bolus on the slope, the density structure of the left and of the right boundaries is different. We have shown above, that in this case APE grows linearly with the extents of the domain, as shown in Figure 5.33. This suggest that the extension of the domain chosen for density sorting will give erroneous result for APE of boluses. That is why in our calculations the extents of the domain for boluses were chosen fixed to include only the density field of the bolus.

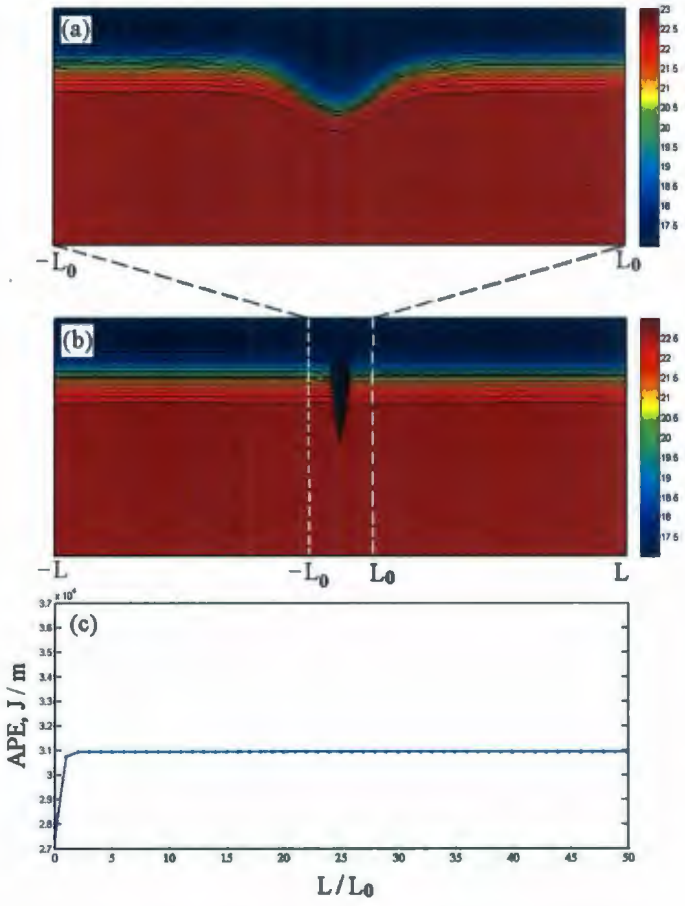

Figure 5.32. Density field corresponding to the ISW of depression without the extension of the domain, (a); density field with extension of the domain by 10 L_0 from both sides (b); APE of the ISW of depression vs the length of the domain scaled by the initial domain width, (c).

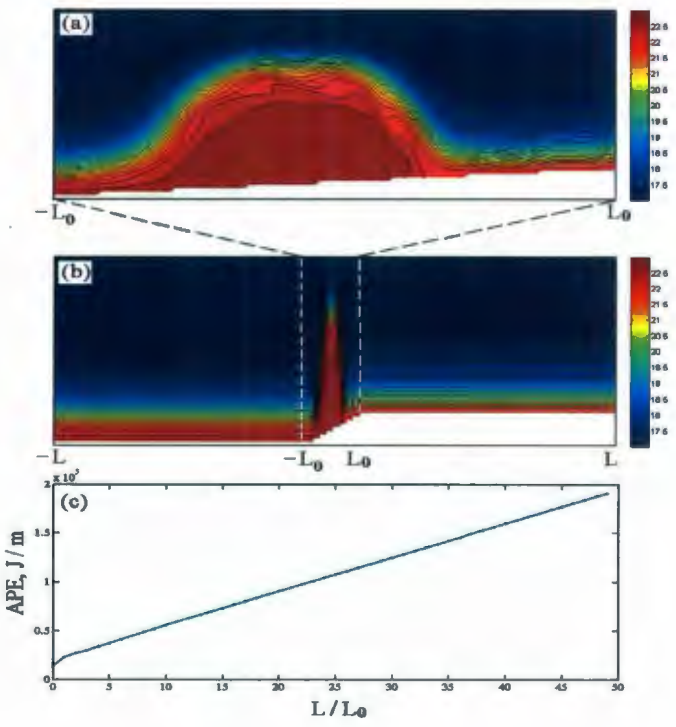

Figure 5.33. Density field corresponding to bolus without the extension of the domain, (a); density field with extension of the domain by 10 L_0 from both sides (b); APE of bolus vs the length of the domain scaled by the initial domain width, (c).

5.5.8 Discussions

Available potential energy plays central role in the analysis of geophysical flows. In the case of internal waves it can be linked to mixing that irreversibly changes the potential energy of the fluid. The task of quantifying the amount of mixing caused by internal waves is of paramount importance. For these reasons, the APE calculation have been under study for more than several decades and as it can be concluded, still, there is no definitive recipe for the available potential energy suitable for all cases.

Here we investigated one aspect of APE calculations for a single "isolated feature". The proper choice of horizontal limits of the domain used for resorting to the minimum reference state is discussed following a number of examples with increasing complexity. It was suggested by *Hebert* [1988] that the horizontal limits of the domain should be extended to infinity for the APE to reach asymptotically a constant value. We have shown that it is only true if the "isolated feature" is symmetric and the density structure on both sides of the feature is exactly the same. This condition is unlikely to be fulfilled in practice and thus the method should be used with care for real life situations. In addition, the adiabatic density sorting can be applied also to a limited number of observations, because it is unlikely that the full 3D density field can be measured in any significant portion of the ocean. That is why sorting technique is exclusively applied to results of numerical simulation. In practice, it is more likely that some distant density profile that can be associated with the reference background field will be used for APE calculations.

5.6 Mass transport

5.6.1 A single internal wave case

Now we proceed with the description of the mass transport of the dense water caused by all boluses formed during the shoaling and/or breaking process of an incident single ISW of depression. A passive tracer is used to investigate the transport properties of boluses to the region above the undisturbed slope-pycnocline intersection. Position of the undisturbed pycnocline is shown in Figure 5.25 as a horizontal line and the area of interest, Ω, in which the mass of the subpycnocline water is calculated is shown schematically by a triangle. The mass of fluid which is located initially in the area Ω depends on the angle of the slope. For linear slopes considered in the present study it can be calculated as:

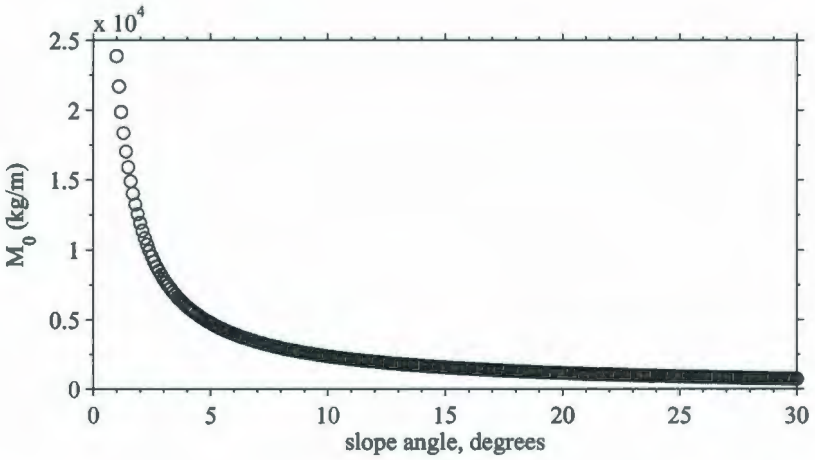

Figure 5.34. Mass of fluid initially located in the region Ω calculated using relation 5.44 (solid line) and calculated from numerical simulations (circules).

$$M_0(\gamma) = \int_\Omega \rho_1(x,z)\,dx\,dz = \frac{1}{2}\rho_1 h_1^2 \tan(90-\gamma). \tag{5.44}$$

This dependence is presented on Figure 5.34 and compared to the mass M_0 calculated during numerical simulations. Let us compare this amount of water to the mass of fluid displaced by the incident wave of depression, M_w, shown in Figure 3.9. It is evident that

small waves with amplitudes less than 5 m depress the amount of fluid equivalent to 8 % of the M_0 and less. However, as the slope angle increase, M_0 quickly decreases and the effect of the wave of depression may be significant.

The mass of the subpycnocline fluid brought to this region by boluses can be calculated as

$$M(t) = \int_{\Omega} \rho_s(x, z, t)\, dx\, dz, \tag{5.45}$$

where

$$\rho_s(x, z, t) = \rho(x, z, t) \qquad \text{if} \qquad C(x, z, t) \neq 0,$$

$$\rho_s(x, z, t) = 0 \qquad \text{if} \qquad C(x, z, t) = 0.$$

Figure 5.35(top) shows how the amount of the tracer brought above the pycnocline changes with the time during a single ISW shoaling. The number of peaks on this graph indicates the number of boluses which entered the area above the pycnocline. Figure 5.35(bottom panel) represents the mass of the subpycnocline fluid brought above the pycnocline per unit across shore distance. Both curves show identical behavior. The final values of the relative mass and tracer after the full dissipation of all boluses do not return to zero values. As illustrated in Figure 5.35, the mass and tracer reach some final steady state values $\mathrm{M_{mix}}$ and $\mathrm{C_{mix}}$. Although M_{mix} is very small $\mathcal{O}(1)$ kg/m, these values can serve as a measure of mixing intensity in the region Ω. Higher mixing intensity results in higher residual values of the mass and tracer. Time t_{max} between the moment when the first bolus enters region Ω and the time when the mass reaches the residual steady-state value $\mathrm{M_{mix}}$ can serve as a measure of the duration of bolus activity (Figure 5.35b).

The maximum of the mass versus time curve in Figure 5.35b represents the maximum amount of dense water transported by all boluses to the region Ω. It depends on properties of an incident ISW of depression and on the slope of the bottom, which influence the number of boluses generated during shoaling event and the strength of the backflow.

To elucidate this dependence, we plot the maximum mass of dense water, M, as a function of the Iribarren number ξ associated with the incident wave of depression for range $0 < \xi < 0.7$. Figure 5.36 shows the results of a number of numerical simulations in which the mass of the subpycnocline water brought above the level of the undisturbed

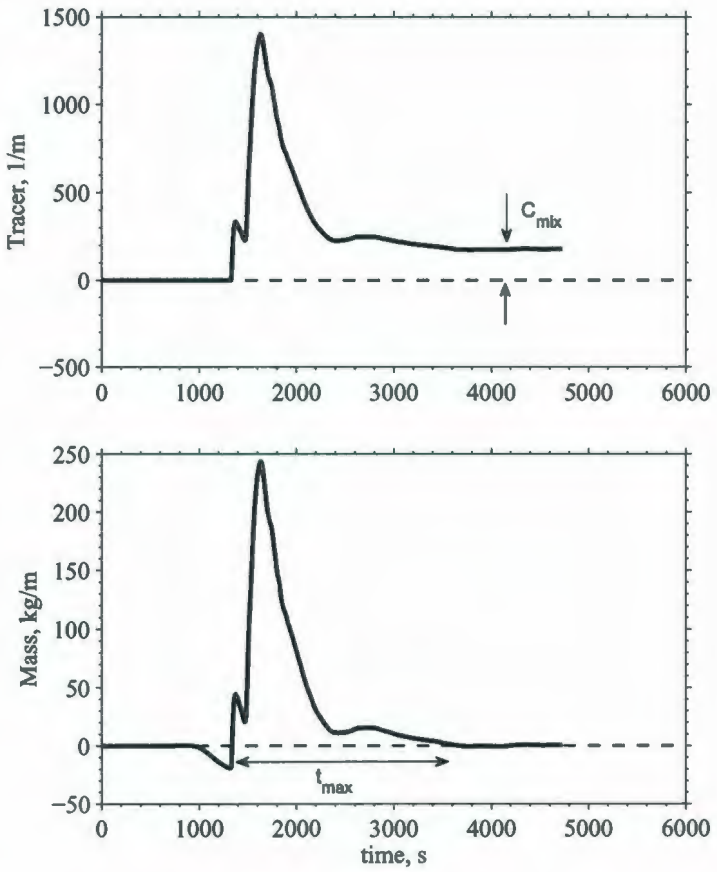

Figure 5.35. The amount of tracer (top) and mass of the dense fluid (bottom) brought above the level of the undisturbed pycnocline by all boluses generated by a single ISW with the Iribarren number $\xi_I = 0.2$. Residual steady state values of relative mass and tracer are M_{mix} and C_{mix}. t_{max} indicates time which the dense fluid has spent in the onshore region.

pycnocline is calculated for incident waves with amplitudes $a = 1.3, 3.3, 4.0, 6.0$ m. The slope of the bottom is varied in the range from $\gamma = 0.85$ to $\gamma = 20$ degrees.

For the small amplitude incident ISW with $a = 1.3$ m, the mass transport depends linearly on bottom slope for all slope values considered. For waves with amplitudes $a =$

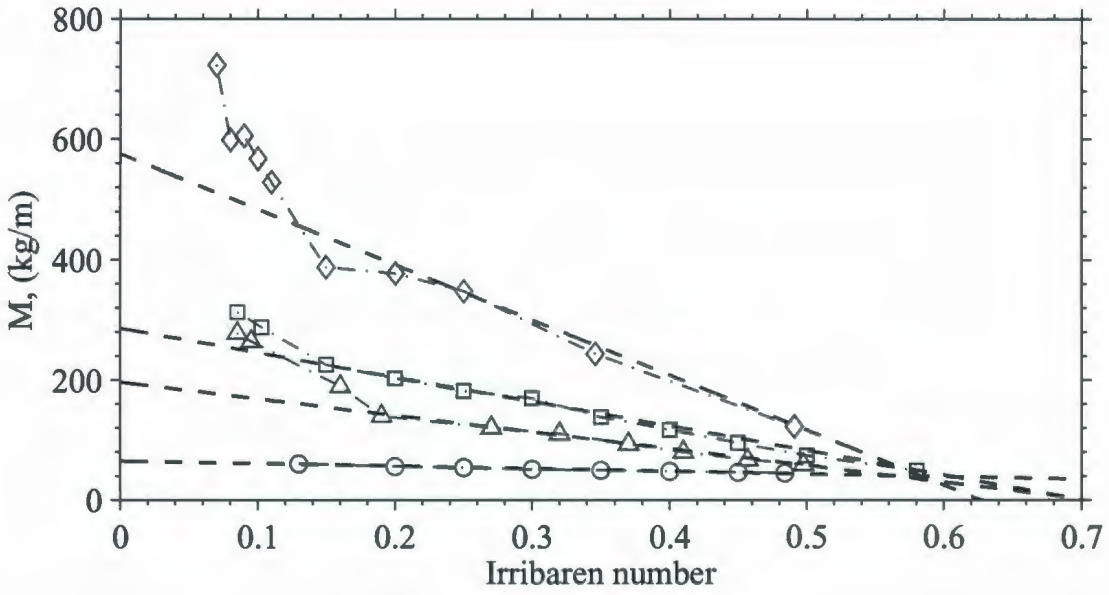

Figure 5.36. Mass of the subpycnocline water brought above the level of the undisturbed pycnocline vs the Iribarren number associated with an incident ISW of depression. The mass was calculated for incident ISWs with amplitudes $a = 5.9$ m (diamonds); $a = 4.0$ m (squares); $a = 3.3$ m (triangles) and $a = 1.3$ m (circles) shoaling over linear slopes with angles from $\gamma = 0.85$ to $\gamma = 11$ degrees. Solid lines are the best fits calculated using relation 5.46.

3.3, 4.0 and 6.0 m, it can be noted that the mass transport dependence on the Iribarren number can be divided into two distinct parts. For $0.2 < \xi < 0.6$ mass transport may be approximated by a linear function of Iribarren number. However, for $0 < \xi < 0.2$ it is characterized by nonlinear dependency. The lines of the best fits to the linear part appear to have slopes proportional to the square of the amplitude of the corresponding incident waves. They are calculated using the relationship

$$y(\xi) = -25.5(a_i)^2\xi + C_i, \tag{5.46}$$

where a_i = 1.3, 3.3, 4.0 and 6.0 m and corresponding constants are C_i = 65.00, 196.67, 286.68 and 575.81. This allows us to seek for the general formula using the new parameter a^2/ξ.

Figure 5.37 presents the mass transport as a function of a^2/ξ for all values of the Irribaren number considered. All points collapse on a single curve, which can be found from

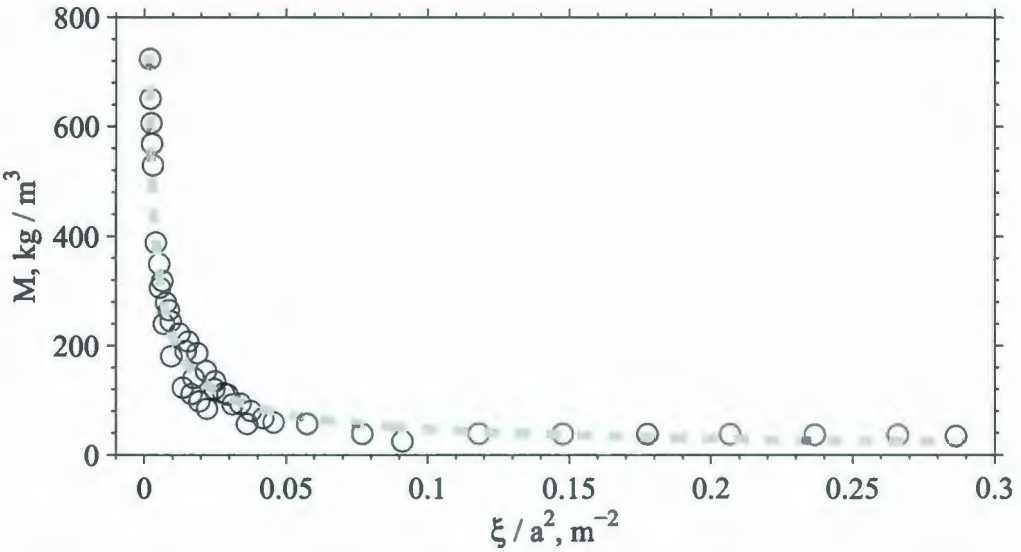

Figure 5.37. Mass of the subpycnocline water brought above the level of the undisturbed pycnocline as a function of parameter a^2/ξ. Gray dotted line is the best fit, described by Equation 5.47

the least-square best-fitting as

$$M = \rho_0 \left(\frac{C\, a^2}{\xi} \right)^{\ell}, \tag{5.47}$$

where $\ell = -\frac{2}{3} \pm 0.11$ and the dimensional constant $C = 0.0097$ m.

It is of interest that boluses with trapped cores were formed for waves with $a = 3.3, 4.0$ and 5.9 m when $\xi < 0.2$, corresponding to the region of nonlinear dependence of mass transport on the Iribarren number. For the incident wave with $a = 1.3$ m boluses with trapped cores are formed for all Iribarren numbers considered.

Figure 5.38(a) shows the net mass transport by boluses normalized by the mass associated with an incident ISW of depression M_w defined by Equation 3.21. It is apparent that the net mass transport by all boluses generated by a shoaling ISW with associated mass M_w decreases with the slope (or Iribarren number). For large Iribarren numbers $\xi \sim 0.5 - 1.5$ the net mass transport is no larger than 5 % of the mass associated with the incident ISW of depression independently of the amplitude of the initial ISW. Figure 5.38(b) compares

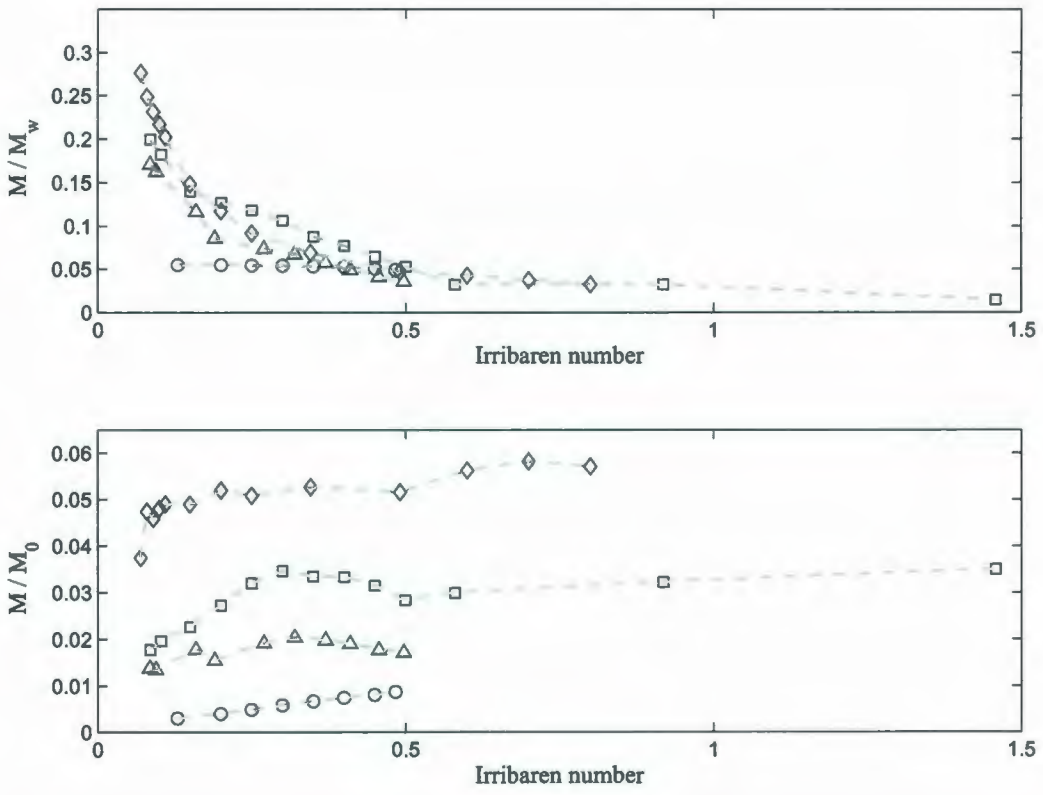

Figure 5.38. Mass of the subpycnocline water brought above the level of the undisturbed pycnocline normalized by the mass associated with an incident ISW of depression (top panel) and by the mass of water which was initially in the region Ω before the arrival of boluses (bottom panel). The mass is calculated for incident ISWs with amplitudes $a = 6.0$ m (triangles); $a = 4.0$ m (squares); $a = 3.3$ m (circles) and $a = 1.3$ m (diamonds) shoaling over linear slopes with angles from $\gamma = 0.85$ to $\gamma = 20$ degrees.

the net mass transport of all boluses to the amount of fluid, M_0, that is initially in the slope region Ω. For the range of parameters used in this study, the largest mass transport is calculated for boluses formed by the shoaling of ISW with amplitude $a = 6.0$ m over the slope of $\gamma = 7.6$ degrees. Those boluses bring the amount of water which is equivalent to 6 % of water mass initially in the slope region above pycnocline. Boluses generated by the incident ISW with amplitude $a = 4.0$ m have resulted in 4 % mass increase, boluses generated by ISW with $a = 3.3$ m brought 2 % and ones generated by ISW with $a = 1.3$ m have the smallest net mass transport of around 1 %, Figure 5.38(b). The amount of the sub-

pycnocline water brought upslope typically depends on a slope value only for small slopes. Referring to Figure 5.38(b) it can be observed that all curves reach a saturation value at Iribarren number $\xi \approx 0.5$. This means that the net mass transport does not depend on the slope for $\gamma > 6$ degrees.

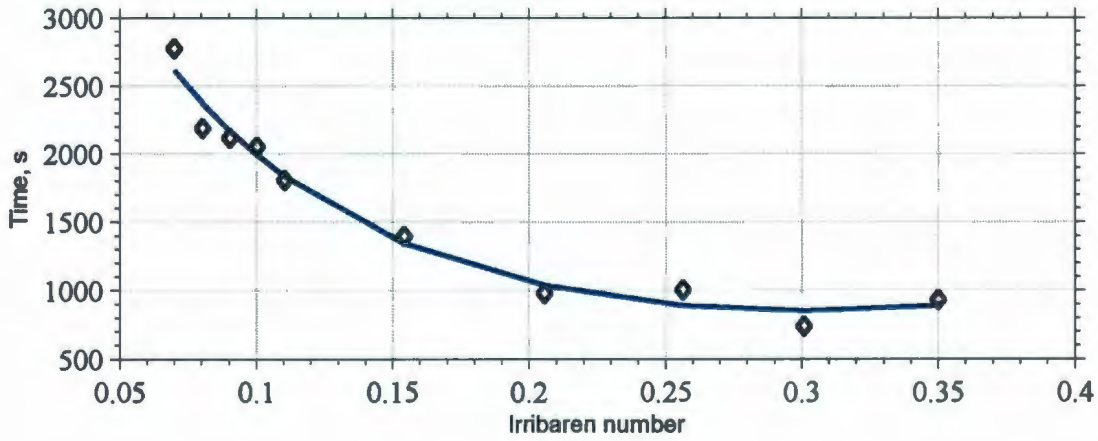

Figure 5.39. The time spent by boluses in the region above slope-pycnocline intersection *vs* the bottom slope.

An important question about the mass transport by boluses is for how long will the dense water from below pycnocline stay in the region above the slope-pycnocline intersection. *Butman et al.* [2006] in their field observations noted that the beam attenuation caused by the bolus activity remained for at least 1 – 2 hours. Figure 5.39 presents results from several numerical simulations during which the residence time defined in Figure 5.35 is measured for incident wave with amplitude $a = 4$ m. It shows that the time that the dense subpycnocline water spends in the surf region strongly depends on the slope angle. The best fit can be expressed by the analytic formula

$$t = t_0 \left(0.35 + e^{-16(\xi - 0.1)}\right), \tag{5.48}$$

where $t_0 = 1899$ s. The maximum time that boluses have spent in the region Ω is recorded to be 40 minutes.

5.6.2 Internal wave train case

The shoaling of an ISW wave train is shown to be a complex phenomenon [*Bourgault et al.*, 2007]. The study of the mass transport caused by an ISW wave train we start with making a simplification. We consider an idealized ISW wave train consisting of two identical ISWs with amplitude $a = 4$ m, placed one wavelength apart from each other. In this section we will use roman I and II superscripts to designate values corresponding to single ISW and two-wave ISW wave train.

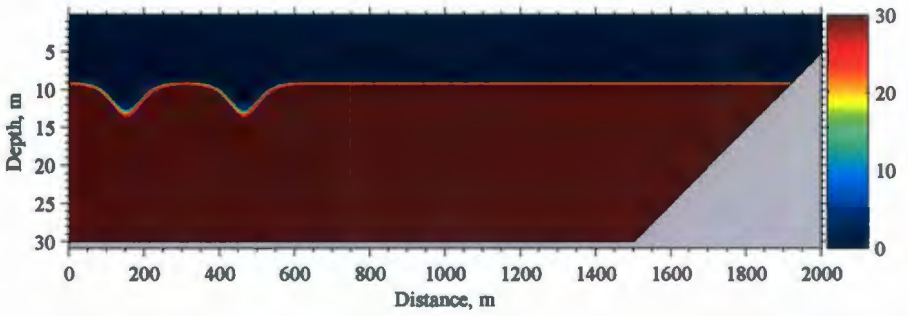

Figure 5.40. The initial tracer distribution for two waves.

The setup of numerical experiments remains the same as for the study of single ISW shoaling. The initial distribution of the tracer is shown in Figure 5.40. Two waves are propagating without signs of interaction with each other. Amplitudes, wavelengths and mass displaced by each wave remains constant during the propagation over the flat bottom portion of the domain. The shoaling of two waves, however, differs significantly from a single ISW case.

Figure 5.41 compares time series of the mass brought upslope by a single ISW and by two identical waves with amplitude $a = 4.0$ m characterizing by Iribarren number $\xi = 0.2$. These parameter values were chosen as a special case. As is clearly seen, although there are substantial differences in the time variations caused by the different number of generated

boluses, the net mass transport (the maximum of the mass vs time curve) for the single ISW $M^{I}_{net} = 2.25 \cdot 10^4$ kg m^{-1} and for two ISWs $M^{II}_{net} = 2.3 \cdot 10^4$ kg m^{-1} are very close.

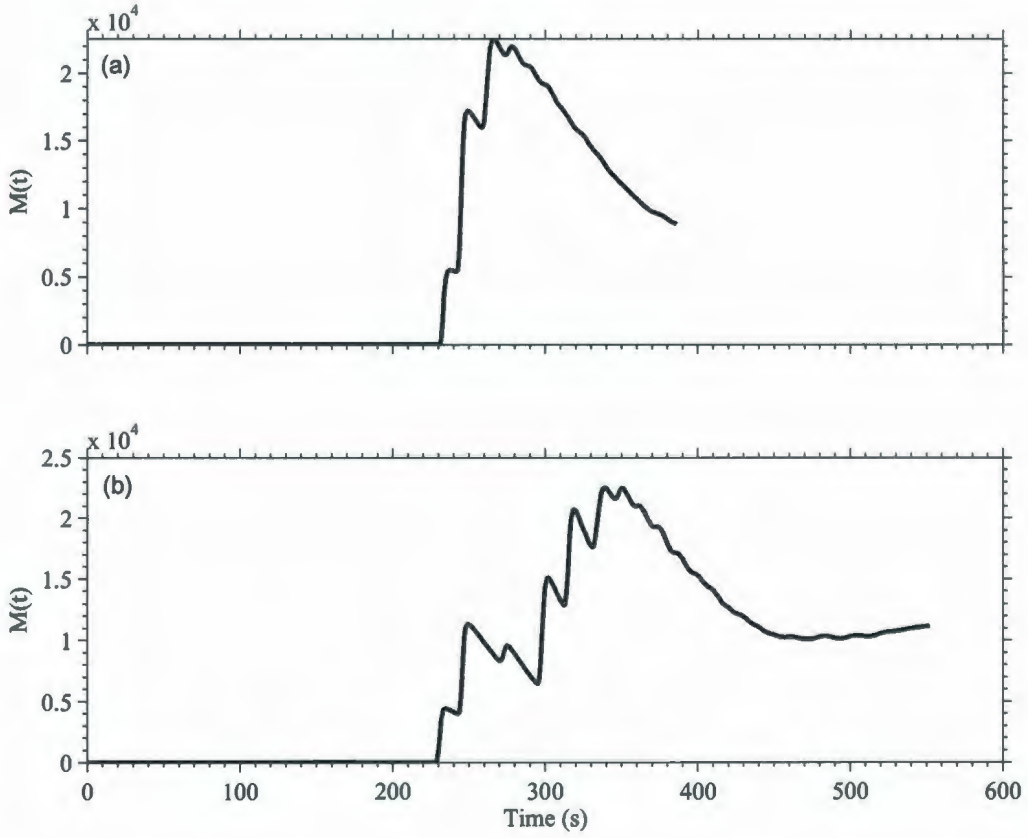

Figure 5.41. The amount of tracer brought above the pycnocline by a single ISW (a) and by two identical waves (b) vs time. The Iribarren number is $\xi_I = 0.2$.

As for the single ISW, mass transport caused by an ISW wave train strongly depends on Iribarren number ξ. Figure 5.42 compares mass transport versus the Iribarren number for a single wave (black) and for ISW wave train (red). Significant differences in mass transport are observed for $\xi < 0.2$. For this parameter range the mass of the subpycnocline water brought upslope by two ISWs is 1.5 times larger than the mass brought by a single ISW. These differences, however, become small for $\xi \geq 0.2$. It is clear from physical considerations that for steep slopes of the bottom the amount of water brought up-slope does not depend on the number of waves comprising the wave train. Wave reflection and

strong back-flow and viscous dissipation are dominant processes controlling the shoaling dynamics for $\xi \geq 0.2$.

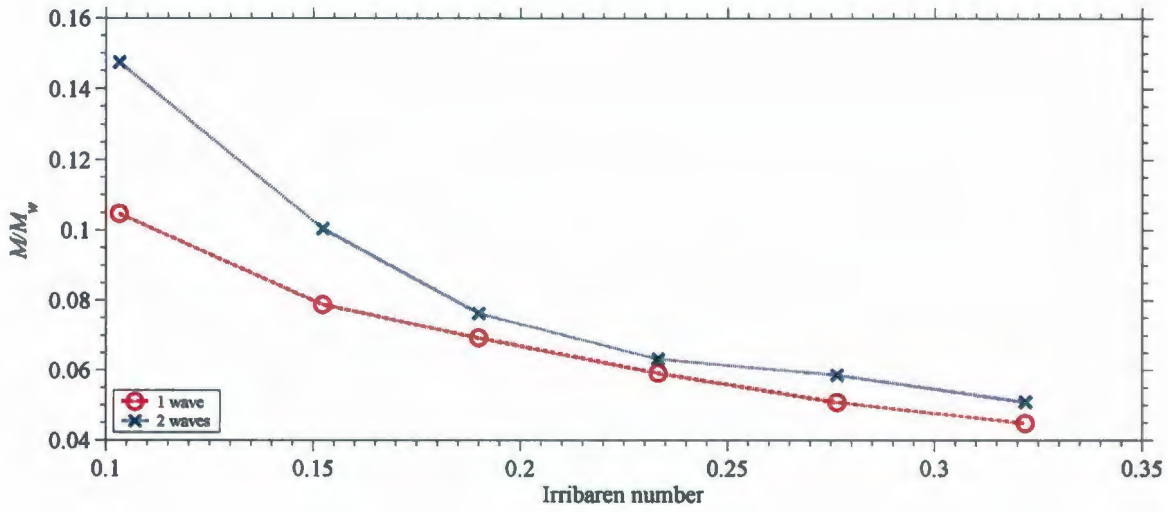

Figure 5.42. The amount of tracer brought above the pycnocline by one (x) and two waves (o) vs the Iribarren number.

Now we compare mass transport obtained for the train of two identical ISWs with the results of field observations by *Bourgault et al.* [2008]. In this study the onshore transport of subpycnocline water is calculated by recording the mass flux at a single point on a slope, F_x, defined by Equation 2.49. The prominent feature of the mass flux time series is the presence of both positive (upslope transport) and negative (downslope transport) peaks. Unfortunately, the observation of the entire wavetrain transformation and generation of boluses was not the main goal of this study, so the parameters of the impinging ISW packet are not precisely known. However, a field study was done at the same place and under similar conditions as their previous observations describing the shoaling of an ISW packet with a leading wave amplitude $a = 6$ m and Iribarren number $\xi = 0.16$[*Bourgault et al.*, 2007]. We will assume that the wavetrain that resulted in generation of boluses in the mass transport study of *Bourgault et al.* [2008] has similar parameters.

The linear slope used in numerical simulations is 0.05 which is equal to the average value of the quasi-linear slope in the region of the field study of *Bourgault et al.* [2007]. To investigate the nature of negative peaks in mass flux reported by *Bourgault et al.* [2008], see their Figure 6, the mass flux in numerical simulations was recorded at several points along the slope for the case of single ISW shoaling and for the case idealized ISW wave train.

The total depth of fluid at the position where mass flux was recorded in the field study was 15 m. The stratification in the region of study is not known precisely, so in numerical simulations bolus mass flux is calculated at several points along the slope. They are chosen relative to the point of slope-pycnocline intersection X_p as $x_1 = X_p - 200$ m, $x_2 = X_p$ and $x_3 = X_p + 100$ m. The first point x_1 is located close to the transition point X_t.

Figure 5.43 presents the mass flux time series at points x_1, x_2, and x_3 for the case of a single shoaling ISW and for an idealized 2-ISW wave train. The mass flux at the point x_1 located below the slope-pycnocline intersection shows a strong offshore mass transport before the arrival of boluses, 1200 s $< t <$ 1600 s for single ISW (panel a) and 1800 s $< t <$ 2200 s for single ISW (panel d). This offshore transport is weaker for the case of 2-ISW wave train due to the influence of the second ISW. After all boluses pass the point x_1 the mass flux returns to zero both for the single ISW and for the ISW wave train. This indicates that no residual downslope mass transport is induced at this point.

Figure 5.43(b) and (e) compare the mass flux at the slope-pycnocline intersection x_2. The difference is in number of boluses generated by single ISW $\mathrm{N}^I = 4$ and by the wave train $\mathrm{N}^{II} = 8$. Although the net mass transport by the ISW wave train is larger than that induced by a single ISW, the masses of individual boluses estimated using Equation 2.50 are bigger for boluses generated by a single ISW. The masses of the first two boluses estimated at the point x_2 are $M^I_{\mathrm{b1}}(x_2) = 2.21 \times 10^4$ kg/m, $M^I_{\mathrm{b2}}(x_2) = 2.66 \times 10^4$ kg/m for the single ISW and $M^{II}_{\mathrm{b1}}(x_2) = 1.52 \times 10^4$ kg/m, $M^{II}_{\mathrm{b2}}(x_2) = 8.34 \times 10^3$ kg/m for the ISW wave train. These values are in reasonable agreement with the average mass of boluses $M_{\mathrm{av}} = 5 \times 10^4$ kg/m found by *Bourgault et al.* [2008] in the field study. This suggests that the location of the observational site B, where mass flux was recorded is close to the slope-pycnocline intersection. The important feature of the mass flux at this point is the generation of the strong downslope mass transport during and after the passage of boluses.

This mass transport is induced by the downslope current generated during ISW shoaling close to the bottom.

Mass flux recorded at point x_3 located 100 meters up the slope from the slope-pycnocline intersection is shown in Figure 5.43(c) and (f). The mass flux is significantly lower at x_3 and this is in agreement with the values of the net mass transport shown in Figure 5.42. The individual masses of the boluses at this point are $M_{b1}^{I}(x_3) = 948.51$ kg/m for the leading boluses recorded for the single ISW case and $M_{b1}^{II}(x_3) = 399.51$ kg/m for the leading bolus in the ISW wave train case. The difference in mass is explained by much stronger downslope flow induced during the shoaling of the ISW wave train.

All time series of mass flux for both single ISW and ISW wave train show no indication of boluses that have negative mass flux and thus could transport water downslope. Figure 5.43 shows that despite the negative values of mass flux caused by the backflow of the fluid, all boluses have positive inputs to the net mass transport. Reported by *Bourgault et al.* [2008] negative mass transport by offshore propagating boluses can be possibly explained by the complex environment and background conditions (e.g. currents, tides, wave-wave interactions, etc.) during the field study.

The process of interaction of the wave train with the slope is significantly different from the case of single incident ISW. This is in agreement with laboratory experiments of *Helfrich* [1992] who observed shoaling of two solitary waves of the same amplitude, separated by several wavelengths over a linear slope. Although, laboratory measurements of the energetics of the breaking for several multiple wave runs gave mixing efficiencies within the range found for single-wave runs. The verification of this result is beyond the scope of the present study and may be considered in the future.

Figures 5.42 and 5.43 show that the number of boluses generated and the amount of mass transport from a two-wave train cannot be found from simple superposition of two isolated ISWs. In nature, other complications arise from the irregularity of wave arrival to the shore. Thus, mass transport resulting from a real internal wave train depends on the distances between waves.

Figure 5.44 presents the results of several numerical simulations in which the free parameter is the distance between two identical waves with amplitudes $a = 1.3$ m. Waves are placed at distances D = 1, 3, 5, 6 wavelength scales from each other. The arrival of

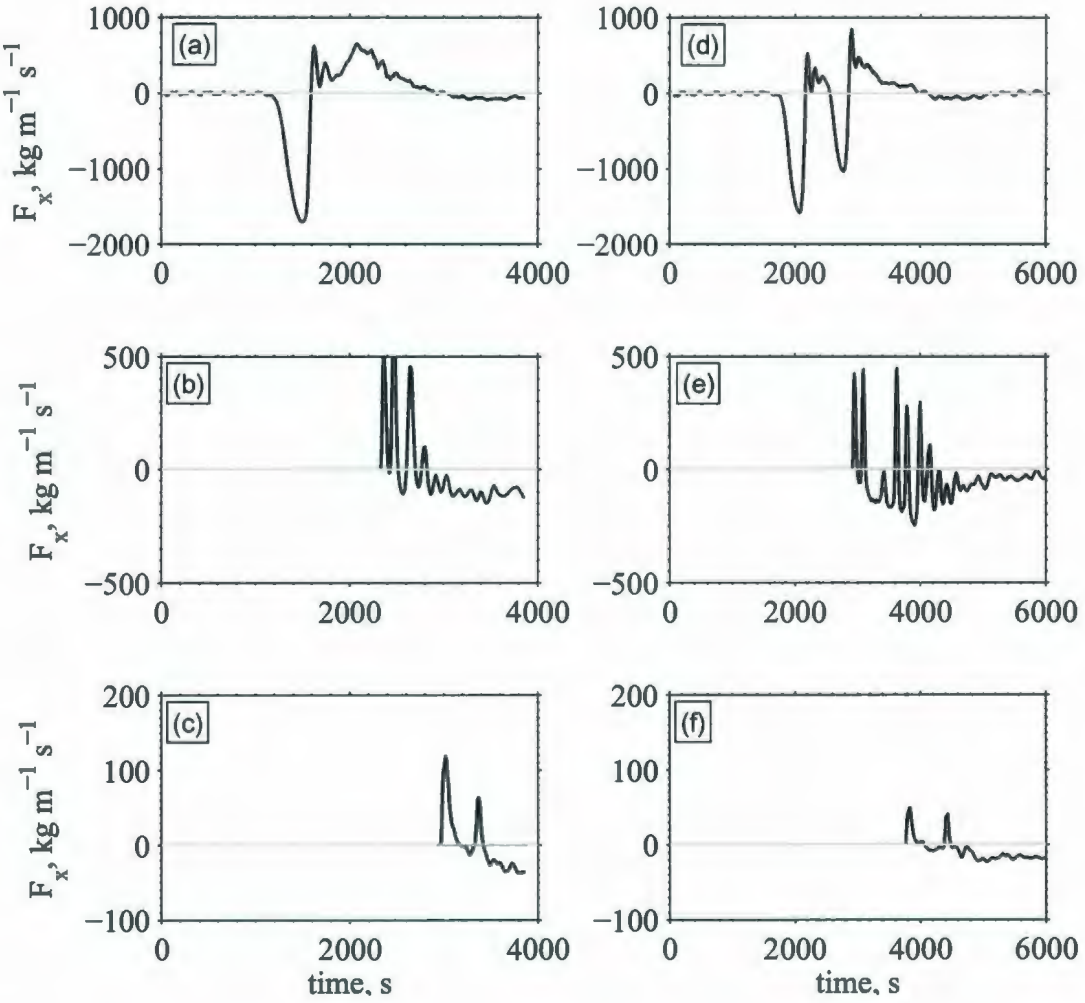

Figure 5.43. Time series of the bolus mass flux generated by the shoaling event of a single ISW (left panels) and by a wave train consisting of two ISWs (right panels). The mass flux was recorded at point $x_1 = X_p - 200$ m (panels a and d) located below slope-pycnocline intersection X_p; second point is located at slope-pycnocline intersection $x_2 = X_p$ (panels b and e); the third point is located further upslope $x_3 = X_p + 100$ m (panels c and f).

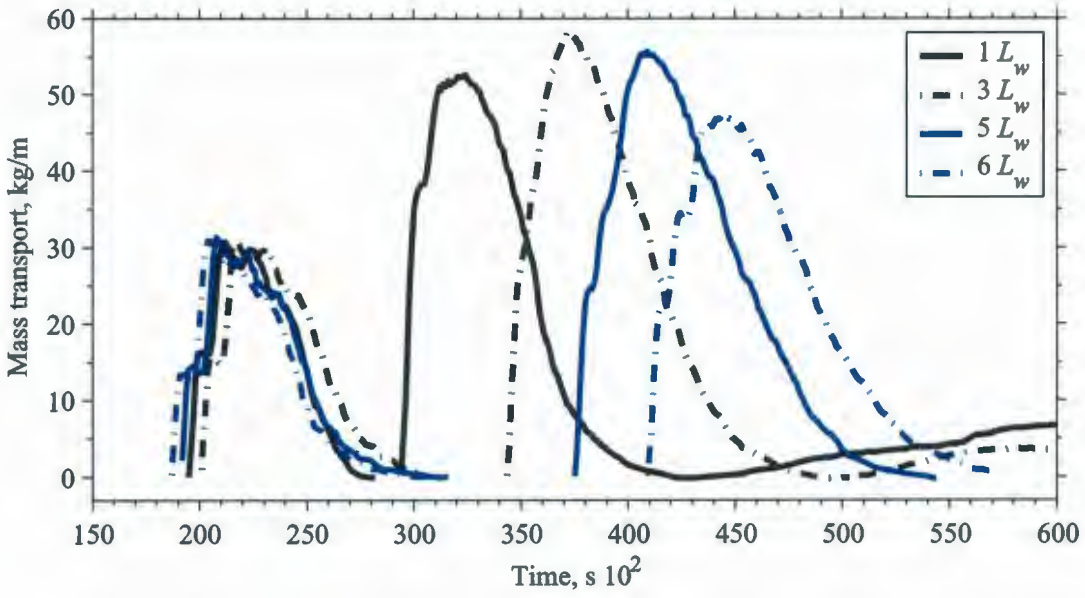

Figure 5.44. Time series of the onshore mass transport generated during the shoaling of two identical ISWs with amplitude $a = 1.3$ m over the linear slope of 2.8 degrees. Waves were separated by several wavelength scales from each other D/L_w = 1, 3, 5, 6 (see the legend).

the first wave is marked by the first peak which is approximately the same height for all cases. It indicates that the first wave in a train is not significantly modified by the presence of the neighbouring wave. The second wave, however, brings much more dense water upslope than the first one. The near bottom current generated during shoaling of the first wave which drains dense water from the slope appears to enhance the mass transport of the second wave almost by a factor of two.

Chapter 6

Summary and Conclusions

A large number of observational studies and numerical simulations have addressed the problem of internal waves in the ocean in the past several decades. Great interest in internal waves stems from their profound influence on ocean dynamics, biological additivity in the coastal waters, engineering offshore projects, military marine surveyance and ecological monitoring of pollutants. The ability of internal wave to propagate in any direction in a continuously stratified fluid defines their important role in vertical redistribution of energy and momentum.

Significant progress has been made in studying the generation mechanisms of internal waves and their properties during propagation through the deep ocean. It has been recognized that two main generation scenarios of internal waves in the ocean are nonlinear steepening of the internal tide and release of the internal lee waves formed by the interaction of the flow with an internal obstacle, such as sill or reef. However, the final stages of the internal wave's evolution are still not fully understood.

Observations performed in many parts of the ocean show that internal waves can travel significant distances and finally approach the coast. An internal wave front experiences refraction and reflection, but the portion of the transmitted internal wave approaching the coast will steepen, similar to the behavior of surface waves on a beach, and may break. Breaking of internal waves results in the production of turbulence and mixing. The hypothesis that the mixing generated by breaking internal waves is responsible for maintaining the balance of the stratification in the ocean has been tested recently both in field observa-

tions and using numerical models. Although many results from turbulence microstructure measurements showed elevated mixing rates in places of possible IW breaking, a favorable conclusion about this hypothesis is still lacking.

Despite an impressive increase in computer power, running large scale numerical models with a resolution needed to take into account all physical processes and their interaction is still not feasible. Internal waves interacting with sloping boundaries may have scales from centimeters to hundred of kilometers. Without the ability to simulate the effect of breaking internal waves directly, one has to modify parametrizations used in large-scale models in order to capture the effects of internal waves in terms of eddy diffusivity and eddy viscosity. Several attempts were done in this direction showed, but the reliable parametrization scheme is still to be developed.

Despite the huge range of spatio-temporal scales on which internal waves evolve, one class of internal waves received special attention. Solitary waves were first observed on the surface of the Scottish Canal by Scott Russell [*Russell*, 1844] and since then found their place in many physical contexts. Internal solitary waves are often generated upon the disintegration of the internal tide front. The deep water propagation of ISWs away from the coastal boundaries is characterized by adiabatic changes of their properties. This means that distances that ISWs travel without changes in their shape can be estimated as hundreds of kilometers. ISWs often travel in packets consisting of several usually rank ordered waves.

High-frequency large amplitude internal solitary waves frequently observed in coastal regions received renewed attention in recent years. ISWs propagating in a two-layer stratified fluid were reasonably well studied using the weakly nonlinear KdV theory and its extensions, fully nonlinear theories as well as numerical simulations. A fairly sharp density interface separating two unstratified layers of fluid is not unrealistic, and in fact, is frequently observed during the summer season. In the last several years increased attention to nonhydrostatic models has resulted in significant improvements in describing ISWs. However, several fundamental aspects of high-frequency ISWs still lack satisfactory explanation. They include transportation of ISWs while they move up the slope, breaking of ISWs, generation of internal waves of elevation and their dissipation.

While there have been many reports on studies of ISWs of depression, only a few studies were aimed at investigating ISWs of elevation. Some observations indicate that internal

solitary waves of elevation or boluses can play a significant role in the dynamics of coastal water. ISWs of elevation may form trapped cores inside themselves and thus effectively transport dense fluid rich in nutrients from below the pycnocline up the slope. Due to high induced velocities boluses are also good candidates for resuspending sediments and forming bottom nepheloid layer.

This thesis addresses this problem using as a tool both a field experiment and numerical simulations. The field experiment was performed at the flank of the Ile-aux-Lièvres Island in the St. Lawrence estuary where frequent occurrence of ISW packets was documented before. High-frequency ISW packets shoaling was observed using towed and moored instruments. Three mooring provided a long time record of flow on different parts of the slope. Based on this field experiment the climatology of ISWs of depression was investigated. The timing of wave arrival was verified to be consistent with tidal forcing generation mechanism. We have investigated the dependence of ISW energy on tidal phase. Towing instruments allowed us to follow a chosen ISW of depression and to document the phases of its evolution up to full dissipation on the slope. The echosounder observations revealed a smooth transformation of the ISW of depression into the set of boluses propagating up the slope. Detailed measurements of bolus properties were performed. Sampling strategy used in the field observations did not allow us to detect breaking of the ISW of depression.

Numerical simulations using a laterally averaged nonhydrostatic model were set up to supplement the field observations. In the numerical experiment, the complex influence of naturally occurring factors such as varying topography and currents can be treated one at a time. To study the conditions required for breaking as well as internal structure, properties of boluses and transport of the dense fluid, idealized numerical simulations were performed. The shoaling of a single ISW or a packet of two identical ISWs was studied in the two-layer fluid using a linear slope geometry. Results show that the net mass transport of the subpycnocline water by boluses propagating upslope depends on the amplitude of the incident ISW of depression. It can be as high as 6 % of the initial mass in the upslope region for incident wave of amplitude $a = 6$ m. On the other hand, the net mass transport almost does not depend on the slope.

To study the mass transport caused by ISW trains, the idealized wave-train was created consisting of two waves with the same amplitudes placed at a distance of one wavelength

from each other. Comparison of the transport generated by this idealized wavetrain with one generated by a single wave showed that a significant increase in net mass transport (2.5 times) is expected only for small values of the Iribarren number. For high Iribarren numbers the strong backflow of fluid resulted in negligible differences in the value of mass transport for a single ISW and the ISW wavetrain. Future work in this direction can include the investigation of mass transport in field experiments and comparison with numerical simulations with realistic bottom and stratification.

6.1 Future work

The work on internal waves in a shallow water and especially on internal waves of elevation has only just begun. Using field observations and numerical experiments the present study revealed a complex picture of the interaction of internal waves with a sloping topography. Many open problems remain for the future studies.

Difficulties associated with field observations of internal waves of elevation are making detailed measurements of near bottom ISWs and boluses sparse. Comparison of bolus properties derived from field experiments with existing weakly and fully nonlinear models presented in this study showed the nonlinear nature of boluses. The ratio of their amplitude to the depth of the fluid can reach as high as $a_b/H = 0.8$. Thus the use of weakly nonlinear theories is limited. At the same time, fully nonlinear two-layer model showed good agreement. However, additional studies are needed for detailed comparison of bolus structure and fully nonlinear model.

Field observations of ISWs of elevation with the focus on their mass transport and mixing properties are yet to be done. Numerical computations performed in the present study have used an idealized topography, an extension to real ocean parameters is advantageous for the direct comparison with field observations.

Our numerical simulations showed the possibility of the formation of trapped cores inside waves of elevation. This is in agreement with field observations by *Hosegood and van Haren* [2004] and laboratory experiments of *Sveen et al.* [2002]. However, the detailed structure of the trapped cores is still under study. A direct comparison between the laboratory experiments would greatly improve understanding of velocity and vorticity fields in trapped

cores.

Internal wave shoaling usually takes place in regions of rapidly varying properties of a waveguide, such as bathymetry and stratification. Although several 2D numerical studies including the present one showed good agreement of wave evolution with field observations, an open question remains about the importance of 3D effects. For example, in three dimensions, the Kelvin - Helmholtz billows, which are forming at the interface inside sufficiently large internal waves (Figure 2.9) are unstable to transverse perturbations and may break down. Several questions which remain to be answered include the determination of parameters of ISWs for which the appearance of the Kelvin-Helmholtz instability is possible. Will the breakage of billows lead to the breaking of the entire wave? Our results using two-dimensional model indicate the possibility of the formation of the billows inside boluses. They are not breaking down and the two-dimensional model would predict the continuous growth of billows via the inverse cascade of two-dimensional turbulence. The present study, however, shows that the subgrid scale mixing model is restraining the growth of the billows (Figure 5.35). The question is: is it the properties of the subgrid parametrization or the properties of billows? To answer the question about the real fate of billows inside boluses and their influence on the bolus lifetime one needs to address 3D nonhydrostatic models.

Bibliography

Alpers, W., W. C. Heng, and H. Lim, Observation of internal waves in the Andaman Sea by ERS SAR, in *Geoscience and Remote Sensing, 1997. IGARSS'97, Singapore 4-8 Aug 1997*, pp. 1518–1520, 1997. 11

Amick, C. J., and R. E. L. Turner, A global theory of internal solitary waves in two-fluid system, *Trans. Amer. Math. Soc.*, *298*, 431–484, 1986. 20

Amick, C. J., and R. E. L. Turner, Small internal waves in two-fluid systems, *Archive for Rational Mechanics and Analysis*, *108*(2), 111–139, 1989. 59

Apel, J. R., Observation of internal wave surface signatures in ASTP photographs, in *Apollo-Soyuz Test Project II*, edited by F.Er-Baz and D.M.Warner, SP-412, NASA publication, 1979. 11, 18

Apel, J. R., Oceanic internal waves and solitons, *An Atlas of Oceanic Internal Solitary Waves*, prepared for the Office of Naval Research - Code 322PO, *http://www.internalwaveatlas.com/*, 2002. 1, 18, 32

Apel, J. R., J. R. Holbrook, A. K. Liu, and J. J. Tsai, The Sulu Sea internal soliton experiment, *J. Phys. Oceanogr.*, *15*, 1625–1651, 1985. 10, 11, 18, 33

Armi, L., and D. Farmer, The flow of Atlantic water through the Strait of Gibraltar, *Progr. Oceanogr.*, *21*, 1–105, 1988. 11

Armstrong, F. A. J., and E. C. LaFond, Chemical nutrient concentrations and their relationship to internal waves and turbidity off Southern California, *Limnol. Oceanogr.*, *11*(4), 538–547, 1966. 5

Baines, P. G., The generation of internal tides by flat-bump topography, *Deep-Sea Res.*, *20*, 179–205, 1973. 4

Benjamin, T. B., Internal waves of finite amplitude and permanent form, *J. Fluid Mech.*, *25*, 241–270, 1966. 13, 21

Benney, D. J., Long nonlinear wave in fluid flows, *J. Math. Phys.*, *45*, 52–63, 1966. 13, 23

Berntsen, J., Users guide for a modesplit s-coordinate numerical ocean model, *Tech. Rep. 135*, Department of Applied Mathematics, University of Bergen, Johs. Bruns gt. 12, N-5008 Bergen, Norway, 2000. 28

Berntsen, J., J. Xing, and G. Alendal, Assessment of non-hydrostatic ocean models using laboratory scale problems, *Continental Shelf Research*, *26*, 1433–1447, 2006. 28

Blumberg, A. F., and G. L. Mellor, A description of a three-dimensional coastal ocean circulation model, in *Three-dimensional coastal ocean models*, edited by N. Heaps, American Geophysical Union, 1987. 28

Boegman, L., G. Ivey, and J. Imberger, The degeneration of internal waves in lakes with sloping topography, *Limnol. Oceanogr.*, *50*(5), 1620–1637, 2005. 1, 44, 67, 69, 73

Bogucki, D., and C. Garrett, A simple model for shear-induced decay of an internal solitary wave, *J. Phys. Oceanogr.*, *23*, 1767–1776, 1993. 29, 30, 88, 96

Bogucki, D., T. Dickey, and L. G. Redekopp, Sediment resuspension and mixing by resonantly generated internal solitary waves, *J. Phys. Oceanogr.*, *27*, 1181–1196, 1997. 5, 29, 30, 41

Bogucki, D., L. G. Redekopp, and J. Barth, Internal solitary waves in the Coastal Mixing and Optics 1996 experiment: Multimodal structure and resuspension, *J. Geophys. Res.*, *110*(C02024), 1–19, 2005. 5

Bourgault, D., and D. E. Kelley, Wave-induced boundary mixing in a partially mixed estuary, *J. Mar. Res.*, *61*(5), 553–576, 2003. 1, 32, 50, 79, 80, 82, 94, 132

Bourgault, D., and D. E. Kelley, A laterally averaged nonhydrostatic ocean model, *J. Atmos. Oceanic Technol.*, *21*(12), 1910–1924, 2004. 28, 54, 55, 61, 86

Bourgault, D., and D. E. Kelley, On the reflectance of uniform slopes for normally incident interfacial solitary waves, *J. Phys. Oceanogr.*, *37*(5), 1156–1162, 2007. 28, 36, 73

Bourgault, D., D. E. Kelley, and P. S. Galbraith, Interfacial solitary wave run-up in the St. Lawrence Estuary, *J. Mar. Res.*, *63*(6), 1001–1015, 2005. 1, 28, 50

Bourgault, D., M. Blokhina, R. Mirshak, and D. E. Kelley, Evolution of a shoaling internal solitary wavetrain, *Geophys. Res. Let.*, *34*(L03601), doi:10.1029/2006GL028,462, 2007. 61, 110, 112, 113, 144, 146, 147

Bourgault, D., D. E. Kelley, and P. S. Galbraith, Turbulence and boluses on an internal beach, *J. Mar. Res.*, *66*, 563–588, 2008. 43, 146, 147, 148

Brandt, P., W. Alpers, and J. O. Backhaus, Study of the generation and propagation of internal waves in the Strait of Gibraltar using a numerical model and synthetic aperture radar images of the European ERS1 satellite, *J. Geophys. Res.*, *101*(C6), 14,237–14,252, 1996. 10, 32

Butman, B., P. Alexander, A. Scotti, R. Beardsley, and S. Anderson, Large internal waves in Massachusetts Bay transport sediments offshore, *Continental Shelf Research*, *26*, 2029–2049, 2006. 43, 48, 143

Cacchione, D. A., and D. E. Drake, Nepheloid layers and internal waves over continental shelves and slopes, *Geo-Marine Lett.*, *6*(3), 147–152, 1986. 5

Cai, S., S. Wang, and X. Long, A simple estimation of the force exerted by internal solitons on cylindrical piles, *Ocean Engineering*, *33*(7), 974–980, 2006. 5

Caldwell, D. R., and J. N. Moum, Turbulence and mixing in the ocean, *Rev. Geophys.*, *33 Suppl.*, 1385–1394, 1995. 6

Camassa, R., W. Choi, H. Michallet, P.-O. Rusas, and J. Sveen, On the realm of validity of strongly nonlinear asymptotic approximations for internal waves, *J. Fluid Mech.*, *549*, 1–23, 2006. 18

Carter, G., M. Gregg, and R. C. Lien, Internal waves, solitary-like waves, and mixing on the Monterey Bay shelf, *Continental Shelf Research*, *25*(12–13), 1499–1520, 2005. 7

Cartwright, D. E., *Tides: A Scientific History*, 292 pp. pp., Cambridge Univ. Press, Cambridge, 1999. 1

Choi, W., and R. Camassa, Fully nonlinear internal waves in a two-fluid system, *J. Fluid Mech.*, *396*, 1–36, 1999. 24, 26, 27

Christie, D. R., K. J. Muirhead, and R. H. Clarke, Solitary waves in the lower atmosphere, *Nature*, *293*, 46–49, 1981. 11

Cummins, P. F., S. Vagle, L. Armi, and D. M. Farmer, Stratified flow over topography: upstream influence and generation of nonlinear internal waves, *Proc. R. Soc. Lond. A*, *459*, 1467–1487, 2003. 11, 33

Davis, R. E., The two-dimensional flow of a stratified fluid over an obstacle, *J. Fluid Mech.*, *36*, 127–143, 1969. 38

Davis, R. E., and A. Acrivos, Solitary internal waves in deep water, *J. Fluid Mech.*, *29*, 593–607, 1967. 38

Denman, K. L., and A. E. Gargett, Biological-physical interactions in the upper ocean: the role of vertical and small scale transport processes, *Annu. Rev. Fluid Mech.*, *27*, 225–255, 1995. 5

Derzho, O., and R. Grimshaw, Solitary waves with a vortex core in a shallow layer of stratifed fluid, *Phys. Fluids*, *9*, 3378–3385, 1997. 38, 104

Derzho, O. G., and R. Grimshaw, Asymmetric internal solitary waves with a trapped core in deep fluids, *J. Fluid Mech.*, *19*(9), 096,601, doi:10.1063/1.2768507, 2007. 104

Djordjevic, V., and L. Redekopp, The fission and disintegration of internal solitary waves moving over two-dimensional topography, *J. Phys. Oceanogr.*, *8*, 1016–1024, 1978. 24

Emery, K. O., and C. G. Gunnerson, Internal swash and surf, *Proc. Nat. Acad. Sci. USA*, *70*(8), 2379–2380, 1973. 37

Ewing, G., Slicks, surface films and internal waves, *J. Mar. Res.*, *9*(C6), 161–187, 1950. 32

Ezer, T., H. Arango, and A. F. Shchepetkin, Developments in terrain-following ocean models: intercomparisons of numerical aspects, *Ocean Modelling*, *4*, 249–267, 2002. 28

Farmer, D., and L. Armi, The flow of Mediterranean water through the Strait of Gibraltar, *Progr. Oceanogr.*, *21*, 1–105, 1988. 11

Farmer, D. M., and L. Armi, The generation and trapping of internal solitary waves over topography, *Science*, *283*(5398), 188–190, 1999. 1, 11, 13

Farmer, D. M., and H. Freeland, The physical oceanography of fjords, *Progr. Oceanogr.*, *12*(2), 147–220, 1983. 13

Farmer, D. M., and J. D. Smith, Nonlinear internal waves in a fjord, in *Hydrodynamics of estuaries and fjords*, edited by J. Nihoul, pp. 465–493, Elsevier, 1977. 1

Farmer, D. M., and J. D. Smith, Tidal interaction of stratified flow with a sill in Knight Inlet, *Deep-Sea Res., 27A*, 239–254, 1980. 11

Fedorov, K. N., and A. I. Ginzburg (Eds.), *The Near-surface Layer of the Ocean*, VSP, Utrecht, the Netherlands, 1992. 1

Filonov, A. E., and A. Trasvina, Internal waves on the continental shelf of the Gulf of Tehuantepec, Mexico, *Estuarine Coastal Shelf Sci., 50*, 531–548, 2000. 33

Fringer, O. B., and R. L. Street, Nonhydrostatic effects of breaking interfacial waves on a sloping boundary, in *5th Workshop on Numerical Modeling of Atmospheric, Surface, and Groundwater Flows*, Trento, 1999. 27

Funakoshi, M., and M. Oikawa, Long internal waves of large amplitude in a two-layer fluid, *J. Phys. Soc. Japan, 55*, 128–144, 1986. 24

Garabato, A. C. N., K. L. Polzin, B. A. King, K. J. Heywood, and M. Visbeck, Widespread intense turbulent mixing in the southern ocean, *Science, 303*(5655), 210–213, 2004. 44

Gargett, A. E., Velcro measurement of turbulence kinetic energy dissipation rate, *J. Atmos. Oceanic Technol., 16*(12), 1973–1993, 1999. 7

Gargett, A. E., and G. Holloway, Dissipation and diffusion by internal wave breaking, *J. Mar. Res., 42*, 15–27, 1984. 6

Garrett, C., Parameterizing the effects of internal waves: simple ideas and things we need to know, in *Internal gravity waves and small-scale turbulence*, edited by P. Muller and R. Pujalet, pp. 171–181, Hawaii Inst of Geophysics, 1984. 6

Garrett, C., An isopycnal view of near-boundary mixing and associated flows, *J. Phys. Oceanogr., 31*, 138–142, 2001. 44

Garrett, C., and W. Munk, Space-time scales of internal waves: A progress report, *J. Geophys. Res., 3*(3), 291–297, 1975. 6

Garrett, C., and W. Munk, Internal waves in the ocean, *Annu. Rev. Fluid Mech., 11*, 339–369, 1979. 2, 3

Gerkema, T., A unified model for the generation and fission of internal tides in a rotating ocean, *J. Mar. Res., 54*, 421–450, 1996. 4

Gerkema, T., and J. Zimmerman, Generation of nonlinear internal tides and solitary waves, *J. Phys. Oceanogr., 25*(6), 1081–1094, 1995. 4, 10

Government of Canada, 1997, *Atlas of tidal currents from Cap de Bon-Désir to Trois-Rivières*, Canadian Hydrographic Service, Fisheries and Oceans Canada, Ottawa, 1997. 80

Gregg, M. C., Diapycnal mixing in the thermocline: a review, *J. Geophys. Res., 92*(C5), 5249–5286, 1987. 44

Gregg, M. C., Scaling turbulent dissipation in the thermocline, *J. Geophys. Res., 94*(C7), 9686–9698, 1989. 6, 7

Gregg, M. C., The study of mixing in the ocean: a brief history, *Oceanography, 4*(1), 39–45, 1991. 7

Grimshaw, R., Internal solitary waves, in *Progress in nonlinear science*, Nizhni Novgorod, 2001. 23

Grimshaw, R., D. Pelinovsky, E. Pelinovsky, and A. Slunyaev, Generation of large-amplitude solitons in the extended Korteweg–de Vries equation, *Chaos*, *12*(4), 1070–1076, doi:10.1063/1.1521391, 2002. 23

Grimshaw, R. H. J., E. Pelinovsky, and T. Talipova, Solitary wave transformation in a medium with sign-variable quadratic nonlinearity and cubic nonlinearity, *Physica D*, *132*, 40–62, 1999. 33

Grue, J., H. A. Friis, E. Palm, and P. O. Rusas, A method for computing unsteady fully nonlinear interfacial waves, *J. Fluid Mech.*, *351*, 223–252, 1997. 20, 24, 27

Grue, J., A. Jensen, P.-O. Rusas, and J. K. Sveen, Properties of large-amplitude internal waves, *J. Fluid Mech.*, *380*, 257–278, 1999. 17, 18, 25, 26, 62, 74, 75, 76, 98

Grue, J., A. Jensen, P.-O. Rusas, and J. K. Sveen, Breaking and broadening of internal solitary waves, *J. Fluid Mech.*, *413*, 181–217, 2000. 104

Haidvogel, D. B., H. Arango, K. Hedstrom, A. Beckmann, P. Malanotte-Rizzoli, and A. Shchepetkin, Model evaluation experiments in the North Atlantic Basin: Simulations in non-linear terrain-following coordinates, *Dynamics of Atmospheres and Oceans*, *32*, 239–281, 2000. 28

Hamrick, J. M., Estuarine environmental impact assessment using a three-dimensional circulation and transport model, in *2nd International Conference Estuarine Coastal Modeling, ed. M. L. Spaulding et al., American Society of Civil Engineers, New York*, pp. 292–303, 1992. 28

Haury, L. R., M. G. Briscoe, and M. H. Orr, Tidally generated internal wave packets in Massachusetts Bay, *Nature*, *278*, 312–317, 1979. 5

Hayes, S., Preliminary measurements of the time-lagged coherence of vertical temperature profiles, *J. Geophys. Res.*, *80*, 307–311, 1975. 32

Hebert, D., The available potential energy of an isolated feature, *J. Geophys. Res.*, *93*(C1), 556–564, 1988. 47, 113, 115, 116, 117, 119, 126, 132, 136

Helfrich, K. R., Internal solitary shoaling and breaking on a uniform slope, *Transactions of the American Geophysical Union, Abstract*, *71*, 1370–1371, 1990. 35

Helfrich, K. R., Internal solitary wave breaking and run-up on a uniform slope, *J. Fluid Mech.*, *243*, 133–154, 1992. 34, 35, 36, 44, 45, 56, 68, 73, 106, 148

Helfrich, K. R., and W. K. Melville, On long nonlinear internal waves over slope-shelf topography, *J. Fluid Mech.*, *167*, 285–308, 1986. 20, 23, 33, 34

Helfrich, K. R., and W. K. Melville, Long nonlinear internal waves, *Annu. Rev. Fluid Mech.*, *38*, 395–425, 2006. 1, 18

Helfrich, K. R., W. K. Melville, and J. W. Miles, On interfacial solitary waves over slowly varying topography, *J. Fluid Mech.*, *149*, 305–317, 1984. 36, 40, 103

Henyey, F. S., J. Wright, and S. M. Flatté, Energy and action flow through the internal wave field, *J. Geophys. Res.*, *91*, 8487–8495, 1986. 7

Hogg, N., P. Biscaye, W. Gardner, and W. S. Jr., On the transport and modification of antarctic bottom water in the vema channel, *J. Mar. Res.*, *40 (Suppl)*, 231–263, 1982. 6

Holliday, D., and M. E. McIntyre, On potential energy density in an incompressible, stratified fluid, *J. Fluid Mech.*, *107*, 221–225, 1981. 46

Holloway, P. E., and M. A. Merrifield, Internal tide generation by seamounts, ridges, and islands, *J. Geophys. Res.*, *104*(C11), 25,937–25,951, 1999. 4, 10

Holloway, P. E., E. Pelinovsky, and T. Talipova, A generalized Korteweg-de Vries model of internal tide transformation in the coastal zone, *J. Geophys. Res.*, *104*(C8), 18,333–18,350, 1999. 4, 23, 33

Hosegood, P., and H. van Haren, Near-bed solibores over the continental slope in the Faeroe-Shetland Channel, *Deep-Sea Res. part II*, *51*, 2943–2971, 2004. 38, 155

Hsu, M. K., and A. K. Liu, Nonlinear internal waves in the South China Sea, *Canadian J. Rem. Sens.*, *26*, 72–81, 2000. 11

Hsu, M. K., A. K. Liu, and C. Liu, A study of internal waves in the China Seas and Yellow Sea using SAR, *Continental Shelf Research*, *20*, 389–410, 2000. 11

Huthnance, J. M., Circulation, exchange and water masses at the ocean margin: the role of physical processes at the shelf edge, *Progr. Oceanogr.*, *35*(4), 353–431, 1995. 41

Hutter, K., G. Bauer, Y. Wang, and P. Güting, Forced motion response in enclosed lakes, in *Physical processes in lakes and oceans*, edited by C. Pattiaratchi, pp. 137–166, Amer. Geophys. Union, 1998. 1

Inall, M. E., G. I. Shapiro, and T. J. Sherwin, Mass transport by non-linear internal waves on the Malin Shelf, *Continental Shelf Research*, *21*, 1449–1472, 2001. 41, 42

Jones, I. S. F., and L. Padman, Semidiurnal internal tides in eastern bass strait, *Australian J. of Marine and Freshwater Res.*, *34*(1), 159–171, 1983. 10

Kao, T. W., F.-S. Pan, and D. Renouard, Internal solitons on the pycnocline: generation, propagation, and shoaling and breaking over a slope, *J. Fluid Mech.*, *169*, 19–53, 1985. 20, 31, 35

Kaup, D. J., and A. C. Newell, Solitons as particles, oscillators, and in slowly changing media: a singular perturbation theory., *Proc. R. Soc. Lond. A*, *361*(C3), 413–446, 1978. 36

Keulegan, G. H., Characteristics of internal solitary waves, *J. Res. Nat. Bur. Stand.*, *51*(3), 133–140, 1953. 13, 36

Klymak, J. M., and J. N. Moum, Internal solitary waves of elevation advancing on a shoaling shelf, *Geophys. Res. Let.*, *30*(20), 2045, doi:10.1029/2003GL017,706, 2003. 37, 38, 45, 97, 108, 110

Knickerbocker, C. J., and A. C. Newell, Internal solitary waves near a turning point, *Phys. Let.*, *75*(A), 326–330, 1980. 103

Koop, G., and G. Butler, An investigation on internal solitary waves in a two-fluid system, *J. Fluid Mech.*, *112*, 225–251, 1981. 18, 20, 24

Kundu, P. K., *Fluid mechanics*, 638 pp., Academic Press, San Diego, 1990. 55, 72

Kunze, E., and S. G. L. Smith, The role of small-scale topography in turbulent mixing of the global ocean, *Oceanography*, *17*(1), 55–64, 2003. 44

Kunze, E., A. J. Williams III, and M. G. Briscoe, Observations of shear and vertical stability from a neutrally buoyant float, *J. Geophys. Res.*, *95*(C10), 18,127–18,142, 1990. 6

Kunze, E., E. Firing, J. M. Hummon, T. K. Chreskin, and A. M. Thurnherr, Global abyssal mixing inferred from lowered ADCP shear and CTD strain profiles, *J. Phys. Oceanogr.*, pp. 1553–1576, 2006. 7

Lacombe, H., and C. Richez, The regime of the strait of gibraltar, in *Hydrodynamics of Semi-Enclosed Seas*, edited by J. C. J. Nihoul, pp. 13–73, Elsevier, New York, 1989. 10

Lamb, K. G., Numerical experiments of internal wave generation by strong tidal flow across a finite amplitude bank edge, *J. Geophys. Res.*, *99*, 843–864, 1994. 11

Lamb, K. G., Particle transport by nonbreaking, solitary internal waves, *J. Geophys. Res.*, *102*(C8), 18,641–18,660, 1997. 41

Lamb, K. G., Are solitary internal waves solitons, *Stud. Appl. Math.*, *101*, 289–308, 1998. 18, 62

Lamb, K. G., Conjugate flows for a three-layer fluid, *Phys. Fluids*, *12*(9), 2169–2185, 2000. 21

Lamb, K. G., A numerical investigation of solitary internal waves with trapped cores formed via shoaling, *J. Fluid Mech.*, *451*, 109–144, 2002. 27, 38, 104

Lamb, K. G., Shoaling solitary internal waves: on a criterion for the formation of waves with trapped cores, *J. Fluid Mech.*, *478*, 81–100 DOI: 10.1017/S0022112002003,269, 2003. 27, 108

Lamb, K. G., Energy and pseudoenergy flux in the internal wave field generated by tidal .ow over topography, *Continental Shelf Research*, *27*, 1208–1232, 2007. 45, 110, 113, 119

Lamb, K. G., On the calculation of the available potential energy of an isolated perturbation in a density-stratified fluid, *J. Fluid Mech.*, *597*, 415–427, 2008. 47, 114, 120, 123, 126, 130, 132

LeBlond, P. H., and L. A. Mysak, *Waves in the ocean*, Elsevier Scientific Publishing, Amsterdam, 1978. 2

Ledwell, J. R., A. J. Watson, and C. S. Law, Evidence for slow mixing across the pycnocline from an open-ocean tracer release experiment, *Nature*, *364*, 701–703, 1993. 6

Ledwell, J. R., K. L. Montgomery, K. L. Polzin, L. C. S. Laurent, R. W. Schmitt, and J. M. Toole, Mixing over rough topography in the Brazil Basin, *Nature*, *403*, 179–182, 2000. 44

Lee, C.-Y., and R. C. Beardsley, The generation of long nonlinear internal waves in a weakly stratified shear flow, *J. Geophys. Res.*, *79*(3), 453–462, 1974. 10, 23

Legg, S., and A. Adcroft, Internal wave breaking at concave and convex continental slopes, *J. Phys. Oceanogr.*, *33*, 2224–2246, 2003. 40

Leichter, J. J., G. Shellenbarger, S. Genovese, and S. R. Wing, Breaking internal waves on a Florida (USA) coral reef: a plankton pump at work?, *Marine Ecology Progress Series*, *166*, 83–97, 1998. 5

Li, H., and H. Yamazaki, Observations of a Kelvin-Helmholtz billow in the ocean, *J. Oceanogr.*, *57*, 709–721, 2001. 97

Lien, R.-C., T. Y. Tang, M. H. Chang, and E. A. D'Asaro, Observations of turbulence in a tidal beam and across a coastal ridge, *J. Geophys. Res.*, *106*(C3), 4575–4591, 2001. 44

Lien, R.-C., T. Y. Tang, M. H. Chang, and E. A. D'Asaro, Energy of nonlinear internal waves in the South China Sea, *Geophys. Res. Let.*, *32*, L05,615, doi:10.1029/2004GL022,012, 2005. 11

Liu, A. K., J. R. Holbrook, and J. R. Apel, Nonlinear internal wave evolution in the Sulu Sea, *J. Phys. Oceanogr.*, *15*(12), 1613–1624, 1985. 11, 18

Long, R. R., Solitary waves in one and two-fluid system, *Tellus*, *8*, 460–471, 1956. 13, 38

Lorenz, E. N., Available potential energy and the maintenance of the general circulation, *Tellus*, *7*, 157–167, 1955. 46

Lu, Y., and R. G. Lueck, Using a broadband ADCP in a tidal channel. Part II: Turbulence, *J. Atmos. Oceanic Technol.*, *16*, 1568–1579, 1999. 44

Lu, Y., R. G. Lueck, and D. Huang, Turbulence characteristics in a tidal channel, *J. Phys. Oceanogr.*, *30*(5), 855–867, 2000. 44

Lueck, R. G., and T. D. Mudge, Topographically induced mixing around a shallow seamount, *Science*, *276*, 1831–1833, 1997. 44

MacIntyre, S., K. M. Flynn, R. Jellison, and J. Romero, Boundary mixing and nutrient fluxes in Mone Lake, California, *Limnol. Oceanogr.*, *44*(3), 512–529, 1999. 5

Margules, M., Uberdie energie der storme jahrb., *Zentralanst. Meteorol., English transl. by C. Abbe in Smithsonian Misc. Coll., 1910*, *40*(5), 1–26, 1909. 46

Marshall, J., C. Hill, L. Perelman, and A. Adcroft, Hydrostatic, quasi-hydrostatic, and nonhydrostatic ocean modelling, *J. Geophys. Res.*, *102*(C3), 5733–5752, 1997. 28

Maxworthy, T., A note on the internal solitary waves produced by tidal flow over a three-dimensional ridge, *J. Geophys. Res.*, *84*(C1), 338–346, 1979. 11

Maxworthy, T., J. Leilich, J. E. Simpson, and E. H. Meiburg, The propagation of a gravity current into a linearly stratified fluid, *J. Fluid Mech.*, *453*, 371–394, 2002. 40, 41, 103

McPhee-Shaw, E. E., and E. Kunze, Boundary-layer intrusions from a sloping bottom: A mechanism for generating intermediate nepheloid layers, *J. Geophys. Res.*, *107*, 3050, doi:10.1029/2001JC000,801, 2002. 87

Mellor, G. L., and T. Yamada, A hierarchy of turbulence closure models for planetary boundary layers, *J. Atmos. Sci.*, *31*, 1791–1806, 1974. 7

Michallet, H., and E. Barthelemy, Experimental study of interfacial solitary waves, *J. Fluid Mech.*, *366*, 159–177, 1998. 20, 25

Michallet, H., and G. N. Ivey, Experiments on mixing due to internal solitary waves breaking on uniform slopes, *J. Geophys. Res.*, *104*(C6), 13,467–13,477, 1999. 35, 36, 44, 45, 73

Miles, J., On the stability of heterogeneous shear flows, *J. Fluid Mech.*, *10*, 496–508, 1961. 29

Miles, J. W., On internal solitary waves, *Tellus*, *31*, 456–462, 1979. 24

Miles, J. W., On internal solitary waves ii, *Tellus*, *33*, 397–401, 1981. 20, 24

Miyata, M., Long internal waves of large amplitude, in *Nonlinear water waves*, edited by K. Horikawa and H. Maruo, pp. 399–406 pp., Springer-Verlag, New-York, 1988. 24

Moum, J. N., D. M. Farmer, W. D. Smyth, L. Armi, and S. Vagle, Structure and generation of turbulence at interfaces strained by internal solitary waves propagating shoreward over continental shelf, *J. Phys. Oceanogr.*, *33*(10), 2093–2112, 2003. 30, 31, 97

Moum, J. N., D. M. Farmer, E. L. Shroyer, W. D. Smyth, and L.Armi, Dissipative losses in nonlinear internal waves propagating across the continental shelf, *J. Phys. Oceanogr.*, *37*, 1989–1995, 2007. 32, 45, 113

Munk, W. H., Abyssal recipes, *Deep-Sea Res.*, *13*, 707–730, 1966. 6, 7, 44

Munk, W. H., and C. Wunsch, Abyssal recipes ii: energetics of tidal and wind mixing, *Deep-Sea Res. part I*, *45*, 1977–2010, 1998. 44

Nash, J. D., and J. N. Moum, River plumes as a source of large-amplitude internal waves in the coastal ocean, *Nature*, *437*(15), doi:10.1038/nature03,936, 2005. 11, 14

Nash, J. D., E. Kunze, J. M. Toole, and R. W. Schmitt, Internal tide reflection and turbulent mixing on the continental slope, *J. Phys. Oceanogr.*, *34*, 1117–1134, 2004. 44

Orr, M. H., and P. C. Mignerey, Nonlinear internal waves in the South China Sea: Observation of the conversion of depression internal waves to elevation internal waves, *J. Geophys. Res.*, *108*(C3), 3064, doi:10.1029/2001JC001,163, 2003. 37

Osborn, T. R., Estimates of the local rate of vertical diffusion from dissipation measurements, *J. Phys. Oceanogr.*, *10*, 83–89, 1980. 44

Osborne, A. R., and T. L. Burch, Internal solitons in the Andaman Sea, *Science*, *208*(4443), 451–459, 1980. 4, 11, 20

Ostrovsky, L. A., and J. Grue, Evolution equations for strongly nonlinear internal waves, *Phys. Fluids*, *15*(10), 2934–2948, 2003. 24, 25

Ostrovsky, L. A., and Y. A. Stepanyants, Do internal solitons exist in the ocean?, *Rev. Geophys.*, *27*(3), 292–319, 1989. 4, 18, 21, 22, 32

Ostrovsky, L. A., and Y. A. Stepanyants, Internal solitons in laboratory experiments: Comparison with theoretical models, *Chaos*, *15*(3), 037,111, 2005. 18, 58

Pawlowicz, R., Quantitative visualization of geophysical flows using low-cost oblique digital time-lapse imaging, *IEEE J. Oceanic. Eng.*, *28*(4), 699–710, 2003. 32

Pelinovsky, E. N., T. Talipova, and V. Ivanov, Estimations of nonlinear properties of internal wave field off the Israel coast, *Nonlinear Processes in Geophysics*, *2*(2), 80–88, 1995. 23

Pinkel, R., Internal solitary waves in the warm pool of the Western Equatorial Pacific, *J. Phys. Oceanogr.*, *30*, 2906–2926, 2000. 18, 31

Polzin, K., J. M. Toole, J. R. Ledwell, and R. W. Schmitt, Spatial variability of turbulent mixing in the abyssal ocean, *Science*, *276*, 93–96, 1997. 44

Polzin, K., E. Kunze, J. Hummon, and E. Firing, The finescale response of lowered adcp velocity profiles, *J. Atmos. Oceanic Technol.*, *19*, 205–224, 2002. 44

Pritchard, M., and R. A. Weller, Observations of internal bores and waves of elevation on the new england inner continental shelf during summer 2001, *J. Geophys. Res.*, *110*(C03020), doi:10.1029/2004JC002,377, 2005. 42

Reid, R. O., B. A. Elliott, and D. B. Olson, Available potential energy: A clarification, *J. Phys. Oceanogr.*, *11*, 15–29, 1981. 46

Russell, J. S., *Report on waves*, 311–390 pp., Murray, London, 1844. 153

Sandstrom, H., and J. A. Elliott, Internal tide and solitons on the Scotian Shelf: A nutrient pump at work, *J. Geophys. Res.*, *89*(C4), 6415–6426, 1984. 13, 20

Sandstrom, H., and N. S. Oakey, Dissipation in internal tides and solitary waves, *J. Phys. Oceanogr.*, *25*, 604–614, 1995. 41

Scotti, A., and C. Meneveau, Generalized Smagorinsky model for anisotropic grids, *Phys. Fluids A*, *5*(9), 2306–2308, 1993. 7

Scotti, A., and J. Pineda, Observation of very large and steep internal waves of elevation near the Massachusetts coast, *Geophys. Res. Let.*, *31*(L22307), doi:10.1029/2004GL021,052, 2004. 38, 39, 45, 104, 106

Scotti, A., R. Beardsley, and B. Butman, On the interpretation of energy and energy fluxes of nonlinear internal waves: an example from Massachusetts bay, *J. Fluid Mech.*, *561*(doi:10.1017/S0022112006000991), 103–112, 2006. 45, 128

Segur, H., and J. Hammack, Soliton models of long internal waves, *J. Fluid Mech.*, *118*, 285–304, 1982. 20

Shepherd, T. G., A unified theory of available potential energy, *Atmosphere Ocean*, *31*(1), 1–26, 1993. 113, 128

Slinn, D. N., and J. J. Riley, Turbulent mixing in the oceanic boundary layer caused by internal wave reflection from sloping terrain, *Dynamics of Atmospheres and Oceans*, *24*, 51–62, 1996. 44

Smagorinsky, J., General circulation experiments with primitive equations. I. The basic experiment, *Monthly Weather Rev.*, *91*(3), 99–164, 1963. 7, 55

Smith, R. K., N. Crook, and G. Roff, An extraordinary atmospheric undular bore, *Q. J. R. Meteorol. Soc.*, *108*, 937–956, 1982. 11

Staquet, C., Gravity and inertia - gravity internal waves: Breaking processes and induced mixing, *Surveys in Geophysics*, *25*, 281–314, 2004. 1

Stegen, G. R., K. Bryan, J. L. Held, and F. Ostapoff, Dropped horizontal coherence based on temperature profiles in the upper thermocline, *J. Geophys. Res.*, *80*, 3841–3847, 1975. 32

Sveen, J. K., Y. Guo, P. A. Davies, and J. Grue, On the breaking of internal solitary waves at a ridge, *J. Fluid Mech.*, *469*, 161–188, 2002. 155

Thorpe, S. A., The excitation, dissipation, and interaction of internal waves in the deep ocean, *J. Geophys. Res.*, *80*(3), 328–338, 1975. 10

Toole, J. M., K. L. Polzin, and R. W. Schmitt, Estimates of diapycnal mixing in the abyssal ocean, *Science*, *264*, 1120–1123, 1994. 6

Tseng, Y. H., and J. H. Ferziger, Mixing and available potential energy in stratified flows, *Phys. Fluids*, *13*(5), 1281–1292, 2001. 131

Venayagamoorthy, S. K., and O. B. Fringer, Numerical simulations of the interaction of internal waves with a shelf break, *Phys. Fluids*, *18*(1), doi:10.1063/1.2221,863, 2006. 27, 68

Venayagamoorthy, S. K., and O. B. Fringer, On the formation and propagation of nonlinear internal boluses across a shelf break, *J. Fluid Mech.*, *577*, 137–139, 2007. 39, 40, 41, 103, 106

Vlasenko, V., and N. Stashchuk, Three-dimensional shoaling of large-amplitude internal waves, *J. Geophys. Res.*, *112*, C11,018, 10.1029/2007JC004,107, 2007. 28

Vlasenko, V., L. Ostrovsky, and K. Hutter, Adiabatic behaviour of strongly nonlinear internal solitary waves in slope-shelf areas, *J. Geophys. Res.*, *110*(C4), C04,006, 2005. 33, 94

Vlasenko, V. I., and K. Hutter, Numerical experiments on the breaking of solitary internal waves over a slope-shelf topography, *J. Phys. Oceanogr.*, *32*, 1779–1793, 2002a. viii, 34, 35, 94

Vlasenko, V. I., and K. Hutter, Transformation and disintegration of strongly nonlinear internal waves by topography in stratified lakes, *Annales Geophysicae*, *20*, 1–17, 2002b. 34

Vlasenko, V. I., N. N. Golenko, V. T. Paka, K. D. Sabinin, and R. Chapman, Dynamics of baroclinic tides in the US shelf, *Izvestiya, Atmospheric and Oceanic Physics*, *33*(5), 651–663, 1997. 11, 12

Vlasenko, V. I., P. Brandt, and A. Rubino, Structure of large-amplitude internal solitary waves, *J. Phys. Oceanogr.*, *30*, 2172–2185, 2000. 15, 28, 58, 61

Wallace, B. C., and D. L. Wilkinson, Run-up of internal waves on a gentle slope in a two-layered system, *J. Fluid Mech.*, *191*, 419–442, 1988. 35, 36, 37, 106

Watson, K. M., B. J. West, and B. I. Cohen, Coupling of surface and internal gravity waves: a mode coupling model, *J. Fluid Mech.*, *77*, 185–208, 1976. 10

Wesson, J. C., and M. C. Gregg, Mixing at Camarinal sill in the Strait of Gibraltar, *J. Geophys. Res.*, *99*(C5), 9847–9878, 1994. 7

Winters, K. B., P. N. Lombard, J. J. Riley, and E. A. D'Asaro, Available potential energy and mixing in density-stratified fluids, *J. Fluid Mech.*, *289*, 115–128, 1995. 46, 114

Wunsch, C., and R. Ferrari, Vertical mixing, energy, and the general circulation of the oceans, *Annu. Rev. Fluid Mech.*, *36*, 281–314, 2004. 7, 44

Zhao, Z., and M. H. Alford, Source and propagation of internal solitary waves in the northeastern South China Sea, *J. Geophys. Res.*, *111*(C11012), doi:10.1029/2006JC003,644, 2006. 11

Zhao, Z., V. Klemas, Q. Zheng, and X.-H. Yan, Remote sensing evidence for baroclinic tide origin of internal solitary waves in the northeastern South China Sea, *Geophys. Res. Let.*, *31*, doi:10.1029/2003GL019,077, 2004. 10